TUDelft

Delft University of Technology

Vibration-based railway track condition monitoring

A physics-based digital twin approach

Shen, C.

Important note
To cite this publication, please use the final published version (if applicable).
Please check the document version above.

VIBRATION-BASED RAILWAY TRACK CONDITION MONITORING

A physics-based digital twin approach

BY C. SHEN

VIBRATION-BASED RAILWAY TRACK CONDITION MONITORING

A PHYSICS-BASED DIGITAL TWIN APPROACH

Vibration‑based railway track condition monitoring

A physics‑based digital twin approach

Dissertation

for the purpose of obtaining the degree of doctor
at Delft University of Technology
by the authority of the Rector Magnificus, prof. dr. ir. T.H.J.J. van der Hagen
chair of the Board for Doctorates
to be defended publicly on
Thursday 2 March 2023 at 10:00 o'clock

by

Chen SHEN

Master of Engineering in Communication and Transportation Engineering
Tongji University, China
born in Xiangyang, China.

This dissertation has been approved by the promotors.

Composition of the doctoral committee:

Rector Magnificus	chairperson
Prof. dr. Z. Li	Delft University of Technology, promotor
Prof. dr. ir. R.P.B.J. Dollevoet	Delft University of Technology, promotor

Independent members:

Prof. dr. ir. B.H.K. De Schutter	Delft University of Technology
Prof. dr. ir. E.C. Slob	Delft University of Technology
Prof. dr. M. Berg	KTH Royal Institute of Technology, Sweden
Prof. dr. J.L. Escalona Franco	University of Seville, Spain
Dr. ir. A. Zoeteman	ProRail

CONTENTS

SUMMARY

Vibration signals measured from railway vehicles and tracks contain useful information regarding track conditions and have been used as a cost-effective source for continuous track monitoring. A variety of physics-based and data-driven methods have been developed and applied for various track condition monitoring problems. A large amount of data have been, are being, and will be generated by the sensors mounted on operational trains and track. However, neither a data-driven only nor a physics-based only approach is sufficient to effectively assimilate these data. This motivates us to explore a new approach that integrates both methods.

The objective of this thesis is to propose and implement a physics-based digital twin approach for vibration-based railway track condition monitoring, as well as to demonstrate its capabilities through real-world applications.

Proposed digital twin framework

A conceptual physics-based digital twin framework is proposed for the vehicle-track interaction (VTI) system. The framework consists of two models to virtually represent a physical VTI system. A physics-based model that emulates the VTI system is used to generate a forward mapping from its track parameter space to a potential feature space of vibration signals. By multiple physics-based simulations, a data set can be generated containing discrete data points representing the inverse mapping from the feature space to the parameter space. Based on the data set, a data-driven Gaussian process (GP) regression model is trained and used to dynamically update the change of track parameters over time and space by assimilating the features of observed vibration data. The proposed framework combines the predictive power of the physics-based VTI model and the computational efficiency of the GP model.

Implementation

To implement the proposed digital twin framework, three key elements are needed, i.e., a set of clearly defined and **interpretable features** of observed vibrations, an **accurate physics-based model** to solve the forward problem, and an **efficient data-driven pipeline** to solve the inverse problem.

Chapter 2 contributes to an experimental approach to identify, sequence, and interpret the multiple frequency features measured by different techniques. The main outcome is a detailed frequency feature map for dynamic VTI in the frequency range of 50 Hz ~ 3000 Hz. A comprehensive field test campaign was carried out using three different measurement techniques, i.e., hammer tests (in both unloaded and loaded conditions), track-side, and axle-box acceleration (ABA) measurements, at a section of well-maintained plain track with no joints, crossings or wheel/rail surface defects. Based on the unloaded and loaded hammer test, a total of sixteen resonances are identified and sequenced based on an underlying physical principle: track and VTI system resonances occur at the lower and upper bounding frequencies of propagating track waves, respectively. With this frequency feature map, peak frequencies identified by different mea-

surement techniques can be associated with the corresponding resonances of the track or VTI system in a consistent and well-founded manner. The sequence patterns can serve as a key feature of a track or VTI system, and be used subsequently for evaluating model accuracy and monitoring track conditions.

Chapter 3 addresses whether and how observed frequency features can be correctly modelled. To this end, a comparative study is conducted for two types of commonly used VTI models, i.e., a low-fidelity beam and a high-fidelity continuum model. The problem we choose here is the wheel-rail impact at rail squats. This is because the excitation frequency of a squat with a typical length of 20 mm ~ 40 mm is approximately between 970 Hz and 1945 Hz (with a vehicle speed of 140 km/h), which is critical for the beam model that is conventionally considered accurate up to about 1500 Hz. Results show that both models can reproduce three dominant frequencies at 340 Hz, 890 Hz, and 1120 Hz in the contact force. The first two frequencies can be associated with two VTI system resonances following the principles in Chapter 2. The third is unique to the wheel-rail impact problem. The effect of various model assumptions on reproducing these features under different vehicle speeds and defect sizes is evaluated. In particular, it is found that the local inertia in the contact patch and stress wave propagation in solids, which can be considered in the continuum but not in the beam model, are critical factors that have been overlooked in previous research. By considering the local inertia in the contact patch, the continuum model produces a lower peak impact force than the beam model. The different modelling of the stress wave propagation in the rail leads to a deviation of track damping around the pin-pin resonance between the two models. As a result, the beam model is only comparable to the continuum model up to about 800 Hz. Above 800 Hz, the contact forces dominate at 890 Hz for the beam while at 1120 Hz for the continuum model.

Applications

In Chapters 4 and 5, a practical data-driven pipeline is implemented for solving the inverse identification problems. The proposed VTI digital twin approach is applied to two inverse identification problems, i.e., evaluating dynamic track stiffness in unloaded tracks by hammer tests (Chapter 4) and in loaded tracks by ABA (Chapter 5). The goal is to infer the stiffness of the railpad and ballast based on the frequency features measured by hammer tests and ABA. We demonstrate how the proposed digital twin approach enables robust, efficient, and high-resolution track stiffness evaluations.

In comparison to using only two features of a frequency response function (FRF) in conventional methods, our approach makes use of up to eleven frequency and magnitude features of an FRF for evaluating track stiffness by hammer tests. In addition, the proposed approach is shown to be robust to incomplete FRF feature measurement, i.e., the approach automatically adapts to the number of measured FRF features. It is also shown that the proposed approach outperforms three optimization-based algorithms both in terms of accuracy and efficiency.

For evaluating track stiffness by ABA, in comparison to existing techniques, our approach enables simultaneous evaluation of the stiffness of the railpad, sleeper, and ballast at sleeper spacing resolution. The evaluations are robust to changing track irregularities as we select distinct frequency features for track stiffness that are insensitive to track irregularities. We validate the proposed method in controlled laboratory condi-

tions by applying it to evaluate the track stiffness of a downscale test rig. We compare the results of the proposed method to those obtained by the hammer test method, as well as the observations of the track component conditions. Results show that the proposed approach is capable of capturing stiffness variations at individual fastened clamps and local substructure misalignments. We also demonstrate that ABA is more accurate than the hammer test method for evaluating track stiffness under loaded conditions.

The measurement and simulation results in this thesis contribute to a better understanding of the frequency features of VTI systems under different excitations. Frequently evaluating track stiffness by ABA can provide a better understanding and prediction of track geometry changes in space and time, making efficient and effective track maintenance, which can be performed on the right components (fastening or ballast) at the right places and the optimal time, possible.

SAMENVATTING

Trillingssignalen gemeten door spoorwegvoertuigen en sporen bevatten nuttige informatie over de spoorcondities en worden gebruikt als een kostenefficiënte bron voor continue spoor conditiebewaking. Een verscheidenheid van fysisch gebaseerde en data gedreven methodes zijn ontwikkeld en toegepast voor verschillende problemen met spoor conditiebewaking. Een grote hoeveelheid data werd, wordt en zal worden gegenereerd door de proliferatie van op operationele treinen en sporen gemonteerde sensoren. Nochtans volstaat noch een uitsluitend op data gedreven noch een uitsluitend op fysisch gebaseerde aanpak om deze gegevens effectief te assimileren. Dit motiveert ons om een nieuwe aanpak te verkennen die beide methoden integreert.

Het doel van dit proefschrift is het voorstellen en implementeren van een fysisch gebaseerde digitale tweeling aanpak voor trillingsgebaseerde spoor conditiebewaking, alsmede het demonstreren van de mogelijkheden ervan door middel van real-world toepassingen.

Voorgesteld raamwerk voor digitale tweeling

Een conceptueel fysisch gebaseerd digitaal tweeling raamwerk wordt voorgesteld voor het voertuig-baan interactie (VTI) systeem. Het raamwerk bestaat uit twee modellen om een fysiek VTI-systeem virtueel weer te geven. Een fysisch-gebaseerd VTI-model dat het VTI-systeem emuleert wordt gebruikt om een voorwaartse mapping te genereren van zijn spoorparameterruimte naar een potentiële kenmerkruimte van trillingssignalen. Door meervoudige op fysisch gebaseerde simulaties kan een gegevensreeks worden gegenereerd met discrete gegevensparen die de inverse afbeelding van de kenmerkruimte naar de parameterruimte weergeven. Op basis van de dataset wordt een data gedreven Gaussian process (GP) regressiemodel getraind en gebruikt om de verandering van de spoorparameters dynamisch bij te werken in tijd en ruimte door de kenmerken van de waargenomen trillingsgegevens te assimileren. Het voorgestelde raamwerk combineert de voorspellende kracht van het op fysisch gebaseerde VTI-model en de reken-efficiëntie van het GP-model.

Implementatie

Om het voorgestelde digitale tweeling raamwerk te implementeren zijn drie sleutelelementen nodig, namelijk een reeks duidelijk gedefinieerde en interpreteerbare kenmerken van waargenomen trillingen, een nauwkeurig fysisch model om het voorwaartse probleem op te lossen en een efficiënte data-gedreven workflow om het inverse probleem op te lossen.

Hoofdstuk 2 van dit proefschrift levert een bijdrage aan een experimentele benadering voor het identificeren, rangschikken en interpreteren van de meervoudige frequentiekenmerken gemeten door verschillende technieken. Het belangrijkste resultaat is een gedetailleerde frequentiekenmerkenkaart voor dynamische VTI in het frequentiegebied van 50 Hz ~ 3000 Hz. Er werd een uitgebreide veldtestcampagne uitgevoerd met gebruikmaking van drie verschillende meettechnieken, d.w.z. hamertests (zowel in onbelaste

als belaste toestand), metingen langs het spoor en aspotversnellingmetingen (ABA), op een baanvak van goed onderhouden spoor. Op basis van onbelaste en belaste hamertests worden in totaal zestien resonanties geïdentificeerd en gerangschikt op basis van een onderliggend fysisch principe: resonanties van het spoor en het VTI-systeem treden op bij de grensfrequenties van voortplantende spoorgolven. Met deze frequentiekenmerkenkaart kunnen de door verschillende meettechnieken geïdentificeerde piekfrequenties op een consistente en gefundeerde manier in verband worden gebracht met de overeenkomstige resonanties van het spoor- of VTI-systeem. De opeenvolgingspatronen kunnen dienen als een belangrijk kenmerk van een spoor- of VTI-systeem, en vervolgens worden gebruikt voor het evalueren van de nauwkeurigheid van modellen en het bewaken van spoorcondities.

In hoofdstuk 3 wordt nagegaan of en hoe waargenomen frequentiekenmarken correct kunnen worden gemodelleerd. Daartoe wordt een vergelijkende studie uitgevoerd voor twee typen veelgebruikte VTI-modellen, te weten een low-fidelity beam en een high-fidelity continuüm model. Het probleem dat we hier kiezen is de impact tussen wiel en spoorstaaf bij squat. De excitatiefrequentie van een squat met een typische lengte van 20 mm ∼ 40 mm ligt ongeveer tussen 970 Hz en 1945 Hz (bij een voertuigsnelheid van 140 km/u), wat kritisch is voor het beam model dat conventioneel als nauwkeurig wordt beschouwd tot ongeveer 1500 Hz. Uit de resultaten blijkt dat beide modellen drie dominante frequenties bij 340 Hz, 890 Hz en 1120 Hz in de contactkracht kunnen reproduceren. De eerste twee frequenties kunnen worden geassocieerd met twee VTI-systeemresonanties volgens de principes in hoofdstuk 2. De derde is uniek voor het wiel-rail impact probleem. Het effect van verschillende modelaannames op de reproductie van deze kenmerken bij verschillende voertuigsnelheden en defectgrootten wordt geëvalueerd. In het bijzonder wordt gevonden dat de lokale traagheid in het contactvlak en de voortplanting van spanningsgolven in vaste stoffen, die wel in het continuüm maar niet in het beam model in aanmerking kunnen worden genomen, kritische factoren zijn die in eerdere onderzoeken over het hoofd zijn gezien. Door rekening te houden met de lokale traagheid in het contactvlak, levert het continuüm model een lagere piekimpactkracht op dan het beam model. De verschillende modellering van de voortplanting van de spanningsgolf in de spoorstaaf leidt tot een afwijking van de spoor-demping rond de pin-pin resonantie tussen de twee modellen. Als gevolg hiervan is het beam model slechts tot ongeveer 800 Hz vergelijkbaar met het continuü mmodel. Boven 800 Hz overheersen de contactkrachten bij 890 Hz voor de beam- en bij 1120 Hz voor het continuüm model.

Toepassingen

In hoofdstuk 4 en 5 wordt een praktische data-gedreven workflow geïmplementeerd voor het oplossen van inverse identificatie problemen. De voorgestelde VTI digitale tweeling wordt toegepast op twee inverse identificatie problemen, namelijk het evalueren van dynamische stijfheid in onbelaste spoor door hamertesten (Hoofdstuk 4) en in belast spoor door ABA (Hoofdstuk 5). Het doel is om de stijfheid van het railpad en de ballast af te leiden op basis van de frequentiekenmerken gemeten door hamertesten en ABA. We demonstreren hoe de voorgestelde digitale tweelingaanpak robuuste, efficiënte en hoge-resolutie spoorstijfheidsevaluaties mogelijk maakt. In vergelijking met het gebruik van slechts twee kenmerken van een frequentieresponsfunctie (FRF) in conven-

tionele methoden, maakt onze aanpak gebruik van maximaal elf frequentie- en magni-tudekenmerken in één enkele FRF voor de evaluatie van de stijfheid van het spoor door hamertests. Bovendien blijkt de voorgestelde aanpak robuust te zijn voor onvolledige meting van FRF-kenmerken, d.w.z. dat de aanpak zich automatisch aanpast aan het aan-tal gemeten FRF-kenmerken. Ook wordt aangetoond dat de voorgestelde aanpak beter presteert dan drie op optimalisatie gebaseerde algoritmen, zowel wat nauwkeurigheid als wat efficiëntie betreft.

Voor het evalueren van de spoorstijfheid door ABA, in vergelijking met bestaande technieken, maakt onze aanpak gelijktijdige evaluatie van de stijfheid van het railpad, de sleeper, en de ballast bij de resolutie van de afstand tussen sleepers mogelijk. De evaluaties zijn robuust tegen veranderende onregelmatigheden van het spoor, aange-zien we verschillende frequentiekenmerken selecteren voor spoorstijfheid die ongevoe-lig zijn voor spooronregelmatigheden. We valideren de voorgestelde methode in gecon-troleerde laboratoriumomstandigheden door deze toe te passen om de spoorstijfheid van een downscale test rig te evalueren. We vergelijken de resultaten met de voorgestelde methode met die verkregen met de hamertestmethode, evenals de waarnemingen van de condities van de spoorcomponenten. De resultaten laten zien dat de voorgestelde aanpak in staat is om stijfheidsvariaties op te vangen bij individuele bevestiger en bij lokale verkeerde uitlijning van de onderbouw. We tonen ook aan dat ABA nauwkeuri-ger is dan de hamertestmethode voor het evalueren van de spoorstijfheid onder belaste toestand.

De meet- en simulatieresultaten in dit proefschrift dragen bij aan een beter begrip van de frequentiekenmerken van VTI-systemen onder verschillende excitaties. Frequente evaluatie van de spoorstijfheid door ABA kan leiden tot een beter begrip en voorspelling van veranderingen in de spoorgeometrie in ruimte en tijd, waardoor efficiënt en effectief spooronderhoud kan worden uitgevoerd, dat kan worden uitgevoerd op de juiste com-ponenten (bevestiging of ballast) op de juiste plaatsen en de optimale tijd, mogelijk.

1

INTRODUCTION

1

1.1. WHY DO WE NEED A PHYSICS-BASED DIGITAL TWIN?

1.1.1. CONVENTIONAL VIBRATION-BASED CONDITION MONITORING

When we take a train, we feel vibrations. But the human body is only sensitive to vibrations ranging from several to tens of Hertz. Nonetheless, we can sometimes perceive that the ride gets bumpy in less well-maintained track sections. Modern sensing technologies mounted on trains and tracks enable continuous measurement of vibration signals sampled at tens of thousands of hertz, resulting in a large amount of data that carry useful information regarding the operational status of the infrastructure. This provides opportunities to exploit measured vibration signals either from the track or train to monitor the conditions of railway tracks.

The question is: how do we map observed vibration signals to the conditions of railway tracks? Vibration-based condition monitoring methods can be classified broadly into two categories: data-driven and physics-based approaches [1–5]. Next, we summarize the work pipelines for each approach with examples in railway applications, as shown in Figure 1.1.
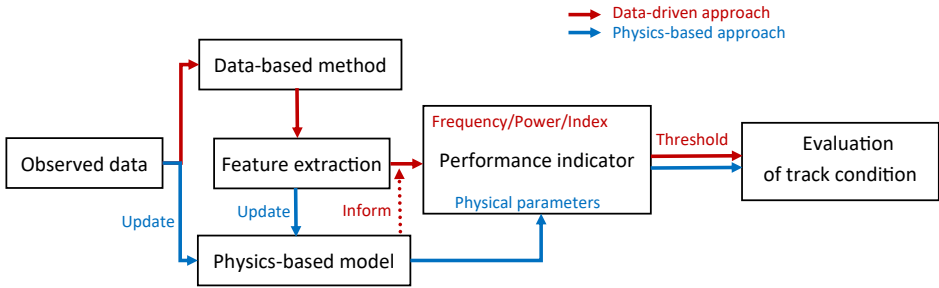
Figure 1.1: Work pipelines for conventional vibration-based condition monitoring methods.

Data-driven approaches employ data-based methods to extract potential features from observed vibration signals. Such data-based methods can be non-parametric, aiming to transform the measured time series into the frequency or time-frequency domain. Examples of non-parametric methods include the power spectrum density (PSD) [6, 7], short-time Fourier transform (STFT) [8, 9], wavelet transform (WT) [10, 11], frequency domain decomposition (FFD) [12] and empirical mode decomposition (EMD) [13–15]. On the other hand, parametric models, such as the Statistical Time Series (STS) method [16] and modal models for frequency response functions (FRFs) [17], can be used to fit measurement data. After applying these methods, performance indicators (PIs) are usually defined in the form of characteristic frequencies, signal powers, or indexes. To evaluate the track condition, data-driven approaches usually require defining a baseline state and a threshold for PIs. With the development of artificial intelligence (AI), machine learning (ML) or deep learning (DL) algorithms have been increasingly used to facilitate data-driven approaches at different stages, such as extracting features and correlating PIs with track conditions [18].

Physics-based approaches require a physics-based model that emulates the vehicle-

track interaction (VTI) system. Using observed data or extracted features thereof, parameters of the physics-based model can be updated by minimizing the differences between model outputs and observations. This model updating process is usually formulated as an optimization problem and solved iteratively. Since the updated parameters have clear physical interpretations, they can be directly used to evaluate the track condition. Besides, as physics-based models offer predictive power, they can be used to evaluate the 'what-if' situations and thus inform data-driven approaches for unseen data. This is particularly useful for feature selections or determining thresholds for PIs.

1.1.2. PROBLEMS WITH CONVENTIONAL METHODS

One major problem with the conventional methods discussed above is their lack of ability to effectively assimilate the large amount of data that has been, is being, and will be generated by the proliferate sensors mounted on operational trains and tracks. If these data cannot be processed in time and translated into useful insights into the track condition, the requirement for data storage will grow, eventually to infinity, as time goes on.

One may argue that using data-driven approaches alone can solve the issue of data assimilation, as they are in general much faster than physics-based approaches in issuing evaluations based on observed data. However, despite their computational efficiency, data-driven approaches show several limitations in applying to vibration-based railway track condition monitoring.

First, vibration data acquired from VTI systems are not essentially "big data". This is because data-driven approaches rely on large quantities of labelled data for training and such data are scarce for vibration measurements in rail applications. Furthermore, vibration signals measured from trains and tracks are partial observations of a high-dimensional VTI system. For example, with only measured axle box accelerations (ABA) and no additional information, it is difficult to infer the vibrations of rail or sleeper using data-driven approaches.

Second, data-driven approaches lack predictive power. For example, a data-driven model trained for rail squat detection cannot be extrapolated for the detection of other rail surface defects or a completely different task such as track stiffness evaluation. This means that a large amount of measured data would still be stored and re-evaluated every time a new task is required.

Therefore, we argue that physics-based approaches are indispensable for solving railway engineering problems due to their interpretability and predictive power. The major issue with physics-based approaches is that iteratively updating physics-based models is too computationally intensive and therefore not suitable for assimilating a large amount of data.

1.1.3. PHYSICS-BASED DIGITAL TWINS: A PARADIGM SHIFT

Given that neither a data-driven only nor a physics-based only approach is sufficient for vibration-based railway track condition monitoring, it is imperative to explore a new paradigm that combines both approaches. This new paradigm is different from simply informing data-driven approaches using insights from physics-based models, as has been shown in Figure 1.1. It requires a framework that integrates both methods and enables frequent communications between observed data and physics-based models.

The emerging digital twin technology offers a potential solution for the new paradigm. Different definitions can be found for digital twins in different applications. Here we adopt a definition that is best suited for the context of this thesis; a digital twin is defined as [19]

*"**A set of virtual information constructs** that mimic the structure, context, and behaviour of an individual/unique physical asset, or a group of physical assets, is **dynamically updated** with data from its physical twin throughout its life cycle and **informs decisions** that realize value."*

A digital twin, as can be seen from the definition above, consists of three key elements. The first two elements, i.e., a set of virtual information constructs and a strategy to dynamically update the digital twin, are the focus of this thesis. The third element is related to the decision-making process, such as providing control strategies for the physical asset. In railway applications, this usually refers to informing decisions of, e.g., predictive maintenance planning, which is beyond the scope of this thesis.

1.1.4. A digital twin framework for VTI Systems

While several conceptual physics-based digital twin framework has been proposed[20–22], they have not been applied in rail applications. **The first contribution of this thesis is to propose a physics-based digital twin framework for the VTI system**. We now give a brief introduction to the VTI digital twin framework.

1.1.4.1. Virtual information constructs

The virtual information constructs are abstractions of a physical VTI system, including four quantities and two models, as shown in Figure 1.2.

The four quantities are defined following [22] to represent the input, output, and state variables of the digital twin and its associated physical VTI system, as shown in Figure 1.2(a).

- *The physical state* can be viewed as a vector that represents the track conditions by a set of real-world track properties. We use S to denote the physical state space, i.e., the space of all possible states. These properties can range from micro-scale to mesoscale (e.g. rail defect sizes), and up to macro-scale (e.g. track geometries). Therefore, space S is a potentially very high-dimensional space and not all parameters are directly observable.

- *The observations* refer to the vibration signals measured from sensors mounted on vehicles and tracks. In practice, vibration signals usually need to be transformed to a feature space X for further analysis.

- *The digital state* is the counterpart of the physical state in the digital twin. It includes all the necessary parameters and assumptions for defining a physics-based VTI model, such as track parameters, irregularities, boundary conditions, element types, mesh sizes, etc. It differs from the physical state in that the digital state space D has a much lower dimension than the physical state space S because of the assumptions and simplifications made in the physics-based VTI model.

(a)

(b)
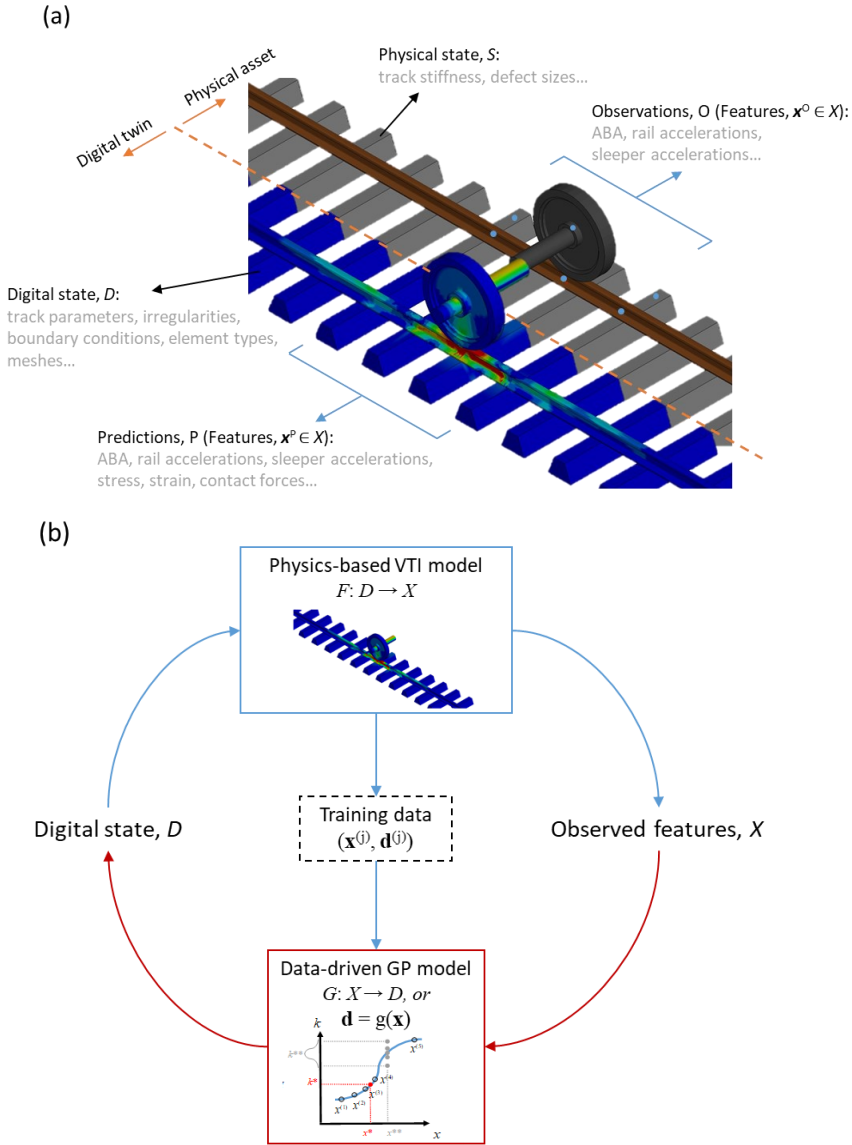
Figure 1.2: Digital twin framework for VTI system. (a) Four quantities representing the digital twin and its associated physical VTI system. (b) Strategy for dynamically updating the digital state of the digital twin by combining a physics-based VTI model and a data-driven GP regression model.

- *The predictions* are the outputs of the physics-based VTI model given a certain digital state. The prediction space P has a higher dimension than the observation space O. For observable data, such as accelerations, it is required that predictions

1

and observations share the same feature space X. In addition, the prediction space also includes quantities that are not easily observable, such as the stress/strain field and contact forces.

1.1.4.2. STRATEGY FOR DYNAMICALLY UPDATING THE DIGITAL TWIN

Two models, i.e., a physics-based VTI model and a data-driven model, are developed to virtually represent the physical VTI system and define the relationships between the quantities, as shown in Figure 1.2(b).

Ideally, the physical state S should be assessed for track condition monitoring. However, S is usually not observable. We, therefore, assess the physical state of a VTI system through the lens of the digital state D of its digital twin. In particular, the task is to dynamically update the digital state $\mathbf{d} \in D$ using features of observed vibration data $\mathbf{x^o} \in X$. This task can be framed as an inverse problem, where we aim to find an inverse mapping from the feature space X to the digital state space D, denoted by

$$G : X \to D \tag{1.1}$$

To solve this inverse problem, the physics-based VTI model is used to generate a corresponding forward mapping from the digital state space D to the feature space X, i.e.,

$$F : D \to X \tag{1.2}$$

This allows us to generate $(\mathbf{x}^{(j)}, \mathbf{d}^{(j)})$ pairs for $j = 1, 2, \ldots, N$, by running N simulations with sampled, e.g., stiffness, values $\mathbf{d}^{(j)} \in D$ as inputs and a corresponding feature vector $\mathbf{x}^{(j)} \in X$ as an output. If the VTI model is capable of reproducing the observed feature space X, the $(\mathbf{x}^{(j)}, \mathbf{d}^{(j)})$ pairs are essentially a discrete form of mapping of Eq. 1.1. Subsequently, a data-driven model can be trained based on the $(\mathbf{x}^{(j)}, \mathbf{d}^{(j)})$ pairs to establish a continuous mapping of Eq.1.1. In this thesis, we propose to use the Gaussian process (GP) regression to train the data-driven model. The simulations and training are time-consuming and can be performed offline.

With the GP model representing Eq.1.1, we can dynamically update the digital state over time and space by assimilating features of observed vibration data. Because of the computational efficiency of the GP model, this process has the potential to be performed online or in near real-time.

1.2. CHALLENGES FOR BUILDING A DIGITAL TWIN FOR THE VTI SYSTEM

To implement the digital twin framework, three key elements are needed, i.e., a set of clearly defined and interpretable features of observed vibrations, an accurate physics-based model to solve the forward problem, and an efficient data-driven pipeline to solve the inverse problem. In the following sections, we discuss the challenges related to identifying frequency features from measured vehicle and track vibrations (section 1.2.1), accurate physics-based modelling (section 1.2.2), and applying the digital twin to solve inverse identification problems (section 1.2.3).

1.2.1. MEASUREMENT: IDENTIFYING FEATURES OF VEHICLE-TRACK VIBRATIONS

To solve the problem defined in Eq.1.1, the first task is to identify interpretable features from observed vibration signals, $\mathbf{x^o} \in X$, that are relevant for estimating the digital state D of the digital twin. For VTI systems, frequency-domain features of vibration signals are commonly used to evaluate railway track conditions [11, 23, 24]. Different frequency ranges of excitations can be associated with the resonant behaviours of different components in the VTI system [25], as shown in Figure 1.3, and thus can be used to monitor the condition of their corresponding components. In this thesis, we focus on the frequency range between 50 Hz and 3000 Hz, as it is most relevant for track components.
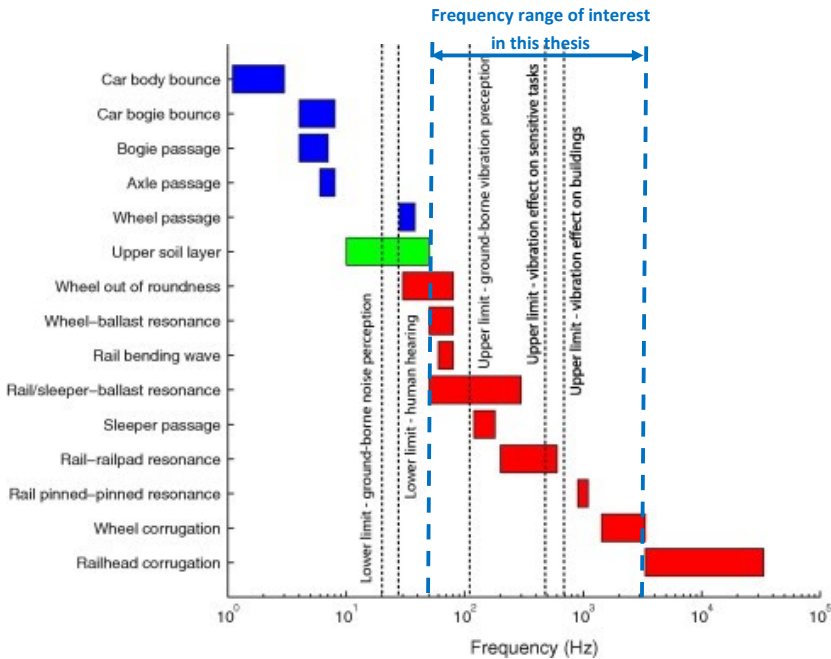
Figure 1.3: Typical frequency ranges associated with different components of the VTI system [25].

Using different measurement techniques, various frequency features have been identified and associated with different resonant behaviours. Based on track FRFs obtained by hammer tests [26], four distinct characteristic frequencies can be identified, corresponding to the **full-track (FT)**, **sleeper-anti (SA)**, **rail (R)**, and **pin-pin (PP)** resonances. With stiff rail pads, **sleeper (S)** resonances due to flexible sleeper bending become visible in rail FRFs [27]. From track-side measurement, the PSDs of measured track vibrations in plain tracks were presented in [6, 28], whereas no further interpretations of the frequency features were provided. From vehicle-based measurement, three peaks at 570 Hz, 830 Hz, and 1100 Hz were identified in the PSDs of measured contact forces [7]. These three peaks were linked to local **rail bending** modes between adjacent **wheelsets (RBW)** in a

bogie. In [9], three frequency bands between 50 Hz and 1000 Hz were observed in the spectrogram of ABA measured in plain tracks. These frequencies were empirically associated with track vibration modes (**P2**, **rail-on-railpad**, and **pip-pin resonances**).

As can be seen, multiple frequency features were associated with different resonant behaviours of the track or VTI system on a case-by-case basis. When these resonances are excited at the same time, the frequency ranges of certain resonances may overlap, and consequently, some resonances may become closely spaced. This makes it more difficult to identify these features. Furthermore, frequency features identified by different measurement techniques are inconsistent. In summary, there is still a lack of physical principles or practical tools to sequence, interpret and link the frequency features measured by different techniques. Thus, **the second contribution of this thesis is the establishment of a detailed frequency feature map for the vibrations of a VTI system between 50 Hz and 3000 Hz (Figure 1.4)**.
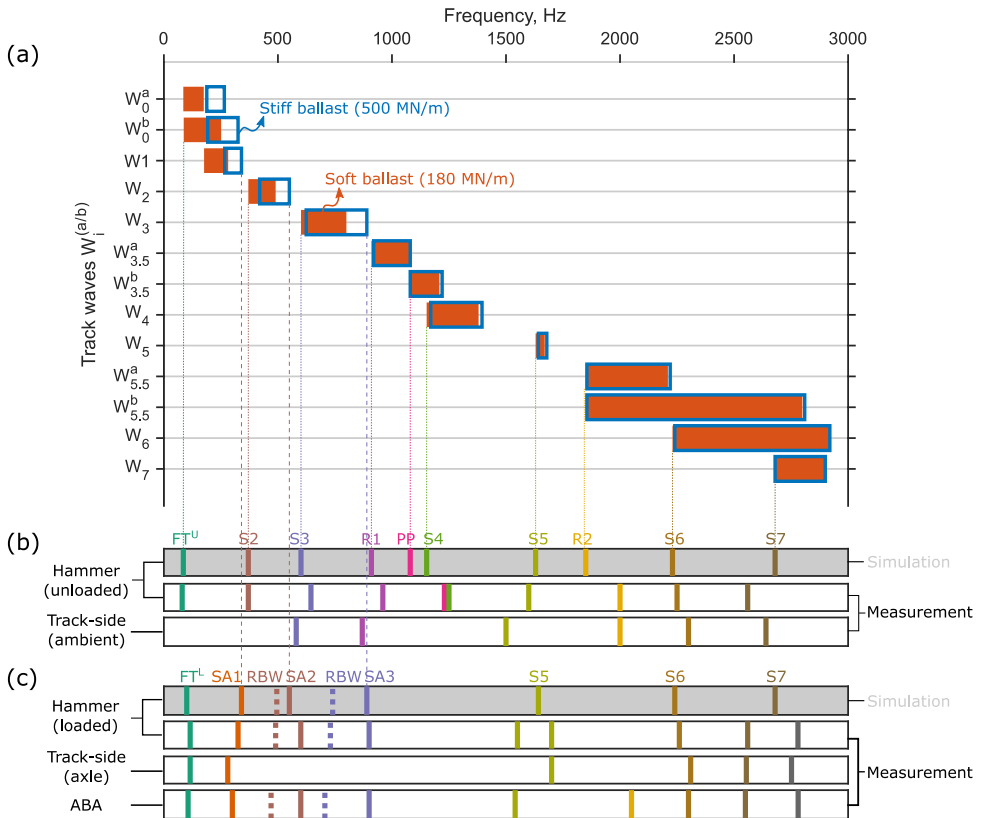
Figure 1.4: Frequency feature map in the frequency range of 50 Hz ~ 3000 Hz. (a) Pass bands of propagating track waves denoted by horizontal bars. (see Chapter 2). (b) and (c) show the sequence patterns, on which frequency features measured by different techniques are marked, sequenced, and linked to the resonances of (b) the track and (c) the VTI system.

To construct the map, we carried out a comprehensive field test campaign using

three different measurement techniques, i.e., hammer tests (in both unloaded and loaded conditions), track-side, and ABA measurements, at a section of well-maintained plain track with no joints, crossings or wheel/rail surface defects. This ensures that the VTI system was excited by random wheel-rail roughness with no clear peak in its PSD. As a result, all frequency features identified are caused by the resonant behaviour of the VTI system.

On the frequency feature map, a complete set of sixteen resonances of the track and VTI system are marked and sequenced based on an underlying **physical principle**: all resonances occur at the bounding frequencies of the pass bands of propagating track waves. With this frequency feature map, peak frequencies identified by different measurement techniques can be easily linked to the corresponding resonances of the track or VTI system in a consistent and principled manner. The sequence patterns in Figure 1.4 (b) and (c) can serve as a key feature of a track or VTI system and can be used subsequently for evaluating model accuracy (section 1.2.2) and monitoring track conditions (section 1.2.3).

1.2.2. Modelling: accurate physics-based VTI model

Another key element in the proposed digital twin framework is an accurate yet efficient physics-based VTI model that solves the forward mapping problem (Eq.1.2). The question would be whether the physics-based VTI model could correctly reproduce observed frequency features. Accurate simulations depend on two main factors: one is the model assumptions and the other is the model parameters (see the digital state in Figure 1.2(a)). While model parameters can be updated via the digital framework shown in Figure 1.2(b), appropriate model assumptions should first be determined.

Depending on the assumptions made, two types of models with different fidelities are commonly used for modelling VTI systems. The first is the beam model, in which rails, and in some cases, sleepers, are modelled using the Euler-Bernoulli or Timoshenko beams [29–38]. The second type is the full three-dimensional (3D) FE models [39–43], which drops the assumptions made in the beam theories and models the components of the VTI system (i.e. the sleeper, rail, wheel, or even railpads) with continuum (or solid) elements, referred to as the continuum models. When compared to low-fidelity models, such as the beam models, high-fidelity models, such as the continuum models, are usually more accurate and include more details in solutions. On the other hand, low-fidelity models are more computationally efficient, making them ideal for use as the VTI model in the digital twin framework.

It is critical to understand and quantify the effects of various model assumptions on simulation results in order to choose model assumptions that lead to a balance between accuracy and efficiency for a given problem. The problem we choose here is the wheel-rail impact at rail squats. This is because conventionally beam models are considered accurate up to about 1500 Hz [44]. The excitation frequency of a squat with a typical length of 20 mm ~ 40 mm [45] is approximately between 970 Hz and 1945 Hz (with a vehicle speed of 140 km/h). Therefore, this can be considered a critical case for beam models.

The third contribution of this thesis is to quantify the effects of various model assumptions made in the wheel, contact, and track models on the frequency features of

wheel-rail impact at squats, through comparisons of a beam and a continuum model.
An overview is shown in Figure 1.5. We identify the frequency features of wheel-rail impact force and associate them with resonances of the VTI system following the principles shown in Figure 1.4. We quantify the effect of various model assumptions on reproducing these features under different vehicle speeds and defect sizes. In particular, the effects of local inertia in the contact patch and stress wave propagation in solids are discussed in detail. With the continuum model, it is shown that the effective inertia of the rail that participates in the vibration of the wheel-track system comes first from the point of contact and then "gradually" expand as the waves spread out. While for the beam model, any vibration always involves the whole cross section, leading to larger inertia participating in the vibration at all times, which results in a larger peak impact force than the continuum model. The different modelling of the stress wave propagation in the rail leads to a deviation of track damping around the pin-pin resonance between the two models. As a result, the beam model is only comparable to the continuum model up to about 800 Hz. Above 800 Hz, the contact forces dominate at 890 Hz for the beam while at 1120 Hz for the continuum model.
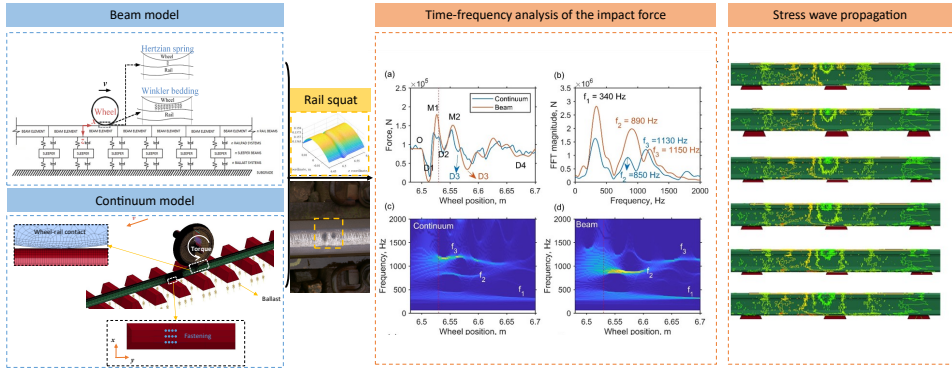
Figure 1.5: Comparison of two VTI models with different fidelities for simulating wheel-rail impact at squats.

1.2.3. APPLICATIONS: TOWARD ROBUST, EFFICIENT AND HIGH-RESOLUTION TRACK STIFFNESS EVALUATIONS

To demonstrate the practical applications of the proposed VTI digital twin, we apply it to two inverse identification problems, i.e., evaluating dynamic track stiffness in unloaded tracks by hammer tests and in loaded tracks by ABA.

For unloaded tracks, dynamic track stiffness is commonly measured using hammer tests and presented in the form of FRFs. Track FRFs have been widely used to identify track parameters [46–51]. Conventionally, ballast and railpad stiffness are manually 'tuned' and identified by fitting simulated FT and R resonances, respectively, to measured ones. However, when more resonances occur in the FRF (as shown in Figure 1.4), manual tuning becomes less robust as it cannot make use of all the available frequency features. Alternatively, optimization-based methods can be adopted [17, 52–55] by fit-

ting simulated FRFs to measured ones. Optimization-based methods are more robust than manual tuning but still lack efficiency.

For tracks subjected to dynamic train loading, dynamic track stiffness can be evaluated using track-side [23, 56, 57] and train-borne measurements [28, 58–65]. Compared to track-side methods, train-borne methods especially with in-service vehicles are more cost-effective and allow for continuous surveys of the entire rail network. Major issues with train-borne methods are the difficulty of obtaining a measurement resolution at the sleeper spacing level and distinguishing the stiffness between different layers.

The last contribution of this thesis is to demonstrate how the proposed physics-based digital twin approach could be used for evaluating dynamic track stiffness. To this end, we establish a practical data-driven pipeline for solving inverse identification problems, as shown in Figure 1.6. Note that it is called a data-driven pipeline because it generates or utilizes data at each step, although some of the data are generated by the physics-based VTI model.
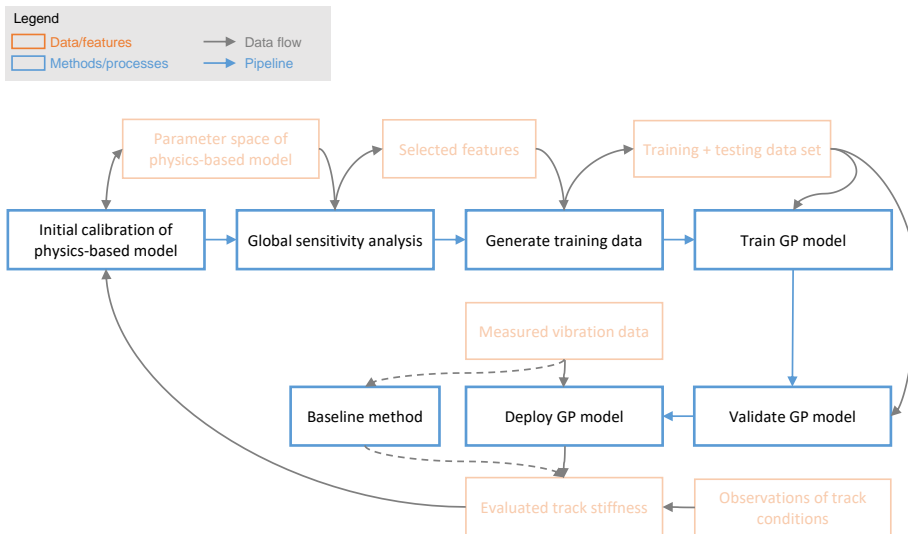
Figure 1.6: Data-driven pipeline for application of the physics-based digital twin.

Furthermore, **we demonstrate how the data-driven pipeline enables robust, efficient, and high-resolution track stiffness evaluations**. Robust evaluations are demonstrated in three aspects. First, in comparison to using two FRF features in conventional methods, our approach makes use of up to eleven frequency and magnitude features of a single FRF. Second, the GP model, as a non-parametric Bayesian model, inherently provides uncertainty quantifications for its predictions. Therefore, it automatically detects unreliable predictions by issuing large confidence intervals, which may indicate modelling errors or measurement noise. Third, track stiffness evaluations by ABA are robust to changing track irregularities because we select distinct frequency features for track stiffness that are insensitive to track irregularities. In addition, the proposed approach

1

is capable of performing rapid assessments of track stiffness and can be easily scaled to long track sections. In comparison to existing vehicle-based techniques, our approach enables simultaneous evaluation of the stiffness of the railpad, sleeper, and ballast at sleeper spacing resolution by ABA.

1.3. RESEARCH OBJECTIVES, QUESTIONS AND SCOPES

The objective of this thesis is to propose, implement, and apply a physics-based digital twin approach for vibration-based railway track condition monitoring. The main research question is:

*How can we build a **physics-based** digital twin for the VTI system that can translate **features** of measured vibration signals into the conditions of its associated physical track asset robustly and efficiently?*

The following questions are addressed for the implementation and application of the digital twin.

Observed features. How can we identify and sequence the frequency features of a VTI system measured by different techniques, as well as associate them with the resonant behaviours of the track or VTI system in a consistent and principled manner? For this question, we focus on the frequency features caused by the resonant behaviour of the VTI system in the frequency range between 50 Hz and 3000 Hz. Frequency features caused by external excitations, such as crossings, joints or wheel/rail defects, are not considered.

Accurate physics-based VTI model. How could the observed frequency features and the corresponding resonances be correctly modelled using physics-based VTI models? What are the effects of the modelling assumptions made in each component on the simulated frequency features? For these questions, we focus on a beam and a continuum model for the wheel-rail impact problem at squats.

Efficient data-driven pipeline. How can we combine a physics-based VTI model with data-driven models to generate an efficient pipeline for solving inverse identification problems?

Application to track stiffness evaluation. How does the digital twin framework enable robust, efficient and high-resolution track stiffness evaluations?

1.4. THESIS OUTLINE

Figure 1.7 shows the outline of this thesis.

Chapter 1 proposes a physics-based digital twin framework for the dynamic VTI system.

The implementation and application of the proposed framework comprise the main body of the thesis. Three key elements are implemented, i.e., a set of clearly defined and interpretable features of observed vibrations (Chapter 2), an accurate physics-based model (Chapter 3), and an efficient data-driven pipeline (Chapters 4 and 5).

Chapter 2 establishes a detailed frequency feature map of a VTI system through an extensive field measurement campaign using different measurement techniques.

Chapter 3 investigates how different model assumptions can affect simulation results, specifically the frequency features identified in Chapter 2, by comparing a beam and a continuum model for the wheel-rail impact at rail squats.

Chapter 4 and 5 implement a data-driven pipeline and apply the physics-based digital twin approach to enable robust, efficient and high-resolution track stiffness evaluations.

Chapter 6 concludes the main outcomes and recommends future research directions.
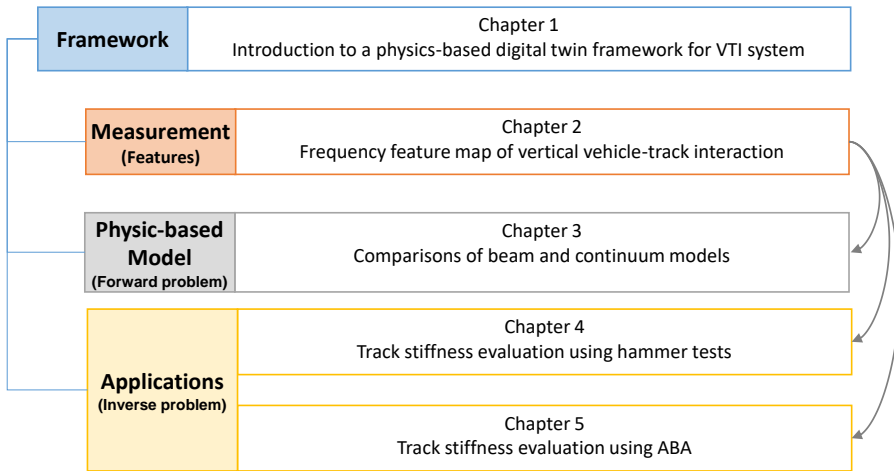
Figure 1.7: Data-driven pipeline for application of the physics-based digital twin.

2

FREQUENCY FEATURE MAP OF VERTICAL DYNAMIC VEHICLE-TRACK INTERACTION

The first task is to identify interpretable features from observed vibration signals that are relevant for railway track condition monitoring. This chapter investigates the frequency features of a vertical vehicle-track interaction (VTI) system caused by its resonant behaviour in the frequency range of 50 Hz to 3000 Hz.

Previous studies have identified multiple peak frequencies for dynamic VTI and interpreted them as different resonances of either the track or VTI system on a case-by-case basis. However, in each case, only a subset of the features was examined. Furthermore, frequency features identified by different measurement techniques are inconsistent. This chapter establishes a detailed frequency feature map for a more general scenario with a complete set of features.

In this chapter, three different measurement techniques are used, i.e., hammer, trackside, and axle-box acceleration (ABA) measurements. First, based on unloaded and loaded hammer tests, seven types and a total of sixteen resonances of the track and VTI system are distinguished, marked, and sequenced on the map. It is found that the resonances of the track and VTI system occur at the lower and upper bounds of the bounding frequencies of propagating track waves, respectively. With this map, we link the frequency features identified by trackside and ABA measurements to the resonances identified by hammer tests. Results show that the frequency features of the trackside measurement vary as the vehicle approaches, passes, and exits the instrumented location. Despite varying vehicle speeds, ABA measurements consistently capture all VTI system resonances, especially the six closely spaced resonances below 1000 Hz, with high resolution. Sequenced feature patterns can be used as key indicators for track condition monitoring.

This chapter will be submitted for international journal publication.

2

2.1. INTRODUCTION

When a rail vehicle travels along a track, it excites vibrations of the vehicle-track inter-action (VTI) system. It is critical to identify and interpret the frequency features of a VTI system from its vibrations, such as the magnitude and peak frequencies of the power spectrum. These features can be used to assess the condition of rail infrastructures [11, 23, 24], as well as to understand the mechanisms underlying the initiation and develop-ment of various rail defects [66–68].

The hammer test, trackside (or pass-by), and train-borne (or vehicle-based) meth-ods are the three most common methods for measuring the vibrations of a track or VTI system. Frequency features identified from these measurements can be interpreted as originating from two sources. One is related to the resonances of the VTI system, while the other is due to the characteristic frequencies of the excitations, such as those caused by sleeper passing and corrugations. This chapter focuses on the frequency features caused by the resonances of the VTI system in the frequency range of 50 Hz ~ 3000 Hz. In sections 2.1.1, 2.1.2, and 2.1.3, we review the related works for the three measurement techniques and discuss the challenges of identifying and interpreting the frequency fea-tures of a VTI system. The major contributions of this work are summarized in section 2.1.4.

2.1.1. HAMMER TEST

2.1.1.1. UNLOADED HAMMER TEST

In unloaded hammer tests, a track section is excited with impulse hammer forces and the track responses are measured to obtain the frequency response functions (FRFs). The purpose is to identify the resonant behaviours of the track. In general, four distinct char-acteristic frequencies can be identified in track FRFs, corresponding to the **full-track** (**FT**), **sleeper-anti** (**SA**), **rail** (**R**), and **pin-pin** (**PP**) resonances [26, 53].

To better understand the generation mechanisms of these resonances, track wave propagation characteristics were investigated analytically [69, 70]. It was found that these track resonances and anti-resonances occur at the bounding frequencies of prop-agating track waves. It should be noted that these conclusions were based on analytical track models with sleepers modelled as rigid masses.

As railpad stiffness increases, the coupling between the rail and sleeper strength-ens. Consequently, **sleeper** (**S**) resonances due to flexible sleeper bending become visi-ble in rail FRFs [27, 71, 72]. When sleepers are modelled as flexible beams, multiple track waves propagate between 300 Hz and 1000 Hz instead of a single wave predicted by rigid sleeper models [69, 70]. These additional track waves correspond to the bending modes of sleepers.

2.1.1.2. LOADED HAMMER TEST

Unloaded hammer tests were frequently used to estimate the track parameters of a VTI model [47–51]. However, track parameters estimated from an unloaded track may not accurately represent those under dynamic train loads. As a result, loaded hammer tests were also conducted [46, 73].

Added loads can affect track FRFs and frequency features in three ways.

First, because of the nonlinearity of ballast and railpad, their stiffness would increase due to increased static preloads. For example, in [46], preloads were applied by a vertical cylinder mounted on an instrumented wagon. The preloads were decoupled from the track via soft springs placed between the cylinder and the rail. Differences between the loaded and unloaded FRFs at the loading point were observed at frequencies up to about 500 Hz.

Second, when a rail vehicle is used as the preload, see e.g. in [73], apart from the effect of static wheel loads, wheel masses are also coupled to the track via wheel-rail contact stiffness. In this case, if the excitation point is close enough to the wheel load, the measured FRF represents the coupled dynamics of the VTI system rather than the track alone. In practice, however, because of the existence of the wheel at the loading point, hammer excitations were usually applied one or two sleeper spans away from the loading point. For example, loaded FRFs were found to be affected at frequencies below approximately 150 Hz with the hammer excitation at one sleeper span away from the loading point [73]. In this study, we perform loaded hammer tests with excitations directly at a wheel loading point to identify the VTI system's resonances.

Third, when a track is loaded with multiple wheels, three additional resonance peaks can be observed between approximately 400 Hz and 1200 Hz in measurements [74, 75]. By using VTI models, these resonances were related to local **rail bending** modes between adjacent **wheelsets** (**RBW**) in a bogie. Note again, sleepers were modelled as rigid masses or excluded in these analyses. The RBW resonances happen to be in the same frequency range as the sleeper bending resonances discussed in section 2.1.1.1. However, neither experimental nor analytical evidence indicates that both types of resonances coexist. This chapter presents a more general scenario where both types of resonance can be excited simultaneously at frequencies between 300 Hz and 1200 Hz. This results in multiple peak frequencies in this frequency range, which makes it more difficult to relate these frequencies to the correct resonances.

2.1.2. TRACKSIDE MEASUREMENT

Trackside or wayside measurement techniques use sensors (such as accelerometers or strain gages) mounted on a track section to measure its dynamic responses to passing vehicles. Ground vibrations and low-frequency VTI (less than about 50 Hz) have been extensively investigated via trackside measurements [76–79]. For high-frequency vibrations, trackside measurements have been primarily used to measure the dynamic responses of wheel-rail impact due to wheel flats [28], corrugations, rail joints [43, 80], and crossings [12, 81, 82]. Besides measuring track responses during train passages, trackside measurements can also be used to measure track responses prior to and following train passages, referred to as ambient vibrations [12, 83]. As can be seen, previous research has focused primarily on low-frequency track or ground vibrations, as well as high-frequency vibrations caused by wheel-rail impact. In [6, 28], the power spectral density (PSD) of track vibrations caused by wheel-rail roughness was presented, whereas no further interpretations of the frequency features were provided regarding their link to the resonances of the track or VTI system. Therefore, there is still a lack of experimental evidence and physical interpretations of the frequency features from trackside measurements in the frequency range of 50 Hz to 3000 Hz.

2.1.3. TRAIN-BORNE MEASUREMENT

In comparison to trackside measurement, train-borne measurement techniques are more suitable for continuous monitoring of rail infrastructure. Vibration signals can be obtained from sensors mounted on different parts of operational vehicles, such as the axle box, bogie frame, and car body [10, 84–86]. Frequency features of measured train-borne vibrations play a vital role in applications such as track condition monitoring and determining the mechanism of rail defect initiation. For example, using ABA measurements, two major characteristic frequencies at around 300 Hz and 1000 Hz have been identified for rail squats [11]. An increase in wavelet power around these two frequencies above a predefined threshold can be used as an indicator for squat detection. In [7], three peaks at 570 Hz, 830 Hz, and 1100 Hz were identified in the PSDs of measured contact forces on a corrugated track. These three peaks were linked to three RBW resonances, as confirmed by simulation results using a VTI model. In [9], three frequency bands between 50 Hz and 1000 Hz were observed in the spectrogram of measured ABA. These frequencies were empirically associated with track vibration modes (P2, rail-on-railpad and pip-pin resonances) without cross-validation against other measurement or simulation results.

2.1.4. CONTRIBUTIONS OF THIS CHAPTER

Multiple frequency features (FT, SA, S, R, PP and RBW) were associated with different resonances of the track or VTI system on a case-by-case basis. This causes two main problems. First, in each case, only a subset of the features was examined. However, when these features are present simultaneously, the frequency ranges of certain resonances may overlap [25], causing some resonances to become closely spaced. This makes it more challenging to relate these features to the resonances. Additionally, the frequency features identified by different measurement techniques in different cases are inconsistent. It remains unclear how the frequency features measured by different techniques are related to each other.

This chapter contributes to a better understanding of the frequency features of dynamic VTI by constructing a detailed frequency feature map for a VTI system between 50 Hz and 3000 Hz (in Section 2.4.3). On the frequency feature map, a complete set of sixteen resonances of the track and VTI system are marked and sequenced based on an underlying physical principle related to propagating track waves. The frequency features identified by different measurement techniques can be correlated with each other and linked to the resonances of the track or VTI system using this map in a consistent and explainable manner.

To construct the frequency feature map, we carried out a comprehensive field test campaign using three different measurement techniques, i.e., hammer tests (in both unloaded and loaded conditions), trackside, and ABA measurements, all at the same track location and with varying vehicle speeds between 80 km/h and 200 km/h (Section 2.2). Based on the unloaded and loaded hammer tests, we identify seven types and a total of sixteen resonant frequencies for the track and VTI system (Section 2.3.1 and 2.3.2). Additionally, we reveal the underlying structure of these resonances based on propagating track waves (Section 2.3.3). Section 2.4 shows the spectral power and peak frequencies of the vibration signals measured from the trackside and axle boxes. The peak frequencies are linked to track or VTI system resonances by comparing them to hammer test results.

Section 2.5 discusses how the findings in this chapter differ from and relate to previous studies. Conclusions are drawn in section 2.6.

2.2. FIELD TEST SETUP

2.2.1. HAMMER TEST

2.2.1.1. UNLOADED CONDITION

The test site is located in Romania at Faurei Railway Test Center. The field test was carried out on a section of a well-maintained ballasted track with no joints, crossings or wheel/rail surface defects. This ensures that the VTI system was excited by random wheel-rail roughness and that the frequency features identified are caused by the resonant behaviour of the VTI system. The track system consists of UIC60 E1 rails, Vossloh W14 fastenings, prestressed concrete sleepers (type B70-W60) with 600 mm spacing, and a ballast layer. We installed 11 accelerometers (PCB 356B21, three-dimensional) on the rail, and four accelerometers (Bruel & Kjaer 4514-004, one-dimensional) on the sleeper, see Figure 2.1. Rail accelerometers were placed over two sleeper spans at seven locations: above the sleeper supports and at ½ and ¼ sleeper spans. Three accelerometers were attached to the rail head, web, and foot, respectively at two locations, i.e. above a sleeper (A6, A7 and A8) and at a mid-span (A2, A3 and A4).

We used two types of hammers for the hammer test, i.e. a small hammer that weighs 0.32 kg (PCB 086D05) and a big hammer that weighs 5.5 kg (PCB 086D50). Hammer excitations were applied at seven locations on the rail top above each rail accelerometer location, see Figure 2.1 (a). The impact was repeated several times for each measurement with each hammer until at least five impacts showed good coherence.
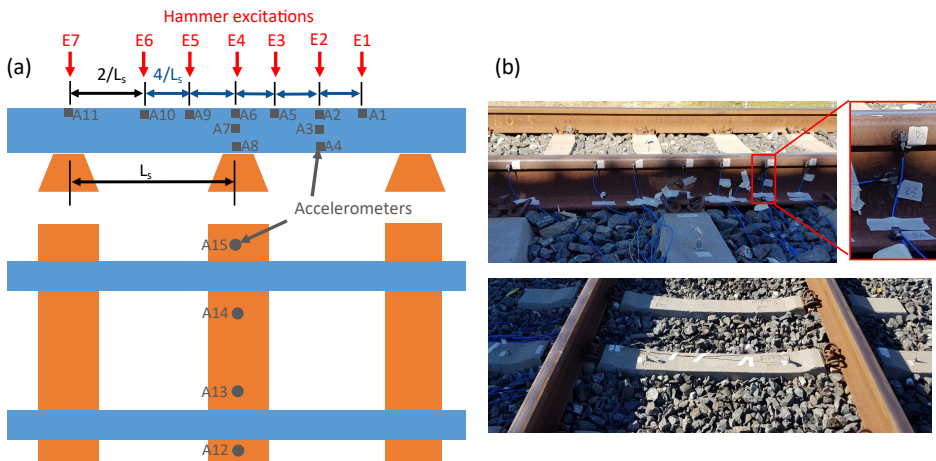

Figure 2.1: Hammer test setup in the unloaded condition. Accelerometers on the rail are three-dimensional and labelled as A1 ~ A11. Accelerometers on the sleeper are one-dimensional (vertical) and labelled as A12 ~ A15. Seven hammer excitation locations are indicated by the red arrows.

2.2.1.2. Loaded condition

To investigate the dynamic characteristics of the VTI system, a passenger wagon was positioned with a wheel directly above the instrumented track section, as shown in Figure 2.2 (a). The sensor configuration is identical to that of the unloaded condition. Hammer excitations were applied at three locations, as shown in Figure 2.2 (b) and (c). Excitation location 2 was on the rim of the wheel at the wheel-rail contact location. With this impact location, it is expected that the eigenmodes of the wheel-track system will be excited. Excitation locations 1 and 3 were on the rail top with one sleeper spacing away from the wheel load. At these locations, the track is still in the loaded condition due to the wheel load, while the effect of wheel inertia coupled to the track is less predominant. Besides, because excitation location 1 was between the two wheels in a bogie, it is expected that the rail waves reflected between the two wheels [74] will also be excited.
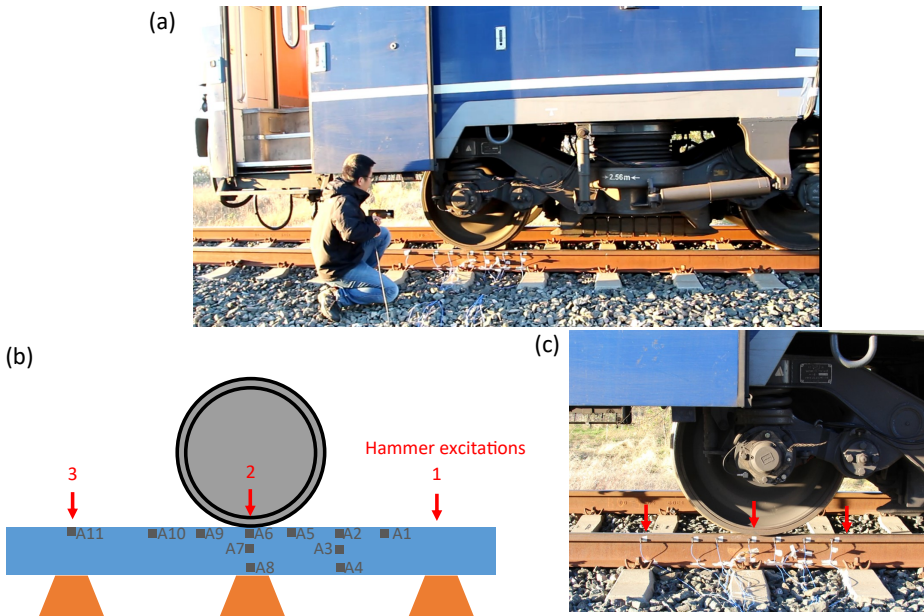
Figure 2.2: Hammer test setup in the loaded condition. (a) A wheel of a passenger wagon was placed on the instrumented track section. (b) and (c) show the hammer excitation locations.

2.2.2. Trackside and ABA measurement

The measurement train consists of a six-axle locomotive and a four-axle passenger wagon (see Figure 2.3). The ABA measurement system that has been used in [11, 24] was installed on the passenger wagon. It includes three major components, i.e., accelerometers mounted on axle boxes, a GPS antenna mounted on the vehicle roof and a tachometer to measure the vehicle speed. In this case, accelerometers were installed on all eight axle boxes of the passenger wagon.

The measurement site has a ring track with a total length of 13.7 km. The instru-

mented track location, as shown in Figure 2.1 and Figure 2.2, was located at approximately the center of a 950 m long straight track. The track section is well-maintained with no joints, crossings or wheel/rail surface defects. This ensures that the VTI system was excited by random wheel-rail roughness with no clear peak in its PSD. As a result, all frequency features identified are caused by the resonant behaviour of the VTI system. The measurement train ran in laps over the instrumented location at five target speeds (80, 120, 140, 180 and 200 km/h) in the same direction. The measurement train ran five laps at each speed. During the entire measurement, ABA and GPS were measured with sampling frequencies of 25600 Hz and 1 Hz, respectively. Accelerations of the track were recorded during the passages of the measurement train. The recordings started and ended when the measurement train was approximately 100 m before and 200 m after the instrumented track section, respectively. The sampling frequency for the trackside measurement was 25600 Hz.

Figure 2.3: Test setup of the trackside and ABA measurement. (a) The measurement train and ABA system. (b) Illustration of the ABA and trackside measurement at the instrumented location with various vehicle speeds. The instrumented location and configuration are the same as the hammer test.

2.3. FREQUENCY FEATURES BY HAMMER TEST

In this section, we identify the resonant frequencies of the unloaded and loaded track system using hammer tests (sections 2.3.1 and 2.3.2). The hammer test results are used to validate two FE models for the unloaded and loaded tracks. To reveal the sequence of these resonances, we use the validated FE models to map the resonant frequencies to the bounding frequencies of propagating track waves (Section 2.3.3).

2.3.1. UNLOADED TRACK

Figure 2.4 shows the unloaded rail receptances measured at mid-span (excited at E2 shown in Figure 2.1) and above sleeper support (excited at E4). Simulated receptances are also shown for comparison. A two-layer discretely supported FE track model was used for the simulations, see Figure 2.4 (e). The rails and sleepers were meshed with Timoshenko beam elements. At each node, only the vertical and in-plane rotational degrees of freedom are considered. The mesh sizes were determined by a convergence analysis, resulting in 10 elements per sleeper span for the rail and 20 elements per sleeper. The total length of the track model is 60 m with 100 sleeper spans. Railpads were modelled using the Kelvin-Voigt (KV) model with an elastic spring and a viscous damper connected in parallel. Ballast was modelled as discretely distributed KV models under each sleeper node. The track parameters were determined by fitting the simulated receptance to the measured receptance (see Chapter 4 for how this is achieved) and are listed in Table 2.1.

Table 2.1: Track parameter values used in the simulations.

Component	Parameter	Value
Rail	Mass per meter	60 kg/m
	Young's modulus	210 GPa
	Poisson's ratio	0.3
	Moment of inertia	3.048×10^{-5} m^4
	Density	7800 kg
	Area of cross section	7.692×10^{-3} m^2
	Timoshenko shear coefficient	0.4
Rail pad	Stiffness	1500 MN/m
	Damping	67.5kNs/m
Sleeper	Young's modulus	74.6 GPa
	Poisson's ratio	0.17
	Moment of inertia (averaged)	1.375×10^{-4} m^4
	Density	2500 kg/m^3
	Area of cross section (averaged)	0.043 m^2
	Timoshenko shear coefficient	0.833
	Length	2.58 m
	Spacing	0.6 m
Ballast	Stiffness	180 MN/m
	Damping	120 kNs/m

Several resonant frequencies can be observed in Figure 2.4, corresponding to four types of track resonances. The first resonance occurs at around 80 Hz. It is the full-track (FT) resonance, where rail and sleeper vibrate together at rail seats, with rigid sleeper modes. The pin-pin resonance (PP) at approximately 1200 Hz is another distinct resonance that can only be seen in the point receptance at mid-span, see Figure 2.4 (a).

The remaining frequencies correspond to either sleeper (S) or rail (R) resonances. In the current case, six sleeper resonances ($S_2 \sim S_7$) and two rail resonances (R_1 and R_2) can be identified in rail receptances below 3000 Hz. The primary distinction between
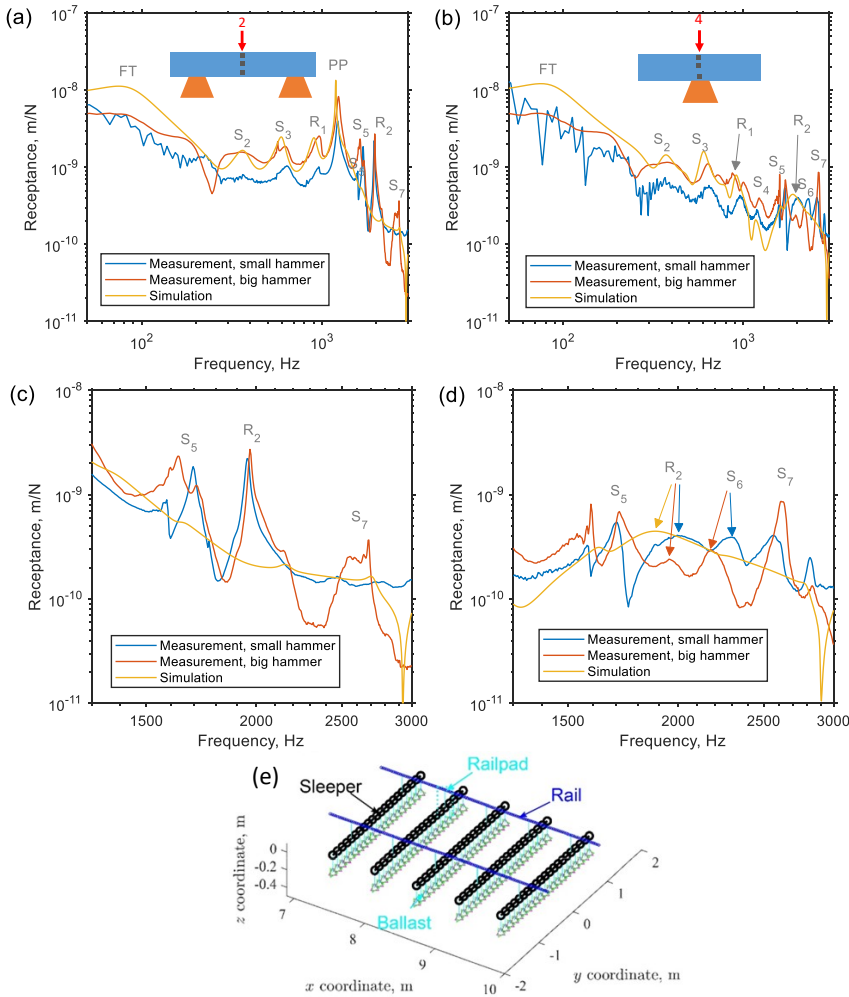
Figure 2.4: Rail receptances for the unloaded track. (a) Point receptance at mid-span. The track was excited at E2 and responses were measured at A2, A3 and A4 (averaged). See Figure 2.1 for the test setup. (b) Point receptance above a sleeper. The track was excited at E4 and responses were measured at A6, A7 and A8 (averaged). (c) and (d) show the zoom-in view of (a) and (b) between 1300 Hz and 3000 Hz. (e) shows the finite element track model used for the simulations.

the rail and sleeper resonances is the rail-sleeper relation at rail seats. At sleeper resonances, rails and sleepers vibrate in phase together at rail seats, with S_n denoting the n th-order sleeper bending modes. At rail resonances, rails vibrate in anti-phase with sleepers at rail seats, with an infinity wavelength and a wavelength of $2Ls$ for R_1 and R_2, respectively, where Ls is the sleeper spacing. Please see section 4.3 for a more in-depth analysis. Detailed mode shapes for these track resonances can be found in Figure 4.4.

Figure 2.5 compares the measured and simulated sleeper receptances in the un-loaded condition. Simulated rail receptance is also shown in each subplot. Higher-order sleeper resonances S_5, S_6 and S_7 can be observed in measured rail and sleeper receptances but only correctly reproduced in simulated sleeper receptances. This could be because each railpad in the track model is simplified to a single spring-damper pair, rather than being distributed over an area as in real tracks. As a result, sleeper bending at rail seats cannot be effectively transmitted to the rail, especially when vibrating at high-order modes.
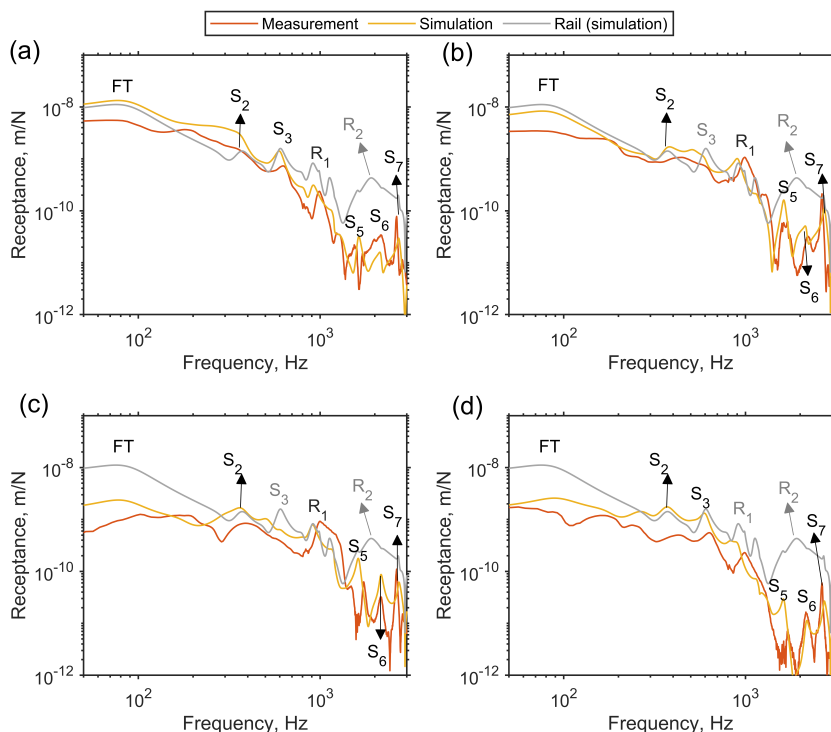
Figure 2.5: Sleeper receptances for the unloaded track. The track was excited at E4 and responses were measured at four sleeper sensors: (a) A12; (b) A13; (c) A14; (d) A15. See Figure 2.1 for the test setup.

2.3.2. LOADED TRACK

Four wheels of a bogie were added to the FE track model to simulate the hammer test under the load of a passenger wagon. Figure 2.6 shows a sketch of the model in the lateral view. We model each wheel as a two-degree-of-freedom system to better simulate wheel flexibility, with two masses (M_w and m_w) connected by a spring [7]. Because the wheel receptance was not measured for the current case, the wheel parameters were initially chosen as in [7] and then tuned to better fit the measurement results of loaded track receptances (see Figure 2.7). The smaller mass of the two masses is connected to the rail

with a linear Hertzian spring to model the wheel-rail contact stiffness. The hammer force is applied at the smaller mass to simulate the hammer test at a wheel load, as indicated by the blue arrow in Figure 2.6.
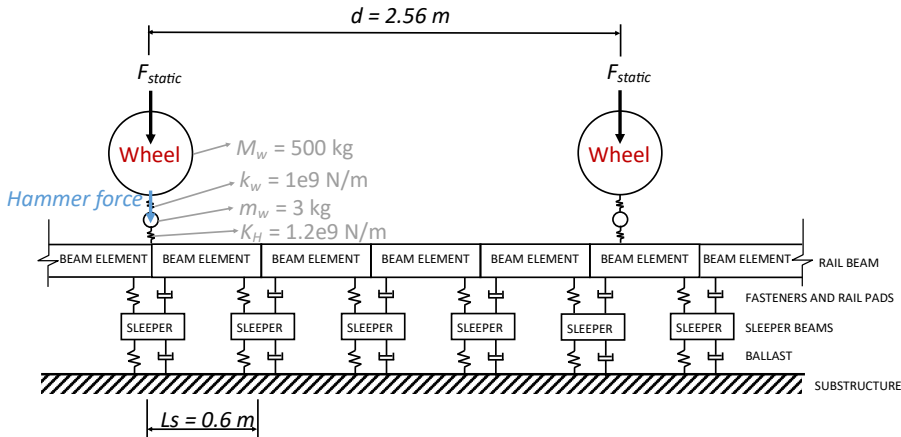
Figure 2.6: Sketch of the model used to simulate the hammer test under loaded conditions, in x-z (longitudinal-vertical) plane. The track model and coordinate system are the same as in Figure 2.4 (e)

Figure 2.7 shows the rail and sleeper receptances for the loaded track, with the hammer excitation on the loading point (excitation point 2 in Figure 2.2). Seven major resonant frequencies can be identified in both the measured and simulated receptances. The first resonant frequency corresponds to the loaded full-track $\left(FT^L\right)$ resonance, with the sleeper, rail and wheel vibrating together on track stiffness. This is also referred to as the P2 resonance in the literature. The three peaks between 100 and 1000 Hz correspond to three sleeper antiresonances ($SA_1, SA_2$ and SA_3). There are three high-order sleeper resonances at frequencies higher than 1000 Hz (S_5, S_6 and S_7). These high-order sleeper resonances, as in the case of the unloaded track, can only be reproduced in simulated sleeper receptance and not in rail receptance. In addition, minor peaks can be observed between SA resonances in the rail receptance, as indicated by the arrows in Figure 2.7 (a). Section 2.3.3 will provide more thorough explanations for these resonances (FT, SA, S, RBW and the minor resonances).

The unloaded hammer test (Figure 2.4) was used to identify track resonances, whereas the loaded hammer test (Figure 2.7) was used to identify resonances of the VTI system. To correlate track resonances with VTI system resonances, we compare track receptances in the loaded and unloaded conditions, see Figure 2.8.

The first resonance of the loaded track $\left(FT^L\right)$ occurs at approximately 100 Hz, which is higher than that of the unloaded track $\left(FT^U\right)$ at 80 Hz. In theory, the loaded track should have a lower FT resonance than the unloaded track (i.e., $FT^L < FT^U$) because of the added wheel mass to the track. A higher frequency of FT^L than FT^U could indicate an increase in track stiffness in the loaded condition. This can be confirmed with simulations, where the FT^L resonance is more accurately reproduced by increasing the ballast
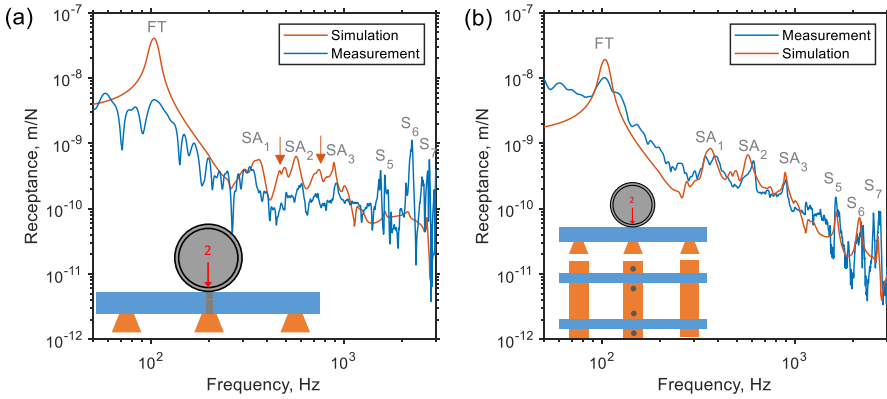
Figure 2.7: Track receptances for the loaded track. The VTI system was excited at the wheel load (i.e., excitation point 2 in Figure 2.2). (a) Rail receptance with responses measured at A6, A7 and A8 (averaged). (b) Sleeper receptance with responses measured at A12, A13, A14 and A15 (averaged).

stiffness from 180 MN/m in the unloaded condition to 500 MN/m in the loaded condition. Such an increase in ballast stiffness is due to its nonlinear behaviour under varying loading conditions.

Between 100 Hz and 1000 Hz, the VTI system resonances (SA_1, SA_2 and SA_3) do not coincide with the track resonances (S_2, S_3 and R_1); instead, they occur close to the anti-resonances of the unloaded track. This shift of resonances and anti-resonances between the loaded and unloaded tracks is caused by the constraints imposed by the added wheel mass at the loading point. The shift is most obvious for tracks with identical ballast stiffness between loaded and unloaded conditions, see the red and grey curves in Figure 2.8 (b). In reality, however, when the increase of ballast stiffness is accounted for, the resonances of the loaded and unloaded track become closer; for example, see Figure 2.8 (b) for the blue S_2 and red SA_1.

At frequencies higher than 1000 Hz, the unloaded track has a rail resonance R_2 in the rail receptance, whereas the loaded track does not, see Figure 2.8 (a) and (b). Besides, simulations show that the three high-order sleeper resonances (S_5, S_6 and S_7) are unaffected by the loading condition, see Figure 2.8 (d). There are, however, minor discrepancies between measured receptances at these resonances, see Figure 2.8 (c). At S_7, for instance, the sleeper receptance of the loaded track splits into two peaks.

2.3.3. TRACK WAVE PROPAGATION, BOUNDING FREQUENCIES AND RESONANCE BEHAVIOURS

Six resonance types (FT, S, SA, R, RBW, PP) and a total of sixteen resonant frequencies have been identified for the track and the VTI system. To reveal how these frequencies are sequenced and structured, we correlate them with propagating track waves.
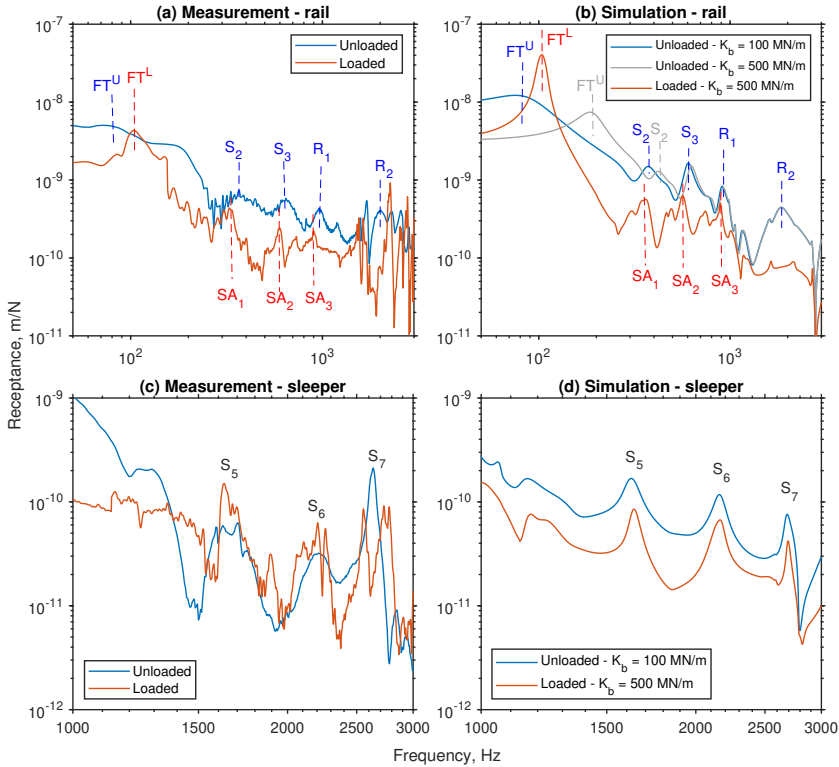
Figure 2.8: Comparison of track receptances between the loaded and unloaded track. (a) and (b) show the measured and simulated rail receptances. The track was excited at point 4 (See Figure 2.1) for the unloaded track and point 2 (see Figure 2.2) for the loaded track. Responses were measured at A6, A7 and A8 (averaged). (c) and (d) show the measured and simulated sleeper receptances. The track was excited at the same locations as in (a) and (b). Responses were measured at sleeper sensors: A12, A13, A14 and A15 (averaged).

2.3.3.1. PROPERTIES OF TRACK WAVES

We calculate the dispersion relations of rail bending waves for both loaded and unloaded tracks using the finite element track models that have been validated in the previous sections (Figure 2.4 (e) and Figure 2.6). To obtain the dispersion relations, we first solve the undamped eigenvalue problem for both track models. Subsequently, at each eigenfrequency, we apply the Fourier transform to the corresponding rail eigenmodes. As a result, we obtain the Fourier amplitudes at spatial frequencies (and thus real wavenumbers) for each eigenmode, denoted as $A(\omega, \beta)$, where ω is the eigenfrequency and β is the real wavenumber.

We plot the amplitudes of $A(\omega, \beta)$ as heat maps, as shown in Figure 2.9 (a) and (b) for the loaded and unloaded track measurements, respectively. The bright yellow curves represent the dispersion relations. Each point on the dispersion curves represents a

wave that can propagate at the corresponding wavenumber and frequency.

Track waves propagate within banded frequencies (passbands). The grey areas in Figure 2.9 denote stop bands within which no wave can propagate. This is a typical characteristic of periodic structures. At the bounding frequencies of passbands, waves propagate at wavenumbers of $0, \pi/L_s$, and $2\pi/L_s$ (see the horizontal dashed lines), which correspond to wavelengths of infinity, $2L_s$ and L_s, respectively, where $L_s = 0.6$ m is the sleeper spacing.

At each frequency, multiple waves may propagate at different wavenumbers. For example, if we draw a vertical line at 200 Hz, it will intersect with the dispersion curve at two wavenumbers. However, the two wavenumbers are not equally dominant. A point on the dispersion curve that is brighter indicates a larger amplitude of $A(\omega, \beta)$ and therefore represents a more dominant wave. In Figure 2.9 (c) and (d), the most dominant wavenumbers at different frequencies are indicated by blue circles.

The dispersion relations in the unloaded and loaded conditions are almost identical. This implies that local wheel loads have a trivial effect on track wave propagation: rail bending waves propagate relatively freely through the wheel-rail interface.

Multiple wave types can be identified from the dispersion relations. Wave types can be classified by the sleeper bending shapes. We use W_i^k to denote different wave types. When i equals a positive integer ($i = 1, 2, \ldots, 7$), sleepers vibrate in the ith order free bending mode, and k is empty. Otherwise, when i is not a positive integer, that is $i = 0, 3.5, 5.5$, the sleeper is not in free bending modes, and $k \in \{a, b\}$, where a and b denote the symmetry and asymmetry of the sleeper shapes, respectively. For example, sleepers vibrate in a rigid translational and rotational mode, for W_0^a and W_0^b, respectively. For $W_{3.5}^a/W_{3.5}^b$ and $W_{5.5}^a/W_{5.5}^b$, rails and sleepers vibrate in anti-phase at rail seats. As a result, sleepers are subjected to greater constraint forces at rail seats and are thus unable to bend freely.

2.3.3.2. CORRELATING RESONANT FREQUENCIES WITH TRACK WAVES

In Figure 2.9, we also plot track receptances on the right vertical axes, overlaid on the dispersion curves. The resonant frequencies are indicated in Figure 2.9 (a) and (b). It can be seen that resonances occur at the bounding frequencies of the passbands, except for a few minor peaks within W_2 and W_3 for the loaded track, see Figure 2.9 (a). The PP resonance occurs at the intersection of $W_{3.5}^a$ and $W_{3.5}^b$.

Below the PP frequency, the track resonances $(FT^U, S_2, S_3$ and $R_1)$ occur at the *lower* bounds of waves W_0, W_2, W_3 and $W_{3.5}$, respectively, whereas the VTI system resonances $(SA_1, SA_2$ and $SA_3)$ occur at the *upper* bounds of wave W_1, W_2, and W_3, respectively. Above the PP frequency, both the track and VTI system resonances $(S_4, S_5, R_2, S_6$ and $S_7)$ occur at the lower bounds of waves $W_4, W_5, W_{5.5}, W_6$ and W_7, respectively.

To verify the generation mechanism of the minor peaks in the receptance of the loaded track, shown in Figure 2.9 (a), we take a closer look at the W_3 wave in Figure 2.10. Despite an overall similarity between the loaded and unloaded tracks, the W_3 wave is split into two waves for the loaded track. One of the waves cut off at the minor peak RBW at around 700 Hz, with a wavenumber of $3\pi/d$, where $d = 2.56$ m is the wheelbase of the bogie (Figure 2.6). This indicates that the minor peak corresponds to a local rail bending mode between the two wheelsets of a bogie with three half wavelengths, see
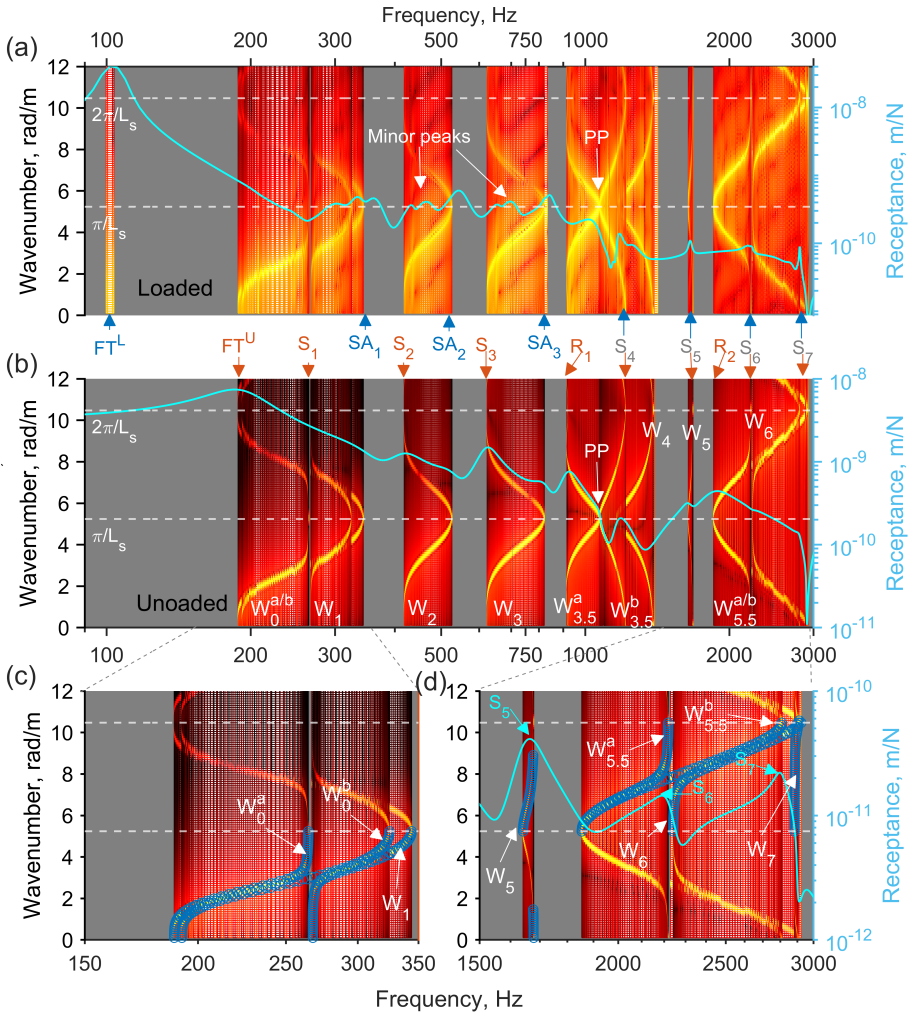
Figure 2.9: Correlations between dispersion relations of rail bending waves (left vertical axis), track receptances (right vertical axis), and frequency features. (a) Loaded condition. (b) Unloaded condition. (c) and (d) show the zoom-in plots of (b) in two frequency ranges. Rail receptances are plotted in (a) and (b). Sleeper receptance is plotted in (d).

Figure 2.10 (a). The reason for the predominance of three half wavelengths over other half wavelengths is that a total wave reflection between the two wheelsets occurs only for three half wavelengths [75]. Table 2.2 summarizes all the track waves and resonance types, as well as their wavenumber and frequency features.
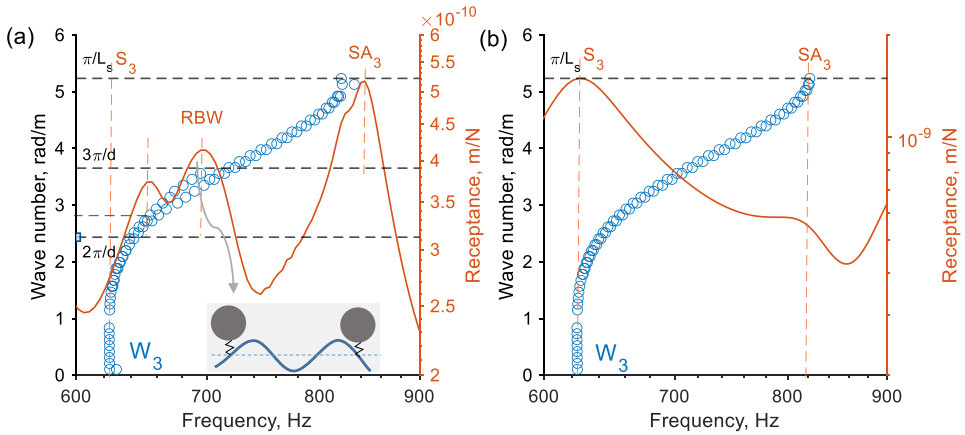
Figure 2.10: Dispersion relation of rail wave W_3 (blue circles, left vertical axis), track receptance (red lines, right vertical axis) and corresponding frequency features. (a) Loaded track. (b) Unloaded track.

2.4. FREQUENCY FEATURES UNDER DYNAMIC TRAIN LOADING

2.4.1. TRACKSIDE MEASUREMENT

2.4.1.1. FREQUENCY FEATURE

Figure 2.11 shows an example of the accelerations measured from the track (sensor A6) during one passage of the measurement train. Figure 2.11 (a) and (c) show the measured time-domain signal mapping to wheel positions. The wheel position represents the distance between the first axle of the locomotive and the sensor A6. The blue line shows the raw signal. The red line shows the envelope of the moving average of 100 samples (sampling frequency: 25600 Hz). The eight distinct peaks in the envelope indicate the passages of eight axles. Figure 2.11 (b) and (d) show the spectrogram of the time-domain signal. The spectrogram was calculated using the short-time Fourier transform with a window length of 1.2 m (two sleeper spacing) and a 90% overlap between adjacent windows.

We divide the whole signal into three parts: two ambient parts and one axle part. The ambient parts measure the vibrations caused by the VTI prior to (SEG1) and following (SEG4) the train passage over the instrumented track section, while the axle part measures the track vibrations during the train passage. In the axle part, we further divide the signal into SEG2 and SEG3, corresponding to the front and rear bogie of the passenger wagon, respectively.

Figure 2.12 compares the PSDs of different segments with different vehicle speeds. The ambient segments (SEG1 and SEG4) and axle segments (SEG2 and SEG3) show peaks at different frequencies in the PSDs. We will delve into the details of these PSD peaks by comparing them to the hammer test results (see section 2.4.1). In addition, the PSDs of the two axle segments (SEG2 and SEG3) are almost identical, whereas, for the two ambient segments, SEG1 has a higher PSD amplitude than SEG4, especially at frequencies between 1000 Hz and 1500 Hz. This is also apparent from the spectrogram in Figure 2.11 (b).

Table 2.2: Correlations between wave types, wave numbers, resonance types and resonant frequencies. Track resonances are denoted by •. VTI system resonances are denoted by ▲.

Wave type	Bounded wave number (rad/m)	Resonance	Frequency (Hz)	
			Simulated	Measured
-	-	• FT^L	100 (stiff ballast)	105 (stiff ballast)
W_0^a, W_0^b	0	▲ FT^L	80 (soft ballast) / 200 (stiff ballast)	80 (soft ballast)
	π/L_s	-	-	-
W_1	0	▲S1	180	-
	π/L_s	•SA1	340	325
W_2	0	▲S2	370	370
	$3\pi/d$	•RBW	495	490
	π/L_s	•SA2	565	600
W_3	0	▲S3	605	645
	$3\pi/d$	•RBW	740	730
	π/L_s	•SA3	890	900
$W_{3.5}^a$	0	▲R1	920	960
	π/L_s	▲PP	1080	1230
$W_{3.5}^b$	π/L_s			
	$2\pi/L_s$	-	-	-
W_4	π/L_s	•▲ S$_4$	1180	1250
	$2\pi/L_s$	-	-	-
W_5	π/L_s	•▲ S5	1640	1500~1700
	$2\pi/L_s$	-	-	-
$W_{5.5}^a, W_{5.5}^b$	π/L_s	▲R2	1850	2000
	$2\pi/L_s$	-	-	-
W_6	π/L_s	•▲ S6	2230	2200~2300
	$2\pi/L_s$	-	-	-
W_7	π/L_s	•▲ S7	2680	2560~2770
	$2\pi/L_s$	-	-	-

2.4.1.2. CORRELATION WITH HAMMER TEST RESULTS

We compare the trackside measurement results with the hammer test results to gain more insights into the frequency features observed in the trackside measurement.

Ambient segments   The instrumented track section is unloaded when the wheel-rail excitation occurs in the ambient segments. Therefore, in Figure 2.13, we compare the frequency features of the ambient vibrations from SEG 4 to the results of the unloaded
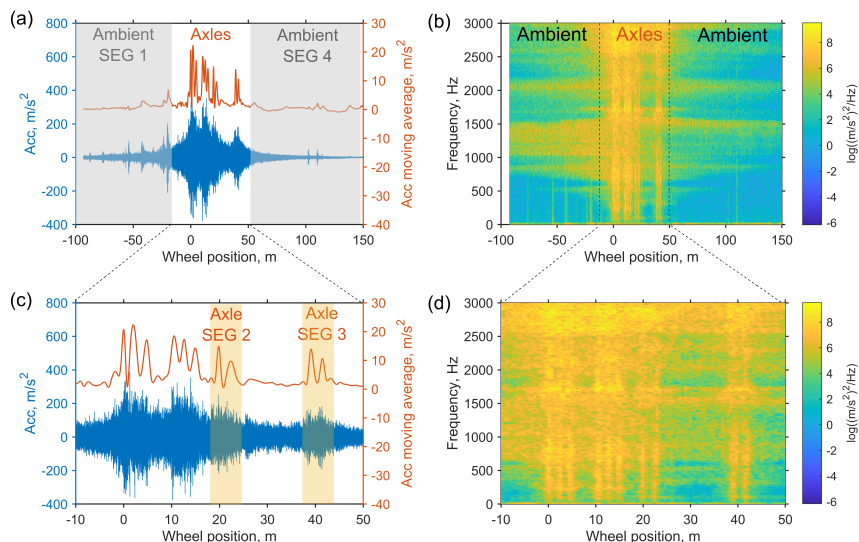
Figure 2.11: Accelerations measured from sensor A6 during a passage of the measurement train at 80 km/h. (a) and (c) show the time domain signal. (b) and (d) show the spectrogram of the time domain signal. The spectrogram was calculated using the short-time Fourier transform with a window length of 1.2 m (two sleeper spacing) and a 90% overlap between adjacent windows.

hammer test. To ensure a fair comparison, the hammer impact location should also be at a distance from the instrumented location as in the ambient excitation. In this manner, the decay of the hammer force between the excitation point and the instrumented location can be accounted for. Such hammer tests, however, were not conducted in this study. To consider the aforementioned decay effect of the excitation, we divide the hammer test responses into two segments (SEG A and SEG B, as illustrated in Figure 2.13 (b)). The decayed response can thus be represented by SEG B.

We first examine the power distribution of ambient vibrations at different frequencies. The ambient segment signal (SEG 4) has more power concentrated at frequencies above 1000 Hz than below 1000 Hz, see Figure 2.13 (c) and (e). The maximum power is observed around 1500 Hz (S_5), which is consistent with the decayed hammer test responses (SEG B), see Figure 2.13 (e). These characteristics of the power distribution are due to the fact that track responses decay more rapidly at low frequencies and less rapidly around 1500 Hz, as can be seen by comparing the PSDs of hammer SEG A and SEG B. The decay characteristics observed here are consistent with previous studies [87].

The trackside PSD has two peaks at frequencies below 1000 Hz (S_3 and R_1) that are more consistent with the PSD peaks of the decayed hammer response (SEG B). The four peaks above 1000 Hz in the trackside PSD (S_5, R_2, S_6, and S_7), on the other hand, agree better with the peaks obtained from the non-decayed hammer response (SEG A). Note that the PSD peaks of hammer SEG A and SEG B are not identical. This is more apparent at low frequencies, as illustrated by S_2 and S_3 in Figure 2.13 (e). It is also worth noting
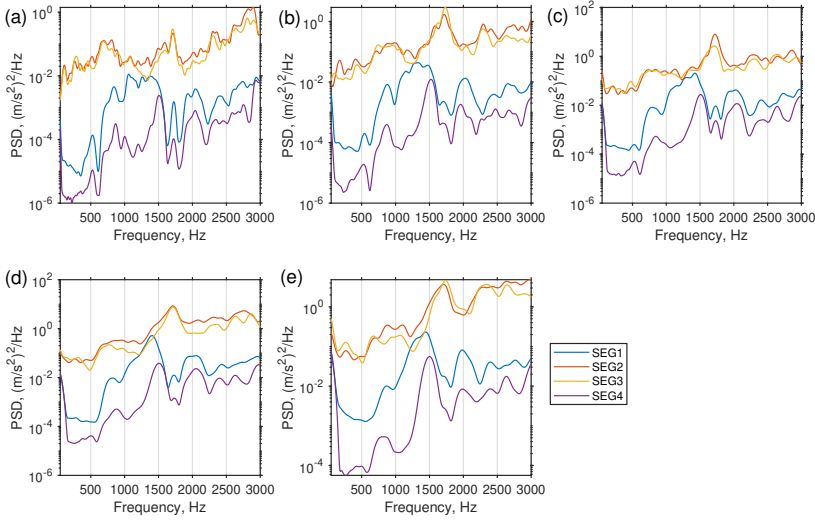
Figure 2.12: PSD of accelerations measured from sensor A6 for different segments (SEG1 ~ SEG4) at different vehicle speeds. (a) ~ (e) show the results for vehicle speeds of 80, 120, 140, 180, and 200 km/h, respectively.

that changing vehicle speed only affects the PSD amplitude but not the peak frequencies.

Axle segments   In the axle segments (SEG2 and SEG3 in Figure 2.11), the instrumented track section is in the loaded condition. We compare in Figure 2.14 the PSDs of the axle segment (SEG3) with those obtained by the loaded hammer test. All PSDs were calculated using the signals measured at sensor A6 (see Figure 2.2). For the loaded hammer test, we calculated both the direct PSD (with the hammer excitation directly above A6) and transfer PSD (with excitations at locations 1 and 3 in Figure 2.2). This is intended to replicate the change in excitation locations that occurs during a wheel passage in the axle segments.

As with the ambient segment, the PSDs of the axle segment exhibit larger amplitudes at frequencies above 1000 Hz than below 1000 Hz. The maximum power occurs at about 1700 Hz (S_5), which is slightly higher than that of the ambient segment (1500 Hz).

In comparison to the ambient segment, the peaks in the PSDs of the axle segment below 1000 Hz are less distinguishable and also less consistent between various speeds. For instance, the full-track (FT^L) and first sleeper-anti (SA_1) resonance can only be identified at certain vehicle speeds. Between SA_2 and about 1300 Hz, the trackside PSDs show no discernible peaks. This agrees with the transfer hammer PSD. There are two possible reasons for the differences between the ambient and axle segments. First, the signal length of the axle segment is significantly shorter than the ambient segment (Figure 2.11). Second, the axle segment signal is non-stationary due to the time-varying nature of the VTI system during wheel passages. At frequencies above 1000 Hz, three high-order sleeper resonances can be identified, while the rail resonances (R_1 and R_2) present in the am-

2

Figure 2.13: Comparison of the PSDs obtained from the trackside measurement (ambient SEG4) and the unloaded hammer test. (a) and (b) show the time domain signal of sensor A6 measured from the trackside and hammer test, respectively. (c) and (d) show the spectrograms corresponding to (a) and (b), respectively. (e) compares the PSDs from the trackside and hammer measurements.

bient segment no longer exist in the axle segment. This is consistent with the loaded hammer test results, i.e., the rail resonances are not excited in the loaded track (see also Figure 2.8).

2.4.2. ABA MEASUREMENT

Figure 2.15 shows the spectrograms of the ABA signals measured from the axle boxes on the side of the hammer test for each axle of the measurement wagon. The frequency features of ABA differ from those of the trackside measurement in two aspects. First,
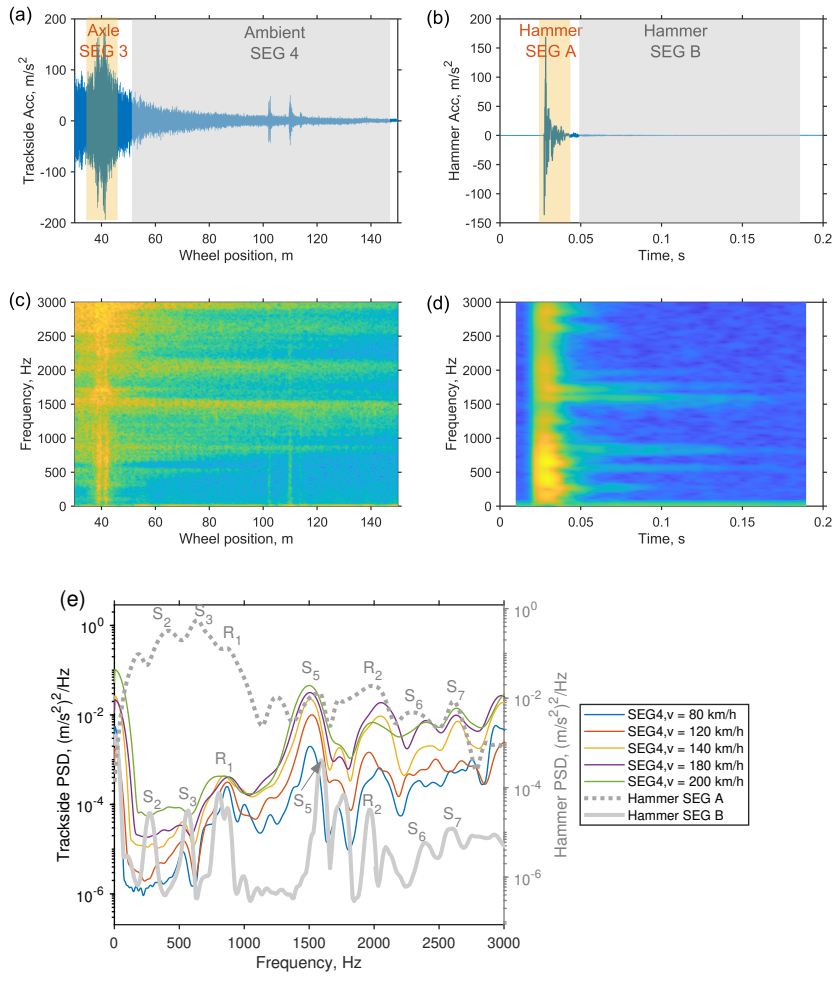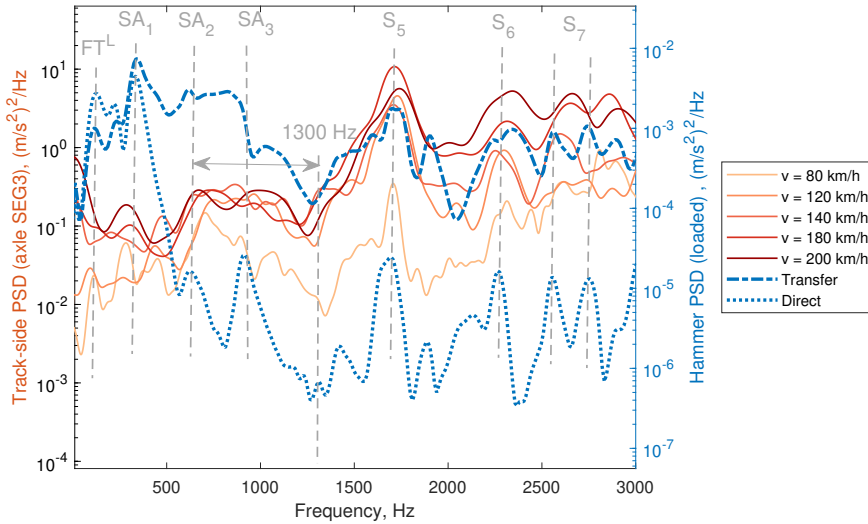
Figure 2.14: Comparison of the PSDs obtained from the trackside measurement (axle segment SEG3) and the loaded hammer test. All PSDs were calculated using the track responses measured at sensor A6. The direct PSD for the hammer test was calculated with the hammer excitation directly above A6, i.e., impact location 2, as shown in Figure 2.2. The transfer PSD was calculated with hammer excitations at locations 1 and 3 in Figure 2.2.

the spectral power of ABA is concentrated more at frequencies below 1000 Hz. Second, the spectrograms of ABA show higher resolution in distinguishing the characteristic frequencies below 1000 Hz: six distinct frequency bands below 1000 Hz can be seen for the ABA.

Figure 2.16 compares the PSDs of ABA and the track receptances obtained by the loaded hammer test. The PSDs below 1000 Hz show six peaks, corresponding to the six resonances of the VTI system identified in the loaded hammer test. These peaks are sharper at low vehicle speeds and become blunt as the vehicle speed increases. This is because we calculate the PSDs at different vehicle speeds using a fixed window length in space (0.6 m). Therefore, the number of sample points within the window decreases as the vehicle speed increases, resulting in a lower frequency resolution. In addition, these PSD peaks best match the receptance peaks at axle 4. This is because axle 4 was used as the preload in the loaded hammer test (Figure 2.2).

At frequencies above 1000 Hz, four peaks can be identified in the PSDs, corresponding to three sleeper resonances (S_5, S_6 and S_7) and one rail resonance (R_2). Notably, the R_2 resonance at 2000 Hz in the ABA measurement is not captured in the loaded hammer test or trackside measurement (see also Figure 2.14). It is also noted that the PP resonance is not present in the ABA measurement.

One way to increase the frequency resolution below 1000 Hz is to use a longer window. Figure 2.17 shows the PSDs of ABA calculated with a window length of 2.4 m (four sleeper spans). It can be seen that the PSD peaks are more distinct compared to those
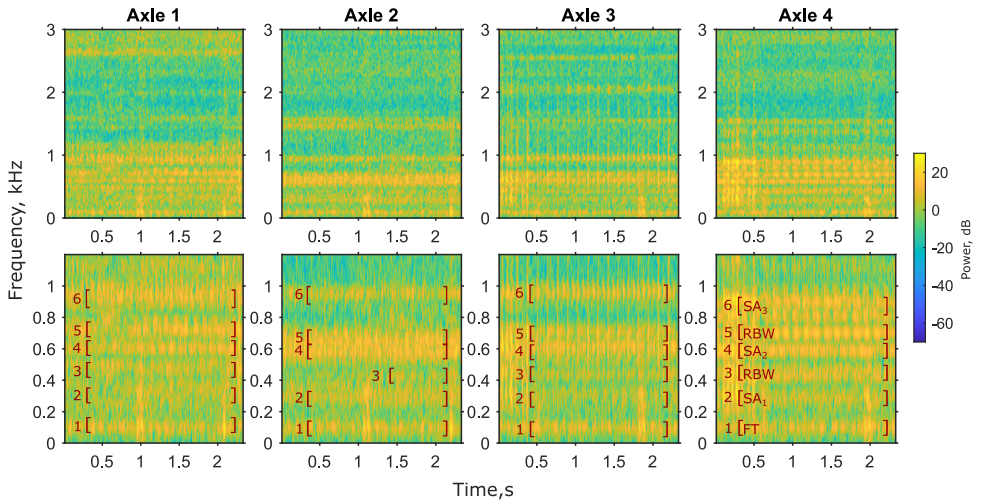
Figure 2.15: Spectrograms of the ABAs measured from the four axles of the measurement wagon. The spectrograms were calculated using the short-time Fourier transform with a window length of 0.6 m (one sleeper spacing) and a 90% overlap between adjacent windows. The first row shows the spectrograms between 0 and 3000 Hz. The second row shows the spectrograms between 0 and 1200 Hz.
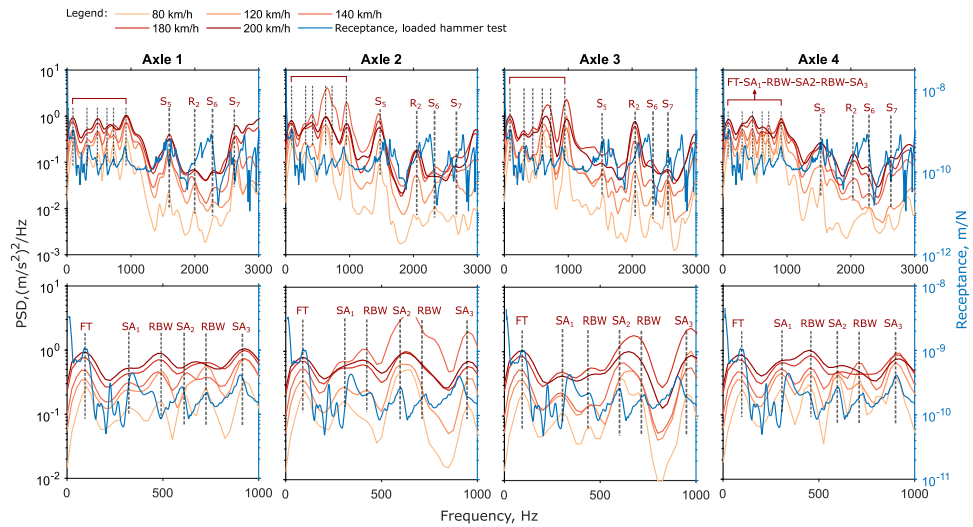
Figure 2.16: Comparison of the PSDs of ABA and the track receptances obtained from the loaded hammer test. The PSDs were calculated with a window length of 0.6 m. The first row shows the PSDs between 0 and 3000 Hz. The second row shows the PSDs between 0 and 1200 Hz.

calculated with a shorter window length, especially for the PSDs measured at axle 2 and axle 3, as well as the PSDs with higher vehicle speeds.
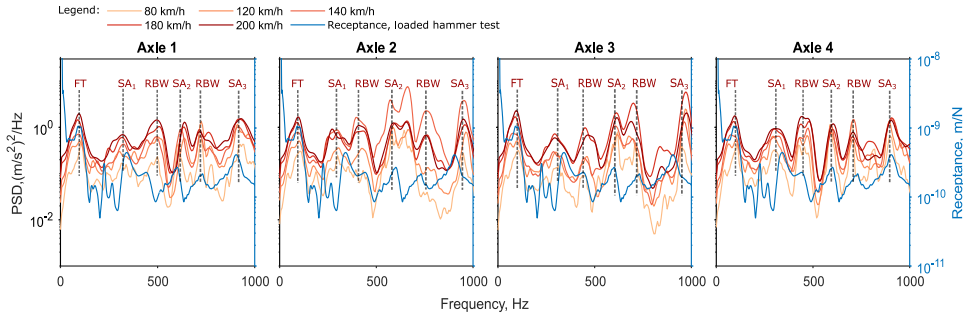
Figure 2.17: Comparison of the PSDs of ABA and the track receptances obtained from the loaded hammer test. The PSDs were calculated with a window length of 2.4 m.

2.4.3. FREQUENCY FEATURE MAP

With all the experimental and simulation results, we construct a frequency feature map for the VTI system, as shown in Figure 2.18. In Figure 2.18 (a), we plot the passbands of propagating track waves. Figure 2.18 (b) and (c) show the sequence patterns of the frequency features measured by different techniques. A complete set of sixteen resonances of the track and VTI system are marked and sequenced based on an underlying physical principle: all resonances occur at the bounding frequencies of the pass bands of propagating track waves. A sequence pattern can serve as a key feature of a track or VTI system, and it can be further associated with track parameters or damages, such as track stiffness, as will be demonstrated in Chapter 4 and Chapter 5. The track conditions can then be evaluated by monitoring the sequence patterns of a VTI system over time or space.

2.5. DISCUSSION

We briefly discuss how the findings in this chapter are related to and different from previous studies.

2.5.1. TRACK WAVE PROPAGATION

The flexible sleeper model used in this chapter results in multiple wave types between 50 Hz and 3000 Hz (Figure 2.9). This is different from previous studies using rigid sleeper models [69, 70], where only two waves can be identified in this frequency range, with one below and the other above the PP resonance. In fact, the dispersion relations shown in Figure 2.9 resemble those obtained by a flexible slab track model [88]. The difference is that the ballasted track has more and wider stop bands than the slab track due to its more discrete structures.

2.5.2. FREQUENCY FEATURES BETWEEN 300 HZ AND 1000 HZ

Loaded hammer tests in previous studies [46, 73] were aimed at investigating the nonlinear track behaviour caused by preloads. It was found that preloads can affect track FRFs up to 500 Hz. In this chapter, the effects of added wheel mass and double wheelsets in

2
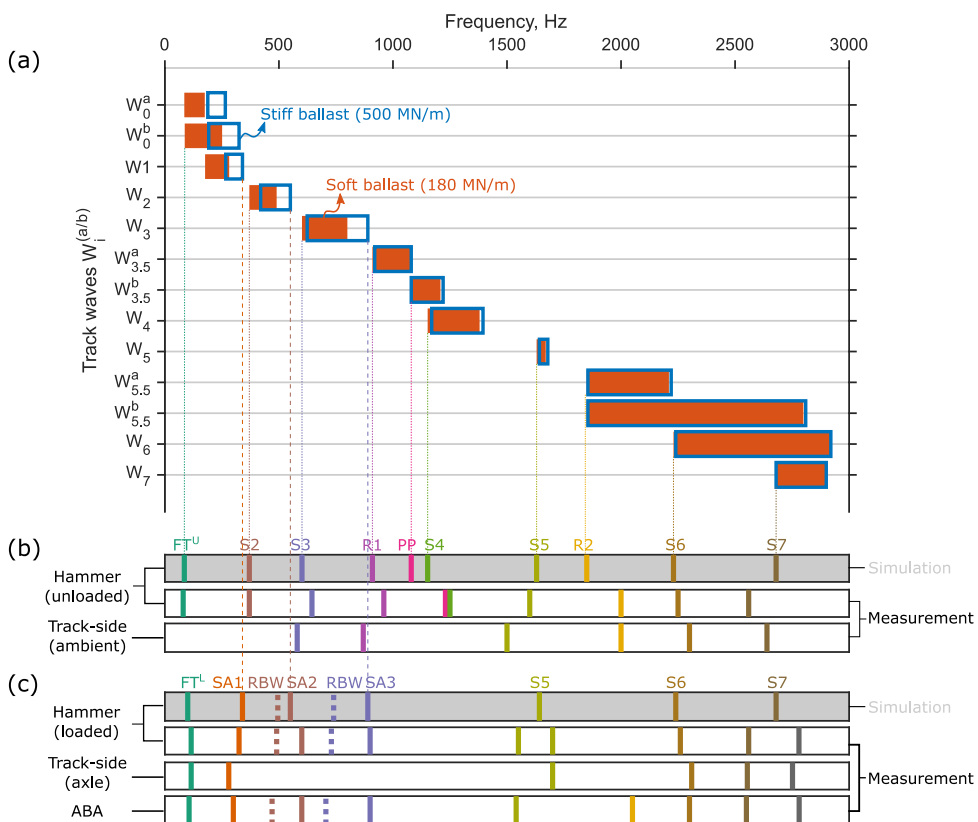
Figure 2.18: Frequency feature map of the VTI system in the frequency range of 50 Hz ~ 3000 Hz. (a) Passbands of propagating track waves are denoted by horizontal bars, which are derived from Figure 2.9. (b) and (c) show the sequence patterns, on which frequency features measured by different techniques are marked and linked to the resonances of (b) the track and (c) the VTI system.

a bogie are also considered. The added wheel mass results in the three SA resonances, while the double wheelsets lead to the two RBW resonances. These resonances are between 300 Hz and 1200 Hz.

Various studies [7, 74, 75, 89, 90] have demonstrated the existence of three peak frequencies between approximately 300 Hz and 1200 Hz. They correspond to local rail bending modes with different half wavelengths between the two wheels of a bogie (RBW). Our findings indicate that the SA and RBW resonances can be excited simultaneously, yielding a maximum of five peak frequencies in this frequency range (see Figure 2.16 and Figure 2.17). In addition, the two RBW resonances identified in this chapter correspond to the same three half wavelengths but are associated with two distinct track wave types (see Figure 2.9 and Figure 2.10).

The primary reason for these discrepancies is that the railpad is stiffer than those in previous studies. As a result, flexible sleepers are considered in this research, which leads to the extra SA resonances that have not been previously identified.

2.5.3. ABA MEASUREMENT

We compare the frequency features of ABA in this chapter to those in [9]. In both cases, the spectral power of ABA is concentrated at frequencies below 1000 Hz. The main difference is the number of frequency peaks detected below 1000 Hz. Three frequency bands between 50 Hz and 1000 Hz were observed in [9] and they were empirically associated with track vibration modes. In this chapter, we show that the ABA measurement is capable of capturing six peak frequencies below 1000 Hz. These frequencies correspond to VTI system resonances instead of track resonances.

2.6. CONCLUSION

Based on extensive field measurements and a validated VTI model, we establish a detailed frequency feature map for the vibrations of a VTI system in the frequency range of 50 Hz to 3000 Hz. On the frequency feature map, seven types and a total of sixteen resonances of the track and VTI system are marked and sequenced based on the passbands of propagating track waves. With the frequency feature map, peak frequencies identified by different measurement techniques can be marked and linked to the corresponding resonances of the track or VTI system, resulting in a sequence pattern that can be used as a key feature for track condition monitoring. The following conclusions can be drawn for the frequency features measured by the different techniques.

- The track resonances $(FT^U, S, R,$ and PP) are identified by the unloaded hammer test, while the VTI system resonances are identified by the loaded hammer test $(FT^L, SA$ and RBW). All resonances occur at the bounding frequencies of the passbands of propagating track waves.

- VTI system resonances differ from track resonances for three major reasons. First, FT^L (100 Hz) occurs at a slightly higher frequency than FT^U (80 Hz) due to the increased ballast stiffness caused by preloads. Second, between 300 Hz and 1000 Hz, the S resonances shift to SA resonances due to the constraints imposed by the added wheel mass at the loading point. Third, the double wheelsets in a bogie lead to the RBW resonances. Consequently, the VTI system has six resonances (FT, 3SA, 2RBW) that are densely spaced below 1000 Hz.

- The trackside measurement can be divided into ambient and axle segments. They show different frequency features. Frequency features of the ambient segments correspond to the track resonances with the decay effect taken into account, while those of the axle segments correspond to the VTI system resonances. The spectral power of trackside measurement peaks between 1500 Hz and 2000 Hz. Trackside measurement cannot capture all track or VTI system resonances below 1000 Hz.

- The spectral power of ABA is concentrated more at frequencies below 1000 Hz. Peak frequencies in the PSDs of ABA are speed invariant and correspond well to VTI system resonances. The ABA is capable of detecting all six VTI system resonances below 1000 Hz, but not the R_1 and PP resonances.

COMPARISON OF BEAM AND CONTINUUM MODELS FOR MODELLING WHEEL-RAIL IMPACT AT SINGULAR RAIL SURFACE DEFECTS

This chapter addresses whether and how observed frequency features in Chapter 2 can be correctly modelled. To this end, we compare two types of commonly used wheel-track interaction models, i.e., a beam and a continuum finite element model. The problem we choose is the wheel-rail impact at rail squats. This is because the excitation frequency of a squat with a typical length of 20 mm ~ 40 mm is approximately between 970 Hz and 1945 Hz (with a vehicle speed of 140 km/h), which is critical for the beam model that is conventionally considered accurate up to about 1500 Hz.

We first reveal the differences between the impact forces predicted by the two models due to a typical rail squat using time-frequency analysis. Subsequently, we identify the causes for the differences by evaluating the effects of different model assumptions and model parameters. Results show that the impact force consists of a forced vibration peak M1 followed by free vibration related oscillations with three dominant frequencies: f_1 (340 Hz), f_2 (890 Hz) and f_3 (1120 Hz). Compared with the continuum model, the beam model with a Hertzian contact spring overestimates the M1 peak force. The discrepancy can be reduced by using a Winkler bedding contact model. For the track model, the beam model is comparable to the continuum model up to about 800 Hz, beyond which the track damping starts to deviate. As a result, above 500 Hz, the contact forces dominate at f_2 for the beam while at f_3 for the continuum model. Finally, we show that the continuum model is more accurate

---

This chapter is based on [91]

than the beam model by comparing them to field observations. The effects of stress wave propagation on the differences are also discussed.

3.1. INTRODUCTION

Wheel-rail vertical impact usually occurs at short wavelength defects (e.g., squats, poor welds, wheel flats, short-pitch corrugations) or structure discontinuities (e.g., insulated joints, crossings). The appropriate modelling of structural flexibility of the wheel-track system is of major concern for the wheel-rail impact problems due to their high-frequency nature [26, 92]. Based on the assumptions adopted, two types of wheel-track interaction models are commonly used for wheel-rail impact problems. The first type is referred to as the beam model in this chapter, in which rails are modelled using the Euler-Bernoulli or Timoshenko beams [29, 31, 93]. The rail can be continuously supported on the elastic or Winkler foundations [32–34], a layer of sleeper beam [35, 36], discretely supported on sleepers [30, 37, 38] or substructures, such as bridges [94] or subgrades [95]. The second type drops the assumptions made in the beam theories and treats the components of the wheel-track system (i.e. the sleeper, rail, wheel, or even railpads) as continua. This type of model is referred to as the continuum model in this chapter. Continuum models are usually solved using the three-dimensional finite element (FE) method [39–42] or the 2.5-dimensional FE (also called waveguide FE) method [27, 96–98]. The focus of those models has been on the transient dynamic characteristics (such as wheel-rail impact), rolling contact solutions, rolling noise and wave propagations.

Different modelling assumptions will lead to variability in simulation results. To quantify and understand the causes of such variability, simulation results with different model assumptions have to be compared. The first step towards such comparisons is to define certain metrics that can characterize the dynamic responses of the problem in hands. For instance, the frequency response function is commonly used to assess the dynamic behaviour of the track. For wheel-rail impact problems, the dynamic characteristics depend on the defect that causes the impact; therefore, different metrics may apply. For example, the wheel-rail impact at dipped joints or wheel flats is usually characterized by the P1/P2 forces [99] (also including the P1 ½ force).

This chapter deals with the wheel-rail impact at a type of short wavelength singular defect in the rail surface, i.e., squats. The typical wavelength of squats is about 20-40 mm, e.g., in the Dutch railway network [45]. With such a geometry, the contact force is characterized by continuous short wavelength peaks in the time domain [100]. In the frequency domain, two major frequencies at around 300 Hz and 1000 Hz have been identified in the simulations and verified by the axle-box acceleration (ABA) measurements [101]. Both the magnitude and frequency content of the impact force need to be correctly modelled because they help better understand the formation [45, 102], development [103] and detection [11] of squats.

Different wheel-track interaction models have been compared through benchmark tests [104–106]. For example, six different beam models were benchmarked against each other in [105]. The P1 forces at a wheel flat ranged from 2 to 7 times the static load. The track vibrations reproduced by the six models were not consistent between each other or compared to the field measurement [106]. Although the discrepancies can be pinpointed by the benchmark tests, it is nonetheless difficult to deduce exactly which

assumption contributes to an identified discrepancy, because there are usually multiple different assumptions between two benchmark participants.

Alternatively, comparative studies have been carried out by changing one assumption at a time per each track component to identify their effects on the dynamic characteristics. For **rail** models, the Euler-Bernoulli beam is considered adequate below about 500 Hz due to the neglecting of the shear deformation [26, 107] whereas the Timoshenko beam is accurate up to about 1500 Hz [44], beyond which the assumption of rigid cross section in the beam theories becomes invalid and the continuum model should be adopted. Moreover, the Euler beam theory tends to overestimate the P1 force compared to the Timoshenko beam theory as well as the measurement [108]. Different **railpad/fastening** models have been compared in terms of the effect of the support length and size for beam models [109, 110] and continuum models [111, 112]. The introduction of **sleepers** as discrete supports has two major effects. First, the pin-pin resonance can be correctly modelled using the discretely supported track [35]. Second, the sleeper layer could effectively reduce the P1 force compared to the beam on elastic foundation model [113]. In the case of soft railpads, the sleeper can be modelled as rigid mass [27, 72]. As the railpad stiffness increases, the coupling between the rail and sleeper becomes stronger. As a result, flexible sleeper models should be adopted to model the extra track resonances due to sleeper bending [27, 71, 72].

Except for the track models, different wheelset and contact models have also been compared. For beam models, the wheelset can be modelled as a rigid mass or a flexible body through modal superposition [7, 114]. Flexible wheelset models can slightly reduce the impact force at wheel flats compared to rigid models [114]. In addition, differences can be observed in the frequency domain of the contact force, limited to narrow frequency bands corresponding to the eigenfrequencies of the flexible wheelset [7]. Different contact models are compared in [115–118]. However, all these contact models are quasi-static, which do not consider the local inertia effects within or in the vicinity of the contact patch. In contrast, the continuum model takes into account the local structural vibrations in the vicinity of the contact patch and the stress wave propagation in the wheel and rail [100]. For example, in [119], wheel-rail contact-induced Rayleigh waves have been reproduced by a continuum model.

In the literature, despite the extensive comparisons between different beam models, comparisons between beam and continuum models can only be found in a few cases, such as in the unloaded condition [27, 72] or under parametric excitations [120], but not for wheel-rail impact problems. Even for the beam models, the comparisons are almost all based on wheel-rail impacts at wheel flats or joints, which are generally larger geometrical irregularities than squats. As a result, the focus was to compare the magnitudes of the contact force, e.g., the P1/P2 forces, whereas the frequency or time-frequency characteristics of the impact force have not been fully explored. Furthermore, the effects of the local inertia in the contact patch and the stress wave propagation in solids on the wheel-rail impact force have not been studied.

This chapter aims to compare the beam and continuum models for simulating the impact forces induced by squats. To this end, two FE models, meshed with beam and solid elements, respectively, have been developed (Section 3.2). We first identify the major characteristics and discrepancies of the wheel-rail impact force simulated by the

two models at a typical squat, in the time, frequency and time-frequency domain (Section 3.3.1). Subsequently, we examine the effects of the model assumptions made in the wheel, contact and track models separately (Sections 3.3.2), as well as the effects of different model parameters (Section 3.3.3). In Section 3.4, a frequency domain model is adopted to investigate the coupled effects of the three components. Finally, we compare the simulated results with field observations and discuss in detail the influence of wave propagation (Section 3.5).

3.2. METHOD

3.2.1. BEAM MODEL

The track is represented by a two-layer discretely supported model, see Figure 3.1 (a). The rails and sleepers are meshed with the Timoshenko beam element. At each node, only the vertical and in-plane rotational degrees of freedom are considered. By a convergence analysis, the optimal mesh sizes for the rail and sleeper are determined, with 24 elements per sleeper span for the rail and 20 elements per sleeper. Ballast and railpads are modelled as discrete spring-damper pairs.

Two track model options are made: the full-track model and the half-track model. The latter is the former halved along the track center line, where the symmetrical boundary conditions are applied. The wheelset is simplified as a rigid body in the full-track model and as a rigid mass in the half-track model. The bogie and car body are simplified as static loads applied vertically on the wheels.

Only the vertical wheel-rail contact is considered with two options. The first one is a non-linear Hertzian spring model, for which the half-space assumption applies. The contact force is calculated as

$$F(x) = \begin{cases} C_H \left(Z_w(x) - Z_r(x) - Z_{irr}(x) \right)^{3/2} & \text{if } Z_w(x) - Z_r(x) - Z_{irr}(x) < 0 \\ 0 & \text{if } Z_w(x) - Z_r(x) - Z_{irr}(x) \geq 0 \end{cases} \tag{3.1}$$

where $Z_w(x), Z_r(x), Z_{irr}(x)$ are the vertical coordinates of the wheel, rail and defect geometry, respectively, and C_H is the Hertzian coefficient and can be approximated as

$$C_H = \frac{2ER^{1/2}}{3\left(1 - v^2\right)} \tag{3.2}$$

where E and v are Young's modulus and Poisson ratio of wheel and rail (assumed equal for both materials), and R is the radius of the railhead in the lateral direction. The defect geometry is analytically defined as a cosine function:

$$Z_{irr}(x) = \frac{D}{2} \left\{ \cos\left[\frac{2\pi}{L}(x - x_0) \right] - 1 \right\}, \text{ for } x_0 \leq x \leq L \tag{3.3}$$

where D, L and x_0 are the depth, the length and the starting location of the defect. The wheel-track interaction model is solved in the time domain using the Newmark integration with a fixed time step length of 4×10^{-5} s. To ensure convergence for the contact force, the Newton-Raphson iteration is adopted within each time step. The solution process is implemented in Matlab.
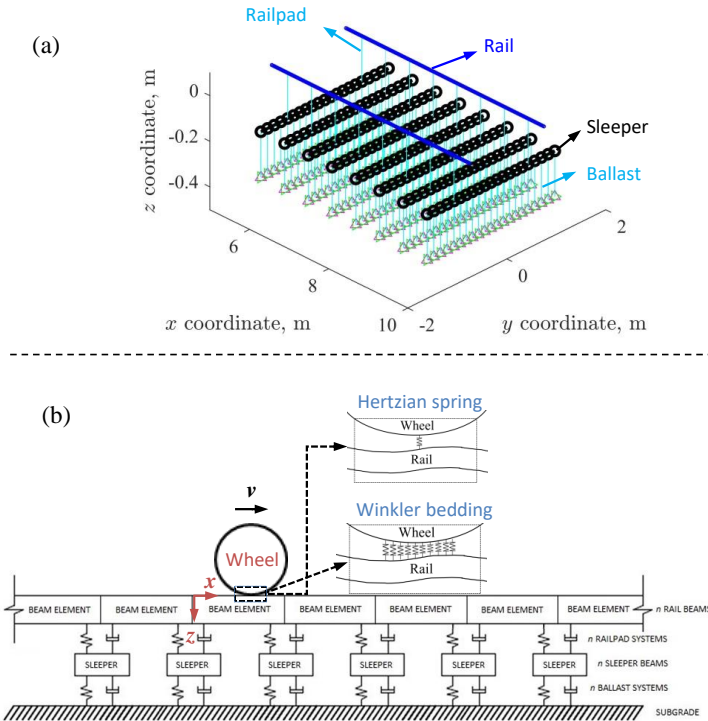
Figure 3.1: The beam model. (a) Track model. (b) Wheel-track interaction model.

3.2.2. CONTINUUM MODEL

The second model is a detailed three-dimensional (3D) FE model meshed with continuum elements, as shown in Figure 3.2. To reduce the computational cost, only halves of the track and wheelset with the symmetrical boundary condition are considered. The bogie and car body are simplified as sprung masses. The railpads and ballast are modelled as discrete spring-damper pairs. For each railpad, a grid of 3 by 4 spring-damper pairs is adopted between the rail and sleeper, see Figure 3.2. The rolling of the wheelset is enabled by applying torque on the axle. This model is developed and solved with the commercial FE program ANSYS/LS-Dyna. An 8-node hexahedra element with reduced integration points is adopted due to its computational efficiency. The length of both track models is 12 m (i.e., 20 spans), which has been shown to be long enough to get rid of the boundary effect for this problem [100]. The wheel-rail contact is solved using a surface-to-surface contact algorithm incorporated in LS-Dyna. This algorithm with a mesh size of 1 mm in the contact patch has been shown to yield satisfactory results in comparison to the Hertz or CONTACT [121] model in the quasi-static wheel-rail contact case [122]. The longitudinal geometry of the irregularity is defined as in Eq. 3.3, while its lateral geometry remains the same as the lateral profile of the rail head, see Figure 3.2.

The dynamic wheel-track interaction is solved using an explicit time integration scheme

(a central difference method) with a time step length of 3e-8 s, which is small enough to ensure both stability and convergence. For the details of the modelling and solution procedure, the readers are referred to [43].
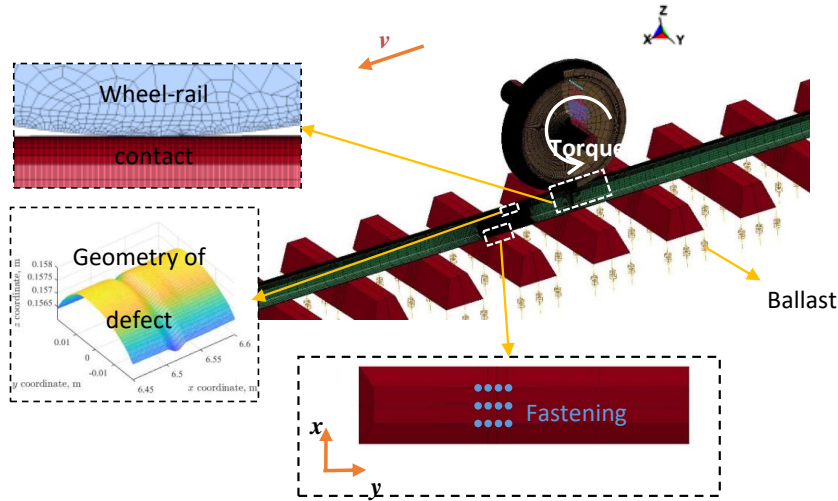

Figure 3.2: The continuum model. The wheel, rail and sleepers are meshed with 8-node 3D FE elements.

3.3. COMPARISONS BETWEEN BEAM AND CONTINUUM MODEL

3.3.1. CHARACTERIZATION OF WHEEL-RAIL IMPACT FORCE

We first consider the wheel-rail impact at a typical squat in the Dutch railway network as a reference case. The model parameters are listed in Table 3.1. These parameters are the same as those used in Chapter 2, which have been validated by ABA measurement [101]. We model the fastening system as spring-damper pairs: railpads sustain compression and clamps and bolts sustain tension. This is a widely accepted simplification in railway track models. As in the loaded condition, the fastening system is in compression; we take the railpad stiffness value as the spring stiffness. The sleeper is a prestressed concrete sleeper of type NS90. We assume a uniform cross section for the sleeper with equivalent cross sectional properties. The squat geometry is defined using Eq. 3.3 with $D = 0.2$ mm, $L = 30$ mm and $x_0 = 6.5$ m. This geometry is chosen because a typical squat in the Netherlands is between 20 mm and 40 mm long [45] and less than 0.4 mm deep [123]. Besides, the squat is located near sleeper support at 6.6 m, which is also typical in the Dutch railway network [45]. For the convenience of comparing to measurements (Section 3.5.1), the velocity of the wheel is set to 30 m/s, which is the same velocity at which the ABA was measured in [101].

Figure 3.3 compares the contact forces calculated by the two models. For the beam model, we adopt the half-track representation with the symmetrical boundary condition (the same as the continuum model) and the non-linear Hertzian spring contact model. The time domain responses (Figure 3.3 (a)) consist of two stages. From 6.5 m to 6.53 m

Table 3.1: Model parameters for the reference case

Component	Parameter	Value
Track		
UIC54 rail	Mass per meter	54.77 kg/m
	Young's modulus	210 GPa
	Poisson's ratio	0.3
	Moment of inertia	2.337×10^{-5} m^4
	Density	7800 kg
	Area of cross section	6.977×10^{-3} m^2
	Timoshenko shear coefficient	0.4
Rail pad	Stiffness	1300 MN/m
	Damping	67500 Ns/m
Sleeper	Young's modulus	74.6 GPa
	Poisson's ratio	0.17
	Moment of inertia (averaged)	1.375×10^{-4} m^4
	Density	2500 kg/m
	Area of cross section (averaged)	0.043
	Timoshenko shear coefficient	0.833
	Length	2.58 m
	Spacing	0.6 m
Ballast	Stiffness	90 MN/m
	Damping	6400 Ns/m
Vehicle		
Sprung mass	Mass	8000 kg
Primary suspension	Stiffness	1.15 MN/m
	Damping	2500 Ns/m
Wheelset	Wheel radius	0.46 m
	Mass (half)	900 kg
	Roll inertia	950 kg$\cdot$m^2
	Speed	30 m/s
Wheel/rail contact		
Hertzian spring	Constant C_H	9×10^{10} N/m$^{3/2}$
	Linearised Coefficient K_H	$4 \times 10^8 \sim 1.2 \times 10^9$ N/m
Squat		
Geometry	Length L	30 mm
	Depth D	0.2 mm

(indicated by the vertical dashed line), the wheel-track system is in a forced vibration stage, excited by the defect geometry. The contact forces show a local dip (D1) followed by a local maximum (M1). The M1 magnitudes are 2.1 and 1.4 times the static load for the beam and continuum model, respectively. From 6.53 m on, the system is in a free vibration stage. The contact forces oscillate in two major wavelengths, i.e. a shorter wave D2M2D3 and a longer wave D3D4. In the frequency domain, there are three major

characteristic frequencies (see f_1, f_2 and f_3 in Figure 3.3 (b)). The magnitudes predicted by the continuum model are lower at f_1 and f_2 than in the beam model. In addition, the dominant frequency above 500 Hz is at f_2 = 890 Hz and f_3 = 1130 Hz for the beam and continuum models, respectively.

The wheel-track system is not a constant but a time-variant system as the wheel position changes. Consequently, the characteristic frequencies should also be changing with the wheel position. To illustrate this, we apply the synchrosqueezed wavelet transform [124] to the contact force and plot the synchrosqueezed wavelet power spectrum (SWPS) in Figure 3.3 (c) ~ (f). Three frequency bands are visible in the plots. There are a number of differences between the SWPS predicted by the two models. The major difference lies between about 6.53 m and 6.6 m, where the largest power concentrates at f_2 and f_3 for the beam and continuum models, respectively. The two dominant frequencies correspond to the two wavelengths of D2M2D3 in Figure 3.3 (a), i.e., approximately 38 mm and 27 mm for the beam and continuum model, respectively. Besides, the frequency change of f_3 is less abrupt for the continuum model than the beam model, as indicated by the white boxes in Figure 3.3 (e) and (f). This is mainly because of the modelling of the railpad as a grid of 3 by 4 spring-damper pairs in the continuum model as opposed to a single spring-damper pair in the beam model (see Figure 3.2 and Figure 3.3 (g)). This unphysical abrupt change of stiffness due to the single-point supported railpad model has also been observed in Timoshenko beam models [125, 126] under parametric excitations. After 6.6 m, the two models show similar results with only f_1 and f_3 presented. The difference is that the contact force decays more quickly for the continuum model than the beam model, resulting in a lower power in the SWPS after 6.6 m.

The simulation results of the two models shown in Figure 3.3 may be influenced by two factors: one is the **model assumptions** and the other is the **model parameters**. To make a more comprehensive comparison of the two models, we investigate the effects of model assumptions and parameters in sections 3.3.2 and 3.3.3, respectively.

3.3.2. EFFECTS OF MODEL ASSUMPTIONS

Compared to the continuum model, more assumptions are made in the beam model in terms of the wheel, contact and track model. In this section, some key assumptions are varied, see Table 3.2, to investigate their effects on the simulation results. While varying model assumptions, we use the same set of model parameters (see Table 3.1) for the analysis in this section.

Table 3.2: Different assumptions adopted in the models to be compared

Model No.	Track model	Wheelset model	Contact model
A1	Beam	Rigid	Hertzian spring
A2	Beam	Rigid	Winkler bedding
A3	Beam	Flexible (modal superposition)	Hertzian spring
B	Continuum	Flexible (solid 3D)	3D Contact

For the wheelset model, a rigid mass is assumed for the beam model used in Section 3.3.1 (Model A1 in Table 3.2). Compared to a flexible wheelset model, this assumption
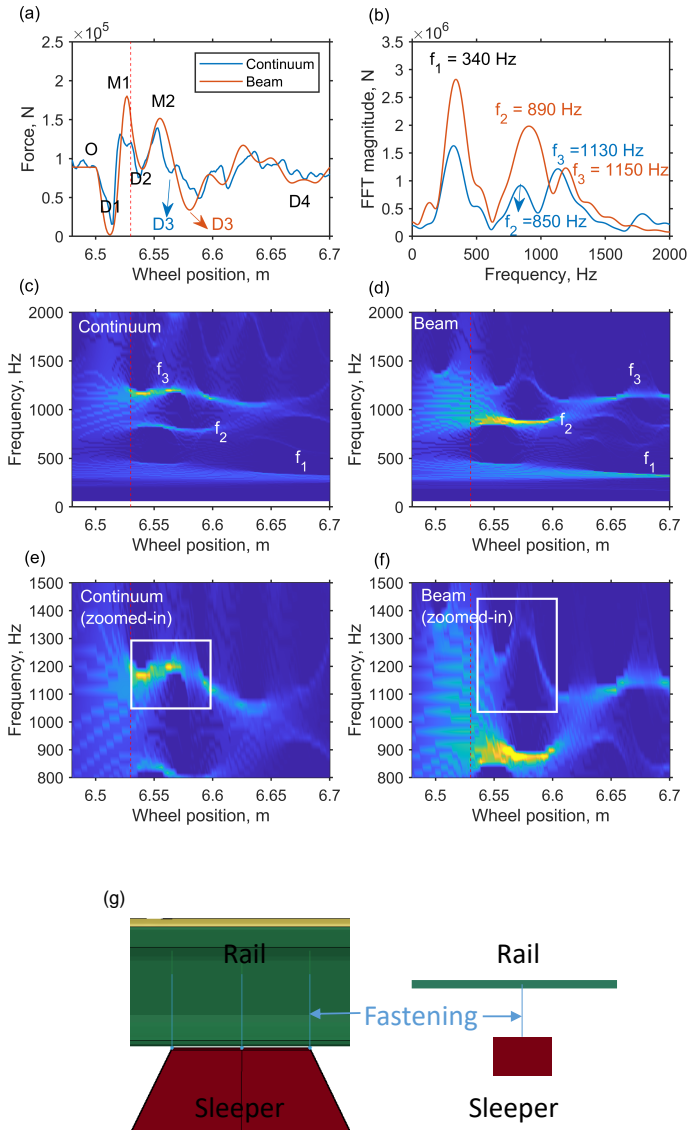
Figure 3.3: Comparisons between the contact forces calculated by the continuum (left column) and beam (right column) model. (a) Time domain; (b) frequency domain; (c) ~ (f) time-frequency representations; (g) the rail-fastening-sleeper model in the continuum model and beam model. The defect starts at 6.5 m with a length of 0.03 m and a depth of 0.2 mm. The dotted vertical lines indicate the end of the defect (6.53 m).

might result in an overestimation of the impact force for wheel flats [114], as well as different frequency contents of the contact force at corrugations [7]. Therefore, in section 3.3.2.1, the effects of wheelset flexibility on the impact force at squats are examined.

For the contact model, the half-space assumption is made in the Hertzian spring model. However, the typical length of a wheel-rail contact patch in the longitudinal direction is approximately 15 mm, which is comparable to the typical length of squats (20 mm ~ 40 mm). This means the half-space assumption may no longer be valid in the longitudinal direction. To account for local geometric variations within the contact area in the longitudinal direction, a two-dimensional contact model with multiple independent springs is considered (Model A3 in Table 3.2), referred to as the Winkler bedding model [127]. This model is compared to the Hertzian spring model and the 3D contact model in Section 3.3.2.2.

For the track model, the main differences between the beam and continuum model are in the assumptions made for the rail and sleeper. It is conventionally believed that the Timoshenko beam is accurate up to about 1500 Hz, due to the assumption of a rigid cross section. Inherent from the different rail and sleeper models are the different fastening models. The rail is assumed to be supported at a single point in the beam model, whereas in reality, the support is over an area, which is more realistically modelled in the continuum model, as shown in Figure 3.2. The effects of these assumptions made in the track models are investigated in 3.3.2.3.

3.3.2.1. WHEELSET FLEXIBILITY
The natural frequencies and mode shapes up to 2000 Hz of the 3D FE wheelset (Figure 3.2) are obtained by eigenanalysis. The mode superposition method is then used to represent the flexible wheelset, of which the total DOF of the wheelset is reduced to 27 modal coordinates. In such a way, the flexible wheelset model is incorporated into the beam model and the wheel-track interaction is solved in the time domain in the same way as the rigid wheelset model.

The contact forces calculated by the flexible and rigid wheelset model are compared in Figure 3.4. The contact force magnitudes of the first two peaks obtained by the flexible wheelset model are slightly smaller than those by the rigid wheelset model (Figure 3.4 (a)). The PSD of the contact force calculated by the flexible wheelset model has three troughs at three wheel resonances compared to the rigid wheel model (Figure 3.4 (b), indicated by the dotted-line boxes). The findings agree with previous studies, see for example [114] for the contact force magnitudes and [7] for the frequency content. In general, the influence of wheelset flexibility on contact force can be neglected. We therefore assume a rigid wheelset for the rest of the chapter.

3.3.2.2. CONTACT MODELS
In this section, we compare two contact models adopted in the beam model, i.e. the Hertzian contact spring (Model 1A in Table 3.2) and the Winkler bedding model (Model 1C), as well as the 3D FE contact model (Model B). Results are shown in Figure 3.5. By changing from the Hertzian spring to the Winkler bedding, the M1 magnitudes, as well as the FFT magnitudes at f_1, f_2 and f_3, are reduced. Such decreases are mainly because the contact filter effect [127] in the longitudinal direction can be taken into account with the Winkler bedding model as opposed to the Hertzian spring model, while it is automatically considered in the 3D FE contact model. Figure 3.6 compares the contact solution of the three models in more detail. When the wheel center is on the descending or ascending edge of the defect, the contact patch centers of the 3D FE model and the Winkler
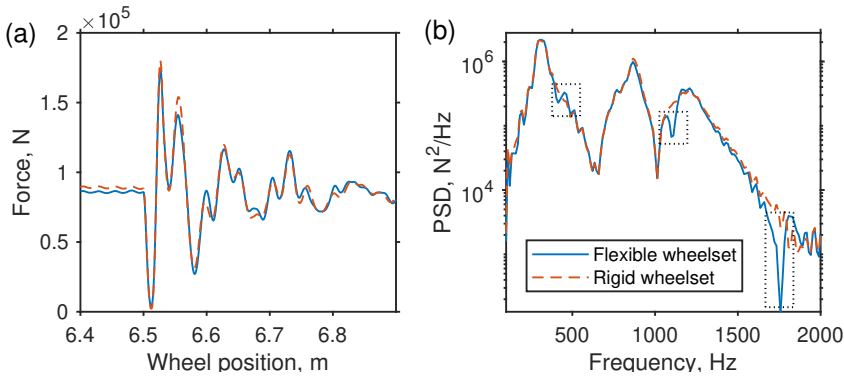
Figure 3.4: Effects of wheelset flexibility on the contact force in (a) time domain and (b) frequency domain.

bedding model do not coincide with the wheel center. In particular, when the wheel center is at the lowest point of the defect, i.e. at 6.515 m, the wheel is in contact with the rail on both the descending and ascending edge of the defect, resulting in two contact patches. In contrast, it is always single-point contact and the contact point is right underneath the wheel center for the Hertzian spring model. The contact filter effect does not change the frequency content; the f_1, f_2 and f_3 are the same for the Hertzian spring and the Winkler bedding. Additionally, with the Winkler bedding model, the dominant frequency above 500 Hz is still at f_2, instead of at f_3 as with the 3D FE model.
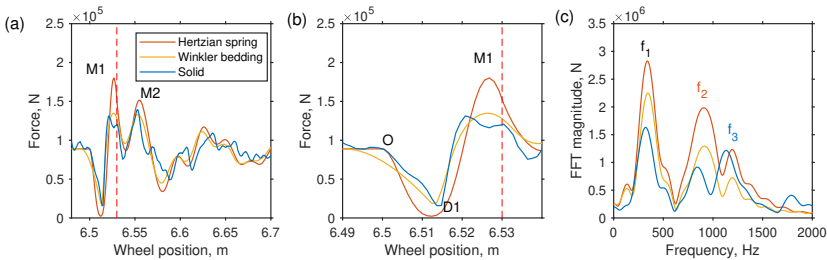

Figure 3.5: Influence of contact models on the contact force. (a) Time domain; (b) zoom-in of (a); (c) frequency domain.

3.3.2.3. TRACK MODELS

To exclude the influence of the wheelset and contact models, we calculate the point receptances of the track at two locations, at 6.5 m and 6.6 m along the longitudinal direction, as shown in Figure 3.7. Figure 3.8 compares the receptances of the two track models at the two locations. Three major track resonances (TRs) are observed for both models in Figure 3.8 (a). TR1 and TR2 are the full-track resonance and the rail resonance, respectively, as defined in section 2.3.1. The peaks at around 1000 Hz are the pin-pin resonances. The receptances are comparable up to the anti-resonance (at about 800 Hz) before the pin-pin resonance. Compared with the beam model, the receptance magnitude
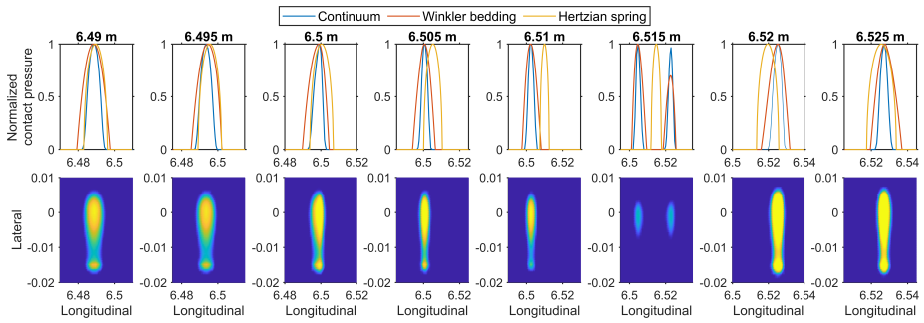
Figure 3.6: Influence of contact models on the contact solution. First row: contact pressure distribution normalized to its maximum value. The title of each subplot indicates the wheel center position. Second row: contact patch and pressure distribution obtained by the continuum model.

of the continuum model at this anti-resonance is larger (i.e. less deep). In addition, the phase change predicted by the continuum model is smaller at this anti-resonance than that by the beam model; see the positive phase change at around 800 Hz in Figure 3.8 (c). Another difference is that the receptance of the beam model at $x = 6.5$ m shows a more distinct peak at the pin-pin resonance. These observations indicate that the damping of the continuum model is larger than that of the beam model before and around the pin-pin resonance. After the pin-pin resonance, however, the beam model predicts smaller changes of both the receptance magnitude and phase at the anti-resonance around 1300 Hz. This means after the pin-pin resonance, there is larger damping in the beam model than in the continuum model. In the track receptances at 6.6 m (Figure 3.8 (b)), the pin-pin resonance completely vanishes for the beam model, whereas for the continuum model, there is still a small peak at around 1000 Hz.
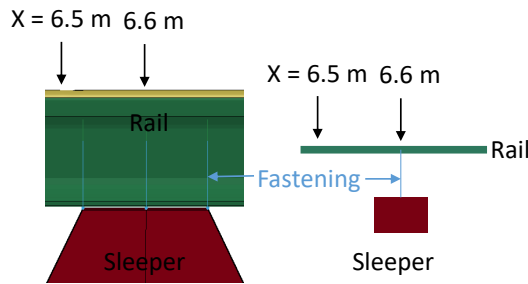
Figure 3.7: The two locations for calculating track receptance.

To compare the damping properties of the two models, the modal properties of the two models are identified using the least square rational fraction (LSRF) method [128] based on the receptances shown in Figure 3.8 (a). Figure 3.9 shows the change of damping ratios with frequencies. Around the pin-pin resonance (between about 800 Hz and 1100 Hz), the damping ratio of the continuum model is higher than the beam model. This is caused by the different fastening models. The rail in the beam model is supported

by a single spring-damper pair, whereas in the continuum model, the rail is supported by a grid of spring-damper pairs over an area; see Figure 3.2 and Figure 3.7. After the pin-pin resonance, there is an abrupt increase of damping for the beam model, resulting in a larger damping ratio between about 1100 Hz and 1800 Hz. This is likely to be caused by the stress wave propagation in the rail, as will be discussed in detail in Section 3.5.2. The calculated damping change is in line with the observations in Figure 3.8.
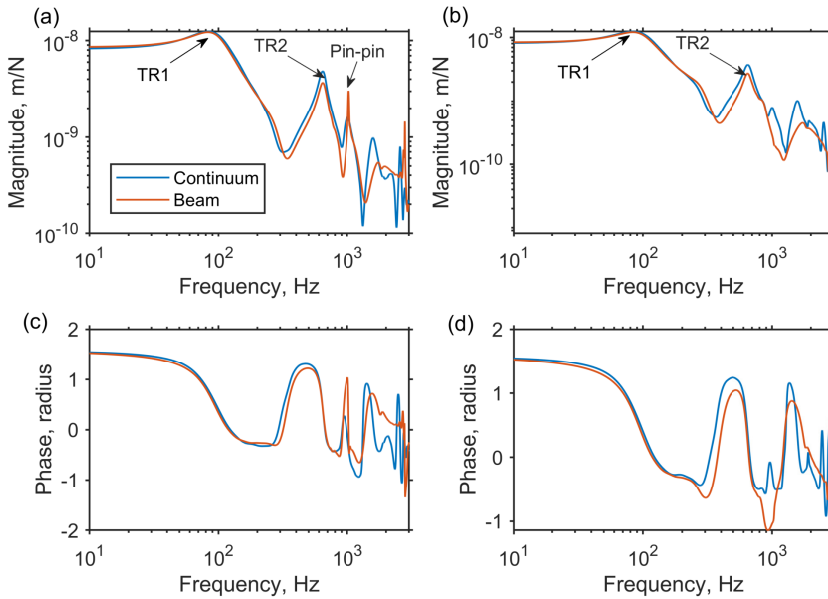

Figure 3.8: Comparisons between the track receptances of the continuum and beam model. (a) and (c) are calculated at $x = 6.5$ m; (b) and (d) are calculated at $x = 6.6$ m.

3.3.3. EFFECTS OF MODEL PARAMETERS

For the analysis in Section 3.3.2, the same set of model parameters was used. In this section, two model parameters, i.e., the wheel speed and defect geometry, are varied to evaluate their effects on the comparison of different models. These two parameters are chosen because they have been shown to have a significant influence on the wheel-rail impact at wheel flats [116] and squats [100, 123]. Besides, as has been shown in Section 3.3.2.2, the impact force is also sensitive to contact models. We, therefore, combine the change of model parameters with different contact models, i.e., Model A1, A2 and B in Table 3.2, in the subsequent analysis. Other model parameters, such as the vehicle and track parameters, are kept the same as in the reference case.

3.3.3.1. WHEEL SPEED

Figure 3.10 shows the impact forces calculated with different wheel speeds ranging from 10 m/s to 40 m/s. In the space domain, the first peak force (M1) calculated by the Winkler
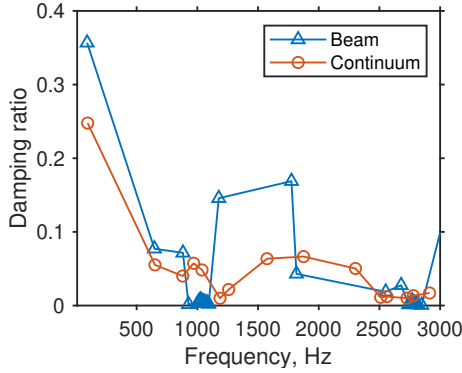
Figure 3.9: Comparisons between the damping ratios of the continuum and beam model. The damping ratios are estimated using the least square rational fraction (LSRF) method. The LSRF method is applied to the receptances shown in Figure 3.8 (a) between 10 Hz and 3000 Hz. The LSRF model order is 38. Only the damping ratios for the stable modes are shown in this figure.

bedding model is almost identical to those by the continuum model for all the speeds. The Hertzian spring model, however, always yields a larger M1 force. In the frequency domain, as the wheel speed increases, high-frequency components become more evident for all three models. At high speeds, e.g., 30 m/s and 40 m/s, the FFT magnitudes become dominant at f_2 for the beam model and at f_3 for the continuum model. In general, the discrepancies between the Winkler bedding model and the continuum model become smaller as the wheel speed decreases.
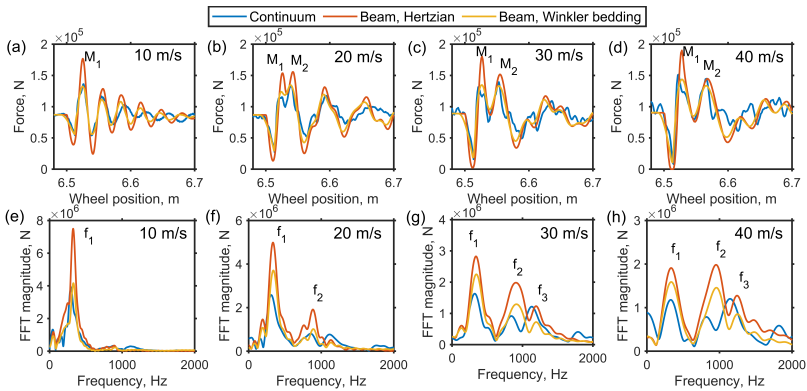

Figure 3.10: Effects of wheel speed on the wheel-rail impact force at a squat (length: 30 mm; depth: 0.2 mm). (a)~(d) Space domain; (e)~(h) frequency domain.

3.3.3.2. DEFECT GEOMETRY
Figure 3.11 compares the impact forces calculated by different models for different squat geometries. It can be seen the impact force is more sensitive to the length than the depth

of squats. In the space domain, the two peak forces M1 and M2 merge into one peak as the length increases. In the frequency domain, the FFT magnitudes at high frequencies (e.g., at f_2 and f_3) gradually diminish as the defect length increases. The FFT magnitudes calculated by the beam models are always larger at f_2 than those at f_3, whereas, for the continuum model, the f_2 magnitude only becomes dominant for longer defects, e.g., longer than 50 mm.

In both the space and frequency domains, the discrepancies between different models become smaller as the defect length increases or as the defect depth decreases. In general, beam models, especially with the Hertzian spring, are only comparable to the continuum model for longer defects, e.g., in the current case at least longer than 50 mm. It should be noted that the maximum defect depth considered here is 0.3 mm, which is typical for squats but might be small for wheel flats. Further investigations are needed as to whether the conclusions made here are still valid for larger defects.

In both Figure 3.10 and Figure 3.11, despite the change in the FFT magnitudes, the characteristic frequencies of f_1, f_2 and f_3 remain the same for each model. This suggests that f_1, f_2 and f_3 represent certain resonances of the coupled wheel-track system. The origin of these resonances will be further investigated in Section 3.4.

3.4. COUPLED DYNAMICS OF THE WHEEL-TRACK SYSTEM

We have analysed the influences of the wheelset, contact and track models separately in Section 3.3.2. The three characteristic frequencies of the impact force, i.e., f_1, f_2 and f_3, are not sensitive to the change of wheelset and contact models. For different track models, we only compared their effects on the track receptance (see Figure 3.8); how the track receptance is correlated with the impact force remains unclear. In this section, we use a frequency domain model to combine the effects of the three components. In such a way, the origin of the characteristic frequencies, as well as the contribution of each model component to the characteristic frequencies are clarified.

3.4.1. FREQUENCY DOMAIN MODEL

The defect geometry $Z_{irr}(x)$ defined in Eq. 3.3 can be transferred into the time domain by dividing $Z_{irr}(x)$ by the velocity of the wheel that passes over the defect. Then the time-domain defect geometry can be further transferred into the frequency domain using the Fast Fourier Transform (FFT). The Fourier coefficient at different frequencies f is denoted as $X(\omega)$, where $\omega = 2\pi f$ is the circular frequency. Figure 3.12 shows the geometries of two short-wave rail surface defects with different lengths. In the frequency domain, the Fourier coefficients are flat up until a certain cut-off frequency and the larger defect has a lower cut-off frequency.

The contact force $Y_F(\omega)$ can then be solved in the frequency domain assuming a linear time-invariant system as

$$Y_F(\omega) = H_F(\omega)X(\omega) \tag{3.4}$$

where $H_F(\omega)$ is the transfer function that represents the characteristics of the wheel-track system and can be formulated as [35, 129],
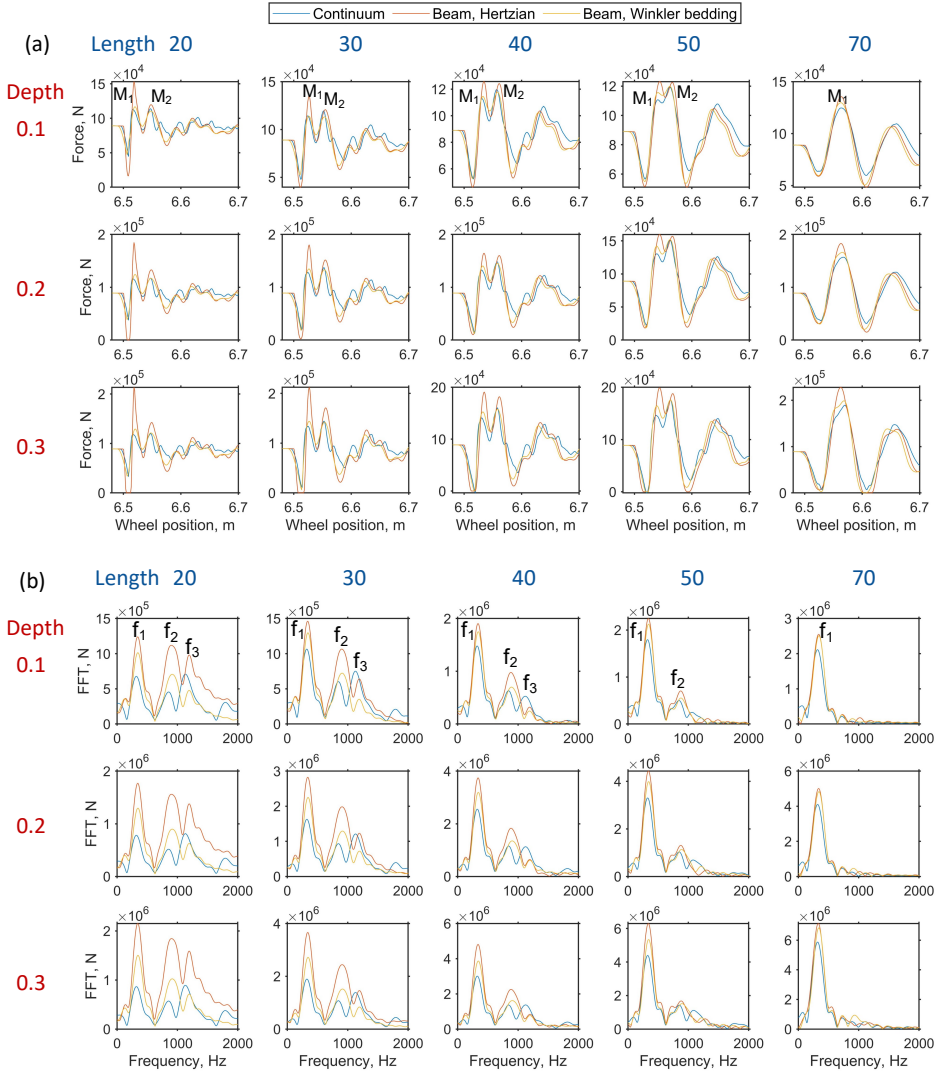
Figure 3.11: Effects of defect geometry on the wheel-rail impact force at a squat with a wheel speed of 30 m/s. (a) Space domain; (b) frequency domain. Different defect geometries are defined according to Eq. 3.3. The lengths and depths of the defects are indicated in the figure with the unit of mm.

$$H_F(\omega) = \frac{1}{\alpha_w(\omega) + \alpha_t(\omega) + \alpha_c(\omega)} \tag{3.5}$$

where $\alpha_w, \alpha_t, \alpha_c$ are the point receptance of the wheel, track and contact spring at the contact point, respectively. It should be noted that Eq. 3.5 is derived under the condition that only half of the track is considered.

To employ this frequency domain model for the analysis, we need to make some as-

Figure 3.12: Geometries of two typical rail surface defects in the space and frequency domain (a) $Z_{irr}(x)$ (b) Magnitude of the Fourier coefficient $X(\omega)$. Blue line: length 30mm, depth 0.2 mm; red line: length 50mm, depth 0.2mm. Both defects start at 6.5m which is near the center of sleeper support at 6.6 m.

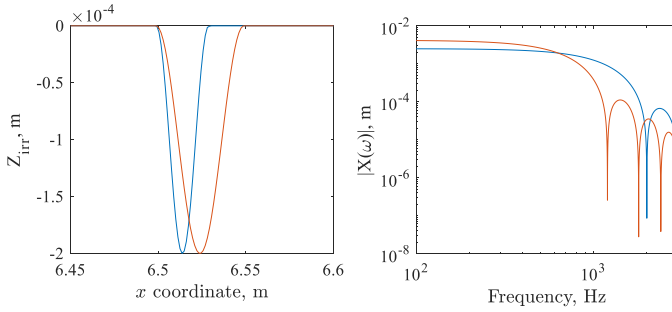sumptions. First, a linearized contact spring stiffness K_H is assumed. To account for the nonlinear behaviour of the Hertzian contact spring, i.e., the change of contact stiffness with contact force, we adopt a range of K_H between 4×10^8 N/m and 1.2×10^9 N/m, according to the range of the contact force, see e.g. Figure 3.3 (a). The receptance of the contact stiffness can be calculated as $\alpha_c(\omega) = 1/K_H$ [35, 129]. Second, as the effect of wheelset flexibility is negligible (see Section 3.3.2), the wheel is considered as a rigid mass of $M_w = 900$ kg (approximately half of a motorized wheelset). Thus the wheel receptance can be calculated as $\alpha_w(\omega) = 1/\omega^2 M_w$ [35, 129]. Third, to represent the non-stationary feature of the wheel-track system as shown in Figure 3.3 (c) $\sim$ (f), we adopt the concept of '*frozen configuration*' [130] of the wheel-track system for each wheel position x. More specifically, we assume that at each wheel position x, the system is '*frozen*' (made stationary) with the track receptance denoted as $\alpha_t(\omega, x)$. Examples of $\alpha_t(\omega, x)$ at $x = 6.5$ m and 6.6 m for different models are shown in Figure 3.8. Thus, the '*frozen*' transfer function $H_F(\omega, x)$ and the force spectrum $Y_F(\omega, x)$ can be calculated according to Eq. 3.5 and 3.4, respectively. In such a way, the non-stationary wheel-track system changing with the wheel position can be represented by a sequence of '*frozen*' stationary systems.

3.4.2. CORRELATING TRACK RECEPTANCE TO IMPACT FORCE

We first calculate the *frozen configuration* response at $x = 6.5$ m. Figure 3.13 shows the receptances $\alpha(\omega)$ (top row) and force spectrums $Y_F(\omega)$ (bottom row) calculated at $x = 6.5$ m for the continuum model (first column) and the beam model (second column). From the frequency domain model, we can see that f_1, f_2 and f_3 are due to the coupling between the different components of the wheel-track system. At these frequencies, the wheel receptance is much smaller than the track and contact receptance. Therefore, the characteristic frequencies of the contact force can be approximated by the intersection points of the track receptance curves with the contact stiffness line, neglecting the effect of wheel mass. More specifically, the contact stiffness line intersects with the receptance curve to the right side (the mass-dominated part) of the three track resonances, i.e., the TR1, TR2 and pin-pin resonance, resulting in f_1, f_2 and f_3, respectively. Hence, $f_i(i = 1, 2, 3)$ can be seen as the resonance frequency of a single-degree-of-freedom system, as

shown in Figure 3.14, with the equivalent mass m_{eq}^i and the contact stiffness K_H

$$\omega_i = 2\pi f_i = \sqrt{K_H / m_{eq}^i} \, (i = 1, 2, 3) \tag{3.6}$$

3

For comparison, the Fourier spectrums from the corresponding time domain models are also presented in Figure 3.13. The f_1, f_2 and f_3 obtained by the time domain models agree relatively well with their counterparts obtained by the frequency domain models with $K_H = 1.2 \times 10^9$ N/m. In terms of the FFT magnitudes, the time-domain continuum model predicts lower magnitudes at f_2 and f_3 compared to its frequency domain model with $K_H = 1.2 \times 10^9$ N/m (Figure 3.13 (c)). This is because the contact filter effect is not considered in the frequency domain model. For the beam model, in which the contact filter effect is also not considered, the FFT magnitudes agree well between the time and frequency domain models. It is also noticed that above 500 Hz the frequency-domain model with $K_H = 1.2 \times 10^9$ N/m predicts a higher magnitude at f_3 for the continuum model whereas at f_2 for the beam model (Figure 3.13 (c) and (d)). This is in line with the time-domain predictions. This means the difference in the dominant frequencies between the two models is due to the difference in the track models. More specifically, it is due to the different damping properties of the two track models. As shown in Figure 3.9, the damping ratio above the pin-pin resonance is much larger in the beam model, which leads to the attenuation of the f_3 magnitude in Figure 3.13 (d). Likewise, as the damping ratio is larger in the continuum model before the pin-pin resonance, the f_2 magnitude in Figure 3.13 (c) is smaller than the f_3 magnitude.

Now we examine the time-variant feature of the wheel-track system using the frequency domain model. We compare the predictions of f_1, f_2 and f_3 by the frequency domain model with those by the time domain models, as shown in Figure 3.15. Comparing the frequency domain solutions (see the red circles in Figure 3.15), the beam model predicts a larger variation of f_3 with the change of wheel positions than the continuum model. This is due to the different support lengths in the longitudinal direction of the fastening models in the two models (see Figure 3.3 (g)).

The time domain response is equal to its '*frozen*' part plus a term representing the dynamic effects [130]. Therefore, by using the frequency domain model as a baseline, we can compare the dynamic effects of the two time domain models. In Figure 3.15, the SWPSs are obtained by the time domain models. Unlike the frequency domain solutions, the time domain solutions of the f_2 and f_3 are asymmetrical about the sleeper support at 6.6 m. For both the continuum and beam model, the largest deviations of the time domain solutions from the frequency domain solutions occur between 6.55 m and 6.6 m, predominately at f_3. The deviations are larger for the beam model than for the continuum model. This means the dynamic effects in the beam model, such as due to wave propagations (to be discussed in Section 3.5.2), are more pronounced than those in the continuum model when the wheel is approaching the support.
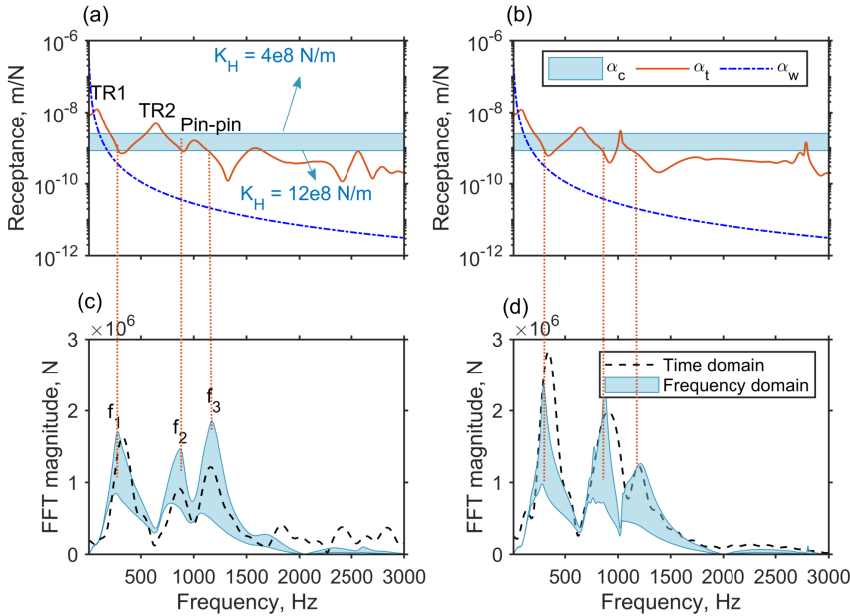
Figure 3.13: Frequency domain model of the wheel-track system '*frozen*' at $x = 6.5$ m. Top row: receptances of contact spring $\alpha_c(\omega)$, track $\alpha_t(\omega)$ and wheel $\alpha_w(\omega)$; the contact receptances α_c are calculated with the contact stiffness between 4×10^8 N/m and 12×10^8 N/m. Bottom row: comparisons between the Fourier spectrums calculated by the frequency domain and time domain models. (a) (c) and (b) (d) show the results for the continuum model and the beam model, respectively.
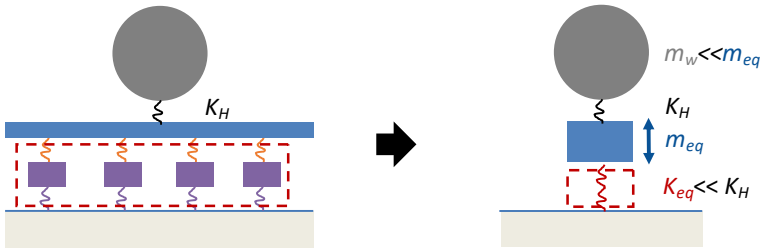
Figure 3.14: An illustration of coupled wheel-track dynamics based on the frequency domain model.

3.5. DISCUSSIONS

3.5.1. ACCURACY OF THE MODELLING RESULTS COMPARED TO FIELD OB-SERVATIONS

Continuum models with similar approaches have been validated using both the axle-box acceleration measurement [101] and the wear patterns observed in the field [68]. We discuss how the simulation results in this chapter fit with these measurements and
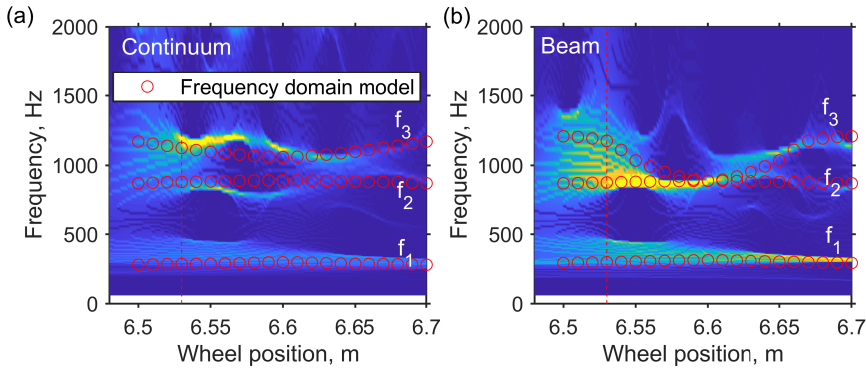
Figure 3.15: Comparisons between the characteristic frequencies predicted by the time domain and frequency domain models. (a) Continuum model; (b) beam model. The SWPSs are obtained by the time domain models. The red circles indicate a sequence of the *frozen configuration* responses at each wheel position obtained by the frequency domain models.

observations.

3.5.1.1. AXLE BOX ACCELERATION

In [101], the ABA signals were obtained with accelerometers mounted on the four axle boxes of a bogie. The sampling frequency was 25000 Hz, which is also the sampling rate we used in this chapter to sample the simulation outputs. The measured ABA signals were low-pass filtered with a cut-off frequency of 2000 Hz. In this chapter, the simulation results were not filtered as they are less noisy than the measurement. However, as the frequency of interest is up to about 1200 Hz in this chapter, the filtered ABA measurements are still valid for comparison with simulations. In addition, a uniform lateral profile of the squat is considered in this chapter, see Figure 3.2. In comparison, the ABA signals were obtained at squats with non-uniform lateral profiles. Nevertheless, it was shown in [131] that the wavelengths or characteristic frequencies of the impact force are not influenced by the lateral profile of squats.

The ABA signals measured at various squats show two distinct frequency bands, with the lower frequencies between 300 Hz and 500 Hz and the higher frequencies between 1000 Hz and 1200 Hz [101]. In this chapter, the two models yield nearly identical f_1 frequencies at around 340 Hz. However, the higher frequency predicted by the beam model is at $f_2 = 890$ Hz and that by the continuum model is at $f_3 = 1120$ Hz. This means the continuum model fits better with the ABA measurements in terms of the higher frequency (between 1000 Hz and 1200 Hz).

3.5.1.2. WEAR PATTERN FOLLOWING SQUAT

Corrugation-like wear patterns can be observed after squats in the train traffic direction [45, 68]. Examples of such patterns are shown in Figure 3.16. The direct dynamic effect of a squat is the first wave pattern after it, which is usually shorter than 30 mm. This wave is caused by the first peak of the contact force after the defect, i.e. the D2M2D3 in Figure 3.3. In this chapter, the continuum model gives a more accurate prediction of this wavelength (26 mm), while the beam model overestimates the wavelength (38 mm).
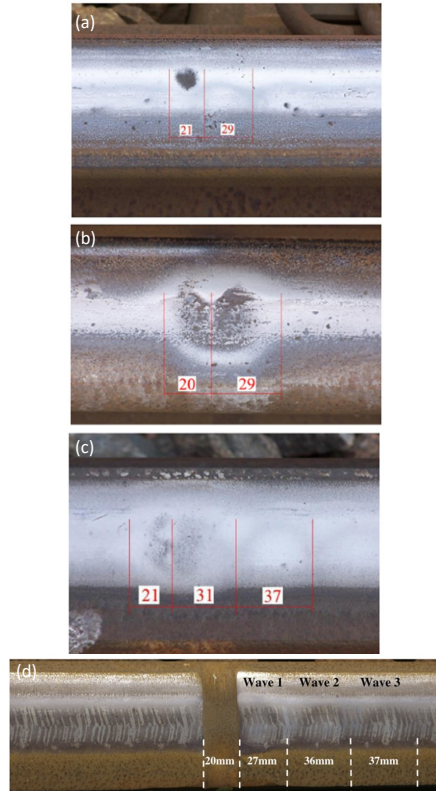
Figure 3.16: Examples of wear patterns after different squats. (a) Class A; (b) class B; (c) class C; (d) an artificial defect cut on the rail surface. (a), (b) and (c) are taken from [45] and (d) is taken from [101].

3.5.2. STRESS WAVE PROPAGATION IN TRACK

One major dynamic effect that is more realistically modelled in the continuum model than in the beam model is the stress waves propagating in solids. In general, there are three types of waves due to dynamic loadings, i.e. Rayleigh waves, shear waves (S-waves) and dilatational waves (P-waves). Rayleigh waves propagate near surfaces while S-waves and P-waves can travel within solids, hence also called body waves. Rayleigh waves generated by the wheel-rail impact have been reproduced and discussed in detail in [119]. Here we show the simulated body waves generated by the wheel-rail impact and their reflections by the sleeper in Figure 3.17. It can be seen that away from the contact point, the velocity is approximately constant across the rail section (see e.g. the section indicated by the dashed red box), meaning the assumption of a rigid cross section of the beam model may reasonably apply. However, near the contact point, the beam model is unable to capture the waves propagating from the rail top to bottom, as well as the reflected waves by the sleeper.

(a) t = 0.017252 s Xw = 6.5176 m   (b) t = 0.017332 s Xw = 6.52 m

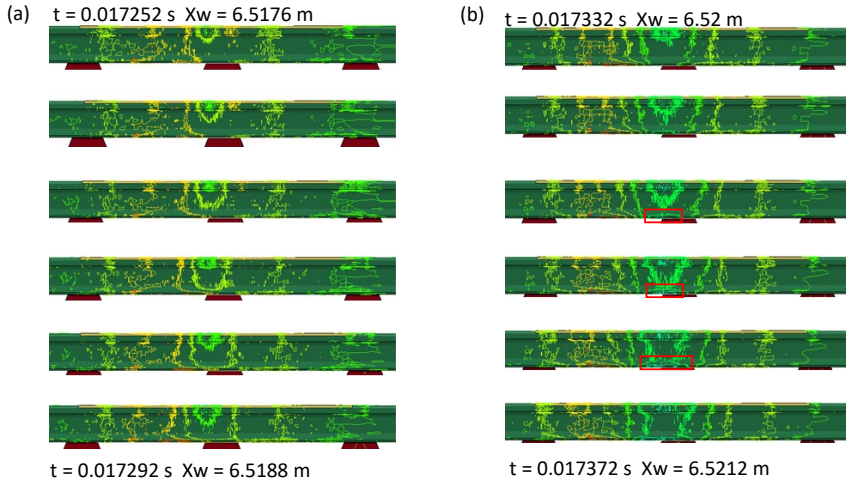t = 0.017292 s Xw = 6.5188 m   t = 0.017372 s Xw = 6.5212 m

Figure 3.17: Simulated wave propagations in the rail due to wheel-rail impact using the continuum model. (a) Wave generation and initial propagation; (b) wave reflected by the sleeper. In each subplot, we show six states of the velocity field, with the beginning and end time stamps and wheel positions indicated in the figure. The time interval between each state is 8 μs. Note the first state in (a) corresponds to the first dip D1 of the contact force, see Figure 3.5 (b).

3.5.2.1. EFFECTS ON M1 MAGNITUDE

Whether wave propagation should be considered depends on the problem of concern. For example, Rayleigh waves influence the contact solutions as they are generated by the wheel-rail creepage within the contact patch and subsequently propagate through the contact patch [119]. More relevant to this chapter are the body waves. For the continuum model, the effective inertia of the rail that participates in the vibration of the wheel-track system (e.g. the m_{eq} shown in Figure 3.14) comes first from the point of contact and then "gradually" expand as the waves spread out, see Figure 3.17. While for the beam model, any vibration always involves the whole cross section, which has larger inertia. A smaller m_{eq} leads to a smaller M1 peak predicted by the continuum model. It should be noted that although the Winkler bedding model produces results that are nearly identical to the continuum model, it tends to underestimate the peak force compared to Kalker's variational method [116, 121]. This means there should be other factors that cause the discrepancies in the M1 magnitude between the two models, such as the effect of wave propagation discussed above. In general, taking into account stress wave propagations will lead to a smaller M1 peak. However, the quantitative effect of the wave propagation on the M1 magnitude depends on many factors and thus needs further investigation.

3.5.2.2. EFFECTS ON f_3 RESONANCE

The wave propagation is asymmetrical to the two sides of the contact point; see the asymmetrical velocity field in Figure 3.17. The stress waves travel more freely in the direction away from the support while are more decayed in the direction towards the support. This asymmetry mainly concerns the frequency region around the pin-pin res-

onance [70]. This may explain why the change of f_3 is asymmetrical about the sleeper support in Figure 3.15.

For the continuum model, the body waves propagate more freely near the rail surface while being more easily reflected and attenuated by the fastenings at the rail bottom (see Figure 3.17). In contrast, the wave propagation in the beam model does not distinguish between the rail top and bottom. As a result, the beam model might experience more reflected waves at the wheel-rail contact, which further leads to larger frequency fluctuations at f_3, especially when the contact is near the sleeper support (see Figure 3.15).

3.5.2.3. Effects on damping

The damping of the track at higher frequencies (above 1000 Hz) is mainly controlled by the railpad damping. In both the continuum and beam model presented in this chapter, the railpads are viscously damped. This means the amount of damping depends on the velocities of the rail and sleeper at rail seats. Figure 3.18 compares the rail and sleeper velocities at the rail seat at 6.6 m. It can be seen the rail velocity magnitude predicted by the beam model is closer to that by the continuum model at the rail top, while is larger than that at the rail bottom. For the sleeper velocity, the beam model also predicts a larger magnitude than the continuum model. The major frequency of the velocities for both models is at around 1100 Hz, which is higher than the pin-pin resonance. Consequently, the continuum model shows lower damping than the beam model at f_3.
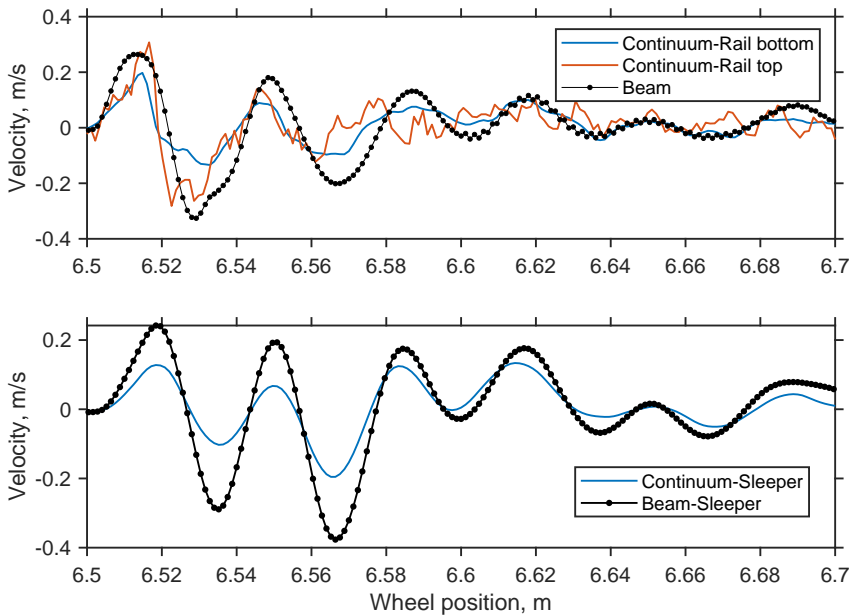

Figure 3.18: Comparisons between the track velocities at the rail seat at 6.6 m. Upper: rail velocity; bottom: sleeper velocity.

3.6. CONCLUSIONS

We compare the simulation results of a continuum and a beam FE model for the wheel-rail impact force at a typical rail squat defect. We also compare the simulations with field measurements and observations, which suggests the continuum model is more accurate than the beam model.

The impact force consists of a forced vibration peak M1 followed by free vibration related oscillations with three dominant frequencies f_1 (340 Hz), f_2 (890 Hz) and f_3 (1120 Hz). The three frequencies are independent of wheel speed and defect geometry. They correspond to the eigenfrequencies of the wheel-track system according to the proposed frequency domain model.

The beam model with a Hertzian contact spring overestimates the M1 peak of the impact force. The discrepancy can be reduced but not eliminated by using the Winkler bedding model, because it can better model the wheel-rail contact solution in the longitudinal direction.

Different from the conventional belief that the Timoshenko beam is accurate up to about 1500 Hz for the rail model, we show that the beam model is only accurate up to about 800 Hz in terms of the track receptance. As to the impact force, the valid frequency range of the beam model is further reduced. The beam models produce larger FFT magnitudes at the first characteristic frequency of about 340 Hz. The beam models are only comparable to the continuum model for long and shallow squats, e.g., longer than 50mm while not deeper than 0.3 mm in the case considered in this chapter.

The two track models show different damping behaviour around the pin-pin resonance, i.e. between about 800 Hz and 1800 Hz. The damping of the continuum model is larger below and at the pin-pin frequency, whereas the damping of the beam model is larger above the pin-pin frequency. The differences in the damping are caused by the different modelling of the stress wave propagation in the rail. As a result, the contact force dominates at f_3 (1120 Hz) for the continuum model while at f_2 (890 Hz) for the beam model.

The propagation of the body waves in the rail caused by the wheel-rail impact is reproduced by the continuum model. We show that the stress wave propagation contributes to the smaller M1 peak and smaller track damping after the pin-pin resonance in the continuum model. The findings contribute to a better understanding of the dynamic characteristics of the wheel-rail impact force, as well as the root causes for the different simulation results between the two models. In engineering practice, this study can assist engineers in choosing the appropriate assumptions for the wheel, contact and track models when solving wheel-rail impact problems.

4

EVALUATING RAILWAY TRACK DYNAMIC STIFFNESS USING FIELD HAMMER TESTS

Track stiffness is a critical parameter that is closely related to track health conditions and should therefore be monitored frequently. In this chapter, we apply the proposed digital twin framework to evaluate track stiffness from measured frequency response functions (FRF) by hammer tests. In particular, we propose to combine a physics-based finite element (FE) track model and a data-driven Gaussian process regression (GPR) model to directly infer railpad and ballast stiffness.

Conventionally, only the rail resonance and full-track resonance are used as the FRF features to identify track stiffness. In this chapter, eleven features, including sleeper resonances, from a single FRF curve are selected as predictors of the GPR models. To deal with incomplete measurements and uncertainties in the FRF features, we train multiple candidate GPR models with different features, kernels, and training sets. Predictions by the candidate models are fused using a weighted Product of Experts method that automatically filters out unreliable predictions. We compare the performance of the proposed method with a model updating method using particle swarm optimization (PSO) on two synthesis datasets in a wide range of scenarios. The results show that the enriched features and the proposed fusion strategy can effectively reduce prediction errors. In the worst-case scenario with only three features and 5% injected noise, the average prediction errors for the railpad and ballast stiffness are approximately 12% and 6%, outperforming the PSO by about 6% and 3%, respectively. Moreover, the method enables fast predictions for large datasets. The predictions for 400 samples take only approximately 10 seconds compared with 40 minutes using the PSO. Finally, a field application example shows that the proposed method is capable of extracting the stiffness values using a simple setup, i.e. with only one accelerometer and one impact location.

This chapter is based on [132]

4.1. Introduction

The stiffness of ballasted railway track is primarily provided by resilient components such as railpads and ballast. The stiffness values of these components are important parameters as they are closely related to track conditions. On one hand, the stiffness of track components changes as their condition deteriorates, e.g., due to ballast damage [133] or worn railpads [134]. On the other hand, deviations in track component stiffness can also accelerate the track degradation process or even lead to new track defects. Therefore, track stiffness should be properly monitored during the whole life cycle of railway tracks. In addition, most of the dynamic train-track interaction models require the stiffness values of the railpad and ballast as inputs. Therefore, accurate identification of the stiffness of track components from field measurement is very much desired.

A typical ballasted railway track system can be modelled as a layered structure that comprises rails, fasteners/railpads, sleepers, and ballast [26]. Track stiffness can be defined as the combined effect of different track components, e.g., the track support stiffness refers to the equivalent stiffness provided by all the track components below the rail [23]. In this chapter, however, we treat the stiffness values of resilient components in the track system separately and mainly focus on the stiffness of the railpad and ballast. The definitions and values of railpad and ballast stiffness are based on their representations in a two-layer discretely supported numerical model (see Section 4.2.2).

Track stiffness can be measured with controlled excitations or under dynamic train loading using specialized measurement vehicles [58] or operational trains [23]. Controlled excitation methods include impact excitations with hammers [135–138], falling weights [139] as well as sinusoidal excitations with hydraulic cylinders [28, 59]. The main advantage of these methods is that the excitation forces can be measured so that the frequency response function (FRF) can be directly derived. Furthermore, as the excitation is generated in a controlled manner, the measurement noise is usually lower compared to that with the train loading. For excitations using hand-held hammers, the test equipment and setup are cost-effective and relatively simple to implement. Because of the aforementioned advantages, although measured track stiffness can be quite dependent on the loading conditions [140], the hammer impact measurement has been widely used to identify track parameters [46–51].

Identification of track stiffness from measurement is in essence an inverse problem. In general, it involves fitting a physical (analytical or numerical) model to measurement. For simple and individual cases in railway applications, modelled FRFs are usually manually 'tuned' to fit measured FRFs based on certain FRF features[46–51]. However, manual adjustment is labour-intensive and time-consuming. In addition, the number of FRF features that can be fitted simultaneously is very limited. Usually, the full-track resonance and the rail resonance are used to determine the ballast and railpad stiffness, respectively [46, 47, 51].

Alternatively, the fitting process can be achieved by solving an optimization problem, where objective functions defining the difference between modelled and measured FRFs are minimized iteratively. This process is also known as model updating. As the process is iterative, a track model has to be evaluated multiple times until the objective functions converge. Therefore, the speed of the optimization process highly depends on the complexity of the model. From simple to complex, the following track models have

been used for the optimization process: a rational fraction polynomial (RFP) [17], a two-degrees-of-freedom (2DOF) model [52], an analytical beam on elastic foundation model [53], a finite element (FE) model consisting of only one sleeper beam and two rail masses [133, 135], a two-layer beam model [54] and a three dimensional FE model [55]. On one hand, simplified models may not fully reproduce the FRF features [72] and thus may not be robust in some scenarios. On the other hand, complex numerical models may be computationally unaffordable due to the iteration process. For simple track models, conventional gradient-based algorithms may yield satisfactory results [52]. For complex track models, more advanced optimization techniques, such as evolutionary algorithms (EAs), are needed to deal with the multimodal and non-convex nature of the problem [141]. Among EAs, particle swarm optimization (PSO) and its variants have been widely used in model updating problems both in railway applications [142] and in more general structural identification problems. Extensive comparison studies between different EAs can be found in the literature for general structural identification problems [143, 144], whereas they have not been compared specifically for the track parameter identification problem.

Besides the model updating methods, one can also establish an inverse mapping between structural inputs and outputs. In such a way, the iterative process can be avoided, which significantly accelerates the identification process. For example, based on a beam on elastic foundation model, track support stiffness was correlated to the ratio of two harmonic velocity amplitudes measured from sleeper vibrations subjected to pass-by train loadings [23]. The selection of the feature requires considerable physical insight so that the correlation between such a feature and track stiffness is strictly monotone; otherwise the predictions would be non-unique. A more general approach is to use data-driven methods, such as neural networks (NN) [145, 146] or the Gaussian process regression (GPR) [147], to learn the inverse relationship, based either on simulated or measured data. An example in railway applications can be found in [59], where twelve features of simulated FRFs were selected to train a NN that can directly predict the properties of railway substructures. For structural identification problems, uncertainties associated with modelling and measurement errors as well as incomplete measurements should be properly addressed to ensure robust identifications. Uncertainties can be reduced by injecting noise into training data [145, 148] and prediction fusion [149]. Incomplete measurements can be treated with a careful feature design for the specific problem in concern [150]. In this chapter, we choose the GPR as the data-driven process because it is a non-parametric Bayesian method, which shows several advantages over other methods. Firstly, compared with conventional parametric regression models, the GPR has more expressive power in the sense that it can handle complex datasets (e.g. with high dimensions) with more flexibility [151]. Another practical motivation to use the GPR is that it can provide both predictions and confidence intervals, as opposed to other kernel-based non-parametric regression methods, such as the support vector machine (SVM) and artificial neural network (ANN), which only offer point estimates. Besides, as a Bayesian approach, the GPR can incorporate prior information and training data to infer a posterior with reduced uncertainty [152]. In this chapter, we make use of such reduced uncertainty from prior to posterior, i.e. the entropy change, as an indicator to weigh and fuse the predictions by multiple GPR models trained with different

datasets.

In this chapter, we propose a non-iterative method to directly infer the stiffness of railpad and ballast from measured FRF features based on the GPR. To make the field test setup as simple as possible, we aim to use only one FRF curve for the identification. Section 4.2 provides an overview of the proposed method. In section 4.3, eleven features are selected from a single FRF based on a global sensitivity analysis. In section 4.4, multiple GPR models are trained and a fusion strategy is proposed. The performance of the proposed method is evaluated by comparing it to a baseline method. Finally, the capabilities of the proposed method are demonstrated with two numerical examples and a field application example in section 4.5.

4.2. Method

4.2.1. Overview

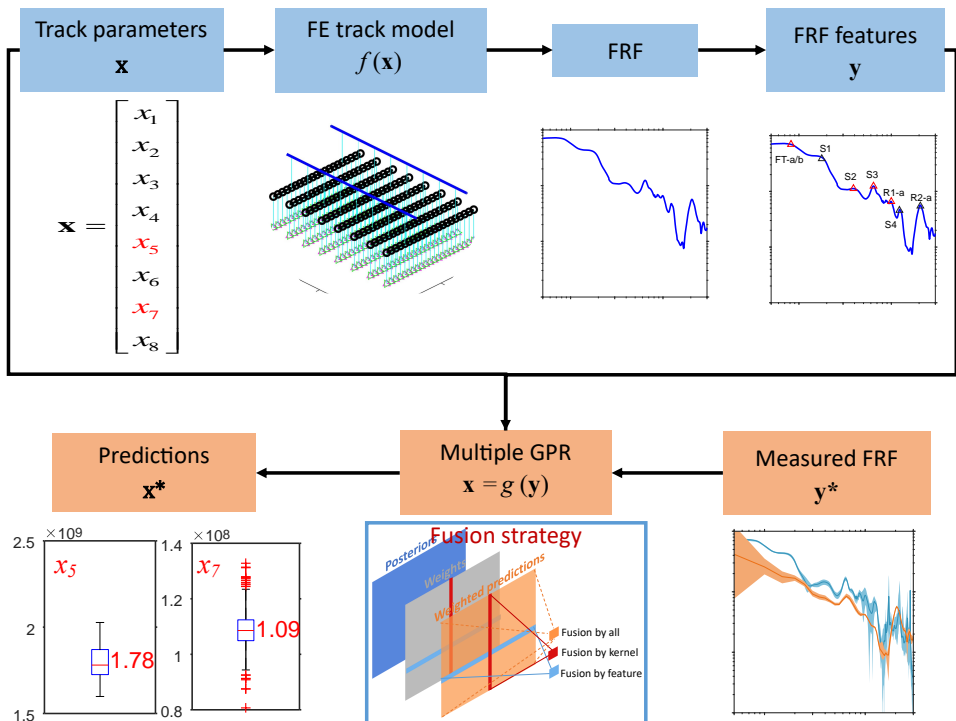An overview of the approach adopted in this chapter is shown in Figure 4.1.

Figure 4.1: Overview of the proposed method.

Two types of relationships (i.e. a forward and an inverse) between track parameters

and FRFs are defined

$$\mathbf{y} = f(\mathbf{x}), \mathbf{x} \in X$$
$$\mathbf{x} = g(\mathbf{y}), \mathbf{y} \in Y$$

(4.1)

where $\mathbf{x} = (x_1, x_2, \ldots, x_m)^T$ is a vector of track parameters defined in m-dimensional space X and $\mathbf{y} = (y_1, y_2, \ldots, y_n)^T$ is a vector containing FRF features defined in n-dimensional space Y. In this chapter, eight track parameters ($m = 8$) are considered: x_1 - rail bending stiffness (EI); x_2 - rail inertia property (ρA); x_3-sleeper (EI); x_4-sleeper ρA; x_5-railpad stiffness; x_6 - railpad damping; x_7 - ballast stiffness; x_8 - ballast damping. For the selection of FRF features $\mathbf{y}$, we use a global sensitivity analysis method to identify the most relevant FRF features in relation to the railpad and ballast stiffness; see Section 4.3.2.

The forward relationship f is established using a finite element (FE) track model which takes the track parameters as inputs and outputs the corresponding FRF features. Section 4.2.2 gives a detailed description of the FE model. The model is validated in Section 4.3.1. With this model, we can generate a discrete mapping of

$$\bar{f} : \mathbf{x}^{(i)} \rightarrow \mathbf{y}^{(i)}, \text{ for } (i = 1, 2, \ldots, d)$$

(4.2)

where d is the number of observations.

The core task is to formulate the inverse relationship $\mathbf{x} = g(\mathbf{y})$, in particular for two track parameters, i.e. x_5 - railpad stiffness and x_7 - ballast stiffness. For this purpose, we construct two datasets, each with d observations, based on the inverse mapping of $\bar{f}$, i.e. $\mathcal{D}_j = \left\{ \left(\mathbf{y}^{(i)}, x_j^{(i)} \right) \mid i = 1, \ldots, d \right\}, j = 5, 7$. Now we need to fit a function g to each dataset $\mathcal{D}_j$, which for any given FRF feature vector $\mathbf{y}^*$ can make a prediction of the track parameter x_j^*. In this chapter, we use the GPR to accomplish the fitting process. The basic theory of GPR is introduced in Section 4.2.3.

A major issue is to consider incomplete measurements as well as uncertainties associated with modelling and measurement errors in the GPR model. Incomplete measurements will lead to dimension changes of FRF features $\mathbf{y}^{(i)}$ for different observations, while uncertainties will lead to noisy observations of $\mathbf{y}^{(i)}$. We address these issues specifically in Section 4.4.

4.2.2. FE TRACK MODEL
The track is represented by a two-layer discretely supported model; see Figure 4.2 (b). The rails and sleepers are meshed with Timoshenko beam elements. At each node, only the vertical and in-plane rotational degrees of freedom are considered. The mesh sizes were determined by a convergence analysis, resulting in 6 elements per sleeper span for the rail and 20 elements per sleeper. The total length of the track model is 12 m with 20 sleeper spans. Railpads are modelled using the Kelvin-Voigt (KV) model with an elastic spring and a viscous damper connected in parallel. The railpad stiffness is defined as the spring stiffness of the KV model. In this chapter, we model railpads as spring-damper pairs, while neglecting the other components, such as clamps, bolts, etc. This is a widely accepted simplification in railway track models. Although bolt tightness cannot be explicitly considered in the current model, it can be reflected in the railpad stiffness. For instance, a loose bolt will lead to a decrease in clamp force, which further results in a decrease in railpad stiffness [52]. Ballast is modelled as discretely distributed

KV models under each sleeper node. The ballast stiffness is thus defined as the spring stiffness of a single KV model multiplied by the number of sleeper nodes.

The field hammer test is usually performed on top of the rail with a hammer excitation either above sleeper support or at the mid-span; see Figure 4.2 (c). The impact test is simulated by applying an impulse force vertically on the rail node either above the sleeper support (at coordinate $x = 6$ m) or at the mid-span ($x = 6.3$ m). The model is solved in the time domain using the Newmark integration with a fixed time step length of 4×10^{-4} s. The model and solution process are implemented in Matlab.
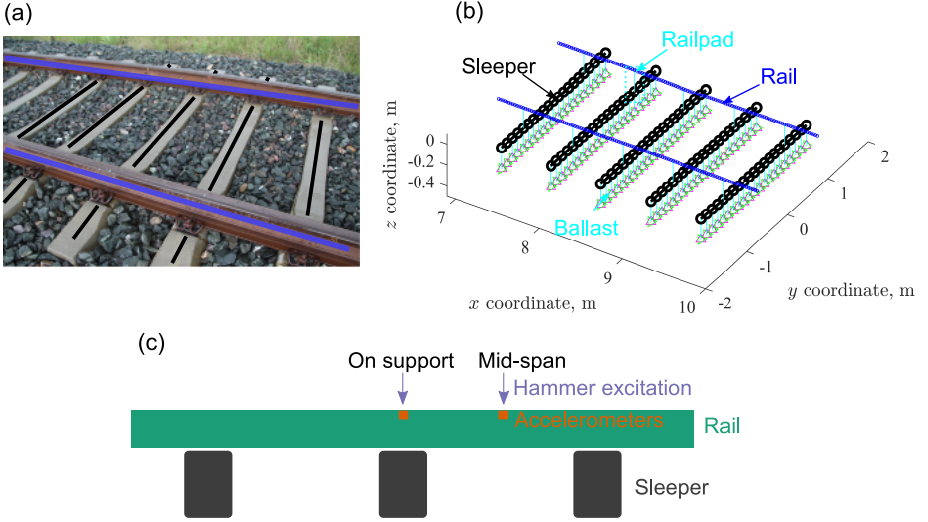
Figure 4.2: Schematics for (a) ballasted railway track, (b) finite element model and (c) hammer test.

4.2.3. GAUSSIAN PROCESS REGRESSION

We assume each track parameter x_j is a collection of random variables $\left\{ x_j^{(i)} \in X_j, i = 1, 2, \ldots \right\}$, dependent on the FRF features, i.e., $x_j = g(\mathbf{y})$. A Gaussian process (GP) is a way to describe a Gaussian distribution over functions. Detailed descriptions of this method can be found in [151]. Here a brief introduction is provided.

We assume the function $x_j = g(\mathbf{y})$ follows a GP, i.e.,

$$x_j = g(\mathbf{y}) \sim GP\left(m(\mathbf{y}), k\left(\mathbf{y}, \mathbf{y}'\right)\right) \tag{4.3}$$

where $m(\mathbf{y})$ is the mean function and $k\left(\mathbf{y}, \mathbf{y}'\right)$ is the covariance (or kernel) function of $\left\{ x_j^{(i)} \in X_j, i = 1, 2, \ldots \right\}$. The GP can be completely defined by these two functions. The goal is to determine the two functions $m(\mathbf{y})$ and $k\left(\mathbf{y}, \mathbf{y}'\right)$ from a training set $\mathcal{D}_j = \left\{ \left(\mathbf{y}^{(i)}, x_j^{(i)} \right) \mid i = 1, \ldots, d \right\}$, for $j = 5, 7$.

In the current case, we assume the track parameter x_j has a zero-mean distribution by normalizing $\left\{x_j^{(i)}, i = 1, \ldots, d\right\}$ between $[-1, 1]$; see also section 4.4.1.2. Thus,

$$m(\mathbf{y}) = \mathbf{0} \tag{4.4}$$

The covariance function measures the correlation between two particular values, $x^{(p)}$ and $x^{(q)}$. A commonly used covariance function is the squared exponential covariance function

$$\text{cov}\left(x^{(p)}, x^{(q)}\right) = k\left(\mathbf{y}^{(p)}, \mathbf{y}^{(q)}\right) = \sigma_f^2 \exp\left[-\frac{1}{2} \sum_{k=1}^{n} \left(\frac{y_k^{(p)} - y_k^{(q)}}{l_k}\right)^2\right] + \sigma_n^2 \delta_{pq} \tag{4.5}$$

where l_k is the length scale, σ_f^2 is the signal variance, σ_n^2 is the noise variance and δ_{pq} is a Kronecker delta which is one if $p = q$ and zero otherwise. The parameters $\Theta = \left\{l_k, \sigma_f^2, \sigma_n^2\right\}$ are called hyperparameters and are determined during the training process. Note if the length scale is the same for all predictors, such a covariance function is isotropic. If the length scale is different for different predictors, such a covariance function implements automatic relevance determination (ARD) and is referred to as an ARD kernel.

We denote the training set as $\mathscr{D} = (\mathbf{Y}, \mathbf{x})$, where $\mathbf{x} = [x_1, x_2, \ldots x_d]^\top$ and $\mathbf{Y} = [\mathbf{y}_1, \mathbf{y}_2, \ldots \mathbf{y}_d]^\top$. With the definition in Eq. 4.4 and 4.5, the track parameter follows a joint Gaussian distribution, i.e.,

$$\mathbf{X} \sim N\left(\mathbf{0}, K(\mathbf{Y}, \mathbf{Y}) + \sigma_n^2 \mathbf{I}\right) \tag{4.6}$$

where $K(\mathbf{Y}, \mathbf{Y})$ is a d by d covariance matrix with each entry defined in Eq. 4.5. The hyperparameters are determined by maximizing the marginal likelihood of $\mathbf{x}$ conditioned on $\mathbf{Y}$ and Θ, i.e.,

$$\log p(\mathbf{x} \mid \mathbf{Y}, \Theta) = -\frac{1}{2}\mathbf{x}^T \left(\mathbf{K} + \sigma_n^2 \mathbf{I}\right)^{-1} \mathbf{x} - \frac{1}{2}\log\left|\mathbf{K} + \sigma_n^2 \mathbf{I}\right| - \frac{n}{2}\log 2\pi \tag{4.7}$$

Now that we have the joint distribution of $\mathbf{X}$ (assuming we trained the GPR on dataset $\mathscr{D}$ to obtain the hyperparameters), we can make a prediction of x^* given any new observation $\mathbf{y}^*$. The training outputs $\mathbf{X}$ and the prediction x^* together should also follow a joint Gaussian distribution, i.e.,

$$\begin{bmatrix} \mathbf{X} \\ x^* \end{bmatrix} \sim N\left(\mathbf{0}, \begin{bmatrix} K(\mathbf{Y}, \mathbf{Y}) + \sigma_n^2 \mathbf{I} & K\left(\mathbf{Y}, \mathbf{y}^*\right) \\ K\left(\mathbf{y}^*, \mathbf{Y}\right) & K\left(\mathbf{y}^*, \mathbf{y}^*\right) \end{bmatrix}\right) \tag{4.8}$$

where $K\left(\mathbf{Y}, \mathbf{y}^*\right)$ denotes the covariance between all the $\mathbf{y}$ in $\mathbf{Y}$ and $\mathbf{y}^*$, and similarly for the other entries. They can be calculated according to Eq. 4.5. The prediction can be made now based on the Bayesian inference and the distribution of x^* can be solved as

$$\begin{aligned} x^* &\sim N\left(\mu^*, \Sigma^*\right) \\ \mu^* &= \mathbf{K}^{*T} \left(\mathbf{K} + \sigma_n^2 \mathbf{I}\right)^{-1} \mathbf{X} \\ \Sigma^* &= \mathbf{K}^{**} - \mathbf{K}^{*T} \left(\mathbf{K} + \sigma_n^2 \mathbf{I}\right)^{-1} \mathbf{K}^* \end{aligned} \tag{4.9}$$

where $\mathbf{K}^* = K\left(\mathbf{Y}, \mathbf{y}^*\right), \mathbf{K}^{**} = K\left(\mathbf{y}^*, \mathbf{y}^*\right)$ and $\mathbf{K} = K(\mathbf{Y}, \mathbf{Y})$.

4.3. FRF FEATURES OF BALLASTED RAILWAY TRACK

4.3.1. TWO INDIVIDUAL CASES

We simulate two individual cases [27, 153] of field hammer tests. The parameters are listed in Table 4.1. The major difference is that the railpad stiffness is 1300 MN/m and 90 MN/m for Cases 1 and 2, respectively. The purpose of simulating the two cases are two folds: (1) to use them as reference models to validate the proposed track model and (2) to identify the features of track FRFs with different track parameters.

Table 4.1: Model parameters for the reference cases.

Component	Parameter	Case 1 [153]	Case 2 [27]
Rail	Mass per meter	54.77 kg/m	56 kg/m
	Young's modulus	210 GPa	210 GPa
	Poisson's ratio	0.3	0.3
	Moment of inertia	2.337×10^{-5} m^4	2.231×10^{-5} m^4
	Density	7800 kg	7800 kg
	Area of cross section	6.977×10^{-3} m^2	7.169×10^{-3} m^2
	Timoshenko shear coefficient	0.4	0.4
Rail pad	Stiffness	1300 MN/m	90 MN/m
	Damping	67.5 kNs/m	16 kNs/m
Sleeper	Young's modulus	74.6 GPa	59 GPa
	Poisson's ratio	0.17	0.2
	Moment of inertia (averaged)	1.375×10^{-4} m^4	1.27×10^{-4} m^4
	Density	2500 kg/m^3	2648 kg/m^3
	Area of cross section (averaged)	0.043	0.045
	Timoshenko shear coefficient	0.833	0.83
	Length	2.58 m	2.5 m
	Spacing	0.6 m	0.65 m
Ballast	Stiffness	90 MN/m	170 MN/m
	Damping	64 kNs/m	55 kNs/m

The FRF magnitudes calculated for Case 1 (stiff railpad) and Case 2 (soft railpad) are shown in Figure 4.3 on the left and right columns, respectively. For each case, we evaluate the point FRFs of the rail above a sleeper (first row of Figure 4.3) and at mid-span (second row of Figure 4.3). The results from the current model are compared with field hammer tests, as well as a 3D [153] and 2.5D FE model [27] for cases 1 and 2, respectively. In general, the current model yields good agreement with the measurements as well as the reference models.

The peaks in the FRF curves indicate track resonances (TR). To identify the TRs associated with each peak, we perform an eigenanalysis of the FE track model. Based on the eigenfrequencies and corresponding eigenmodes of the rail, we construct the dispersion relations of the vertical rail bending waves; see Figure 4.3 (e)~(f). Note here only the bending waves are shown; a more detailed measurement and definition of other rail waves can be found in [154]. We can pinpoint the eigenfrequencies of the TRs at the cut-

on frequencies of the rail waves (Wave 1~9). Some of the track resonances correspond to the peaks in FRF curves (see the red triangles in Figure 4.3) while the others do not (the black triangles). This is the consequence of incomplete measurements. Because only the FRFs at two locations on the rail top are measured, TRs associated with sleepers or with the measurement point as nodes cannot be reflected in the FRFs.
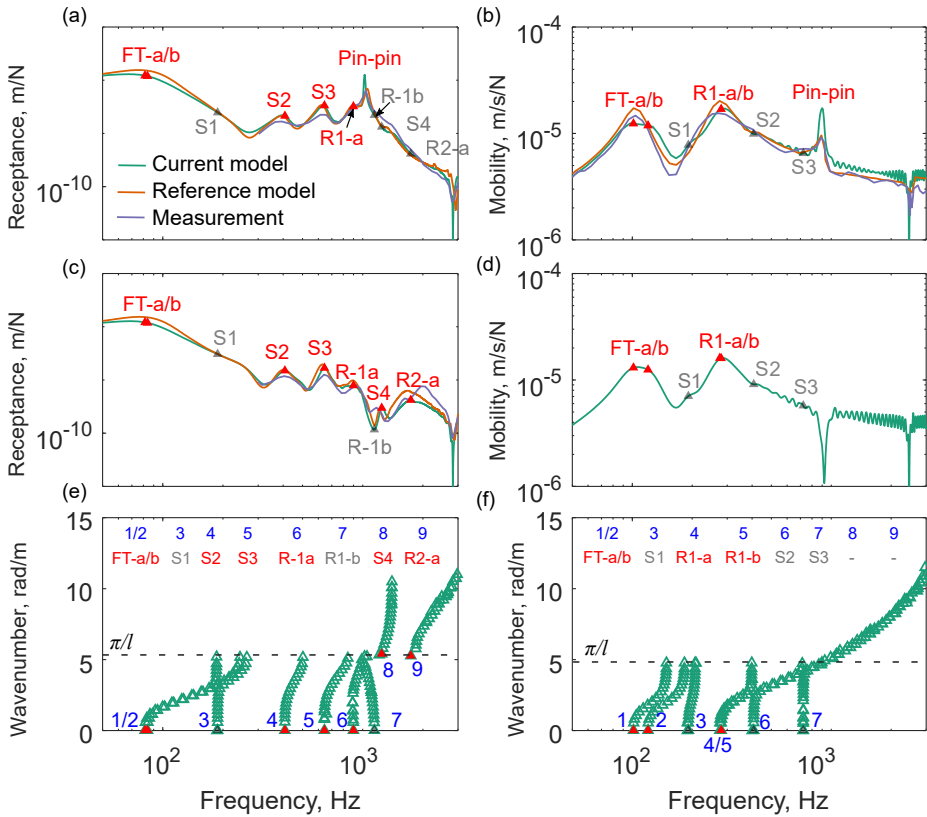

Figure 4.3: Vertical track FRFs and dispersion relations for Case 1 (Left column) and Case 2 (Right column). First row: the point FRF of the rail above the sleeper. Second row: the point FRF of the rail at mid-span. Third row: the dispersion relations of rail vertical bending waves. Track resonances (TRs) are identified at the cut-on frequencies of the waves (Number 1~9). Each triangle represents an eigenmode of the FE track model. Red and black triangles indicate the TRs that can and cannot be identified as the peaks in the track FRFs, respectively.

Figure 4.4 shows the mode shapes of the identified track resonances (TR 1 ~ 9). The main features of these TRs are summarized in Table 4.2 and are briefly described below:

- **Full-track resonances** (FT-a/b): the rail and sleeper vibrate in-phase at rail seats, with translational (symmetrical) and rotational (anti-symmetrical) rigid sleeper modes, respectively.

- **Sleeper resonances** (S1 ~ S4): the sleeper vibrates in-phase with rail at rail seats, in the first four flexible sleeper bending modes.

Table 4.2: Characteristics of vertical track resonances.

Code	Rail wavelength	Sleeper mode	Symmetry	Sleeper-rail relation
FT-a	Infinity	Translation	Symmetric	In-phase
FT-b	Infinity	Rotation	Anti-symmetric	In-phase
S1	Infinity	1st bending	Symmetric	In-phase
S2	Infinity	2nd bending	Anti-symmetric	In-phase
S3	Infinity	3rd bending	Symmetric	In-phase
R1-a	Infinity	N/A	Anti-symmetric	Out-of-phase
R1-b	Infinity	N/A	Symmetric	Out-of-phase
Pin-pin	$2L^*$	N/A	N/A	N/A
S4	$2L$ (phase shift**)	4th bending	Anti-symmetric	In-phase
R2-a	$2L$ (phase shift**)	N/A	Symmetric	Out-of-phase

* L is the length of a sleeper span.
** The rail vibrations of S4 and R2-a show a phase shift of $\pi/2$ compared to the pin-pin mode.

- **Rail resonances** (R1-a/b, R2-a/b): the rail vibrates in anti-phase with the sleeper at rail seats, with the wavenumber of 0 (i.e. infinite wavelength) and π/L (i.e. wavelength of $2L$) for R1 and R2, respectively, where L is the sleeper spacing. The mode shape of the rail at R2 shows patterns with nodes (at which the displacements are zero) located at the mid-span.

- **Pin-pin resonance**: the rail vibrates with the wavenumber of π/L (i.e. wavelength of $2L$) and nodes above the sleeper, i.e. with the same wavelength but a phase shift of $\pi/2$ compared to R2.

The idea is to use (some of) the TRs as the features of the FRFs to infer track stiffness. Qualitatively, from the mode shapes of different TRs, the railpad stiffness is mainly associated with the rail resonances (R1 and R2) because of the anti-phase vibration between rails and sleepers at rail seats, whereas the ballast stiffness is more related to the full-track resonances (FT-a/b). In fact, the manual fitting of a modelled FRF to measurement is usually performed based on these two resonances [46–51]. In addition, the sleeper resonances should also provide valuable information for the identification of both railpad and ballast stiffness. However, the sleeper resonances are not always identifiable in the rail FRFs. For example, in Case 2 the sleeper resonances (S2 and S3) are well isolated by the soft pads and therefore are not reflected in the rail FRFs. Moreover, due to the change in railpad stiffness, the sleeper resonances and the rail resonances switch in sequence in TR 4 ~ 7. These issues add to the difficulties of including the sleeper resonances in the FRF features.

Compared with the FRFs, the features of dispersion relations are more consistent, because TR 1 ~ 7 are always 'identifiable' in the dispersion relations. We will take this advantage to generate the training datasets for the GPR model (see section 4.4.1.2).
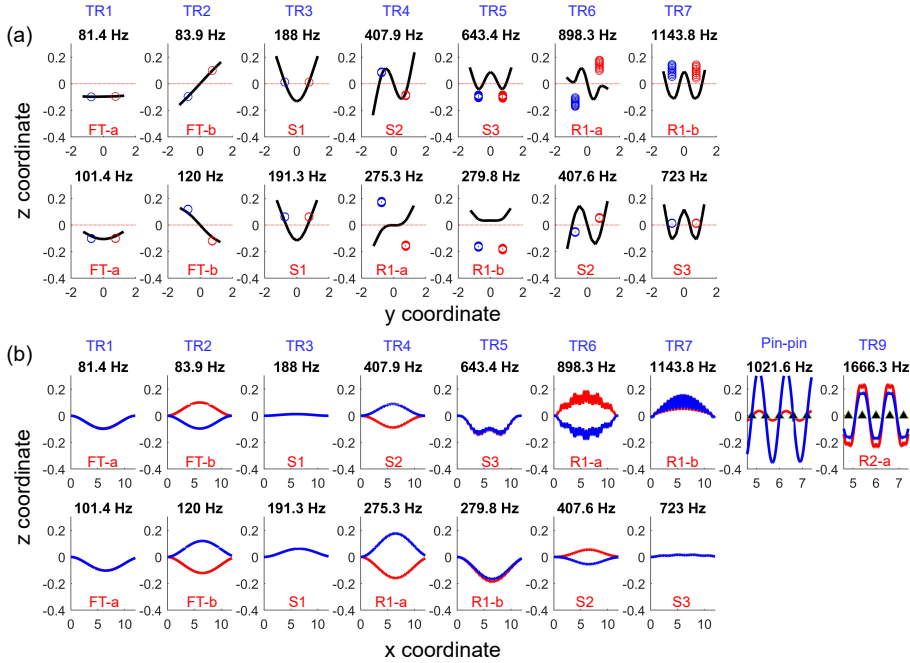
Figure 4.4: Mode shapes of track resonances. (a) Sleeper in $y - z$ (lateral-vertical) plane. (b) Rail in $x - z$ (longitudinal-vertical) plane. For the pin-pin resonance and TR9, sleeper positions are indicated by black triangles. In both (a) and (b), the upper and lower row shows the mode shapes from Case 1 and Case 2, respectively.

4.3.2. GLOBAL SENSITIVITY ANALYSIS

To facilitate the selection of FRF features, we perform a global sensitivity analysis [155] over a predefined parameter space to evaluate the sensitivities of several FRF features to railpad and ballast stiffness.

4.3.2.1. METHOD

Parameter space   To perform the global sensitivity analysis, the parameter space X has to be first defined. This means to determine the upper bound x_i^u and lower bound x_i^l of the track parameters $x_i (i = 1, 2, \ldots, 8)$. Rail parameters are relatively easy to determine from the nominal design values. Here we use the properties of UIC54 type rail as the nominal values, which are increased and decreased by 5% to obtain the upper and lower bound, respectively. The value ranges of sleeper, ballast and railpad are determined based on the values reported in a wide range of literature [7, 27, 49, 51, 104, 140, 153, 156–160]. The defined parameter space is listed in Table 4.3.

Global sensitivity analysis   We assume each track parameter is uniformly distributed in the parameter space defined in Table 4.3, i.e., $x_i \sim U\left(x_i^u, x_i^l\right), i = 1, 2, \ldots, 8$. Subsequently, we use the Sobol sequence sampling method to generate N samples of track parameters $\mathbf{x}^{(k)} \in X^8 (k = 1, 2, \ldots, N)$ from the distribution. With the sampled track param-

Table 4.3: Parameter space for eight track parameters.

Parameter	Rail		Sleeper		Railpad		Ballast	
	EI $(N \cdot m^2)$	ρA (kg/m)	EI $(N \cdot m^2)$	ρA (kg/m)	Stiffness (N/m)	Damping $(N \cdot s/m)$	Stiffness (N/m)	Damping $(N \cdot s/m)$
Lower	4.75e6	51.3	5.53e6	105	1e8	1e4	6e7	4e4
Upper	5.25e6	56.7	1.12e7	158	1.5e9	7e4	2.8e8	2.8e5

eters, we perform both the time-domain analysis and eigenanalysis using the FE track model. Furthermore, to rank the sensitivity of different track parameters, a variance-based global sensitivity index is calculated following a numerical procedure based on Monte Carlo Simulations. The details of the procedure can be found in [155].

4.3.2.2. MAGNITUDE FEATURES OF FRF
In this chapter, to ensure a simple test setup, we propose to use the point FRF above the sleeper support for the identification of track stiffness. Figure 4.5 shows the simulated point FRFs above the sleeper support with sampled track parameters as inputs. Herein, we use MAG1, MAG2 and MAG3 as the magnitude features of the FRFs. They denote the sum of the magnitudes of the point receptance in three different frequency bands, i.e., between 10 ~ 100 Hz, 150 ~ 900 Hz and 1050 ~ 2500 Hz, respectively.
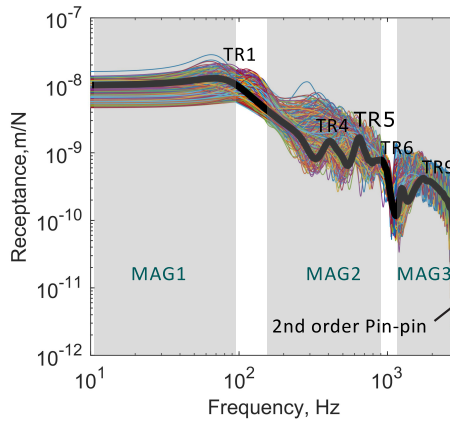

Figure 4.5: Magnitude features (MAG1 ~ MAG3) of the point receptance above the sleeper calculated by 5000 sets of parameters (colored lines). The bold black line indicates the result of Case 1.

The scatter plots in Figure 4.6 show the correlations between the FRF magnitude and different track parameters. In the plots, a uniform cloud of points means the magnitude is not sensitive to the change of the parameter (see the grey cloud points in Figure 4.6). On the other hand, if a 'pattern' can be observed, e.g., the blue and red points, the corresponding parameter is considered to be influential. It can be seen the FRF magnitudes below 100 Hz (MAG1) are most sensitive to the ballast stiffness, while in the mid-frequency range of 150 ~ 900 Hz (MAG2), the magnitudes are most sensitive to the

railpad stiffness. The sensitivity indexes of different track parameters are presented in Figure 4.6 (c). For MAG3, railpad damping (x_6) and stiffness (x_5) are the two most sensitive parameters. Furthermore, an exponential correlation can be observed between the ballast/ railpad stiffness and MAG1/MAG2. This means MAG1 or MAG2 becomes less sensitive to ballast or railpad as they become stiffer. Therefore, if we use only MAG1 and MAG2 to predict the ballast and railpad stiffness, the predictions would be less accurate for larger stiffness values.

4.3.2.3. Frequency features of FRF

The frequencies of TR1, TR4, TR5, TR6 and the pin-pin resonance are selected as the frequency features for the sensitivity analysis. The influences of different track parameters on these features are shown in Figure 4.7. The sensitivity index in Figure 4.7 (b) indicates that the pin-pin resonance at around 1000 Hz is most sensitive to the rail properties (x_1, x_2) and therefore should be excluded from the FRF features for the identification of railpad and ballast stiffness. In contrast, TR1, TR4 and TR5 should be considered for the identification of ballast stiffness (x_7), while TR4, TR5 and TR6 should be considered for the identification of railpad stiffness (x_5). This confirms that the sleeper resonances are also correlated with railpad and ballast stiffness.

Besides, the resonant frequencies of TR4 ~ TR6 increase nonlinearly with increasing railpad stiffness; see x_5 in Figure 4.7 (a). Such nonlinearity has two consequences. First, TR4 and 5 converge to a single resonance at low railpad stiffness; see Figure 4.3 (b) as an example. Second, as railpad stiffness increases, it becomes less influential on the resonant frequencies of TR4 and TR5.

4.4. Gaussian process regression model

4.4.1. Dataset preparation

4.4.1.1. FRF features as input predictors

We choose 11 features from the FRF curve as the potential predictors for the GPR model, see features 1 ~ 11 in Table 4.4. The 11 FRF features are chosen based on the processes of feature identification (section 4.3.1) and feature selection (section 4.3.2).

First, in section 4.3.1, we investigated the track resonance behaviour and extracted corresponding FRF peaks as the potential features. More specifically, the natural frequencies and FRF magnitudes at TR 1/2, TR4, TR5, TR6 and the pin-pin resonance are chosen as the potential features. In addition, we choose MAG1, MAG2 and MAG3 as shown in Figure 4.5 to reflect the general trend of the FRF curve.

Subsequently, in section 4.3.2, we performed a global sensitivity analysis to further select the most sensitive features to the change of railpad and ballast stiffness, respectively. As a result, we select 11 features in total. Besides, as the sleeper properties (EI and ρA) may be known a prior and are correlated with certain FRF features (see e.g. TR4 ~ 6 in Figure 4.6), they are also selected as the potential predictors (features 12 and 13 in Table 4.4).

4.4.1.2. Datasets generation

We generate the datasets used for training and testing following the procedure below:
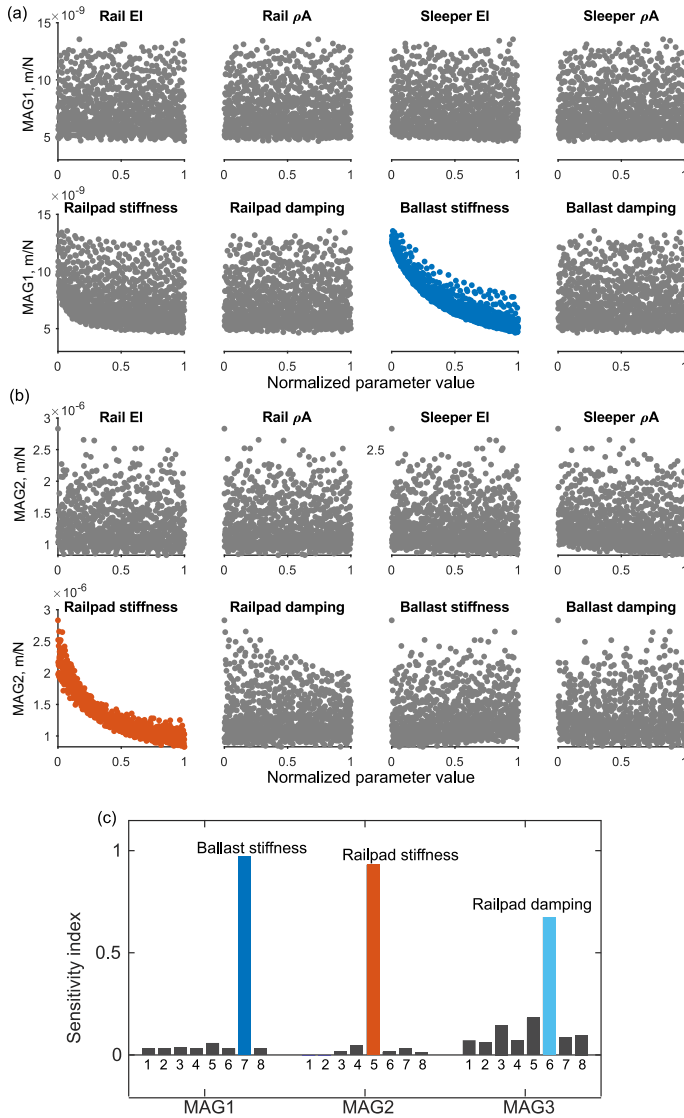
Figure 4.6: Sensitivity of the magnitude features of FRF to track parameters. (a) MAG1; (b) MAG2; (c) sensitivity index.

1. Follow the same procedure as in Section 4.3.2.1 to sample N sets of track parameters $\mathbf{x}^{(k)} \in X^8$ $(k = 1, 2, \dots, N)$.

2. With each sample $\mathbf{x}^{(k)}$, perform an eigenanalysis and construct the dispersion relations as shown in Figure 4.3 (e) and (f). The cut-on frequencies of Wave 1, 4, 5, and 6 are stored in the feature vector $y_j^{(k)}$ ($j = 8, 9, 10, 11$). This ensures that we can

(a)

(b)
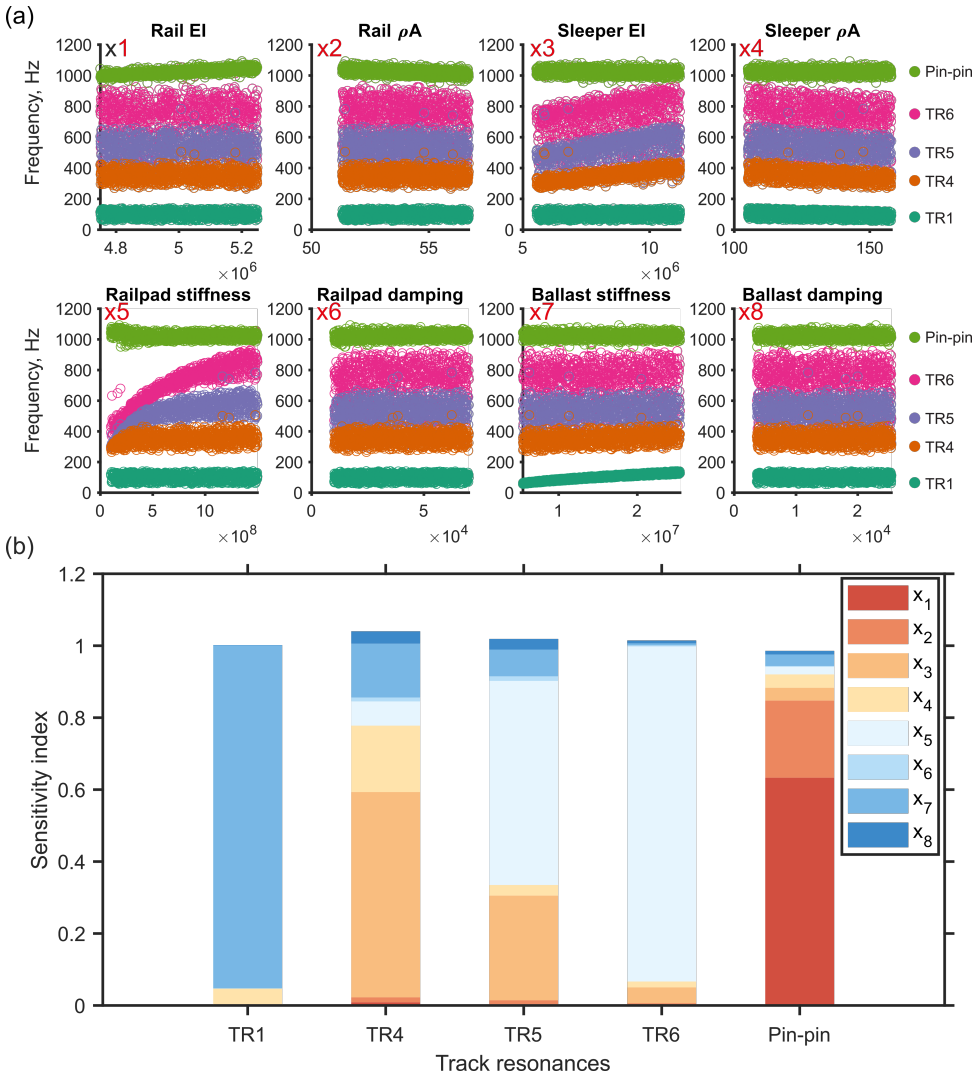
Figure 4.7: Sensitivity of the frequency features of FRF to track parameters. (a) TR1 ~ 4 and the pin-pin resonance; (b) sensitivity index.

always extract the frequencies of TR5 and TR6 even if they are not identifiable in FRF curves (e.g., as in Figure 4.3 (b)).

3. With each input sample $\mathbf{x}^{(k)}$, calculate the point receptance of the rail node above the sleeper located at the middle of the track length.

(a) Interpolate the magnitude of the receptance at the cut-on frequencies $y_j^{(k)}$ ($j = 8, 9, 10, 11$) and store the values in $y_j^{(k)}$ ($j = 1, 2, 3, 4$).

Table 4.4: Selected features of the FRF

Features	Description
1	Log magnitude of FRF at TR1
2	Log magnitude of FRF at TR4
3	Log magnitude of FRF at TR5
4	Log magnitude of FRF at TR6
5	Log of MAG1
6	Log of MAG2
7	Log of MAG3
8	Frequency of TR1
9	Frequency of TR4
10	Frequency of TR5
11	Frequency of TR6
12	Sleeper inertia (ρA)
13	Sleeper bending stiffness (EI)

     (b) Calculate MAG1, 2 and 3 and store the values in $y_j^{(k)}$ ($j = 5, 6, 7$).

4. Copy the sleeper properties $x_i^{(k)}$ ($i = 3, 4$) to $y_j^{(k)}$ ($j = 12, 13$).

5. Repeat steps 2 ~ 4 for $k = 1, 2, \ldots, N$.

In such a way, we generate two datasets $\mathscr{D}_i = \left\{ \left(\mathbf{y}^{(k)}, x_i^{(k)} \right) \mid k = 1, \ldots, N, \mathbf{y}^{(k)} \in Y^{13} \right\}$, $i = 5, 7$, for the identification of railpad and ballast stiffness, respectively. Then we organize each dataset in an N by 14 matrix, with the first 13 columns as the features and the last column as the target. Since the range of different features varies widely, we normalize each feature in the range of $[-1, 1]$. In this chapter, we generate $N = 9000$ samples for each dataset and split them into a training set with 5000 samples and a test set with 4000 samples. During training, we hold out 1000 samples for validation. The influence of the number of training samples is investigated in Section 4.4.4.2.

4.4.1.3. NOISE INJECTION

Because the dataset is generated based on numerical simulations, the uncertainties introduced by measurement noise and modelling errors should be properly considered to ensure robust performance when applied to real measurement data. In the current case, the uncertainties are mainly associated with the FRF features. Hence, we add Gaussian noise to each feature,

$$\tilde{\mathbf{y}}^{(k)} = \mathbf{y}^{(k)}(1 + \eta) \tag{4.10}$$

where $\eta \sim N\left(0, \sigma_y^2\right)$. The standard deviation of the noise σ_y is set to 5%. Consequently, we generate two noisy dataset $\widetilde{\mathscr{D}}_i = \left\{ \left(\tilde{\mathbf{y}}^{(k)}, x_i^{(k)} \right) \mid k = 1, \ldots, N, \mathbf{y}^{(k)} \in Y^{13} \right\}$ ($i = 5, 7$) in addition to the noise-free dataset $\mathscr{D}_i$.

It should be noted that adding noise to the inputs of a GPR model is equivalent to treating the inputs as deterministic while adding an extra term to the output noise $\sigma_n^2 \mathbf{I}$

in the covariance matrix in Eq. 4.5 [161]. Ideally, a heteroscedastic GPR model [162] should be used to model this extra term with more accuracy. In this chapter, however, we still resort to the standard GPR model and include this term in the output noise $\sigma_n^2 \mathbf{I}$ for simplicity. Hereafter, we refer to the GPR models trained by the noise-free datasets as the noise-free model, and those trained by the noisy datasets as the noisy model, although they all include a noise term in the outputs.

4.4.2. TRAINING MULTIPLE GPR MODELS

4.4.2.1. INCOMPLETE MEASUREMENT OF FRF FEATURES

In real-life applications, extracting all 11 features from a measured FRF is not always possible, which will lead to incomplete measurements of FRF features. There are two main sources of incomplete measurements. The first source is associated with railpad stiffness as discussed in section 4.3. For example, in the reference Case 2, only 7 features can be extracted due to the soft railpad, i.e., features 1,2,5,6,7,8 and 9; see Figure 4.8 (b). The second source is related to the valid frequency ranges of different types of hammers used for excitation. In principle, an impact hammer with light weight can only effectively excite the structure vibrations in mid- to high-frequency ranges (approximately zone II(*) and III in Figure 4.8), whereas a heavier hammer is more accurate in low to mid-frequencies (approximately zone I and (II(*)) in Figure 4.8) [53].
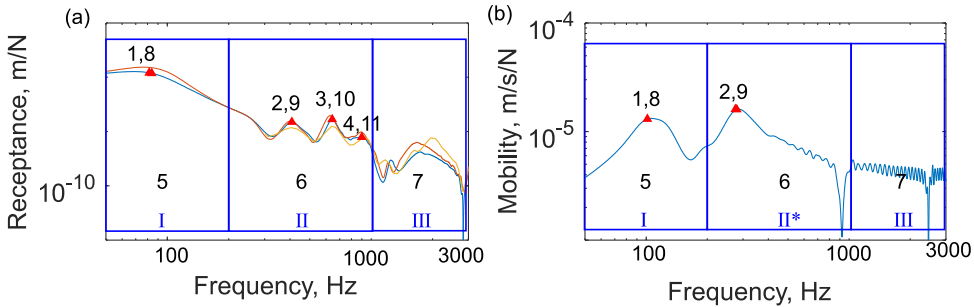

Figure 4.8: Examples of identifiable features from FRF magnitudes. (a) Case 1; (b) Case 2. Feature numbers defined in Table 4.4 are indicated in the figures.

Because of the two sources of incomplete measurements, we expect different combinations of FRF features in different scenarios, as summarized in Table 4.5. In particular, we use five feature classes, i.e. A, B, C, D and E, to describe the variability of the valid frequency ranges. Within each feature class, we further include four feature combinations to consider the variability due to different railpad stiffness. We select 12 and 10 feature combinations for the identification of railpad and ballast stiffness, respectively, based on the results of the sensitivity analysis in section 4.3.2.

4.4.2.2. KERNEL FUNCTIONS

Four different types of covariance functions are considered in this study, i.e. the exponential (EXP), the squared exponential (SE), the rational quadratic (RQ) and the Matern 32 (M32) covariance functions. For each type, we implement both the isotropic kernels

Table 4.5: Different feature combinations due to incomplete measurements

Feature combination	Zones	Feature index	Number of features	Railpad	Ballast
A1	I + II + III	{1,2,3,4,5,6,7,8,9,10,11,12,13}	13	✓	✓
A2	I + II + III	{1,2,3,4,5,6,7,8,9,10,11}	11	✓	✓
A3	I + II* + III	{1,2,5,6,7,8,9,12,13}	9	✓	✓
A4	I + II* + III	{1,2,5,6,7,8,9}	7	✓	✓
B1	II + III	{2,3,4,6,7,9,10,11,12,13}	10	✓	
B2	II + III	{2,3,4,6,7,9,10,11}	8	✓	
B3	II* + III	{2,6,7,9,12,13}	6	✓	
B4	II* + III	{2,6,7,9}	4	✓	
C1	I + II	{1,2,3,4,5,6,8,9,10,11,12,13}	12		✓
C2	I + II	{1,2,3,4,5,6,8,9,10,11}	10		✓
C3	I + II*	{1,2,5,6,8,9,12,13}	8		✓
C4	I + II*	{1,2,5,6,8,9}	6		✓
D1	I	{1,5,8,12,13}	5		✓
D2	I	{1,5,8}	3		✓
E1	II	{2,3,4,6,9,10,11,12,13}	9	✓	
E2	II	{2,3,4,6,9,10,11}	7	✓	
E3	II*	{2,6,9,12,13}	5	✓	
E4	II*	{2,6,9}	3	✓	

with the same length scale for all predictors, as well as the ARD kernels with separate length scales per predictor (see Section 4.2.3). The details of these kernels can be found in the literature, e.g. [151], and thus are not repeated here.

4.4.3. PREDICTION FUSION

With each training set $\mathcal{D}_i$ or $\widetilde{\mathcal{D}}_i$ generated in section 4.4.1, we can select a feature combination and a kernel from section 4.4.2 to train a candidate model. The prediction process starts with a feature vector $\mathbf{y}^*$ extracted from an FRF curve. If the feature index of a feature combination in Table 4.5 is a subset of the feature index of $\mathbf{y}^*$, candidate models trained by this feature combination can be used to make predictions of x^*. In general, a feature vector will activate more than one candidate model and therefore register multiple predictions. We use a generalized Product of Experts (PoE) method [163] to fuse the predictions by different candidate models. Each candidate model is regarded as an expert. The fused probability distribution is the product of the posterior distribution of each expert, weighted by a factor, taking the form

$$P\left(x^* \mid \mathbf{y}^*\right) = \frac{1}{Z} \prod_i p_i^{\alpha_i(y^*)}\left(x^* \mid \mathbf{y}^*\right) \tag{4.11}$$

where $p_i\left(x^* \mid \mathbf{y}^*\right)$ is the posterior predicted by the i-th expert, $\alpha_i\left(\mathbf{y}^*\right)$ is a weighing factor depending on the reliability of the i-th expert, and Z is to normalize the fused prediction $P\left(x^* \mid \mathbf{y}^*\right)$ so that it sums to one.

The purpose of $\alpha_i\left(\mathbf{y}^*\right)$ is to give more weight to the experts with more reliability while less weight to less reliable experts. Therefore, $\alpha_i\left(\mathbf{y}^*\right)$ is defined as the change in entropy from prior to posterior. Entropy is a measure of the amount of uncertainty in a distribution

$$H(N(\mu, \Sigma)) = \frac{1}{2} \log|\Sigma| + \frac{1}{2} \log 2\pi e \tag{4.12}$$

Thus, the entropy change from prior to posterior is

$$\alpha_i\left(\mathbf{y}^*\right) = \Delta H = \frac{1}{2}\log\left|K\left(\mathbf{y}^*,\mathbf{y}^*\right)\right| - \frac{1}{2}\log\left|\Sigma_i^*\right| \tag{4.13}$$

where $K\left(\mathbf{y}^*,\mathbf{y}^*\right)$ and Σ_i^* are the variances of the prior and posterior distribution, respectively; see Eq. 4.9. Note that the prediction fusion takes almost no extra computation time, because $K\left(\mathbf{y}^*,\mathbf{y}^*\right)$ and Σ_i^* in Eq. 4.13 are readily available once the predictions are made.

In the current case, if a candidate model is not activated, the posterior is the same as the prior, i.e. $\alpha_i = 0$. This means an inactive model would not contribute to the fused prediction. Also, a larger entropy change $\alpha_i\left(\mathbf{y}^*\right)$ means the model is more certain about the prediction, and thus gives a larger weight in the fused prediction according to Eq. (4.11). The fused prediction is also a Gaussian with mean and variance

$$\begin{aligned} \mu_{\text{fused}} &= \left(\sum_i \mu_i^* \alpha_i\left(\mathbf{y}^*\right) T_i^*\right)\left(\sum_i \alpha_i\left(\mathbf{y}^*\right) T_i^*\right)^{-1} \\ \Sigma_{\text{fused}} &= \left(\sum_i \alpha_i\left(\mathbf{y}^*\right) T_i^*\right)^{-1} \end{aligned} \tag{4.14}$$

where $T_i^* = \left(\Sigma_i^*\right)^{-1}, \mu_i^*$ and Σ_i^* are the mean and variance of the posterior by the i-th expert and can be obtained according to Eq. 4.9.

Figure 4.9 shows the process of prediction fusion for railpad stiffness as an example. For each training set, we consider twelve feature combinations (see Table 4.5) and eight kernels. Thus, we have in total 96 candidate models arranged in a 12 by 8 matrix. According to Eq. 4.11, raising a posterior to the power of a weight gives a weighted prediction for each candidate model. The fused prediction is the product of selected weighted predictions. In theory, we can fuse any combination of elements in the matrix. In practice, we usually fuse the predictions by different kernels for each feature combination or fuse the predictions by different feature combinations for each kernel, as indicated by the red and blue blocks in Figure 4.9.

4.4.4. PERFORMANCE ANALYSIS
We evaluate the performance of the proposed method using the two test sets from $\mathcal{D}_i$ (noise-free) and $\widetilde{\mathcal{D}}_i$ (with 5% injected noise) defined in section 4.4.1.2. The mean absolute percentage error (MAPE) is used as the metric for the evaluations,

$$MAPE = \frac{1}{N}\sum_{k=1}^{N}\left|\frac{\hat{x}^{*(k)} - x^{*(k)}}{x^{*(k)}}\right| \tag{4.15}$$

where $\hat{x}^{*(k)}$ and $x^{*(k)}$ are the predicted and target values of the k-th sample.

4.4.4.1. BASELINE METHOD
We use a model updating method implementing the particle swarm optimization (PSO) [164] as the baseline model. Because the PSO is computationally intensive, to ensure fast
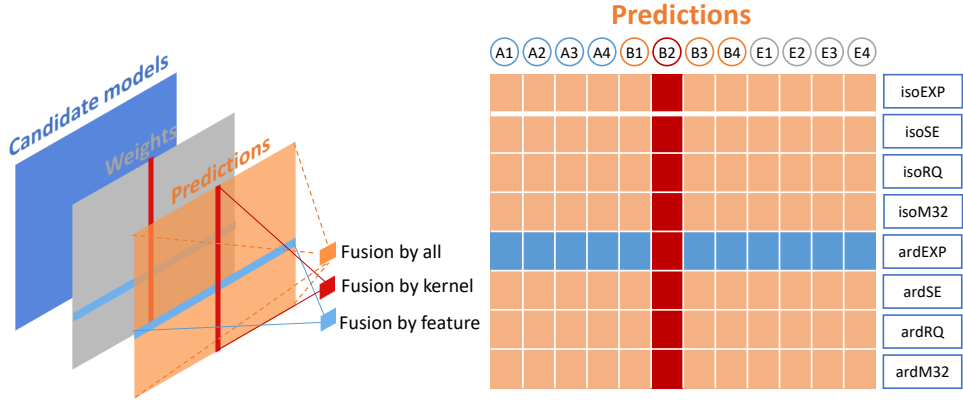
Figure 4.9: A schematic of the prediction fusion process for the prediction of railpad stiffness. Each plane represents a two-dimensional matrix storing the results for candidate models, with columns representing feature combinations and rows representing kernels. The red and blue blocks show two examples of the fusion strategies, i.e. fusion by kernel and fusion by feature, respectively.

evaluations, we employ meta-models of the FE track model in the optimization process. The approach is similar to that in [165, 166], but with a different optimization algorithm. The meta-models are also GPR models trained and tested on datasets generated in a similar way as in section 4.4.1.2, only with the track parameters **x** as inputs and different FRF features y_j as outputs. The objective function is defined as

$$\Pi = \sum_j \left(\frac{\hat{y}_{j,\mathbf{x}} - y_j}{y_j} \right)^2 \tag{4.16}$$

where $\hat{y}_{j,\mathbf{x}}$ and y_j are the simulated value given **x** and the target value for the j-th FRF feature, respectively.

4.4.4.2. PREDICTION ACCURACY

We first compare the performance of different kernels on the two test sets; see Figure 4.10. For the railpad stiffness, the ARD kernels outperform the isotropic kernels. The ardM32 kernel shows the most balanced performance, with a slightly higher MAPE than the baseline method on both test sets. For the ballast stiffness, the ardM32, ardRQ and ardSE perform the best with nearly identical results. In both cases, fused predictions by all kernels outperform all the individual kernels, as well as the baseline method, by a large margin.

To evaluate the performance of the proposed method for incomplete FRF measurements, we further compare the performance of the candidate models with different feature combinations; see Figure 4.11. In the noise-free case, fusing the predictions by different kernels does not seem to improve the performance compared to a single kernel,
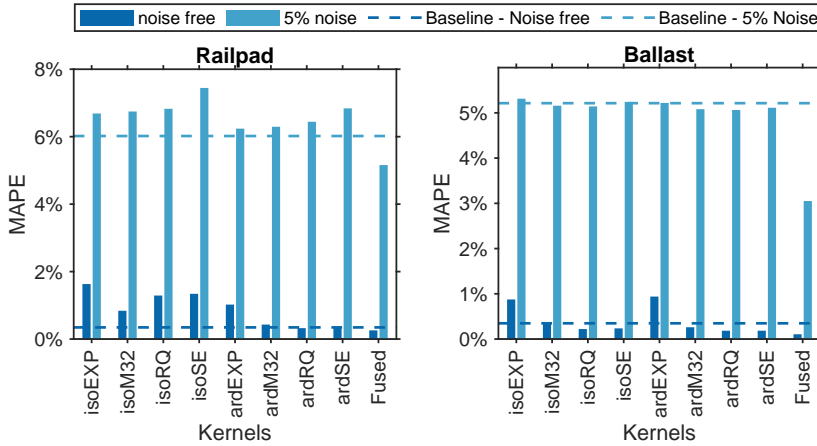
Figure 4.10: Comparisons between candidate models with different kernel functions. For each kernel, the results show the fused predictions by all the feature combinations assuming all 13 features are known. See the fusion strategy indicated by the blue blocks in Figure 4.9. The last columns in both plots show the fused predictions by candidate models. The noise-free model is used on the noise-free test set and the noisy model is used on the noisy test set.

with comparable performance to the baseline method. In the noisy case, however, fusing the predictions by different kernels outperform the baseline method as well as the model with a single kernel.

We now discuss how incomplete measurements in different scenarios influence the models' performance. For the prediction of railpad stiffness, including the sleeper-related features can improve the model performance. For example, A1 and A2 outperform A3 and A4 because they include the sleeper resonances in the predictors; see features 3 and 4 in Table 4.5. A1 and A3 outperform A2 and A4, respectively, because they include the sleeper properties (features 12 and 13) in the predictors. The same applies to feature classes B and C. In addition, including the features in a wider frequency range, in general, improves the performance; see the decrease of MAPE from feature class E to B and further to A.

For the prediction of ballast stiffness, the candidate models with the sleeper properties in the predictors (A1, A3, C1, C3, D1) perform better than their counterparts without the sleeper properties. Furthermore, all models show consistent performance, except for models D1 and D2 with features only in the low-frequency range (Zone I in Figure 4.8). In the worst-case scenarios with only three features as the predictors (E4 and D2), the MAPEs predicted by the fused model are approximately 12% and 6% for the railpad and ballast stiffness, respectively. Based on the results in Figure 4.10 and Figure 4.11, fusion by kernels is more effective than fusion by features.

4.4.4.3. TIME EFFICIENCY

Training   We perform all the training and testing on a workstation with an 8-core CPU (Intel Xeon E5-2687W v2). Figure 4.12 shows an example of the training time and prediction errors in relation to the number of samples used for training. The most time-
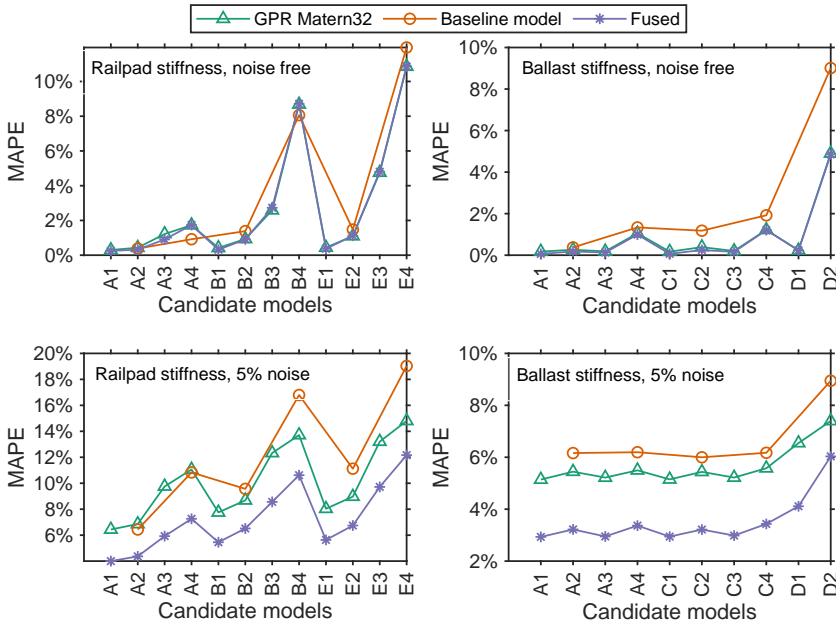
Figure 4.11: Comparisons between candidate models with different feature combinations. The first and second rows show the results of the noise-free and noisy test sets, respectively. For each feature combination, the results show the fused predictions by all the kernels. See the fusion strategy indicated by the red blocks in Figure 4.9.

consuming step in training is inversing the covariance matrix, which has the complexity of $O(N^3)$, where N is the number of training data samples. A good balance between accuracy and efficiency lies around 3000 samples; the training time is approximately a quarter of that with 5000 samples, whereas the performance of the two is almost identical.

For each training set, we consider 96 and 80 candidate models for the prediction of railpad and ballast stiffness, respectively. Although the numbers seem to be large, each candidate model can be trained independently in parallel. Moreover, as ballasted railway tracks share almost the same structure and are periodic, once the candidate models are trained, they can virtually be applied to almost all ballasted railway tracks.

Predicting   We compare the prediction time between the proposed and the baseline method in Table 4.6, assuming all 13 features are known. A clear advantage of the proposed method is that it is highly scalable. Making predictions of 400 samples only takes slightly more time than the prediction of one sample. With the proposed method, the most time-consuming step for a single prediction is inversing the covariance matrix shown on the right-hand side of Eq. 4.9. Once the inversed covariance matrix is available, the prediction takes almost no time as it is non-iterative and only involves simple matrix multiplications (see Eq. 4.9). For multiple predictions in a batch, e.g., the case of
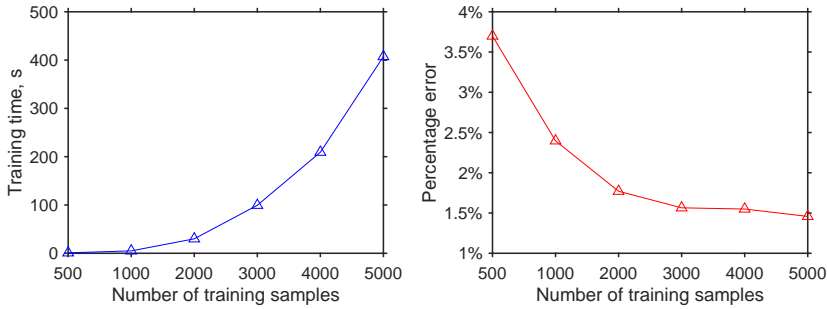
Figure 4.12: Training time and prediction errors using the isotropic squared exponential kernel.

400 samples shown in Table 4.6, the inversion is performed only once at the beginning of the procedure and stored in the memory for all the predictions in the batch. This means the marginal time cost for an additional prediction is trivial. In contrast, with the PSO, each prediction involves an iterative process, which takes about 30 s ~ 100 s, depending on the test cases. For multiple predictions, the total required time is the addition of all the predictions and therefore the baseline method is much more time-consuming than the proposed method.

Table 4.6: Comparisons of the prediction time (in seconds) for predicting railpad stiffness between the proposed and the baseline method.

Number of samples	Fusion by feature	Fusion by kernel	Baseline
1	13.0	7.9	50.5*
400	14.6	8.1	2343**

* Mean value of 400 samples with a minimum value of 32.2 s and a maximum of 105.7 s.
** Computed with 8 cores in parallel.

4.5. APPLICATION EXAMPLES

4.5.1. NUMERICAL EXAMPLES

We applied the proposed method to the two reference cases presented in Section 4.3.1. The simulated FRF curves and dispersion relations are used for the feature extraction and subsequent predictions. Figure 4.13 gives an example of the predictions made by a single kernel (ardM32) with different feature combinations. It is noticed that the predictions by the noisy models (Figure 4.13 (a) and (c)) have larger confidence intervals than the noise-free models (Figure 4.13 (b) and (d)). Meanwhile, the mean predictions by different noisy models are less biased than those by the noise-free models. In other words, the noisy models show more consistent performance with incomplete measurements.

Figure 4.14 shows the predictions by different kernels, fused by feature combinations for each kernel. As is the case in Figure 4.13, the predictions by the noisy models show larger confidence intervals while being more consistent in terms of the mean predic-
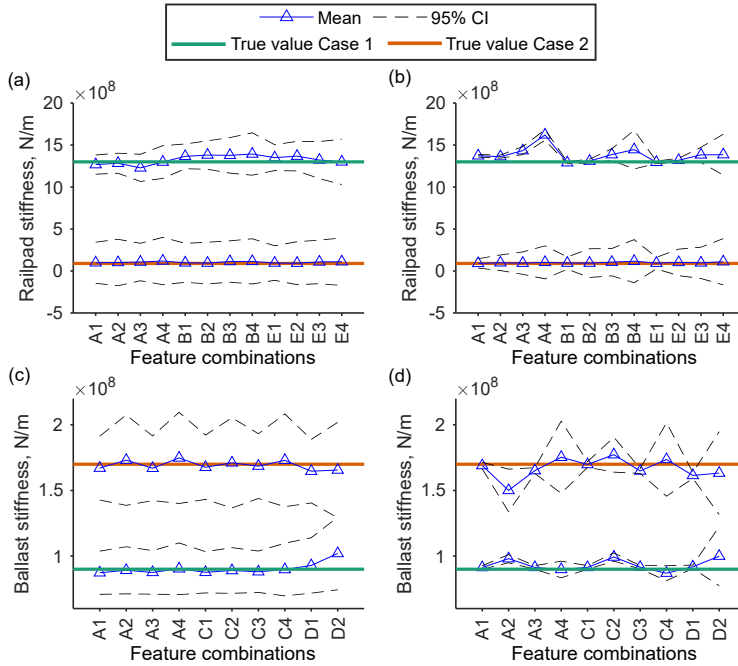
Figure 4.13: Predictions by the ardM32 kernel with different feature combinations for the reference cases. (a) and (c) show the predictions made by the GPR models trained by the noise-free datasets. (a) and (c) show the predictions made by the GPR models trained with 5% injected noise. (b) and (d) show the predictions made by the GPR models trained by the noise-free datasets.

tions.

We further fuse the predictions of all the kernels for the noise-free and noisy models, respectively. Results are compared with the true values in Table 4.7. The prediction errors for Case 2 are larger than those for Case 1. This is because in Case 2 the track model has a shorter sleeper length and a larger sleeper spacing compared to the FE model used for training the GPR models. This means the noise level due to modelling errors are higher compared to Case 1. In addition, Case 2 has a set of incomplete FRF features, which according to Figure 4.11 also leads to larger prediction errors.

Table 4.7: Fused predictions of railpad and ballast stiffness (in MN/m) for the numerical examples.

		True values	Noise-free	Difference	Noisy	Difference
Case 1	Railpad	1300	1309.00	0.69%	1312.31	0.95%
	Ballast	90	91.95	2.16%	89.62	−0.43%
Case 2	Railpad	90	101.09	12.33%	101.48	12.75%
	Ballast	170	166.03	−2.34%	156.79	−7.77%
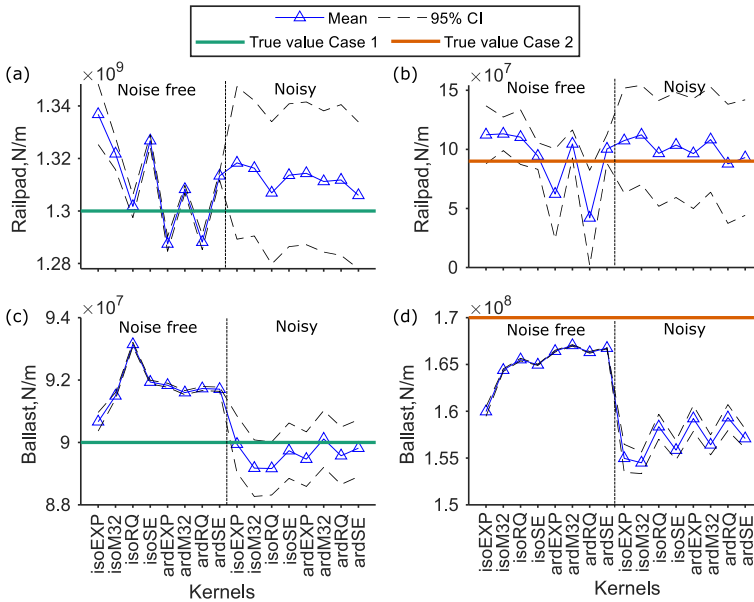
Figure 4.14: Predictions by different kernels for the reference cases. For Case 1, the results show the fused predictions by all the feature combinations for each kernel. For Case 2, due to the incomplete measurement as shown in Figure 4.8 (b), the fusion is by A3, A4, B3, B4, E3, E4 for the railpad stiffness and A3, A4, C3, C4, D1, D2 for the ballast stiffness. See Table 4.5 for the details of the feature combinations.

4.5.2. FIELD APPLICATION EXAMPLE

4.5.2.1. FIELD TEST SETUP

The test site is located at Faurei Railway Test Center in Romania. The field test was conducted on a section of well-maintained ballasted track. The track system consists of UIC60 E1 rails, Vossloh W14 fastenings, prestressed concrete sleepers (type B70-W60) with 600 mm spacing and a ballast layer. We have installed 11 accelerometers (PCB 356B21, three-dimensional) on the rail, as well as 4 accelerometers (Bruel & Kjaer 4514-004, one-dimensional) on the sleeper, see Figure 4.15. We attached three accelerometers to the rail head, web and foot, respectively at two locations, i.e. above the sleeper (R6, R7 and R8) and at mid-span (R2, R3 and R4).

We used two types of hammers for the hammer test: i.e. a small hammer that weighs 0.32 kg (PCB 086D05) and a big hammer that weighs 5.5 kg (PCB 086D50). Hammer impacts were applied at two locations, one on the rail top above the instrumented sleeper and the other on the center of the sleeper. For each measurement with each hammer, the impact was repeated several times until at least five impacts show good coherence.

4.5.2.2. FEATURE EXTRACTION

As the GPMs are trained with the point receptance of the rail above a sleeper, we use the hammer force at impact location 1 and measured accelerations from R6, R7 and R8 to construct the FRF curves for the feature extraction. For each hammer type, the test was
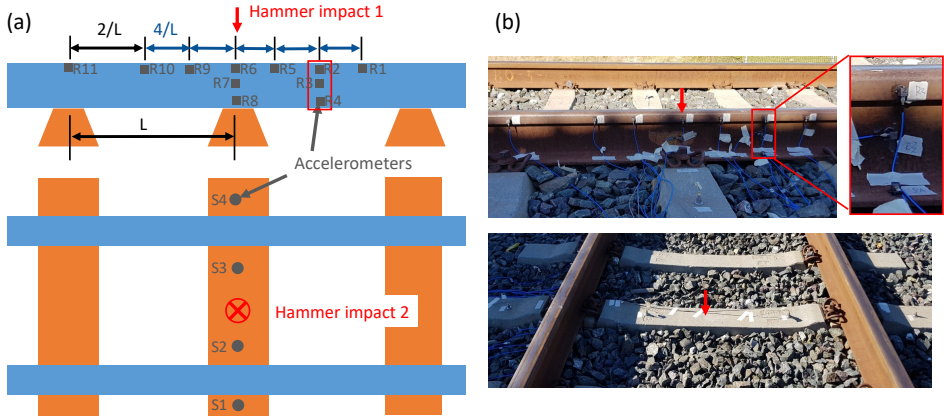
Figure 4.15: Configuration of accelerometers and hammer impact locations. Accelerometers on the rail are three-dimensional and labelled as R1 ~ R11. Accelerometers on the sleeper are one-dimensional (vertical) and labelled as S1 ~ S4. Two impact locations are indicated by the red arrows.

repeated five times and therefore we can construct 15 FRFs with the three sensors. The results are shown in Figure 4.16 (a).

The validity of the results from the two hammer types can be evaluated from two perspectives. The first perspective is based on the coherence between different measurements. For the big hammer, the results are consistent till about 800 Hz with small variance (see the shadings in Figure 4.16 (a)), whereas the results for the small hammer can be considered reliable above about 300 Hz. Note that the shadings include the signals from three accelerometers while still maintaining small variance. This means we can use any of the three accelerometers for the feature extraction without affecting the final results. The other perspective is the ability to provide adequate energy to excite the necessary track resonances. Between 300 Hz till about 1400 Hz, the consistency of the results from the small hammer is better than that from the big hammer. However, some of the track resonances (e.g. S2, R1-a, S4) cannot be fully excited by the small hammer because of its low excitation energy. Therefore, the information from the results of both hammers should be used between 300 Hz and 1400 Hz. As a result, we construct a new FRF curve for the feature extraction, as indicated by the dashed line in Figure 4.16 (a). The FRFs of the big hammer and small hammer are used for frequencies below 300 Hz and above 1400 Hz, respectively. In between, the average results of the two methods are adopted. The features of the new FRF curve are shown in Figure 4.16 (b).

4.5.2.3. Prediction results
Compared to the numerical examples, the measured FRF features contain a higher level of measurement noise. Additionally, modelling errors also exist due to the assumptions such as linearity and homogeneity, which might not hold in the current application. As a result, the predictions made by the noise-free models deviate from those of the noisy models; see Figure 4.17. Despite this, the predictions by the noisy models are very close to those made by the baseline method; see Table 4.8. For real-life measurements, it is
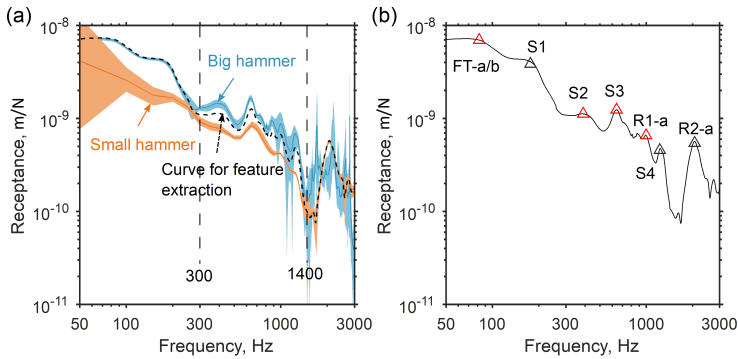
Figure 4.16: Measured vertical track receptance with input from impact location 1 and outputs from R6, R7 and R8. (a) Receptances from both the big and small hammer measurements. For each hammer type, 15 FRF curves are shown with the mean values (solid lines) and the envelope (shadings). The FRF curve used for prediction is indicated by the dashed line. (b) Extracted TR features. TRs with red triangles are used for the predictions.
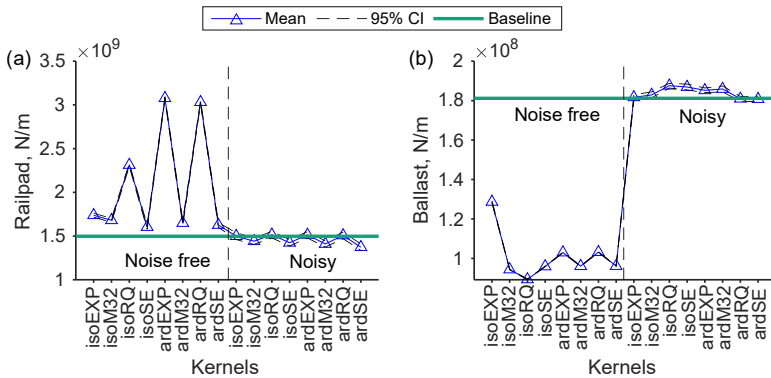
recommended to use the noisy model for the predictions.

Figure 4.17: Predictions by different kernels for the field application example. For each kernel, the results show the fused predictions by all the feature combinations. (a) Railpad; (b) ballast.

Table 4.8: Comparison between the predictions (in MN/m) by the proposed method and the baseline method.

	Baseline	Proposed method			
		Noise-free	Difference	Noisy	Difference
Railpad	1498.1	2287.1	52.70%	1458.9	-2.60%
Ballast	181.2	97.4	-46.30%	184	1.60%

With the predicted track stiffness, we simulate the field hammer tests for the two impact locations as shown in Figure 4.16. Figure 4.18 (a) and (b) compare the calcu-

lated and measured FRFs with different accelerometers for the impact on the rail and the sleeper, respectively. Note that the predictions of track stiffness are made based only on the measured point rail FRF above the sleeper, i.e. the first graph in Figure 4.18 (a). It can be seen that the calculated FRFs are in good agreement with the measurement not only for the point FRFs but also for the other transfer FRFs.

It is also noted that in the measured FRFs, three distinct peaks can be observed above 1000 Hz, especially for the impact on the sleeper, see Figure 4.18 (c). These peaks are less damped than those below 1000 Hz. Therefore, by reducing the ballast damping from $120\,\text{kN}\cdot\text{s/m}$ to merely $0.12\text{kN}\cdot\text{s/m}$, we can reproduce these peaks as shown in Figure 4.18 (c). This suggests that the ballast properties are frequency dependent and the ballast damping reduces to a very low level above 1000 Hz in this case. The three peaks turn out to be three high-order sleeper bending modes.

4.6. DISCUSSIONS

4.6.1. LIMITATIONS OF PROPOSED METHOD

There are some limitations of the proposed method in estimating the track stiffness.

First, the railpad and ballast stiffness are measured in the unloaded condition. In reality, the railpad and ballast stiffness are non-linear and increase with the preload on the track [52, 134, 140]. This means the track stiffness measured with the proposed method may deviate from that under train loading. In future studies, a train-borne measurement system based on ABA can be developed to measure the track stiffness under the loaded condition.

Second, the stiffness of the railpad and ballast is assumed homogeneous in the track model. This means the proposed method does not consider the stiffness variations at different sleeper supports or under a single sleeper. As the influence of a dynamic wheel load is within about five sleeper spans [39], the hammer impact used in the proposed method should have an even smaller range of influence. Therefore, the track stiffness estimated by the current method represents the averaged stiffness in the vicinity of the hammer impact location. To be able to consider the stiffness variations, the stiffness values of the railpad and ballast should be defined and identified separately for each sleeper. With more track parameters to be identified, using only one FRF may be insufficient as the problem becomes under-determined. Instead of using a single accelerometer in the proposed method, a more complex instrumentation setup is required [23, 135].

4.6.2. COMPARISON WITH PREVIOUS TECHNIQUES

As discussed in section 4.1, the techniques that have been used for the track parameter identification in the literature are all optimization-based methods, see Table 4.9. These methods usually consist of three key components, i.e. a track model, a single or multiple objective functions and an optimization technique. However, there has not been a comparison study between different techniques as to their performance, which makes the choice of a baseline method difficult. In this section, we provide a comparison between the different techniques to justify the choice of the baseline model in this chapter and also to further demonstrate the advantages of the proposed method.

Table 4.9: A list of optimization-based methods for track parameter identification in the literature.

References	Track model	Optimization technique	Objective function
[54]	Two-layer continuous beams	Any conventional technique	FRF
[52]	2-DOF mass-spring	Least squares	FRF
[17]	Rational fraction polynomials	Multi-objective GA	FRF + Coeffienct of fitted polynomials
[55]	3D FE model	Multi-objective PSO	Natural frequency + FRF
[135]	Rail masses + single sleeper beam	MCMC-based Bayesian approach	Time domain response
Baseline	Rail beams + discrete sleeper beams	PSO	Natural frequency + FRF magnitude features

4.6.2.1. TRACK MODELS

The most accurate track models are 3D solid FE models [27, 55, 153], as they make the least assumptions and simplifications. The main drawback is however the high computational costs they require. The track model in this chapter uses the Timoshenko beam element instead of solid elements to model the rail and sleeper, which greatly reduces the degrees of freedom of the system and therefore is much faster to solve. In terms of accuracy, we have shown in Figure 4.3 that the track model used in this chapter is accurate up to about 1000 Hz compared to the solid FE model, which is adequate for the current problem. The other track models listed in Table 4.9 further simplify the rail, sleeper or both as rigid masses. Such simplifications will result in a lack of certain track resonances in the FRF. For example, when the sleepers are modelled as rigid masses, track resonances related to sleeper bending modes (see S1 ~ S3 in Figure 4.3 and Table 4.9) are not present in the FRF [27, 72]. In summary, the current track model shows a good balance between accuracy and efficiency.

4.6.2.2. OBJECTIVE FUNCTIONS

In structural identification problems, objective functions are usually based on modal parameters (i.e. natural frequencies and mode shapes) or FRFs. In the track parameter identification, mode shapes are usually not used in the objective function, as shown in Table 4.9, mainly because they are not easily measurable with simple instrumentations. In the baseline model used in this chapter, the objective function (Eq. 4.16) is based on a combination of natural frequencies and FRF features.

Note that we only make use of the FRF features instead of the whole FRF curve. This is mainly for practical reasons. First, our method is based on the meta-models of the FE track model (see section 4.4.4.1), which means for each feature we train a meta-model. By selecting only a few features, we keep the training cost as low as possible. Furthermore, some frequencies are redundant for the identification of parameters; the best approach is to select a few frequencies that carry as much information as possible [167].

Moreover, we adopt a single objective function that combines the natural frequencies and FRF magnitude features, instead of two multi-objective functions that treat them separately as in [55]. The two approaches will be compared in the next section.

4.6.2.3. OPTIMIZATION ALGORITHMS

For simple track models, conventional gradient-based algorithms may yield satisfactory results [52]. For more complex track models, more advanced optimization techniques are needed to deal with the multimodal and non-convex nature of the problem. We compare three commonly used EAs, i.e. the PSO, GA and multi-objective GA both in

terms of robustness and time complexity, as shown in Figure 4.19 and Figure 4.20, respectively. It can be seen that the PSO in general performs the best among the selected EAs. Only in the worst-case scenario, i.e. with only three features available in the measured FRF (see E4 in Figure 4.19), the multi-objective GA outperforms the PSO. However, the multi-objective GA is also more computationally expensive than the other methods.

In addition, the proposed method is more robust than the selected EAs; see Figure 4.19. Only with feature combinations A2 and A4, the PSO performs slightly better than the proposed method. In terms of the time complexity of the proposed method, the time required of running multiple predictions is only slightly larger than a single prediction, whereas the selected EAs take a much longer time to run multiple predictions. The highly scalable feature of the proposed method is a major advantage of the proposed method.

4.7. CONCLUSIONS

We propose a new method to directly infer railpad and ballast stiffness from a single FRF using the GPR. The robustness of the method is ensured by a careful selection of eleven FRF features as the predictors, as well as the prediction fusion strategies that automatically filter out unreliable predictions from multiple candidate GPR models. We show that including more features related to sleeper resonances and fusing the predictions by different kernels are two effective ways to reduce prediction errors.

We compare the performance of the proposed method with a model updating method using PSO on two synthesis datasets in a wide range of scenarios. In general, the proposed method outperforms the PSO method both in terms of accuracy and time efficiency. In the worst-case scenario with only three available features and 5% injected noise, the average prediction errors by the proposed method for the railpad and ballast stiffness are approximately 12% and 6%, respectively. Moreover, the method is highly scalable in the sense that it enables fast predictions for large datasets.

Both the numerical and field application examples show that the candidate models trained with injected noise are more consistent with each other and therefore are more suitable for real-life applications. The field application example also shows that the proposed method is capable of extracting the stiffness values using only the point FRF of the rail above sleeper support with a simple setup, i.e. only one accelerometer and one impact location.

In future studies, the proposed method can be applied to field measurement data for the monitoring of track conditions. Although the proposed method focuses on the FRFs measured by field hammer test, it can be extended to features measured in operational conditions, especially considering the characteristic frequencies of railway tracks excited by ambient vibrations agree with the TRs identified by hammer tests [12].
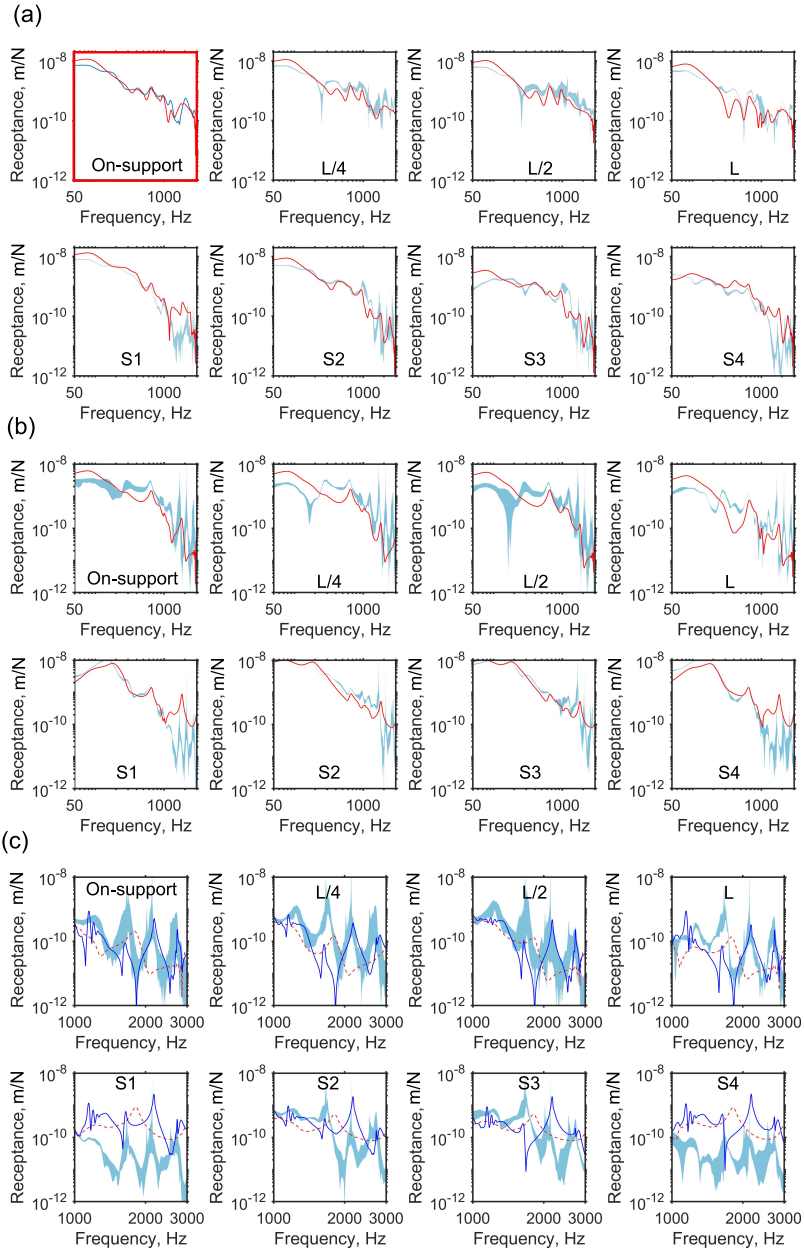
Figure 4.18: Comparisons between predicted FRF curves (solid lines) and the measurements (shadings). (a) Impact on the rail. (b) Impact on the sleeper. (c) Impact on the sleeper with the same ballast damping (dashed red lines) as in (a) and (b), but a lower ballast damping (solid blue lines). For each sub-figure, the first row shows the FRFs measured from the rail at the impact location (On-support), quarter span ($L/4$), mid-span ($L/2$) and one span away (L) from the impact location. The second row shows the FRFs measured from the sleeper (S1 ~ S4). See Figure 4.2 for the two impact locations and sensor arrangement.
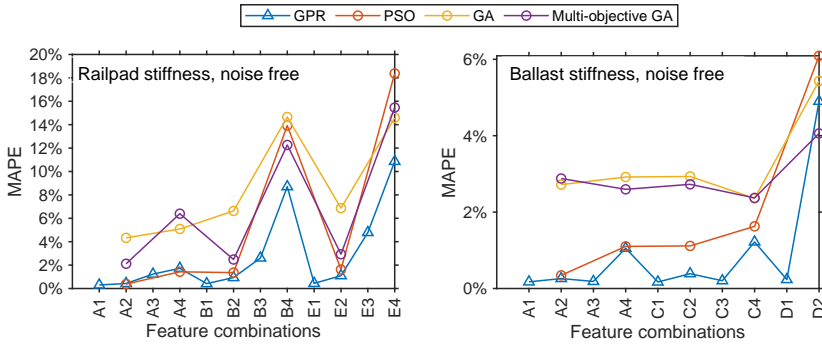
Figure 4.19: Comparisons of the accuracy between different optimization-based algorithms and the proposed method (GPR). PSO is used as the baseline in this chapter. See Table 4.5 for the definition of different feature combinations.
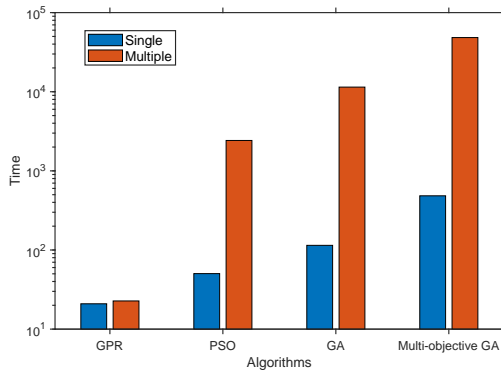
Figure 4.20: Comparisons of the time complexity between different optimization-based algorithms and the proposed method (GPR). The results for the multiple predictions include 400 samples.

5

EVALUATING RAILWAY TRACK DYNAMIC STIFFNESS USING AXLE BOX ACCELERATIONS

In this chapter, we apply the digital twin framework to the vehicle-track interaction (VTI) system to enable near real-time track stiffness evaluations based on the measurement of axle box accelerations (ABA). In comparison to existing techniques, our method can simultaneously evaluate the respective stiffness of the railpad, sleeper and ballast layers, as well as the track irregularities at sleeper spacing resolution. This is accomplished by employing a localized frequency domain ABA feature capable of distinguishing the characteristics of the different track layers. Furthermore, our method enables rapid track stiffness evaluations. This is achieved by a model library derived from physics-based simulations of a range of track conditions. We develop two data-driven models that can quickly select or interpolate between the model instances contained in the library. In operation, the data-driven models take observed ABA features as input and then infer the stiffness for the different track layers based on selected or interpolated model instances. We apply the proposed method to evaluate the track stiffness of a downscale test rig in a case study. We compare the results of the proposed method to those obtained by a hammer test method, as well as the observations of the track component conditions. Results show that the proposed method is capable of capturing stiffness variations due to periodically fastened clamps and substructure misalignments. We also demonstrate that the proposed method is superior to the commonly used hammer test method for evaluating track stiffness under operational conditions.

5.1. Introduction

Railway track stiffness is an important track property that is closely related to track condition and maintenance. Track stiffness variations occur over time and space due to dynamic train loading and the aging of track components. Worn railpads, hanging sleepers and ballast fouling are some of the degradation types. Track stiffness variations may further lead to geometry deteriorations [168, 169] and consequently major maintenance costs. It is therefore essential to continuously monitor track stiffness variations, as well as related track component degradations, over time and space so that preventive and targeted maintenance can be performed to reduce the life-cycle cost of rail infrastructures.

The ballasted railway track is a multi-layered structure that includes rails, fasteners, railpads, sleepers, ballast, and subgrade. Track stiffness is most commonly defined as the equivalent stiffness provided by all the track components beneath the rail [23], also known as the overall track stiffness or track modulus. However, because each layer has well-defined, distinct design/target stiffness values, it is desirable to differentiate the stiffness of individual track layers. This enables us to set consistent and reasonable stiffness thresholds for each layer, which aids in the decision-making process for track maintenance. The goal of this chapter is to evaluate the stiffness of individual track layers separately.

Methods for measuring track dynamic stiffness can be classified into two categories based on whether the stiffness is measured in a loaded or unloaded condition. In an unloaded condition, external excitation forces are provided by impact hammers [135–138, 170] or falling weights [12, 139]. Both the input force and output responses are recorded during measurement to obtain the track dynamic stiffness in the form of frequency response functions (FRFs). However, because track stiffness varies depending on loading conditions [171–173], measured track stiffness in an unloaded condition may not accurately reflect the track stiffness in a train-passing scenario.

The other approach is to measure track stiffness under dynamic train load. Measurement techniques include trackside [23, 56, 57] and train-borne measurements [28, 58–65]. Trackside measurement allows sensors to be mounted on each sleeper so that the measurement resolution of stiffness variation can be at the sleeper spacing level. Nonetheless, because of the cost of sensor deployment, trackside measurement is more suited for discrete locations of special interest in the rail network, such as transition zones [174]. To scan the track stiffness over a much longer distance, specialized measurement vehicles were developed [28, 58, 59], which enable continuous measurement of track stiffness but at low speed and frequency. In comparison, train-borne measurement with in-service vehicles is more cost-effective and allows for more frequent surveys of the entire rail network. Among various train-borne measurement techniques, axle box accelerations (ABA) show good potential for the condition monitoring of railway tracks and have been used for the detection of rail defects [11], bolt tightness of fish-plated joints [175], corrugations [84], and longer wave irregularities [10]. In this study, we further explore the potential of ABA for evaluating track stiffness.

One major issue with the train-borne method is the difficulty of obtaining a measurement resolution at the sleeper spacing level. For example, Yang et al [65] evaluated track stiffness variations at a resolution of 20 m. Quirke et al [60] proposed a method for evalu-

ating track stiffness variations at different sleeper supports. However, the stiffness value at each sleeper was not evaluated individually. Instead, a track stiffness profile template was used to represent the stiffness variation along a track length, thereby reducing the total number of stiffness variables. Zhu et al [64] considered a track section of about 80 sleepers. Stiffness values were defined individually for each sleeper support at three track layers, namely the railpad, ballast and foundation layer. It was shown that by using an adaptive regularization approach track stiffness can be evaluated at a sleeper spacing resolution when stiffness variations only exist in a single track layer. The approach was unable to discriminate between stiffness variations at multiple track layers simultaneously. It was also discovered in both [64] and [65] that a high sampling rate combined with a low to moderate vehicle speed is required to ensure a reliable high-resolution evaluation. This is to ensure that sufficient data points are collected within a short track segment, such as a sleeper span.

Additionally, there seems to be a lack of experimental and field validation for the train-borne track stiffness evaluation method. The trackside techniques in [23, 56, 57] have been validated by field measurement data, whereas train-borne measurement techniques have been demonstrated solely through numerical examples [60, 62, 64, 65] or simple lab setups [63].

Evaluating track stiffness from measurements is essentially an inverse problem that involves fitting a vehicle-track interaction (VTI) model to measurements. There are two commonly used approaches for this task. The first approach is to solve an optimization problem, where objective functions defining the difference between modelled and measured dynamic responses are minimized iteratively [60, 64]. However, when ABA is measured regularly and frequently using in-service vehicles, a large amount of data is generated and needs to be processed. Conventional optimization-based iterative methods would be too slow for this purpose. Alternatively, a direct mapping between measured dynamic responses and track stiffness can be established. A major challenge is identifying features in the dynamic responses that can be correlated to track stiffness. Several frequency domain features have been proposed in this regard to evaluate the overall track stiffness [23, 62, 79] or local stiffness loss [63, 176]. These features, however, are unable to distinguish between the track stiffness at different layers. Multiple features that can be distinctly correlated to different layers must be defined for multi-layer track stiffness evaluations [59]. In Chapter 4, we demonstrated that track stiffness at different layers correlates with different FRF features. This opens up the possibility of using ABA measurements for the same purpose.

5.2. Contributions of this chapter

In this chapter, we propose a digital twin framework for the vehicle-track system that enables near real-time track stiffness evaluations based on measured axle box accelerations (ABA). Our method makes three major contributions.

First, our method is capable of evaluating the stiffness of multiple track layers simultaneously at high resolutions, i.e., at sleeper spacing level. To achieve this, we propose a localized frequency domain representation of ABA that can be calculated at each sleeper, which enables high-resolution stiffness evaluations. Besides, we show that the stiffness of each track layer is related to distinct characteristics of the proposed ABA representa-

tion, which enables multi-layer track stiffness evaluations.

Second, our method allows for fast track stiffness evaluations. Fast evaluations rely on a model library that is constructed using a physics-based VTI model. The model library contains a collection of possible model instances generated through simulations within a predefined track parameter space. We propose a model selection algorithm for rapidly locating the model instances (and thus the corresponding track parameters) in the model library that best matches the observed ABA. Additionally, we use the discrete data in the model library to train a Gaussian process (GP) regression model, which can interpolate between model instances, so that track stiffness predictions, as well as the confidence intervals, can be obtained for observed ABA that does not match well with any model instance in the library.

Third, our method can quantify the uncertainties associated with evaluated stiffness values. Assumptions and simplifications are inevitable in a physics-based model. Therefore, the model library, which is generated from the physics-based model, contains inherent uncertainties from these assumptions and simplifications. Uncertainty quantification is accomplished through the use of GP models that can provide confidence intervals for each stiffness evaluation.

We demonstrate our methodology through a case study, in which we create a digital twin for a downscale test rig of vehicle-track interaction called V-Track [177]. The track stiffness and its variations evaluated by the proposed method are presented and verified by comparing to hammer test results and observations of track conditions, e.g. the clamps and substructure changes.

The rest of the chapter is organized as follows. Section 5.3 describes the structure and general principles of the proposed digital twin framework. Section 5.4 delves into the implementation of the physics-based VTI model and how it facilitates the model library construction and ABA feature selection. Section 5.5 demonstrates the performance of the model library and two data-driven methods. Section 5.6 presents the case study and section 5.7 concludes the chapter.

5.3. DIGITAL TWIN FRAMEWORK FOR VEHICLE-TRACK INTERACTIONS

5.3.1. PROBLEM STATEMENT

The observed ABA data for a track section can be represented using a feature vector, denoted as $\mathbf{x}^* \in X$, where X is the feature space, i.e., the space of all possible ABA features. The stiffness values of different track components for the same track section are denoted by a vector $\mathbf{k}^* \in K$, where K is the parameter space of all possible stiffness values. The task is to use observed ABA data $\mathbf{x}^*$ to infer the stiffness values of its track components $\mathbf{k}^*$. This task can be framed as an inverse problem, where we aim to find an inverse mapping from the feature space X to the parameter space K, which can be denoted by

$$G : X \rightarrow K \tag{5.1}$$

5.3.2. Digital twin framework

To address the problem defined in Eq. 5.1, we propose a digital twin framework consisting of three major components, i.e., a physics-based FE model, a model library and data-driven models associated with the library, as illustrated in Figure 5.1. The physics-based model provides predictions and interpretations of ABA under various track stiffness conditions. The data-driven models are used to make fast and direct evaluations of track stiffness based on measured ABA. The model library bridges the gap between the physics-based and data-driven models: it is generated from the physics-based model while containing only the data necessary for building data-driven models for a particular task.
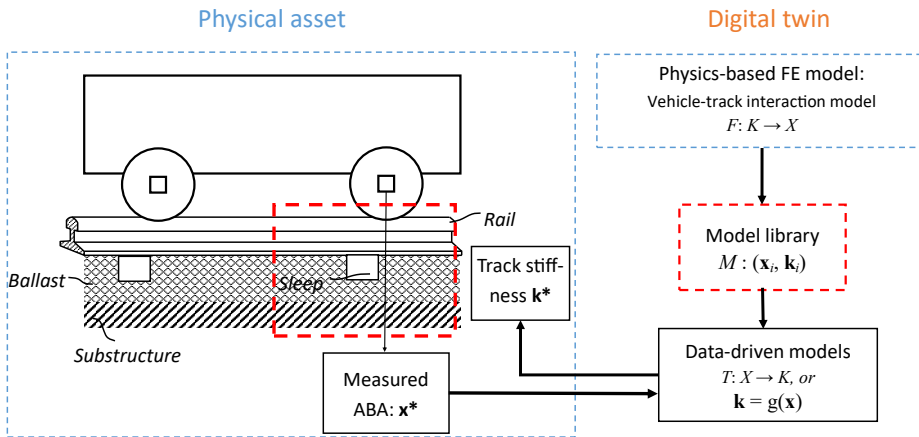
Figure 5.1: Digital twin framework for evaluating track dynamic stiffness based on ABA.

5.3.2.1. Physics-based FE model

We develop a physics-based FE model to simulate the dynamic vehicle-track interactions. Because of its predictive and interpretability capabilities, the physics-based model serves two major functions. First, by virtue of its predictive capability, it establishes a forward mapping from the parameter space K to the feature space X,

$$\mathrm{F}: K \to X \tag{5.2}$$

This allows us to generate $\left(\mathbf{x}^{(j)}, \mathbf{k}^{(j)}\right)$ pairs for $j = 1, 2, \ldots, N$, by running N simulations with sampled stiffness values $\mathbf{k}^{(j)} \in K$ as inputs and a corresponding feature vector $\mathbf{x}^{(j)} \in X$ as an output. The $\left(\mathbf{x}^{(j)}, \mathbf{k}^{(j)}\right)$ pairs are essentially a discrete form of mapping of Eq. 5.1, which we will use in the following step to build a model library (see section 5.3.2.2).

Additionally, the interpretability capability of the physics-based model can provide physical insights into tasks that require expert or domain knowledge, such as the ABA feature selection. Section 5.4 demonstrates in detail the implementation of the FE model and how it facilitates the feature selection process. Moreover, the physical insights gained

from the physics-based model can also help interpret the evaluations by data-driven models. We demonstrate this in section 5.6 with the case study.

5.3.2.2. Model library

Each simulation case by the FE model represents a possible state of the physical asset, called a model instance, denoted as $m_j \in M$, where M is a model library including all the simulated model instances. Each model instance $m_j \in M$ is associated with a $\left(\mathbf{x}^{(j)}, \mathbf{k}^{(j)}\right)$ pair as its property.

Unlike the physics-based model, which serves as a general-purpose simulation engine that models a long distance of the track, a key consideration of the model library is data efficiency: it should contain only the data necessary for a specific task. The model library is used in this chapter to represent the states of a local track section, as illustrated in Figure 5.1, with the length of a sleeper spacing centered above a sleeper. A major advantage of such a local representation for the model library is that the dimensions of both the feature space X and track parameter space K are reduced. As will be shown in section 5.3.4, the feature space is reduced by using a local and sparse frequency domain representation of ABA. Meanwhile, the parameter space only contains the stiffness values of the railpad, sleeper and ballast over a single span. Reduced space dimensions are advantageous because building data-driven models in high-dimensional spaces may become difficult, if not possible, due to the curse of dimensionality. Furthermore, because the railway track is a periodic structure, the model library can be shared across multiple track spans. By creating a digital twin for each sleeper span, the approach can be easily scaled to any track length.

However, by using a local model library representation, we assume that the ABA measured over sleeper support is only related to the local track stiffness at that support. In reality, this assumption holds only when the track stiffness is uniform across multiple sleeper spans. When stiffness variations exist, the evaluations by the local model library usually indicate an averaged stiffness across adjacent sleeper spans. Nonetheless, such an assumption is used in many applications because it allows for more efficient analysis of the large volumes of data required to understand variation over a long track.

5.3.2.3. Data-driven models

With the model library, we aim to make fast evaluations of track stiffness $\mathbf{k}^*$ given an observed ABA feature vector $\mathbf{x}^*$. We propose two data-driven methods to accomplish this, as shown in Figure 5.2.

Model selector   The first method is a model selection algorithm that searches directly within the model library M for one or several model instances $m_i \sim \left(\mathbf{x}^{(j)}, \mathbf{k}^{(j)}\right)$ that best describe the observation $\mathbf{x}^*$. We call the algorithm a model selector, denoted as

$$\mathrm{T}: X \to M \tag{5.3}$$

The basic principle is to search for the nearest neighbours of $\mathbf{x}^*$ in $\mathbf{x}^{(j)}$, for $j = 1, 2, \ldots, N$, as illustrated by the dashed oval in the left plot of Figure 5-2. The algorithm is outlined below.
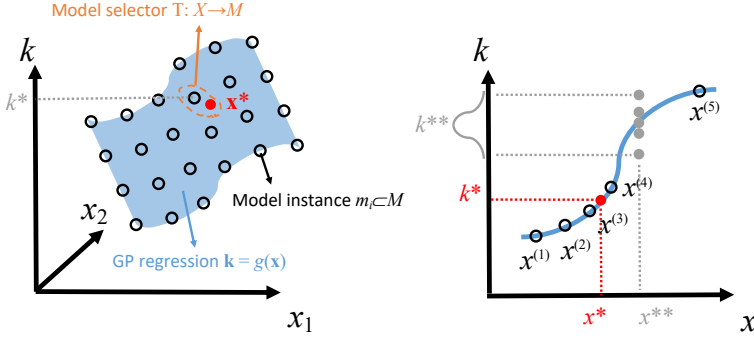
Figure 5.2: Data-driven models for fast track stiffness evaluations. Left: model library M, model selector T and GP regression model g demonstrated in a three-dimensional space. Right: the principle of uncertainty quantification by the GP model demonstrated in a two-dimensional space.

1. Calculate the Euclidean distance between $\mathbf{x}^*$ and $\mathbf{x}^{(j)}$

$$\mathbf{d} = \{d_j\} = \left\| \mathbf{x}^* - \mathbf{x}^{(j)} \right\|_2, j = 1, 2, \dots N;$$ (5.4)

2. sort $\mathbf{d}$ in ascending order to obtain a sorted vector $\mathbf{p} = \{p_i\}$;

3. return a ranking vector r_j for each d_j so that $\mathbf{d}(r_j) = p_j \, j = 1, 2, \dots, N$;

4. return the top $n < N$ matches of $\mathbf{x}^*$ in $m_i \sim (\mathbf{x}^{(j)}, \mathbf{k}^{(j)})$, denoted as $m_i^* \sim (\mathbf{x}^{*(i)}, \mathbf{k}^{*(i)})$, where $m_i^* = m_{r_i}, i = 1, 2, \dots, n$;

5. Calculate the prediction for $\mathbf{k}^*$ by taking the average of the top n matches

$$\overline{\mathbf{k}}^* = \frac{1}{n} \sum_{i=1}^{n} \mathbf{k}^{*(i)}.$$ (5.5)

The model selector has the advantage of being directly applicable to the model library, without the need to train a data model. While it can be used independently as a track stiffness evaluation method, it also serves as an efficient first step for evaluating the quality of the model library before it is used for building data-driven models. The evaluation can be based on the Euclidean distances between the target ABA feature and the features in the model library (Eq. 5.4). We demonstrate the capabilities of the model library and model selector in section 5.5.1.

Gaussian process (GP) regression   Because feature space X is a potentially high-dimensional space, the features $\mathbf{x}^{(j)}$ in the model library are likely to be sparsely distributed. As a result, it is possible that a target ABA feature is not sufficiently close to any feature in the model library. In this case, we propose using the GP regression method to interpolate between model instances, as illustrated in Figure 5.2 by the blue plane or curve. The GP

regression theory can be found in [151] and a detailed implementation for a similar task is described in Chapter 4.

A practical motivation to use the GP regression is that it can provide uncertainty quantifications for the evaluated track stiffness. To illustrate this, consider the two-dimensional space depicted in the second plot of Figure 5.2. The model library contains five model instances, as indicated by the black circles. The five instances are not distributed evenly, with a large gap between $x^{(4)}$ and $x^{(5)}$. The goal is to determine the stiffness values associated with two observed ABA features, x^* and x^{**}. Because x^* is close to both $x^{(3)}$ and $x^{(4)}$, the GP model can make a high-confidence prediction of k^*. In comparison, x^{**} is separated from any model instance. Consequently, the prediction of k^{**} has a higher degree of uncertainty. When a prediction with a high level of uncertainty is encountered, it is possible that the model library needs to be more densely sampled, or that it is due to modelling errors that can only be corrected with a more realistic VTI model. The implementation and performance of the GP model are demonstrated in section 5.5.2.

5.3.3. PHYSICAL ASSET: V-TRACK

We demonstrate the implementation and capabilities of the proposed framework by building a digital twin for a downscale vehicle-track interaction test rig called V-Track. In this section, we briefly introduce the V-Track setup for ABA measurement.

V-Track consists of a maximum of four-wheel assemblies running over a ring track system. In the configuration for the current work, one wheel assembly was used, as shown in Figure 5.3 (a). Figure 5.3 (b) shows the structure of the wheel assembly. A wheel (1) with a diameter of 130 mm is mounted on a guiding block (3) through an axle box (2). The wheel assembly is mounted on an arm of a steel frame (4) and vertically loaded through two springs. The combined stiffness of the two springs is 230 N/mm. A motor drives the steel frame so that the wheel assemblies are pulled to move along the ring track. The speed range of the wheel assemblies is between 0 and 40 km/h. A more detailed description can be found in [177, 178].

The ring track, which has a radius of 2 m, consists of four pieces of rails connected by four rail joints. The ring rail, which has a standard S7 profile, is supported on railpads. The rail and railapds are fixed on steel sleepers by fasteners, as shown in Figure 5.3 (d). It is worth noting that clamps are used only every three or four sleepers to vary the track stiffness for the tests. A total of 100 steel sleepers are used and the sleeper spacing is approximately 0.125 m. All sleepers are numbered from 1 to 100 for positioning; for instance, S1 designates sleeper 1. Underneath the sleepers are rubber pads, which are used to simulate the elasticity and damping of a ballast layer. The subgrade is simulated by plywood layers.

Track stiffness was varied along the V-track at different track layers. For example, a missing railpad was set at S91 (see Figure 5.3 (e)), a missing sleeper bolt was set at S94 (see Figure 5.3 (f)), and fastening clamps (see Figure 5.3 (d)) were used at S92 and S96. Gaps between plywood were also present (see for example between S94 and S95 in Figure 5.3 (d)).

Three 1D accelerometers are placed on the wheel axle box to measure the ABA in three directions, as shown in Figure 5.3 (c). Vertical ABA is used in this work to assess
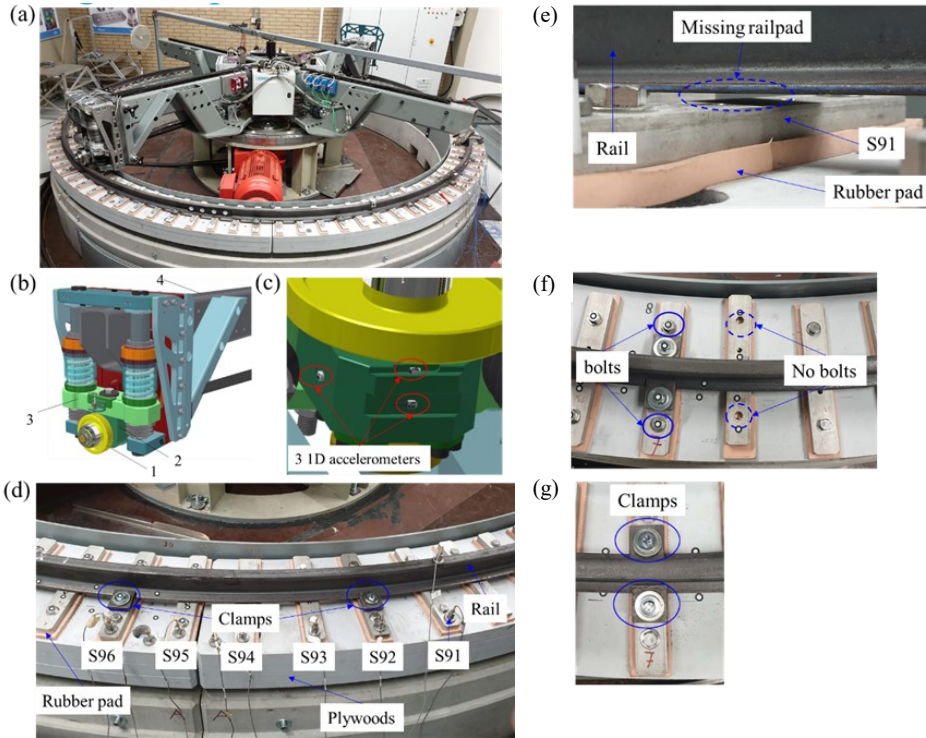
Figure 5.3: V-Track and experimental setup for ABA measurement. (a) V-Track test rig; (b) structure of wheel assembly: 1) wheel, 2) axle box, 3) guiding block, 4) steel frame; (c) accelerometers for ABA measurement; (d) track structure overview for a section of V-track; (e) missing railpad at S91;(f) missing sleeper bolts at S94;(g) top view of fastening clamps.

track stiffness. The sampling frequency of the ABA signals is 100 kHz. When recording the ABA, the running speed of the wheel assembly on the ring track was 13 km/h (equivalent to 65 km/h in real tracks) [177]. The wheel preload was 4500 N.

5.3.4. ABA feature: local wavelet power spectrum (LWPS)

To achieve the goal of evaluating track stiffness at multiple layers and sleeper spacing resolution, we propose a local frequency domain representation of ABA, i.e., a local wavelet power spectrum (LWPS) based on the synchro-squeezed wavelet transform (SSWT) [124].

SSWT is a time-frequency analysis method that can identify oscillatory components with time-varying frequency and amplitude. SSWT is robust to bounded perturbations of the signals and to Gaussian white noise, which is inevitable in numerous engineering measurement signals. Compared to other time-frequency transforms, such as continuous wavelet transform (CWT) and short-time Fourier transform (STFT), SSWT can compensate for the spreading in time and frequency by applying a post-processing "reassignment" map. This "reassignment" map focuses the spectrogram's energy toward

the instantaneous frequency curves and results in a sharpened time-frequency representation. In this sense, the SSWT is a more sparse representation than CWT. We use the 'wsst' function in MATLAB's wavelet toolbox to calculate the SSWT. Detailed algorithms can be found in [179, 180].

Figure 5.4 (b) and (c) compare the wavelet power spectrum (WPS) of CWT and SSWT of the same ABA signal (5.4 (a)). It can be seen that this ABA signal has three major frequency components below 2000 Hz, 100-200 Hz, 500-620 Hz, and 950-1200 Hz, respectively, indicated by the dashed pink lines. However, compared to more smearing and distortion in the CWT spectrum, the time-varying frequency components are more clearly distinguished in the SSWT spectrum.
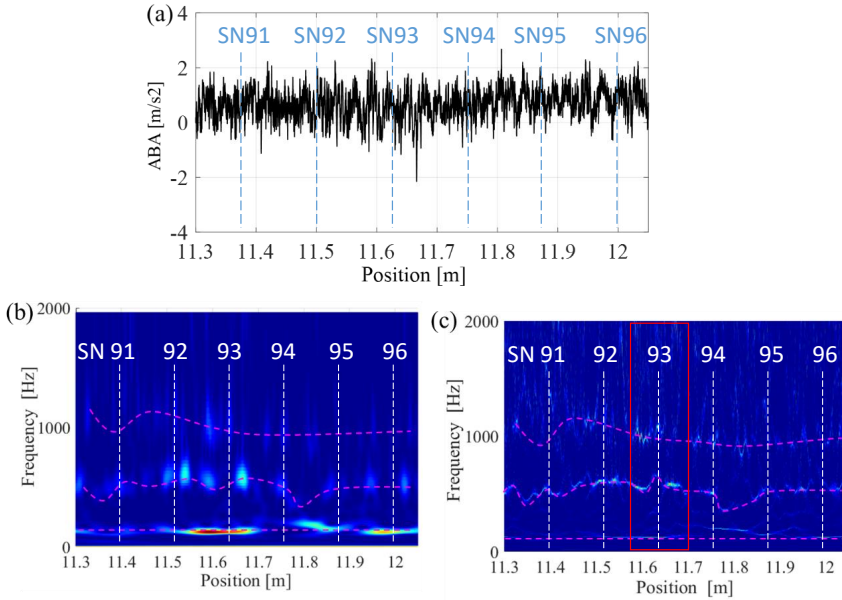
Figure 5.4: Time domain ABA signal (a) and its WPS calculated with CWT (b) and SSWT (c). The dashed pink lines indicate major frequency components. The vertical dashed lines indicate the position of sleeper numbers (S91 ~ S96). The red rectangle represents a vertical sliced window that is used to calculate the LWPS.

We hypothesize that the time-varying WPS features shown in Figure 5.4 are related to the stiffness variations along the track. To obtain the frequency components of ABA at a local position, we take a window through the WPS, as indicated with the red rectangle in Figure 5.4 (c). Subsequently, we can calculate the LWPS as the wavelet power averaged over the windowed position, that is

$$\bar{W}_n^2(\omega) = \frac{1}{n_a} \sum_{n=r_1}^{n_2} |W_n(\omega)|^2 \tag{5.6}$$

where $|W_n(\omega)|^2$ is the wavelet power obtained by the SSWT at the position indexed n and frequency ω. n_1 and n_2 are the starting and ending index of the sliced window, respectively, and the total number of positions within the window is $n_a = n_2 - n_1 + 1$. Figure

5.5 shows the LWPS measured at six sleeper positions (S91 ~ S96) in the frequency range of 100 Hz ~ 10000 Hz. Five major frequency components are found and indicated by the dashed pink circles. We also observe clear LWPS variations between different sleepers, which can be used to evaluate spatial track stiffness variations.
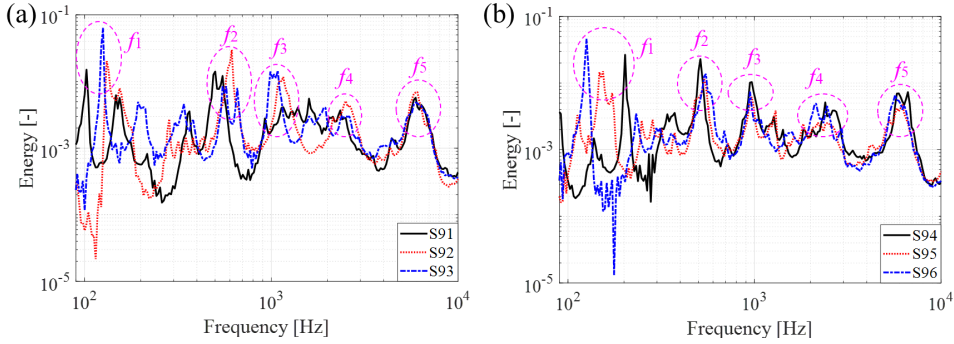
Figure 5.5: Examples of LWPS of ABA at different sleepers: (a) S91 ~ S93; (b) S94 ~ S96. The dashed pink circles indicated five major characteristic frequencies f_1 ~ f_5.

5.4. PHYSICS-BASED VEHICLE TRACK INTERACTION MODEL

5.4.1. VEHICLE-TRACK INTERACTION MODEL

To model the V-track system described in section 5.3.3, a two-layer discretely supported VTI model is developed using the finite element method, as shown in Figure 5.6. The rail and sleepers are meshed with Timoshenko beam elements [181]. The element has two nodes and four degrees of freedom. At each node, only the vertical and in-plane rotational degrees of freedom are considered. Ballast and railpads are modelled as discrete spring-damper pairs. Note that we neglect other components in the fastening system, such as clamps, bolts, etc. This is a widely accepted simplification for railway track models. While clamps and bolts are not taken into account explicitly in the current model, their stiffness can be reflected in the railpad stiffness. For example, a loose bolt reduces clamp force, which further reduces railpad stiffness. The track length is 3.14 m, which is a quarter of the length of the test ring, consisting of 25 sleeper spans. The wheel is simplified as a rigid mass. The load from the suspension springs is applied as the vertical load on the wheel. The wheel-rail contact is modelled as a Hertzian spring, with the contact force calculated as

$$F(x) = \begin{cases} C_H \left(Z_w(x) - Z_r(x) - Z_{irr}(x) \right)^{3/2} & \text{if } Z_w(x) - Z_r(x) - Z_{irr}(x) < 0 \\ 0 & \text{if } Z_w(x) - Z_r(x) - Z_{irr}(x) \geq 0 \end{cases} \tag{5.7}$$

where $Z_w(x), Z_r(x), Z_{irr}(x)$ are the vertical coordinates of the wheel, rail, and defect geometry, respectively, and C_H is the Hertzian coefficient and can be approximated as

$$C_H = \frac{2ER^{1/2}}{3\left(1 - v^2\right)} \tag{5.8}$$

where E and ν are Young's modulus and Poisson ratio of wheel and rail (assumed equal for both materials), and R is the radius of the railhead in the lateral direction.
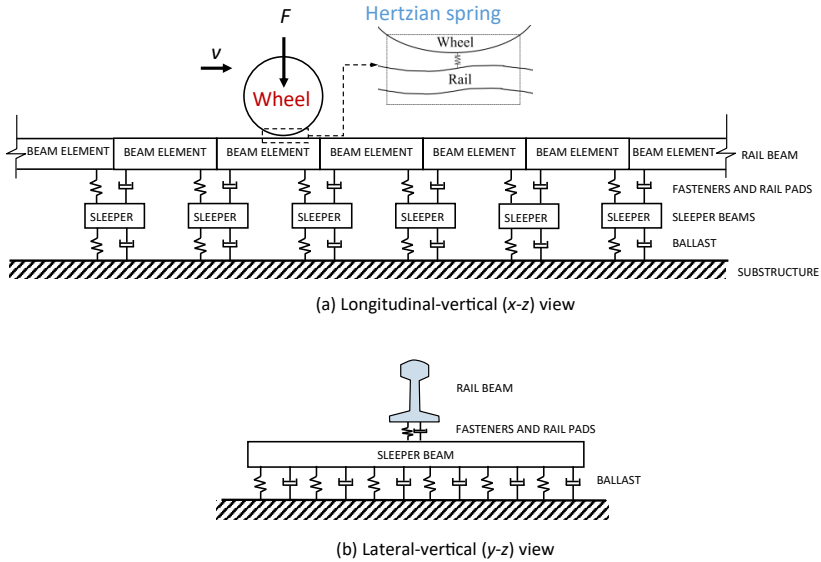

(a) Longitudinal-vertical (x-z) view

(b) Lateral-vertical (y-z) view

Figure 5.6: FE vehicle-track interaction model.

5.4.2. PARAMETER SPACE

We consider a parameter space K that includes six uncertain track parameters, namely the railpad stiffness, railpad damping, ballast stiffness, ballast damping, sleeper bending stiffness (EI) and track irregularity level. The value ranges are defined based on the nominal/design values of the track components, as well as parameter values that represent potential component degradations. For example, the lower bound of the railpad stiffness is 10 MN/m, which is much lower than the design value. This is to account for the possibility of stiffness loss due to, e.g., a lost railpad (see Figure 5.3 (e)). Furthermore, to account for the effect of sleeper bolts (see Figure 5.3 (f)), the upper bound of sleeper bending stiffness is increased to approximately three times its design value. The other track parameters are held constant based on their design/nominal values. The track parameters and their values ranges used for the VTI model are listed in Table 5.1.

Besides track parameters, different track irregularities $Z_{irr}(x)$ are also considered in the simulations. The simulated track irregularities are generated as random variables following a PSD function [182] in the form of

$$S(\Omega) = kA_{irr}\frac{\Omega_c^2}{\left(\Omega^2 + \Omega_c^2\right)\Omega^2} \tag{5.9}$$

where $k = 0.25, \Omega_c = 0.8242[\text{rad/m}]$. The PSD amplitude is controlled by the coefficient A_{irr}. The value range of A_{irr} is determined by calibrating the simulated PSD with a measured PSD, as shown in Figure 5.7. The measured PSD is based on the track irregularity

Table 5.1: Parameters and value ranges used in simulations.

Parameter	Design value			Value range
	Scaled track	Real track	Scale factor	
Railpad				
Stiffness, K_p (MN/m)	100-312	500-1560	1/5	10-300
Damping, C_p (kN·s/m)	1.2-2.7	30-68	1/25	4-9
Ballast (rubber, half-track)				
Stiffness, K_b (MN/m)	8-14	40-70	1/5	4-22
Damping, C_b (kN·s/m)	0.4-1.3	10-32	1/25	0.4-1.3
Sleeper (steel, half-track)				
Spacing, L_s (m)	0.12-0.13	0.60-0.65	1/5	0.125
Weight, m_s (kg)	1-1.36	120-170	1/125	1.12
Length (m)	0.24	-	-	0.24
Density, ρ_S (kg/m^3)	7800	-	-	7800
Cross section area, A_S (m^2)	6.00E-04	-	-	6.00E-04
Young's modulus, E_S (GPa)	210	-	-	-
Cross section modulus, I_S (m^4)	1.12E-08	-	-	-
EI_S (N·m^2)	2362.5	-	-	3543-7086
Rail (Steel, S7 profile)				
Density, ρ_R (kg/m^3)	7800	-	-	7800
Cross section area, A_R (m^2)	8.65E-04	-	-	8.65E-04
Young's modulus, E_R (GPa)	210	-	-	210
Cross section modulus, I_S (m^4)	5.15E-07	-	-	5.15E-07
Track irregularity level, A_{irr}	-	-	-	1-5
Wheel				
Radius, m	0.065	-	1/5	0.065
Weight, kg	44	-	-	44
Wheel load, N	4500	-	-	4500
Speed, km/h	13	65	1/5	13

measured in the V-track between S91 and S95. For the convenience of interpretation, we normalize A_{irr} between 1 and 5 to represent different track irregularity levels, with 5 being the worst. It should be noted that the simulated PSDs do not perfectly match the measured one. Simulated PSD tends to overestimate track irregularity below about 300 Hz while underestimating it between 300 and 3000 Hz.

5.4.3. Validation of the VTI model

With the parameter space and value ranges defined in Table 5.1, we use the Sobol sequence sampling technique [183] to obtain 10000 sets of space-filling input parameters for the VTI model. In this section, we compare the simulated and measured FRF and ABA to ensure that the parameter space and value ranges are well-defined and that the
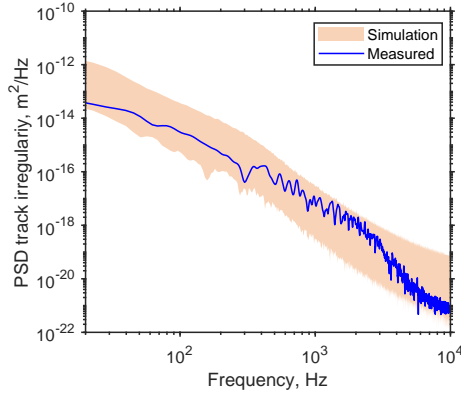
Figure 5.7: Comparison of measured and simulated track irregularities. The frequency is calculated based on the measurement speed of 13 km/h.

numerical model adequately captures the primary dynamic characteristics of the wheel-track system.

We first compare the simulated and measured FRFs for the V-track system, as shown in Figure 5.8. Hammer tests were used to obtain the FRFs at 46 locations along the V-track (23 at mid-span and 23 above sleepers). To eliminate the effect of boundary conditions, hammer tests were simulated at the center of the tack model. In general, the simulation and measurement agree well for the FRFs above a sleeper (Figure 5.8 (a)) and at mid-span (Figure 5.8 (b)). FRF peaks correspond to track resonances (see sections 2.3 and 4.3). Measured FRFs reveal four peaks at approximately 300 Hz, 1000 Hz, 3000 Hz and 6000 Hz. We used modal analysis on both the rail and the sleepers to determine the mode shapes at these frequencies. According to the modal analysis results, the four frequencies correspond to the full-track (FT), sleeper 1st bending (S1), clamp 2nd pinned-pinned (c2PP), and pin-pin (PP) resonances, respectively. The c2PP resonance is caused by the special constraint of fastening clamps in V-Track, which are used every three or four sleepers to vary the track stiffness, as shown in Figure 5.3. As a result, it is unique to the V-track system. Simulated FRFs can reproduce the FT, S1, and PP resonances, but not the c2PP resonance, because the FE model does not account for stiffness variations along the track. However, simulated FRFs show a peak representing the sleeper 3rd bending mode (S3) near the c2PP resonance (around 3000 Hz). The simulated PP resonance frequency is lower than the measured frequency. This could be because the Timoshenko beam element is incapable of modelling the S7 rail profile adequately at such a high frequency of around 6000 Hz. Another possible explanation is that the modelling of the fastening system was simplified to point support, instead of over the length of sleeper support.

To demonstrate the capability of the V-track system in representing real track systems, we scale the measured FRFs on the V-track according to the scaling law and compare them to a typical track FRF in the Dutch rail network (from [153] and also shown in Figure 4.3), as shown in Figure 5.8 (c) and (d). The V-track system reproduces the

general trend of FRF magnitudes measured above sleeper support (Figure 5.8 (c)). Deviations between the FRF magnitudes of the V-track and real track are observed above about 300 Hz for FRFs measured at mid-span (Figure 5.8 (d)). In terms of track resonances, FT and PP can be found at similar frequencies for both tracks. Major differences exist for the sleeper bending modes (S1~S3). This is primarily due to the use of a half-track (-sleeper) set up in the V-track. For example, the S1 resonance is not visible in the FRFs of the real track because the sleeper vibrates with nodes on rail seats (Figure 5.8 (e)). The same explanation applies to S2, which is absent from the FRFs of the V-track (Figure 5.8 (f)).
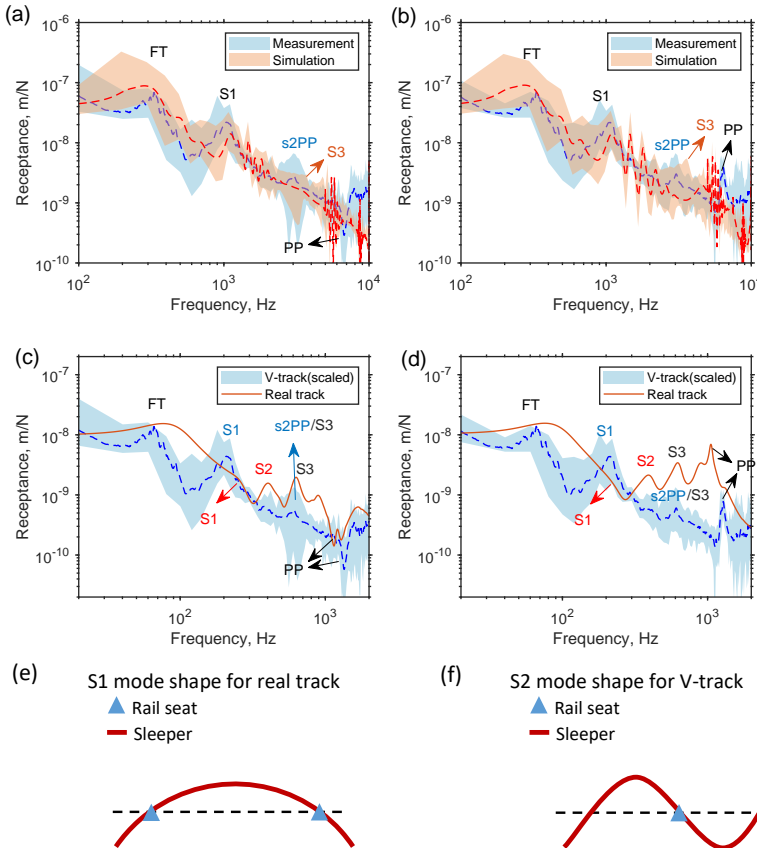
Figure 5.8: Validation of the FE model based on FRF. The left and right columns show the rail's point receptances above sleeper support and at mid-span, respectively. (a) and (b) compare the measured and simulated receptances of the V-track. The dashed lines are the mean receptances and the shaded areas are the envelopes. (c) and (d) compare the measured receptances of the V-track to those of a real track system (from [153] and also shown in Figure 4.3. The receptances of the V-track are scaled by 1/5 in both frequency and magnitude. For easier comparison, the axes in (c) and (d) are also scaled by 1/5 compared to (a) and (b). (e) and (f) show the first and second sleeper bending modes for the real track and V-track, respectively.

Figure 5.9 shows the comparison of the measured and simulated LWPS of ABA. As

can be seen, the simulations reproduce the first four characteristic frequencies ($f_1 \sim f_4$) relatively well when compared to the measurements. At f_5, the measured magnitude of the LWPS is greater than that predicted by simulations. Again, this could be attributed to the inaccurate high-frequency performance of the Timoshenko beam element or the simplified fastening system models.
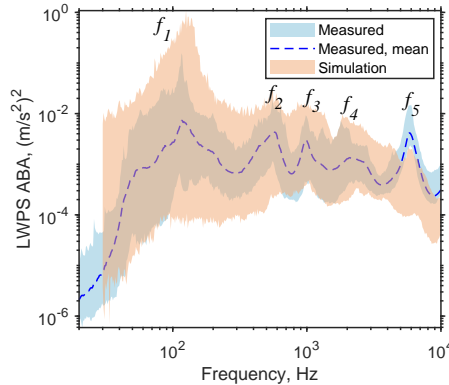
Figure 5.9: Validation of the FE model based on ABA measurement. The measured LWPS shown in the figure includes the measurements for all the 100 sleepers in the V-track.

5.4.4. SENSITIVITY ANALYSIS

Figure 5.10 shows the sensitivity of the LWPS to different track parameters based on the 10000 simulation cases. The value range of each track parameter is divided into five sub-ranges, as illustrated in the legend. Each curve represents the average LWPS of all the simulation cases with the corresponding parameter value that falls within the specified sub-range. The LWPS is overall more sensitive to the ballast stiffness (Figure 5.10 (c)) and track irregularity (Figure 5.10 (d)). The sensitivity of LWPS to the railpad stiffness is non-linear(Figure 5.10 (b)). It is sensitive to the railpad stiffness only when it is low (less than 100 MN/m in the V-track, equivalent to 500 MN/m in a real track), and becomes less sensitive as the railpad stiffness increases. A similar nonlinear relationship has been observed in Figure 4.6 (b) for the track FRF. This may result in a greater degree of uncertainty when evaluating railpad stiffness variations for stiff railpads.

Each track parameter depicted in Figure 5.10 corresponds to a unique characteristic of the LWPS. Variations in ballast stiffness result in changes in the magnitude and characteristic frequencies of the LWPS below approximately 1000 Hz. In a wide frequency range, the track irregularity level has the greatest influence on the LWPS magnitude. Even though the sleeper bending stiffness and railpad stiffness have overlapping frequency ranges, the former is more related to the change of characteristic frequencies, whereas the latter is more related to the change of LWPS magnitude. These distinct characteristics imply that LWPS can be used to evaluate track stiffness at multiple layers concurrently.
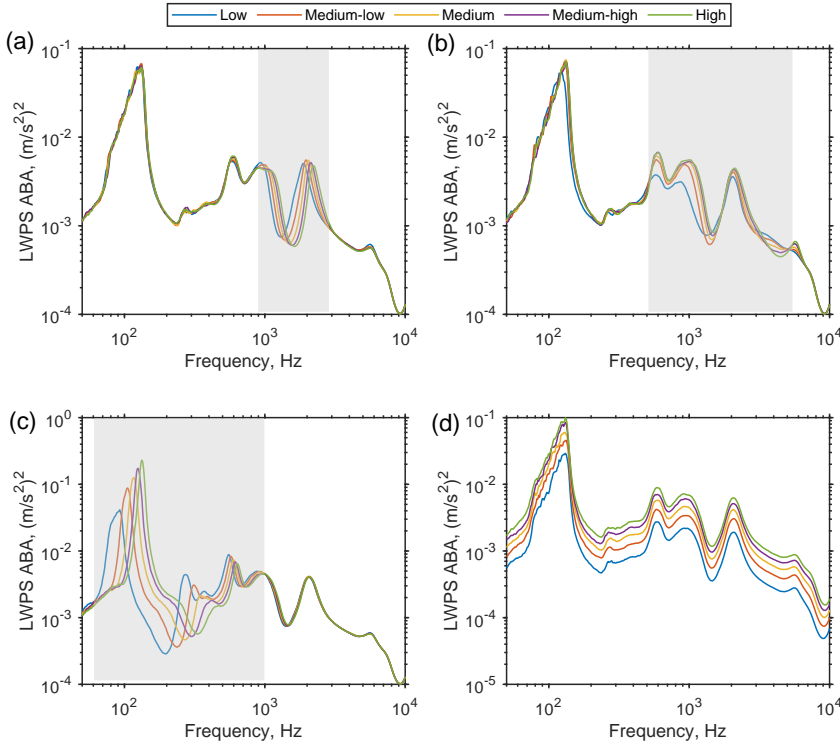
Figure 5.10: Sensitivity of LWPS to the change of track parameters. (a) Sleeper bending stiffness; (b) railpad stiffness; (c) ballast stiffness; (d) track irregularity level.

5.5. DATA-DRIVEN MODEL LIBRARY

In this section, we demonstrate the implementation and performance of the data-driven models.

5.5.1. MODEL SELECTION VIA FEATURE MATCHING

5.5.1.1. FEATURE DEFINITION

To implement the model selection algorithm in section 5.3.2.3, we first define the feature vectors. Based on the sensitivity analysis shown in Figure 5.10, we propose using the LWPS in different frequency ranges as feature vectors

$$\mathbf{x} = \left\{ w_1 \log\left(\bar{W}_n^2(\omega_1)\right), w_2 \log\left(\bar{W}_n^2(\omega_2)\right), \ldots, w_N \log\left(\bar{W}_n^2(\omega_N)\right) \right\}^T$$

$$\left\{ \begin{array}{ll} \mathbf{x}^{GF} : \text{for} & \omega_i \in [50, 4000] \\ \mathbf{x}^{LF1} : \text{for} & \omega_i \in [50, 200] \\ \mathbf{x}^{LF2} : \text{for} & \omega_i \in [400, 700] \\ \mathbf{x}^{LF3} : \text{for} & \omega_i \in [800, 1500] \\ \mathbf{x}^{LF4} : \text{for} & \omega_i \in [1500, 4000] \end{array} \right\} w_i = 1, \text{ otherwise }, w_i = 0 \tag{5.10}$$

where ω_i is the frequency point in Hz, $\bar{W}_n^2(\omega_i)$ is the LWPS at ω_i, and w_i is a binary weighting factor for $\bar{W}_n^2(\omega_i)$. In particular, a global feature (GF) vector is defined as the log magnitude of LWPS between 50 Hz and 4000 Hz. The LWPS above 4000 Hz is excluded because the overall agreement between measured and simulated LWPS deviates in that frequency range (Figure 5.9). Furthermore, four local feature (LF1~LF4) vectors are defined in four local frequency ranges approximately centered on the first four characteristic frequencies of the LWPS. This is because the stiffness of a particular track layer is only affected by certain local characteristics (Figure 5.10). Including irrelevant features can sometimes degrade the performance of data-driven models.

5.5.1.2. Performance analysis

Figure 5.11 shows comparisons of the top ten matches selected from the model library and the measured LWPS. Each row corresponds to a feature vector defined in Eq. 5.10 and each column corresponds to a sleeper (S91~S95). Though measured LWPS varies between sleepers, the model selection algorithm can consistently match the measured LWPS. When the GF is used for the model selection (first row), the largest discrepancies are observed below approximately 400 Hz: the LWPS selected from the model library exhibit larger magnitudes than the measurement. This could be because the track irregularities used in the simulations have a magnitude greater than the measured ones below approximately 400 Hz (Figure 5.7). Such discrepancies can be reduced by selecting models using LF1 rather than GF (see the second row in Figure 5.11). While this results in a more accurate local match, it does not guarantee a good match for the rest frequencies of the LWPS.

We use the mean absolute percentage error (MAPE) to quantify the differences between the simulated and the measured ABA features, defined as

$$MAPE = \frac{1}{N} \sum_{k=1}^{N} \left| \frac{\hat{x}_k - x_k}{\hat{x}_k} \right| \tag{5.11}$$

where $\hat{x}_k$ and $x_k (k = 1, 2, \dots N)$ are the elements of the measured and simulated feature vectors (see Eq. 5.10), respectively. N is the length of the feature vector.

For each ABA feature, MAPEs are calculated for the top ten matches at each sleeper in the V-track; the results are shown in Figure 5.12. When the GF is used to select models, the MAPEs between the best-matching models and the measurements are approximately 4% to 6%. Low-frequency local features are more difficult to match than high-frequency local features. MAPEs are also seen to increase significantly at rail joints (indicated by the vertical grey lines). Because rail joints are not taken into account in the VTI model, the model library is less capable of matching the LWPS caused by the local vehicle-joint interaction.

As the number of top matching models increases, the MAPEs increase as well, as shown in Figure 5.12 (b). However, when the GF is used for model selection, the largest MAPE is still less than 20%. This indicates that the model library as a whole is capable of accurately representing the actual physical system. This is because we have already incorporated a significant amount of prior information into the model library during its construction. These pieces of information include our prior knowledge of the track parameters' design values, as well as the physics of the vehicle track system encoded in the VTI model.
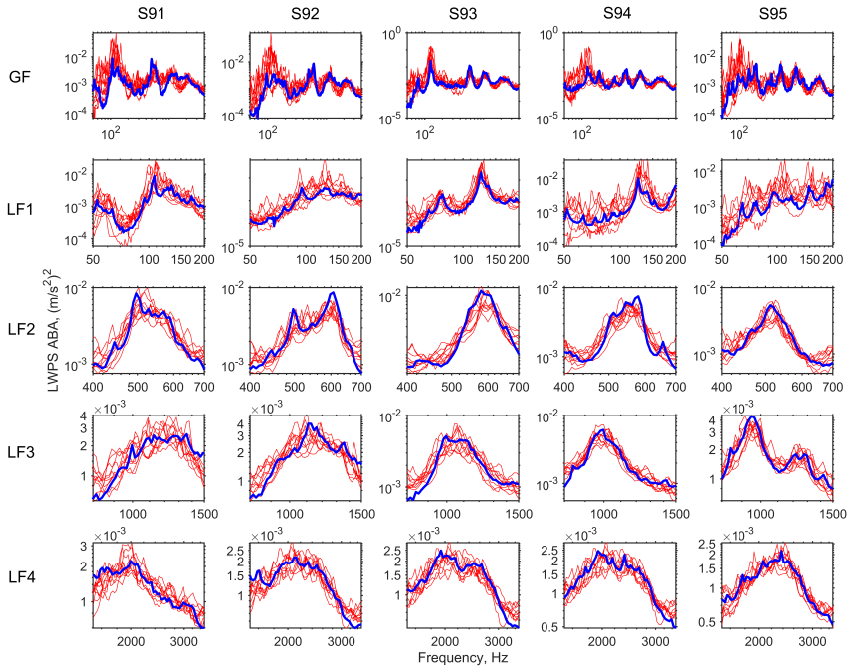
Figure 5.11: Examples of the measured ABA LWPS (blue line) compared to their top ten matches selected from the model library (red lines). Each row shows the models selected based on a feature vector. Each column shows the LPWS for a sleeper.
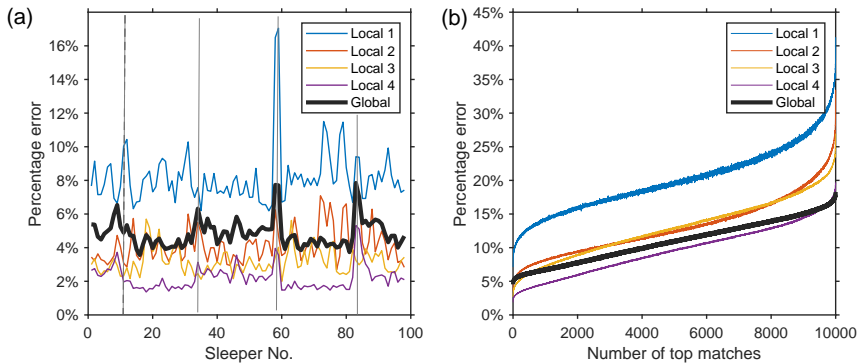

Figure 5.12: Performance of the model selection algorithm in matching the measured ABA features. Vertical grey lines indicate the location of rail joints. (a) Averaged MAPEs of the top ten matches at each sleeper. (b) Relationships between the MAPE and the number of top matches included in the calculations.

5.5.2. MODEL REGRESSION VIA GAUSSIAN PROCESS

5.5.2.1. GP MODEL TRAINING

We have in total five feature vectors $\mathbf{x}^{(p)}$, $p = \mathrm{GF}, \mathrm{LF1}, \mathrm{LF2}, \mathrm{LF3}, \mathrm{LF4}$ and four track parameters of interest $k^{(q)}$, $q = 1, 2, 3, 4$. The four track parameters are ballast stiffness (k_b), railpad stiffness (k_p), sleeper bending stiffness (EI_S), and track irregularity level (A_{irr}). For each combination of a feature vector and a track parameter, we create a data set $D(p, q) = \left\{ \mathbf{x}_i^{(p)}, k_i^{(q)}, i = 1, 2, \ldots, N \right\}$. The data set $D(p, q)$ with size $N = 10000$ is randomly divided into two sets, each with 5000 samples. We use one as the training set and the other for testing. Five-fold validation was used during the training process to prevent overfitting.

Trained GP models are denoted as $g^{(p,q)}$ and the test set is denoted as $\tilde{D}(p, q) = \left\{ \tilde{\mathbf{x}}_i^{(p)}, \tilde{k}_i^{(q)}, i = 1, 2, \ldots, 5000 \right\}$. We employ trained GP models to predict the track parameter values in the test set given the corresponding feature vectors, i.e., $\tilde{k}_i^{(q)*} = g^{(p,q)} \left(\tilde{\mathbf{x}}_i^{(p)} \right), i = 1, 2, \ldots, 5000$.

5.5.2.2. PERFORMANCE ANALYSIS

The performance of the GP model on the test set is evaluated using the mean absolute scaled error (MASE), which is the mean absolute error of the predicted values of a parameter, divided by the value range of the parameter, that is

$$\mathrm{MASE} = \frac{1}{N} \sum_{i=1}^{N} \left| \frac{\tilde{k}_i^{(q)} - \tilde{k}_i^{(q)*}}{\max\left(\tilde{k}^{(q)}\right) - \min\left(\tilde{k}^{(q)}\right)} \right| \tag{5.12}$$

The MASE is useful for comparing the GP model performance across parameters with different scales. The MASEs for the four track parameters are shown in the first row of Figure 5.13. The track irregularity level can be accurately predicted with less than 5% MASE. Even when only the local features are considered, the MASE is still less than 10%. The ballast stiffness can also be predicted with high accuracy using the GF or LF1 (around 5% MASE). The MASEs for the predictions of the sleeper bending stiffness using LF3, LF4 and GF are approximately 10%, while those for the railpad are about 15%. This means that for the railpad stiffness with the value range of about 300 MN/m considered in this chapter, the expectation of the absolute error of a prediction is approximately 45 MN/m.

It is also worth noting that the feature vectors with relatively low prediction errors for each track parameter correspond well to the sensitive features for that track parameter shown in Figure 5.10. This means that the GP model inferred the correct physics underlying the evaluations from the data. When evaluating ballast stiffness, for instance, the GP model automatically weights more on LF1, which is consistent with the sensitivity analysis. To summarize, the GF outperforms LFs for all four track parameters. Certain LFs can produce similar MASE levels as the GF for a particular track parameter because they are sensitive to the change of that track parameter.

The second row shows scatter plots of the true and predicted values for each track parameter calculated with the global feature (GF). As can be seen, prediction errors are smaller when the railpad stiffness is low and increase as the railpad stiffness increases.

This is because the ABA features become less sensitive to high railpad stiffness values (Figure 5.10). The prediction errors for the remaining three track parameters are fairly constant across the value ranges.
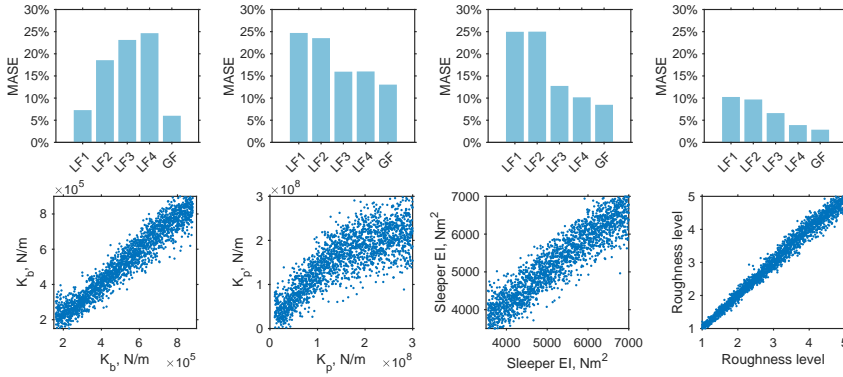

Figure 5.13: Performance of the GP models on the test dataset. The four columns correspond to four track parameters, namely ballast stiffness (K_b), railpad stiffness (K_p), sleeper bending stiffness (EI_S), and track irregularity level (A_{irr}). The first row shows the MASEs of the predictions made by the GP models with various feature vectors. The second row shows the scatter plots of the true and predicted values obtained using the global feature (GF).

5.6. CASE STUDY

In this section, we apply the proposed method to evaluate the track stiffness of the V-track using measured ABA and compare the results of the two proposed data-driven models. Additionally, we compare the evaluation results to observed track structure variations and to those obtained using the hammer test method developed in Chapter 4.

5.6.1. COMPARISON OF THE MODEL SELECTOR AND GP MODEL

Figure 5.14 shows the evaluation results obtained by the GP models and model selector. The general trends of the evaluations by the two methods are in good agreement. The entire test ring is comprised of four rail segments (Rail 1~4), which are connected via four rail joints (J1~J4), as illustrated in the first subplot of Figure 5.14. Rails 1 and 3 have a higher level of track irregularity and railpad stiffness than rails 2 and 4. Additionally, there is a local increase in the level of track irregularity at rail joints. These increases at J3 and J4 are greater than at J1 and J2, implying that J3 and J4 are in worse conditions, which has been confirmed by visual inspection. The sleeper bending stiffness (EI_S) fluctuates around 5000 N·m² which is more than twice the nominal value (2300 N·m²). This reflects the effect of the sleeper bolts used in the V-track, which constrain the sleeper bending movement (see Figure 5.3 (f)) but are not considered in the VTI model. Furthermore, as shown in the right column, the degree of evaluation uncertainty for all parameters increases significantly at four rail joints, indicating larger modelling errors. This is because rail joints are not taken into account in the VTI model.

We do not have a direct measurement to verify that the irregularity level and railpad
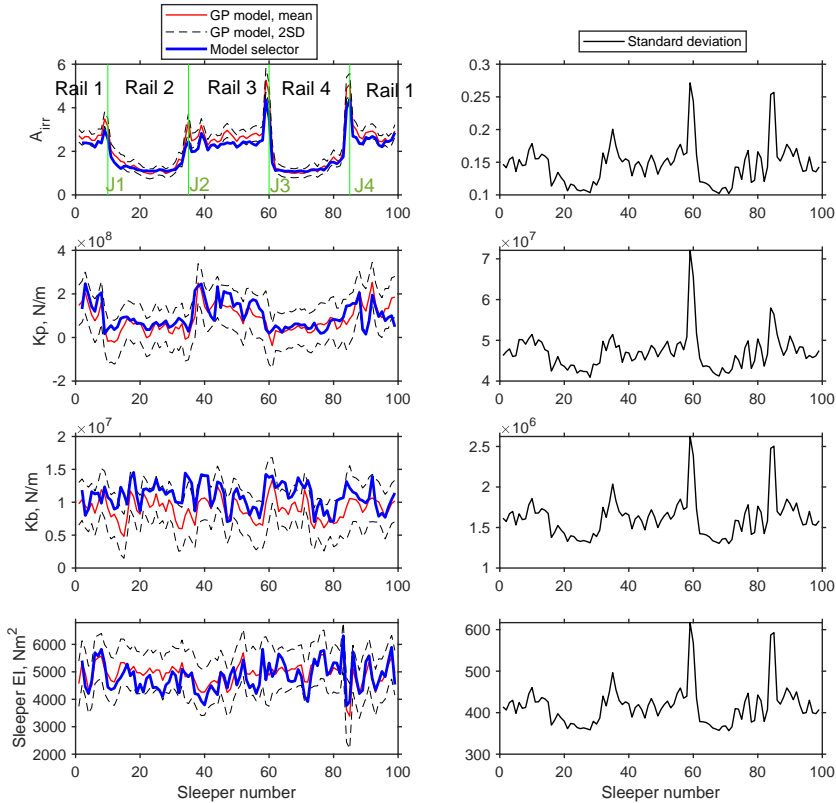
Figure 5.14: Track irregularity level (first row) and stiffness variations (second to fourth rows) of the V-track. The left column shows the comparisons of the GP models and the model selector. The results of the model selector represent the averaged values of the top ten matches. The vertical green lines indicate the position of rail joints. To demonstrate more clearly the prediction uncertainty, the right column shows the standard deviations of the evaluations at each sleeper.

stiffness are higher at Rails 1 and 3, as observed in Figure 5.14. We can however justify this by comparing the LWPS measured at different rail segments, as shown in Figure 5.15. The LWPS magnitudes are larger for Rails 1 and 3 than those for rails 2 and 4, most notably between f_2 and f_4 (700 Hz~4000 Hz). According to the sensitivity analysis shown in Figure 5.10, a local magnitude change at f_2 and f_3 indicates railpad stiffness variation, while a magnitude change in a wider frequency range indicates variation in the track irregularity level. This explains why our data-driven models predict higher irregularity levels and railpad stiffness at Rails 1 and 3. It is also noted that the magnitude differences are not evenly distributed, with larger differences between approximately 700 and 4000 Hz. This could be due to the unevenly distributed PSD for the track irregularity as shown in Figure 5.7. The track irregularity was measured on Rail 1 (between S91 and S96), which has a higher PSD magnitude between 400 Hz and 4000 Hz, in overlap with the frequency

range where large LWPS differences exist. It then can be postulated that because Rail 1 and 3 have larger railpad stiffness than Rails 2 and 4, probably due to installation, track irregularities first emerged and developed on Rails 1 and 3 between approximately 0.9 mm ~ 9 mm (calculated based on 400 Hz ~ 4000 Hz with the speed of 13 km/h).
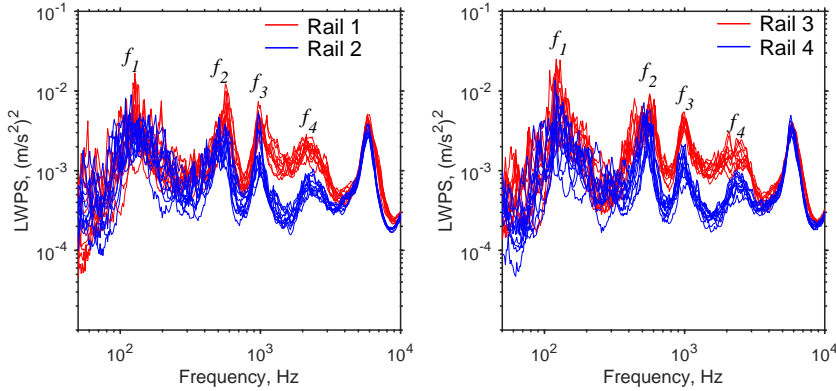
Figure 5.15: Comparisons of LWPS measured at different rail segments.

5.6.2. COMPARISON WITH OBSERVED TRACK STRUCTURE VARIATIONS

To further verify the evaluation results, we compare the track stiffness variations with track structure variations observed in the V-track. The rail is periodically clamped to sleepers in the V-track, see Figure 5.3 (d) for an example. Such periodicity in the track structure is well reflected by the local peaks in the railpad stiffness variations evaluated using the proposed method, as can be seen from the upper plot in Figure 5.16. The green triangles denote clamp positions that correspond to local peaks.

Another type of track structure variation considered here is the gap between the plywood in the substructure, as illustrated in the lower plot of Figure 5.16. Even though the substructure is not modelled in the VTI model, such changes can still be captured as ballast stiffness variations. Note that the blue curves shown in the lower plot of Figure 5.16 represent the moving averaged ballast stiffness with a window of 10 sleeper spans. It can be seen that the gap positions correspond well to the locations of local ballast stiffness changes.

5.6.3. COMPARISON OF THE EVALUATIONS BY ABA AND FRF

We also compare the track stiffness evaluated by ABA with those by hammer tests (see Chapter 4). The track FRFs were measured by hammer tests over three track segments, denoted as HT1, HT2 and HT3. The comparisons are shown in Figure 5.17.

The railpad stiffness evaluated by the two methods follows similar trends in each segment. The clamps at sleeper numbers 4, 76, 92 and 96 can be captured by both methods as the local peaks in stiffness variations. The local peaks may not exactly correspond to the clamp locations. For example, the railpad stiffness evaluated by the ABA and FRF shows local peaks at S3 and S97, respectively, with a shift of one sleeper relative to the
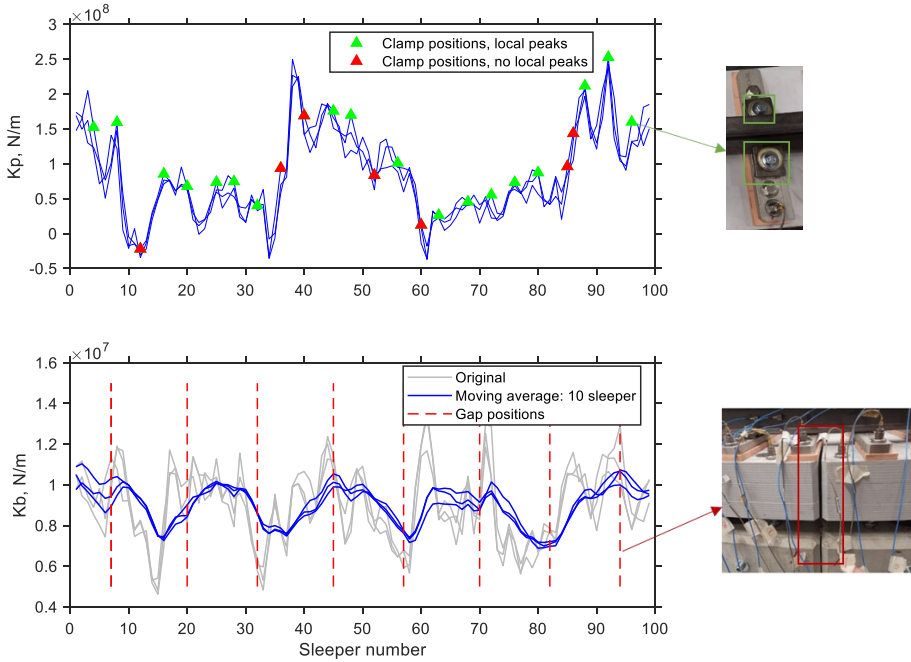
Figure 5.16: Correlations between track stiffness variations and structural changes in the V-track. The upper plot shows the correlation between the clamp positions and the local peaks of the evaluated railpad stiffness. The lower plot shows the correlation between the gap positions and variations in ballast stiffness. The results of three repeated measurements are shown in both plots.

clamp position. A large local dip is also observed at S90 for the railpad stiffness evaluated by the ABA, which should correspond to a missing railpad observed at S91 (Figure 5.3 (e)), also with a one-sleeper shift. The reason for the shift could be that the adopted track model assumes uniform track stiffness and thus does not consider very local stiffness variations. Therefore, the track stiffness evaluated by the proposed method represents the averaged stiffness values within a few sleeper spans, and thus may not always detect the precise locations with very local stiffness changes.

Additionally, the railpad stiffness values evaluated by the ABA are higher at HT1 and HT3 compared to those evaluated by the FRF. This is because the loading conditions for the two methods are different. As the rail is not fastened to each sleeper, the rail and sleepers may not come into direct contact under unloaded conditions. For the hammer test, the hammer loads are relatively small and thus cannot close any possible gaps between track layers. This leads to lower stiffness evaluations, as shown for HT1 and HT3. In contrast, when the track is loaded, the large wheel loads enable firm contact between the various track layers, resulting in increased track stiffness where there are greater structural differences between loaded and unloaded conditions. In this regard, the evaluation of track stiffness using ABA is more accurate than using the hammer test, because it represents the actual loaded condition.

The ballast stiffness evaluated by the two methods agrees well. Both methods predict a large stiffness change between S94 and S95 as a result of the gaps in the substructure, as discussed in section 5.6.2. Additionally, the FRF-based method shows local peaks at the clamp locations S4, S76, S92 and S96(97) in the ballast stiffness variations, despite clamps being in the fastening system. This means that the effect of fastening stiffness on the ballast layer is difficult to be separated by hammer test. The ABA-based method, on the other hand, does not show such changes. This again could be attributed to the different loading conditions. Under loaded conditions, the wheel load is much greater than the clamping force. As a result, the stiffness differences between clamped and unclamped conditions are not significant enough to make difference in the ballast layer. This demonstrates that the ABA is more capable of discriminating track stiffness between different layers under loaded conditions.
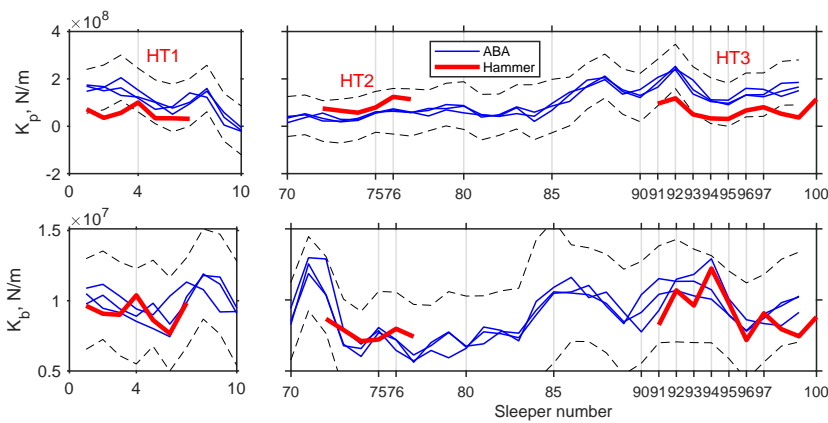
Figure 5.17: Comparisons of track stiffness evaluations by ABA and FRF. The FRFs are obtained by hammer tests at three track segments HT1 (S1~S7), HT2 (S72~S77) and HT3 (S91~S100). First row: railpad stiffness; second row: ballast stiffness.

5.6.4. TIME EFFICIENCY

The GP model is capable of performing rapid assessments of track stiffness. The evaluation time for a single sleeper span is 0.0093 s in the case study with an 8-core CPU (Intel Xeon E5-2687 W v2). This is calculated by dividing the total amount of time spent on evaluation by the number of sleeper spans. As previously demonstrated in section 4.4.4.3, inverting a covariance matrix is the most time-consuming step for a single evaluation. Once the inversed covariance matrix is available, the prediction procedure is almost instantaneous because it only requires simple matrix multiplications. In practice, the inversion is performed only once at the start of the procedure and is retained in memory for the duration of evaluations. As a result, the proposed approach easily scales to long track sections.

The SSWT procedure appears to be the bottleneck in applying the method to real-time applications. The SSWT was performed on a signal length of 3485 sampled points

for each sleeper in the current case, resulting in an average calculation time of 0.32 s. By comparison, halving the signal length to 1742 points reduces the calculation time to 0.15 s. This, however, may come at the expense of decreased precision.

5.7. Conclusions

We develop a digital twin framework to rapidly and reliably evaluate track stiffness at different track layers. The framework consists of a physics-based VTI model, a model library and two data-driven methods. The proposed framework is capable of evaluating the stiffness of multiple track layers simultaneously at sleeper spacing resolution.

We compare the proposed method to an FRF-based hammer test method, for evaluating the stiffness of three track sections over 23 sleepers on the V-track. The average values of the ballast and railpad stiffness evaluated by the two methods agree well, indicating the general validity of both methods. Additionally, the proposed method is more accurate than the hammer test method, because it represents the track stiffness in the operational loaded condition.

The controlled lab measurements and observations show that the developed method can evaluate the stiffness of the fastenings and ballast, as well as their variations in space. When ABA is regularly measured from tracks, the fastening and ballast stiffness and their changes in time can be assessed. This can provide a better understanding and prediction of track geometry changes in space and time, making efficient and effective track maintenance, which can be performed on the right components (fastening or ballast) at the right places and the optimal time, possible.

The proposed digital twin framework is highly scalable and computationally efficient. This is beneficial because a large amount of data will be generated due to the high sampling rate required for high-resolution evaluations. In the case study, we show that our method compresses 3485 data points of a time-domain ABA signal to a sparse four-element vector that is physically meaningful within approximately 0.33 seconds per sleeper span. Because of the simple and fast calculation process, it can be done on the edge of the infrastructure, such as an on-board computer, without the need to transfer a large amount of data to the cloud or operational centers.

6

CONCLUSIONS AND RECOMMENDATIONS

6.1. CONCLUSIONS

In this thesis, we propose, implement, and apply a physics-based digital twin approach for vibration-based railway track condition monitoring. The main findings are summarized in this section.

6.1.1. PROPOSED PHYSICS-BASED DIGITAL TWIN FRAMEWORK

The condition monitoring problem is framed as an inverse identification problem. The digital twin consists of a physics-based VTI model solving the forward problem and a data-driven GP model solving the inverse problem. Due to its predictive power, the physics-based VTI model is used to explore various possible states of its associated physical VTI system. This generates data for training the GP model that would otherwise not be available from measurement. On the other hand, the GP model is computationally efficient and suitable for online or near real-time condition monitoring. In addition, the GP model, as a non-parametric Bayesian model, inherently provides uncertainty quantifications for its predictions. Therefore, it automatically detects unreliable predictions by issuing large confidence intervals. This may indicate modelling errors or measurement noise.

6.1.2. IMPLEMENTATION

To implement the proposed digital twin framework, we establish a frequency feature map, develop and compare two VTI models, and implement an efficient data-driven pipeline.

A detailed frequency feature map is established for the vibrations of a VTI system between 50 Hz and 3000 Hz based on a comprehensive field measurement campaign using three different measurement techniques.

- A total of sixteen resonances of the track and VTI system are identified.

  – The track resonances (FT^U, S, R, and PP) are identified by the unloaded hammer test.

  – The VTI system resonances are identified by the loaded hammer test (FT^L, SA and RBW).

- These resonances are sequenced based on an underlying physical principle: track and VTI system resonances occur at the lower and upper bounding frequencies of propagating track waves, respectively.

- With the frequency feature map, peak frequencies identified by different measurement techniques are better understood by linking them to the corresponding resonances of the track or VTI system.

  – VTI system resonances differ from track resonances in three aspects. First, FT^L (100 Hz) occurs at a slightly higher frequency than FT^U (80 Hz) due to the increase of ballast stiffness caused by preloads. Second, between 300 Hz and 1000 Hz, the S resonances shift to SA resonances due to the constraints imposed by the added wheel mass at the loading point. Third, the double

wheelsets in a bogie lead to the RBW resonances. Consequently, the VTI system has six resonances (FT, 3SA, 2RBW) that are densely spaced below 1000 Hz.

– The track-side measurement can be divided into ambient and axle segments. They show different frequency features. Peak frequencies of the ambient segments correspond to the track resonances with the decay effect taken into account, while those of the axle segments correspond to the VTI system resonances.

– Peak frequencies of ABA are speed invariant and correspond well to VTI system resonances. The ABA is capable of detecting all six VTI system resonances below 1000 Hz, but not the R_1 and PP resonances.

• The sequence pattern of the resonances can serve as a key feature of a track or VTI system, and be used subsequently for evaluating model accuracy and monitoring track conditions.

Two commonly used VTI models, i.e., a low-fidelity beam and a high-fidelity continuum model, are developed and compared for simulating the wheel-rail impact at squats.

• Both models can reproduce three dominant frequencies at 340 Hz, 890 Hz and 1120 Hz in the contact force. The first two frequencies can be associated with two VTI system resonances on the frequency feature map. The third is unique to the wheel-rail impact problem.

• The beam model with a Hertzian contact spring overestimates the first peak of the impact force. The discrepancy can be reduced but not eliminated by using the Winkler bedding model.

• The local inertia in the contact patch and stress wave propagation in solids, which can be considered in the continuum but not in the beam model, are critical factors that have been overlooked in previous research.

– The different modelling of the stress wave propagation in the rail leads to a deviation of track damping around the pin-pin resonance. As a result, the beam model is only comparable to the continuum model up to about 800 Hz. Above 800 Hz, the contact forces dominate at 890 Hz for the beam while at 1120 Hz for the continuum model.

– By considering the local inertia in the contact patch and stress wave propagation in the continuum model, it is shown that the effective inertia of the rail that participates in the vibration of the wheel-track system comes first from the point of contact and then "gradually" expand as the waves spread out. While for the beam model, any vibration always involves the whole cross section, leading to larger inertia participating in the vibration at all times.

6.1.3. APPLICATIONS

A generic and practical data-driven pipeline for solving inverse identification problems is implemented. The proposed VTI digital twin approach is applied to two inverse identification problems, i.e., evaluating dynamic track stiffness in unloaded tracks by hammer tests (Chapter 4) and in loaded tracks by ABA (Chapter 5). It is demonstrated how the proposed digital twin approach enables robust, efficient and high-resolution track stiffness evaluations.

6.1.3.1. TRACK STIFFNESS EVALUATION BY HAMMER TEST

- In comparison to using two features of an FRF in conventional methods, our approach makes use of up to eleven frequency and magnitude features of an FRF for evaluating track stiffness by hammer tests.

- In real-life applications, extracting all the features from a measured FRF is not always possible, which will lead to incomplete measurements of FRF features.

- To deal with incomplete measurements, we train multiple candidate GPR models with different features, kernels and training sets. Predictions by the candidate models are fused using a weighted Product of Experts method that automatically filters out unreliable predictions.

- Including more features and fusing the predictions by different kernels are two effective ways to reduce prediction errors.

- The proposed method outperforms three other optimization-based methods both in terms of accuracy and time efficiency.

6.1.3.2. TRACK STIFFNESS EVALUATION BY ABA

- The proposed approach is robust to changing track irregularities because we select distinct frequency features for track stiffness that are insensitive to track irregularities.

- In comparison to existing techniques, the proposed approach enables simultaneous evaluation of the stiffness of the railpad, sleeper, and ballast at sleeper spacing resolution.

- We apply the proposed method to evaluate the track stiffness of a downscale test rig.

  – We compare the results of the proposed method to those obtained by the hammer test method, as well as the observations of the track component conditions. Results show that the proposed approach is capable of capturing stiffness variations at individual fastened clamps and local substructure misalignments.

  – The proposed method is capable of performing rapid assessments of track stiffness. Evaluating the stiffness of a single sleeper span takes approximately 0.32 s for feature extraction and 0.0093 s for GP model predictions (on an 8-core CPU). When scaled to long track sections, i.e., n sleeper spans, the proposed method has a linear time complexity, i.e., $\mathcal{O}(n)$.

– We also demonstrate that ABA is superior to the hammer test method for evaluating track stiffness under loaded conditions.

6.2. RECOMMENDATIONS FOR FURTHER RESEARCH

Based on the findings and insights from this research, the following research directions are recommended.

- In Chapter 2, measured vibration signals were analyzed only in the vertical direction. It is recommended to further explore the longitudinal and lateral dynamics of the VTI system, as they can also be used for track condition monitoring [184]. In the test campaign presented in Chapter 2, three-dimensional sensors were attached to the rail and ABAs were measured in three directions. For hammer tests, excitations were also applied in three directions. This provides the opportunity to identify and correlate the frequency features of the VTI system in the lateral and longitudinal directions. For this purpose, a VTI model that accounts for lateral and longitudinal dynamics is also required.

- The frequency feature map generated in Chapter 2 was based on one specific test location with a specific set of track parameters and operational conditions. Only the vehicle speed was varied during the test. It is recommended to further investigate how different track parameters and operational conditions influence the frequency features of the VTI system. Of special interest are, for example, the effects of different rail defect types and vehicle types. In Chapter 4, the effects of track parameters on FRF features were investigated using a global sensitivity analysis. The same approach can be applied to the frequency features of the VTI system.

- The frequency feature map approach can be further applied to other track structures such as switches and crossings and insulated joints to enhance the understanding of their dynamic characteristics. Some previous experimental studies can be found [12, 185, 186].

- In Chapter 3, all simulation cases for comparing the two models used the same track parameters. Model assumptions were also left unchanged (except for the contact model for the beam model). It is recommended to investigate how changing track parameters and model assumptions would affect the simulation results. This may guide when a certain model assumption should be dropped or adopted. For instance, it is found that for track FRFs the rigid sleeper assumption can be adopted when the railpad is soft [27, 72].

- In the literature, different VTI models have been compared through benchmark tests for different problems [104–106, 187]. However, they were all for beam models and continuum models were excluded from these benchmarks. In addition, it is difficult to deduce exactly which assumption contributes to an identified discrepancy from benchmark tests, because there is usually more than one different assumption between two benchmark participants and not all assumptions made for each participant are available. This provides the opportunities to apply the

6

two models developed in this thesis for these available benchmark problems, especially those wheel-rail impact problems, e.g., at insulated joints, wheel flats and crossings.

- The physics-based VTI model can be improved in several ways.

    – A key assumption made in the VTI model is that the stiffness of the railpad and ballast is homogeneous. This means that the proposed method does not consider stiffness variations at different sleeper supports or under a single sleeper. When stiffness variations exist, the evaluations usually indicate an averaged stiffness across adjacent sleeper spans. To be able to consider stiffness variations, the stiffness values of the railpad and ballast should be defined and identified separately for each sleeper. This greatly increases the dimension of the problem and therefore the corresponding inverse identification problem may be ill-posed. A possible solution is, e.g., to assume a parametrized longitudinal stiffness profile within a track section [60], thereby reducing the total number of stiffness variables.

    – Based on the findings in Chapter 3, a beam model may be considered adequate up to about 800 Hz. This means for track condition monitoring tasks related to high-frequency VTI, such as rail defect detection, a high-fidelity continuum model is required. However, continuum models in their current form are too time-consuming to evaluate and thus not suitable for use in the proposed digital twin framework. There can be two ways to solve this. First, model order reduction techniques, such as the proper orthogonal decomposition, can be applied to the continuum model. A key challenge is to preserve the necessary physics, such as the local inertial in the contact patch, in the reduced-order model. Alternatively, high-fidelity and low-fidelity can be combined through multi-fidelity simulations [188].

- It is recommended to apply the proposed digital twin framework for other track condition monitoring problems. A promising direction is to evaluate the track irregularity level. It was shown in Chapter 5 that track irregularity levels correspond to distinct frequency features that can be separated from other track parameters. In addition, as the GP model is a regression model, it is suitable for tasks such as quantifying defect sizes.

BIBLIOGRAPHY

[1] Peter Carden and Paul Fanning. "Vibration Based Condition Monitoring: A Review". In: *Structural Health Monitoring* 3.4 (2004), pp. 355–377.

[2] M. I. Friswell, J. E.T. Penny, and D. A.L. Wilson. "Using vibration data and statistical measures to locate damage in structures". In: *Modal Analysis: The International Journal of Analytical and Experimental Modal Analysis* 9.4 (Oct. 1994), pp. 239–254.

[3] Bart Peeters, Johan Maeck, and Guido De Roeck. "Vibration-based damage detection in civil engineering: excitation sources and temperature effects". In: *Smart Mater. Struct* 10 (2001), pp. 518–527.

[4] Scott W Doebling, Charles R Farrar, and Michael B Prime. "A Summary Review of Vibration-Based Damage Identification Methods". In: *Journal of Applied Mechanics* 111.2 (1989), pp. 270–78. DOI: 10.1177/058310249803000201.

[5] Sherif Beskhyroun, Leon D Wegner, and Bruce F Sparling. "New methodology for the application of vibration-based damage detection techniques". In: *Structural Control and Health Monitoring* May 2011 (2011), pp. 632–649. DOI: 10.1002/stc.456.

[6] Guo-dong Yue et al. "WSN-Based Vibration Characteristic Research for Various Railway Track Structures for Pattern Classification". In: *International Journal of Pattern Recognition and Artificial Intelligence* 30.10 (Dec. 2016), p. 1650020. DOI: 10.1142/S0218001416500208.

[7] J. C O Nielsen. "High-frequency vertical wheel-rail contact forces-Validation of a prediction model by field testing". In: *Wear* 265.9-10 (2008), pp. 1465–1471. DOI: 10.1016/j.wear.2008.02.038.

[8] Anders Rønnquist and Petter Nåvik. "Dynamic assessment of existing soft catenary systems using modal analysis to explore higher train velocities: A case study of a Norwegian contact line system". In: *Vehicle System Dynamics* (2015). DOI: 10.1080/00423114.2015.1013040.

[9] Pablo Salvador et al. "Axlebox accelerations: Their acquisition and time–frequency characterisation for railway track monitoring purposes". In: *Measurement* 82 (2016), pp. 301–312. DOI: http://dx.doi.org/10.1016/j.measurement.2016.01.012.

[10] Daniel Cantero and Biswajit Basu. "Railway infrastructure damage detection using wavelet transformed acceleration response of traversing vehicle". In: *Structural Control and Health Monitoring* 22.1 (Jan. 2015), pp. 62–70. DOI: 10.1002/stc.1660.

[11] M Molodova et al. "Automatic Detection of Squats in Railway Infrastructure". In: *IEEE Transactions on Intelligent Transportation Systems* 15.5 (2014), pp. 1980–1990. DOI: 10.1109/TITS.2014.2307955.

[12] Chen Shen, Zili Li, and Rolf Dollovoet. "A Novel Method for Railway Crossing Monitoring Based on Ambient Vibration Caused by Train-Track Interaction". In: *Lecture Notes in Mechanical Engineering*. 2020, pp. 133–141. DOI: 10.1007/978-3-030-38077-9_16.

[13] Jing Ning, Jianhui Lin, and Bing Zhang. "Time–frequency processing of track irregularities in high-speed train". In: *Mechanical Systems and Signal Processing* 66-67 (Jan. 2016), pp. 339–348. DOI: 10.1016/J.YMSSP.2015.04.031.

[14] Zhigang Liu et al. "Ensemble EMD-Based Automatic Extraction of the Catenary Structure Wavelength from the Pantograph-Catenary Contact Force". In: *IEEE Transactions on Instrumentation and Measurement* 65.10 (2016), pp. 2272–2283. DOI: 10.1109/TIM.2016.2579360.

[15] Hitoshi Tsunashima and Ryota Hirose. "Condition monitoring of railway track from car-body vibration using time–frequency analysis". In: *Vehicle System Dynamics* 60.4 (2020), pp. 1170–1187. DOI: 10.1080/00423114.2020.1850808.

[16] I. A. Iliopoulos, J. S. Sakellariou, and S. D. Fassois. "Track segment automated characterisation via railway–vehicle–based random vibration signals and statistical time series methods". In: *Vehicle System Dynamics* 60.10 (2022), pp. 3336–3357. DOI: 10.1080/00423114.2021.1948079.

[17] N. Correa et al. "A rational fraction polynomials model to study vertical dynamic wheel–rail interaction". In: *Journal of Sound and Vibration* 331.8 (Apr. 2012), pp. 1844–1858. DOI: 10.1016/J.JSV.2011.12.012.

[18] A. Malekloo et al. "Machine learning and structural health monitoring overview with emerging technology and high-dimensional data source highlights". In: *Structural Health Monitoring* 21.4 (Aug. 2022), pp. 1906–1955. DOI: https://journals.sagepub.com/doi/10.1177/14759217211036880.

[19] AIAA Digital Engineering Integration Committee. *DIGITAL TWIN: DEFINITION & VALUE An AIAA and AIA Position Paper*. Tech. rep. 2020.

[20] T. G. Ritto and F. A. Rochinha. "Digital twin, physics-based model, and machine learning applied to damage detection in structures". In: *Mechanical Systems and Signal Processing* 155 (June 2021), p. 107614. DOI: 10.1016/J.YMSSP.2021.107614.

[21] S. Chakraborty and S. Adhikari. "Machine learning based digital twin for dynamical systems with multiple time-scales". In: *Computers & Structures* 243 (Jan. 2021), p. 106410. DOI: 10.1016/J.COMPSTRUC.2020.106410.

[22] Michael G Kapteyn. "Mathematical and Computational Foundations to Enable Predictive Digital Twins at Scale". PhD thesis. Massachusetts Institute of Technology, 2021.

6

[23]   Louis Le Pen et al. "Evaluating railway track support stiffness from trackside measurements in the absence of wheel load data". In: *Canadian Geotechnical Journal* February (2016), pp. 2015–0268. DOI: 10.1139/cgj-2015-0268.

[24]   Zilong Wei et al. "Evaluating Degradation at Railway Crossings Using Axle Box Acceleration Measurements". In: *Sensors* 17.10 (Sept. 2017), p. 2236. DOI: 10.3390/s17102236.

[25]   D.P. Connolly et al. "Benchmarking railway vibrations – Track, vehicle, ground and building effects". In: *Construction and Building Materials* 92 (Sept. 2015), pp. 64–81. DOI: 10.1016/j.conbuildmat.2014.07.042.

[26]   K L Knothe and S L Grassie. "Modelling of Railway Track and Vehicle/Track Interaction at High Frequencies". In: *Vehicle System Dynamics* 22.3-4 (1993), pp. 209–262. DOI: 10.1080/00423119308969027.

[27]   Xianying Zhang et al. "A model of a discretely supported railway track based on a 2.5D finite element approach". In: *Journal of Sound and Vibration* (2019). DOI: 10.1016/j.jsv.2018.09.026.

[28]   M. Fermér and J. C.O. Nielsen. "Vertical interaction between train and track with soft and stiff railpads—full-scale experiments and theory". In: *Proceedings of the Institution of Mechanical Engineers, Part F: Journal of Rail and Rapid Transit* 209.1 (Jan. 1995), pp. 39–47. DOI: 10.1243/PIME_PROC_1995_209_253_02.

[29]   J C O Nielsen and T J S Abrahamsson. "Coupling of physical and modal components for analysis of moving non-linear dynamic systems on general beam structures". In: *International Journal for Numerical Methods in Engineering* 33.9 (1992), pp. 1843–1859. DOI: 10.1002/nme.1620330906.

[30]   L. Baeza, A. Roda, and J. C O Nielsen. "Railway vehicle/track interaction analysis using a modal substructuring approach". In: *Journal of Sound and Vibration* 293.1-2 (2006), pp. 112–124. DOI: 10.1016/j.jsv.2005.09.006.

[31]   Z. Cai, G. P. Raymond, and R. J. Bathurst. "Natural vibration analysis of rail track as a system of elastically coupled beam structures on Winkler foundation". In: *Computers and Structures* 53.6 (1994), pp. 1427–1436. DOI: 10.1016/0045-7949(94)90408-1.

[32]   S.G. Newton and R.A. Clark. "An investigation into the dynamic effects on the track of wheelflats on railway vehicles". In: *J. of Mech. Eng. Science* 21.2 (1979), pp. 287–297. DOI: 10.1243/JMES_JOUR_1979_021_046_02.

[33]   Michaël J.M.M. Steenbergen. "Quantification of dynamic wheel-rail contact forces at short rail irregularities and application to measured rail welds". In: *Journal of Sound and Vibration* (2008). DOI: 10.1016/j.jsv.2007.11.004.

[34]   R. Toscano Corrêa, A. Pinto da Costa, and F. M.F. Simões. "Finite element modeling of a rail resting on a Winkler-Coulomb foundation and subjected to a moving concentrated load". In: *International Journal of Mechanical Sciences* (2018). DOI: 10.1016/j.ijmecsci.2018.03.022.

6

[35] S. L. Grassie et al. "The Dynamic Response of Railway Track to High Frequency Vertical Excitation". In: *Journal of Mechanical Engineering Science* 24.2 (June 1982), pp. 77–90. DOI: 10.1243/JMES_JOUR_1982_024_016_02.

[36] X. Sheng, C. J.C. Jones, and M. Petyt. "Ground vibration generated by a harmonic load acting on a railway track". In: *Journal of Sound and Vibration* 225.1 (1999), pp. 3–28. DOI: 10.1006/jsvi.1999.2232.

[37] J.C.O. Nielsen and A. Igeland. "Vertical Dynamic Interaction Between Train and Track Influence of Wheel and Track Imperfections". In: *Journal of Sound and Vibration* 187.5 (1995), pp. 825–839. DOI: 10.1006/jsvi.1995.0566.

[38] T. X. Wu and D. J. Thompson. "On the impact noise generation due to a wheel passing over rail joints". In: *Journal of Sound and Vibration* 267.3 (2003), pp. 485–496. DOI: 10.1016/S0022-460X(03)00709-0.

[39] X. Zhao, Z. Li, and J. Liu. "Wheel-rail impact and the dynamic forces at discrete supports of rails in the presence of singular rail surface defects". In: *Proceedings of the Institution of Mechanical Engineers, Part F: Journal of Rail and Rapid Transit* 226.2 (2011), pp. 124–139. DOI: 10.1177/0954409711413975.

[40] Jian Bian, Yuantong Gu, and Martin Howard Murray. "A dynamic wheel-rail impact analysis of railway track under wheel flat by finite element analysis". In: *Vehicle System Dynamics* 51.6 (2013), pp. 784–797. DOI: 10.1080/00423114.2013.774031.

[41] M. Pletz, W. Daves, and H. Ossberger. "A wheel set/crossing model regarding impact, sliding and deformation-Explicit finite element approach". In: *Wear* 294-295 (2012), pp. 446–456. DOI: 10.1016/j.wear.2012.07.033.

[42] Zilong Wei et al. "Wheel–Rail Impact at Crossings: Relating Dynamic Frictional Contact to Degradation". In: *Journal of Computational and Nonlinear Dynamics* 12.4 (July 2017). DOI: 10.1115/1.4035823.

[43] Zhen Yang, Xiangyun Deng, and Zili Li. "Numerical modeling of dynamic frictional rolling contact with an explicit finite element method". In: *Tribology International* 129 (Jan. 2019), pp. 214–231. DOI: 10.1016/j.triboint.2018.08.028.

[44] D.J. Thompson. "Experimental Analysis of Wave Propagation in Railway Tracks". In: *Journal of Sound and Vibration* 203.5 (1997), pp. 867–888. DOI: 10.1006/jsvi.1997.0903.

[45] Zili Li et al. "An investigation into the causes of squats-Correlation analysis and numerical modeling". In: *Wear* 265.9-10 (2008), pp. 1349–1355. DOI: 10.1016/j.wear.2008.02.037.

[46] M. Fermér and J. C. O. Nielsen. "Wheel/Rail Contact Forces for Flexible versus Solid Wheels due to Tread Irregularities". In: *Vehicle System Dynamics* 23.sup1 (1994), pp. 142–157. DOI: 10.1080/00423119308969511.

[47] Nicolas Vincent and David J. Thompson. "Track Dynamic Behaviour at High Frequencies. Part 2: Experimental Results and Comparisons with Theory". In: *Vehicle System Dynamics* 24.sup1 (1995), pp. 100–114. DOI: 10.1080/00423119508969618.

[48]   K Knothe and Y Wu. "Receptance behaviour of railway track and subgrade". In: *Archive of Applied Mechanics* 68.470 (1998). DOI: 10.1007/s004190050179.

[49]   Martin Hiensch, Jens C.O. Nielsen, and Edwin Verheijen. "Rail corrugation in The Netherlands—measurements and simulations". In: *Wear* 253.1-2 (July 2002), pp. 140–149. DOI: 10.1016/S0043-1648(02)00093-5.

[50]   Jiannan Yang and David J. Thompson. "Time-domain prediction of impact noise from wheel flats based on measured profiles". In: *Journal of Sound and Vibration* (2014). DOI: 10.1016/j.jsv.2014.04.026.

[51]   Qi Li, David J Thompson, and Martin GR Toward. "Estimation of track parameters and wheel–rail combined roughness from rail vibration". In: *Proceedings of the Institution of Mechanical Engineers, Part F: Journal of Rail and Rapid Transit* 232.4 (Apr. 2018), pp. 1149–1167. DOI: 10.1177/0954409717710126.

[52]   Sakdirat Kaewunruen and Alex M. Remennikov. "Field trials for dynamic characteristics of railway track and its components using impact excitation technique". In: *NDT and E International* 40.7 (2007), pp. 510–519. DOI: 10.1016/j.ndteint.2007.03.004.

[53]   A P De Man. "A survey of dynamic railway track properties and their quality". PhD thesis. TU Delft, Delft University of Technology, 2002, p. 236.

[54]   V L Markine, A P de Man, and C Esveld. "Identification of Dynamic Properties of a Railway Track". In: *IUTAM Symposium on Field Analyses for Determination of Material Parameters — Experimental and Numerical Aspects: Proceedingsof the IUTAM Symposium held in Abisko National Park, Kiruna, Sweden, July 31 - August 4, 2000.* Ed. by P Ståhle and K G Sundin. Dordrecht: Springer Netherlands, 2003, pp. 27–36. DOI: 10.1007/978-94-010-0109-0_5.

[55]   A. Núñez, M. Oregui, and M. Molodova. "An expensive optimization based computational intelligence method for railway track parameter identification". In: *Civil-Comp Proceedings* 106 (2014), pp. 1–21. DOI: 10.4203/ccp.106.173.

[56]   J. A. Priest and W. Powrie. "Determination of Dynamic Track Modulus from Measurement of Track Velocity during Train Passage". In: *Journal of Geotechnical and Geoenvironmental Engineering* 135.11 (Nov. 2009), pp. 1732–1740. DOI: 10.1061/(ASCE)GT.1943-5606.0000130.

[57]   David Milne et al. "The influence of variation in track level and support system stiffness over longer lengths of track for track performance and vehicle track interaction". In: *Vehicle System Dynamics* 59.2 (2021), pp. 245–268. DOI: 10.1080/00423114.2019.1677920.

[58]   Eric G Berggren, Arne Nissen, and Björn S Paulsson. "Track deflection and stiffness measurements from a track recording car". In: *Proceedings of the Institution of Mechanical Engineers, Part F: Journal of Rail and Rapid Transit* 228.6 (Apr. 2014), pp. 570–580. DOI: 10.1177/0954409714529267.

6

[59] Eric G. Berggren, Amir M. Kaynia, and Björn Dehlbom. "Identification of sub-structure properties of railway tracks by dynamic stiffness measurements and simulations". In: *Journal of Sound and Vibration* 329.19 (Sept. 2010), pp. 3999–4016. DOI: 10.1016/j.jsv.2010.04.015.

[60] Paraic Quirke et al. "Drive-by detection of railway track stiffness variation using in-service vehicles". In: *Proceedings of the Institution of Mechanical Engineers, Part F: Journal of Rail and Rapid Transit* 231.4 (Apr. 2017), pp. 498–514. DOI: 10.1177/0954409716634752.

[61] Abdollah Malekjafarian et al. "Railway Track Loss-of-Stiffness Detection Using Bogie Filtered Displacement Data Measured on a Passing Train". In: *Infrastructures* 6.6 (June 2021), p. 93. DOI: 10.3390/infrastructures6060093.

[62] Y. B. Yang et al. "Two-axle test vehicle for damage detection for railway tracks modeled as simply supported beams with elastic foundation". In: *Engineering Structures* 219 (Sept. 2020), p. 110908. DOI: 10.1016/j.engstruct.2020.110908.

[63] Longqi Wang, Yao Zhang, and Seng Tjhen Lie. "Detection of damaged supports under railway track based on frequency shift". In: *Journal of Sound and Vibration* 392 (Mar. 2017), pp. 142–153. DOI: 10.1016/j.jsv.2016.11.018.

[64] X. Q. Zhu, S. S. Law, and L. Huang. "Identification of Railway Ballasted Track Systems from Dynamic Responses of In-Service Trains". In: *Journal of Aerospace Engineering* 31.5 (2018), p. 04018060. DOI: 10.1061/(asce)as.1943-5525.0000898.

[65] Y. B. Yang et al. "Track modulus detection by vehicle scanning method". In: *Acta Mechanica* 231.7 (July 2020), pp. 2955–2978. DOI: 10.1007/s00707-020-02684-w.

[66] Jens C.O. Nielsen et al. "Train-track interaction and mechanisms of irregular wear on wheel and rail surfaces". In: *Vehicle System Dynamics* 40.1-3 (2003), pp. 3–54. DOI: 10.1076/vesd.40.1.3.15874.

[67] S L Grassie. "Rail corrugation: characteristics, causes, and treatments". In: (2009), pp. 581–596. DOI: 10.1243/09544097JRRT264.

[68] Zili Li et al. "Squat growth-Some observations and the validation of numerical predictions". In: *Wear* 271.1-2 (2011), pp. 148–157. DOI: 10.1016/j.wear.2010.10.051.

[69] X. Sheng and M.H. Li. "Propagation constants of railway tracks as a periodic structure". In: *Journal of Sound and Vibration* 299.4-5 (Feb. 2007), pp. 1114–1123. DOI: 10.1016/J.JSV.2006.08.010.

[70] David Thompson. "CHAPTER 3 - Track Vibration". In: ed. by David B T - Railway Noise Thompson and Vibration. Oxford: Elsevier, 2009, pp. 29–95. DOI: https://doi.org/10.1016/B978-0-08-045147-3.00003-7.

[71] S.L. Grassie and S.J. Cox. "Dynamic Response of Railway Track With Flexible Sleepers To High Frequency Vertical Excitation." In: *Proceedings of the Institution of Mechanical Engineers, Part D: Transport Engineering* 198.7 (1984), pp. 117–124. DOI: 10.1243/PIME_PROC_1984_198_137_02.

[72] J.-Y. Shih et al. "Modelling options for ballast track dynamics". In: *24th International Congress on Sound and Vibration, ICSV 2017* (2017), pp. 1–8.

[73] S. L. Grassie and S. J. Cox. "The Dynamic Response of Railway Track With Unsupported Sleepers". In: *Proceedings of the Institution of Mechanical Engineers, Part D: Transport Engineering* 199.2 (Apr. 1985), pp. 123–136. DOI: 10.1243/PIME_PROC_1985_199_149_01.

[74] T. X. Wu and D. J. Thompson. "Vibration analysis of railway track with multiple wheels on the rail". In: *Journal of Sound and Vibration* 239.1 (Jan. 2001), pp. 69–97. DOI: 10.1006/jsvi.2000.3157.

[75] Simian Lei et al. "Wave interference in railway track due to multiple wheels". In: *Journal of Sound and Vibration* 520 (Mar. 2022), p. 116620. DOI: 10.1016/J.JSV.2021.116620.

[76] G. Lombaert et al. "The experimental validation of a numerical model for the prediction of railway induced vibrations". In: *Journal of Sound and Vibration* 297.3-5 (2006), pp. 512–535. DOI: 10.1016/j.jsv.2006.03.048.

[77] X. Sheng, C. J.C. Jones, and D. J. Thompson. "A comparison of a theoretical model for quasi-statically and dynamically induced environmental vibration from trains with measurements". In: *Journal of Sound and Vibration* 267.3 (Oct. 2003), pp. 621–635. DOI: 10.1016/S0022-460X(03)00728-4.

[78] N. Triepaischajonsak et al. "Ground vibration from trains: Experimental parameter characterization and validation of a numerical model". In: *Proceedings of the Institution of Mechanical Engineers, Part F: Journal of Rail and Rapid Transit* 225.2 (Mar. 2011), pp. 140–153. DOI: 10.1177/09544097JRRT370.

[79] D.R.M. Milne et al. "Properties of train load frequencies and their applications". In: *Journal of Sound and Vibration* 397 (June 2017), pp. 123–140. DOI: 10.1016/j.jsv.2017.03.006.

[80] H. Askarinejad et al. "Field Measurement of Wheel-Rail Impact Force at Insulated Rail Joint". In: *Experimental Techniques* 39.5 (2015), pp. 61–69. DOI: 10.1111/j.1747-1567.2012.00867.x.

[81] X. Liu et al. "Experimental tools for railway crossing condition monitoring (crossing condition monitoring tools)". In: *Measurement* 129 (Dec. 2018), pp. 424–435. DOI: 10.1016/J.MEASUREMENT.2018.07.062.

[82] M.A. Boogaard, Z. Li, and R.P.B.J. Dollevoet. "In situ measurements of the crossing vibrations of a railway turnout". In: *Measurement* 125 (Sept. 2018), pp. 313–324. DOI: 10.1016/J.MEASUREMENT.2018.04.094.

6

[83] M. D.G. Milošević et al. "On tailored signal processing tools for operational condition monitoring of railway switches and crossings". In: *Proceedings of ISMA 2020 - International Conference on Noise and Vibration Engineering and USD 2020 - International Conference on Uncertainty in Structural Dynamics* (2020), pp. 2639–2653.

[84] M Bocciolone et al. "A measurement system for quick rail inspection and effective track maintenance strategy". In: *Mechanical Systems and Signal Processing* 21.3 (2007), pp. 1242–1254. DOI: 10.1016/j.ymssp.2006.02.007.

[85] J S Lee et al. "Estimation of Rail Irregularity by Axle-Box Accelerometers on a High-Speed Train". English. In: *Noise and Vibration Mitigation for Rail Transportation Systems* 118 (2012), pp. 571–578.

[86] Zilong Wei et al. "Carriage interior noise-based inspection for rail corrugation on high-speed railway track". In: *Applied Acoustics* 196 (2022), p. 108881. DOI: 10.1016/j.apacoust.2022.108881.

[87] C. J.C. Jones, D. J. Thompson, and R. J. Diehl. "The use of decay rates to analyse the performance of railway track in rolling noise generation". In: *Journal of Sound and Vibration* 293.3-5 (2006), pp. 485–495. DOI: 10.1016/j.jsv.2005.08.060.

[88] X. Sheng, T. Zhong, and Y. Li. "Vibration and sound radiation of slab high-speed railway tracks subject to a moving harmonic load". In: *Journal of Sound and Vibration* 395 (May 2017), pp. 160–186. DOI: 10.1016/J.JSV.2017.02.024.

[89] Anders Johansson and Jens C.O. Nielsen. "Rail corrugation growth-Influence of powered wheelsets with wheel tread irregularities". In: *Wear* 262.11-12 (2007), pp. 1296–1307. DOI: 10.1016/j.wear.2007.01.004.

[90] Chaozhi Ma et al. "The dynamic resonance under multiple flexible wheelset-rail interactions and its influence on rail corrugation for high-speed railway". In: *Journal of Sound and Vibration* 498 (2021), p. 115968. DOI: 10.1016/j.jsv.2021.115968.

[91] Chen Shen et al. "Comparisons between beam and continuum models for modelling wheel-rail impact at a singular rail surface defect". In: *International Journal of Mechanical Sciences* 198 (May 2021), p. 106400. DOI: 10.1016/j.ijmecsci.2021.106400.

[92] Karl Popp, Holger Kruse, and Ingo Kaiser. "Vehicle-Track Dynamics in the Mid-Frequency Range". In: *Vehicle System Dynamics* 31.5-6 (1999), pp. 423–464. DOI: 10.1076/vesd.31.5.423.8363.

[93] Hamidreza Heydari-Noghabi et al. "Investigating the influence of auxiliary rails on dynamic behavior of railway transition zone by a 3D train-track interaction model". In: *Latin American Journal of Solids and Structures* (2017). DOI: 10.1590/1679-78253906.

[94] Zhi Ping Zeng et al. "Three-dimensional rail–bridge coupling element of unequal lengths for analyzing train–track–bridge interaction system". In: *Latin American Journal of Solids and Structures* (2016). DOI: 10.1590/1679-78252551.

[95] Fran Ribes-Llario et al. "Study of vibrations in a short-span bridge under reso-
nance conditions considering train-track interaction". In: *Latin American Jour-
nal of Solids and Structures* (2016). DOI: 10.1590/1679-78252773.

[96] L. Gavrić. "Computation of propagative waves in free rail using a finite element
technique". In: *Journal of Sound and Vibration* 185.3 (1995), pp. 531–543. DOI:
10.1006/jsvi.1995.0398.

[97] D. Kostovasilis, D. J. Thompson, and M. F.M. Hussein. "A semi-analytical beam
model for the vibration of railway tracks". In: *Journal of Sound and Vibration* 393
(2017), pp. 321–337. DOI: 10.1016/j.jsv.2016.12.033.

[98] L. Gry. "Dynamic modelling of railway track based on wave propagation". In:
Journal of Sound and Vibration 195.3 (1996), pp. 477–505. DOI: 10.1006/jsvi.
1996.0438.

[99] H. H. Jenkins et al. "Effect of Track and Vehicle Parameters on Wheel/Rail Vertical
Dynamic Forces." In: *Railw Eng J* 3.1 (1974), pp. 2–16.

[100] Xin Zhao, Zili Li, and Rolf Dollevoet. "The vertical and the longitudinal dynamic
responses of the vehicle–track system to squat-type short wavelength irregular-
ity". In: *Vehicle System Dynamics* 51.12 (2013), pp. 1918–1937. DOI: 10.1080/
00423114.2013.847466.

[101] Maria Molodova et al. "Validation of a finite element model for axle box accelera-
tion at squats in the high frequency range". In: *Computers & Structures* 141 (Aug.
2014), pp. 84–93. DOI: 10.1016/j.compstruc.2014.05.005.

[102] Zili Li et al. "Differential wear and plastic deformation as causes of squat at track
local stiffness change combined with other track short defects". In: *Vehicle System
Dynamics* 46.SUPPL.1 (2008), pp. 237–246. DOI: 10.1080/00423110801935855.

[103] Xiangyun Deng et al. "Pre-cracking development of weld-induced squats due to
plastic deformation: Five-year field monitoring and numerical analysis". In: *In-
ternational Journal of Fatigue* 127 (Oct. 2019), pp. 431–444. DOI: 10.1016/j.
ijfatigue.2019.06.013.

[104] STUART L. GRASSIE. "Models of Railway Track and Vehicle/Track Interaction
at High Frequencies: Results of Benchmark Test". In: *Vehicle System Dynamics*
25.sup1 (1996), pp. 243–262. DOI: 10.1080/00423119608969199.

[105] David Martyn Steffens. "Identification and development of a model of railway
track dynamic behaviour". PhD thesis. Queensland University of Technology, 2005,
p. 317.

[106] Jeffrey Leong, Martin H Murray, and David Steffens. "Examination of railway track
dynamic models capabilities against measured field data". In: *International Heavy
Haul Conference Specialist Technical Session, High Tech in Heavy Haul*. Ed. by Per-
Olof Larsson-Kraik and Gun-Marie Toyra. Kiruna, Sweden: International Heavy
Haul Association Inc., 2007, pp. 257–267.

6

[107]   Xianying Zhang, David Thompson, and Xiaozhen Sheng. "Differences between
        Euler-Bernoulli and Timoshenko beam formulations for calculating the effects
        of moving loads on a periodically supported beam". In: *Journal of Sound and
        Vibration* 481 (Sept. 2020), p. 115432. DOI: 10.1016/j.jsv.2020.115432.

[108]   Rao V. Dukkipati and Renguand Dong. "Impact Loads due to Wheel Flats and
        Shells". In: *International Journal of Vehicle Mechanics and Mobility* 3114.Septem-
        ber (1999), pp. 1–22. DOI: 10.1076/vesd.31.1.1.2097.

[109]   R. Ferrara, G. Leonardi, and F. Jourdan. "A contact-area model for rail-pads con-
        nections in 2-D simulations: Sensitivity analysis of train-induced vibrations". In:
        Vehicle System Dynamics 51.9 (2013), pp. 1342–1362. DOI: 10.1080/00423114.
        2013.801996.

[110]   B. Blanco et al. "Distributed support modelling for vertical track dynamic analy-
        sis". In: *Vehicle System Dynamics* 56.4 (2018), pp. 529–552. DOI: 10.1080/00423114.
        2017.1394473.

[111]   Xin Zhao, Zili Li, and Rolf Dollevoet. "Influence of the fastening modeling on the
        vehicle-track interaction at singular rail surface defects". In: *Journal of Computa-
        tional and Nonlinear Dynamics* 9.3 (2014). DOI: 10.1115/1.4025895.

[112]   M. Oregui, Z. Li, and R. Dollevoet. "An investigation into the modeling of railway
        fastening". In: *International Journal of Mechanical Sciences* 92 (Mar. 2015), pp. 1–
        11. DOI: 10.1016/j.ijmecsci.2014.11.019.

[113]   Egidio Di Gialleonardo, Francesco Braghin, and Stefano Bruni. "The influence of
        track modelling options on the simulation of rail vehicle dynamics". In: *Journal
        of Sound and Vibration* 331.19 (2012), pp. 4246–4258. DOI: 10.1016/j.jsv.
        2012.04.024.

[114]   L Baeza et al. "High frequency railway vehicle-track dynamics through flexible
        rotating wheelsets". In: *Vehicle System Dynamics* 46.7 (2008), pp. 647–659. DOI:
        10.1080/00423110701656148.

[115]   M. Wiest et al. "Assessment of methods for calculating contact pressure in wheel-
        rail/switch contact". In: *Wear* 265.9-10 (2008), pp. 1439–1445. DOI: 10.1016/j.
        wear.2008.02.039.

[116]   A. Pieringer, W. Kropp, and J. C.O. Nielsen. "The influence of contact modelling
        on simulated wheel/rail interaction due to wheel flats". In: *Wear* 314.1-2 (2014),
        pp. 273–281. DOI: 10.1016/j.wear.2013.12.005.

[117]   R.A.J. Ford and D.J. Thompson. "Simplified contact filters in wheel/rail noise pre-
        diction". In: *Journal of Sound and Vibration* 293.3-5 (June 2006), pp. 807–818. DOI:
        10.1016/J.JSV.2005.08.049.

[118]   Xiangyun Deng et al. "Applicability of half-space-based methods to non-conforming
        elastic normal contact problems". In: *International Journal of Mechanical Sci-
        ences* 126 (June 2017), pp. 229–234. DOI: 10.1016/j.ijmecsci.2017.04.002.

[119]   Zhen Yang and Zili Li. "A numerical study on waves induced by wheel-rail con-
        tact". In: *International Journal of Mechanical Sciences* 161-162 (Oct. 2019), p. 105069.
        DOI: 10.1016/j.ijmecsci.2019.105069.

[120]   K. Nguyen, J. M. Goicolea, and F. Galbadón. "Comparison of dynamic effects of high-speed traffic load on ballasted track using a simplified two-dimensional and full three-dimensional model". In: *Proceedings of the Institution of Mechanical Engineers, Part F: Journal of Rail and Rapid Transit* 228.2 (2014), pp. 128–142. DOI: 10.1177/0954409712465710.

[121]   J. J. Kalker. *Three-Dimensional Elastic Bodies in Rolling Contact*. Vol. 2. Solid Mechanics and Its Applications 12. Dordrecht: Kluwer Academic Publishers, Dec. 1990, pp. 7250–7. DOI: 10.1007/978-94-015-7889-9.

[122]   Xin Zhao and Zili Li. "The solution of frictional wheel-rail rolling contact with a 3D transient finite element model: Validation and error analysis". In: *Wear* 271.1-2 (2011), pp. 444–452. DOI: 10.1016/j.wear.2010.10.007.

[123]   M. Molodova et al. "Parametric study of axle box acceleration at squats". In: *Proceedings of the Institution of Mechanical Engineers, Part F: Journal of Rail and Rapid Transit* 229.8 (2015), pp. 841–851. DOI: 10.1177/0954409714523583.

[124]   Ingrid Daubechies, Jianfeng Lu, and Hau Tieng Wu. "Synchrosqueezed wavelet transforms: An empirical mode decomposition-like tool". In: *Applied and Computational Harmonic Analysis* 30.2 (2011), pp. 243–261. DOI: 10.1016/j.acha.2010.08.002.

[125]   K. Koro et al. "Timoshenko beam finite element for vehicle—track vibration analysis and its application to jointed railway track". In: *Proceedings of the Institution of Mechanical Engineers, Part F: Journal of Rail and Rapid Transit* 218.2 (Mar. 2004), pp. 159–172. DOI: 10.1243/0954409041319687.

[126]   S. C. Yang. "Enhancement of the finite-element method for the analysis of vertical train-track interactions". In: *Proceedings of the Institution of Mechanical Engineers, Part F: Journal of Rail and Rapid Transit* 223.6 (2009), pp. 609–620. DOI: 10.1243/09544097JRRT285.

[127]   A. Pieringer, W. Kropp, and D. J. Thompson. "Investigation of the dynamic contact filter effect in vertical wheel/rail interaction using a 2D and a 3D non-Hertzian contact model". In: *Wear* 271.1-2 (2011), pp. 328–338. DOI: 10.1016/j.wear.2010.10.029.

[128]   Ahmet Arda Ozdemir and Suat Gumussoy. "Transfer Function Estimation in System Identification Toolbox via Vector Fitting". In: *IFAC-PapersOnLine* 50.1 (July 2017), pp. 6232–6237. DOI: 10.1016/j.ifacol.2017.08.1026.

[129]   David Thompson. "Wheel/Rail Interaction and Excitation by Roughness". In: *Railway Noise and Vibration*. 2009, pp. 127–173. DOI: 10.1016/b978-0-08-045147-3.00005-0.

[130]   M. D. Spiridonakos and S. D. Fassois. "Non-stationary random vibration modelling and analysis via functional series time-dependent ARMA (FS-TARMA) models - A critical survey". In: *Mechanical Systems and Signal Processing* 47.1-2 (2014), pp. 175–224. DOI: 10.1016/j.ymssp.2013.06.024.

6

[131]   M Molodova, Z L Li, and R Dollevoet. "Axle box acceleration: Measurement and simulation for detection of short track defects". In: *Wear* 271.1-2 (2011), pp. 349–356. DOI: 10.1016/j.wear.2010.10.003.

[132]   Chen Shen, Rolf Dollevoet, and Zili Li. "Fast and robust identification of railway track stiffness from simple field measurement". In: *Mechanical Systems and Signal Processing* 152 (May 2021), p. 107431. DOI: 10.1016/j.ymssp.2020.107431.

[133]   H. F. Lam, M. T. Wong, and Y. B. Yang. "A feasibility study on railway ballast damage detection utilizing measured vibration of in situ concrete sleeper". In: *Engineering Structures* 45 (2012), pp. 284–298. DOI: 10.1016/j.engstruct.2012.06.022.

[134]   M. Oregui et al. "Obtaining railpad properties via dynamic mechanical analysis". In: *Journal of Sound and Vibration* 363 (Feb. 2016), pp. 460–472. DOI: 10.1016/J.JSV.2015.11.009.

[135]   Heung Fai Lam, Stephen Adeyemi Alabi, and Jia Hua Yang. "Identification of rail-sleeper-ballast system through time-domain Markov chain Monte Carlo-based Bayesian approach". In: *Engineering Structures* 140 (June 2017), pp. 421–436. DOI: 10.1016/j.engstruct.2017.03.001.

[136]   M. Oregui, Z. Li, and R. Dollevoet. "Identification of characteristic frequencies of damaged railway tracks using field hammer test measurements". In: *Mechanical Systems and Signal Processing* 54-55 (Mar. 2015), pp. 224–242. DOI: 10.1016/J.YMSSP.2014.08.024.

[137]   Alex Remennikov and S. Kaewunruen. "Experimental investigation on dynamic railway sleeper/ballast interaction". In: *Experimental Mechanics* 46.1 (2006), pp. 57–66. DOI: 10.1007/s11340-006-5868-z.

[138]   E. Arlaud, S. Costa D'Aguiar, and E. Balmes. "Receptance of railway tracks at low frequency: Numerical and experimental approaches". In: *Transportation Geotechnics* 9 (Dec. 2016), pp. 1–16. DOI: 10.1016/J.TRGEO.2016.06.003.

[139]   Michael P.N. Burrow, Andrew H.C. Chan, and Aung Shein. "Deflectometer-based analysis of ballasted railway tracks". In: *Proceedings of the Institution of Civil Engineers: Geotechnical Engineering* (2007). DOI: 10.1680/geng.2007.160.3.169.

[140]   T X Wu and D J Thompson. "The effects of track non-linearity on wheel / rail impact". In: *Proceedings of the Institution of Mechanical Engineers, Part F: Journal of Rail and Rapid Transit* 218 (2004), pp. 1–15. DOI: 10.1243/095440904322804394.

[141]   Reza Jafarkhani and Sami F. Masri. "Finite element model updating using evolutionary strategy for damage detection". In: *Computer-Aided Civil and Infrastructure Engineering* (2011). DOI: 10.1111/j.1467-8667.2010.00687.x.

[142]   Qing Wu, Colin Cole, and Tim McSweeney. "Applications of particle swarm optimization in the railway domain". In: *International Journal of Rail Transportation* 4.3 (2016), pp. 167–190. DOI: 10.1080/23248378.2016.1179599.

[143] Mayank Mishra et al. "Performance Studies of 10 Metaheuristic Techniques in Determination of Damages for Large-Scale Spatial Trusses from Changes in Vibration Responses". In: *Journal of Computing in Civil Engineering* 34.2 (Mar. 2020), p. 04019052. DOI: 10.1061/(ASCE)CP.1943-5487.0000872.

[144] Mayank Mishra et al. "Ant lion optimisation algorithm for structural damage detection using vibration data". In: *Journal of Civil Structural Health Monitoring* 9.1 (Feb. 2019), pp. 117–136. DOI: 10.1007/s13349-018-0318-z.

[145] Chung-Bang Yun and Eun Young Bahng. "Substructural identification using neural networks". In: *Computers & Structures* 77.1 (June 2000), pp. 41–52. DOI: 10.1016/S0045-7949(99)00199-6.

[146] Md Sazzad Hossain et al. "Artificial neural networks for vibration based inverse parametric identifications: A review". In: *Applied Soft Computing Journal* 52 (2017), pp. 203–219. DOI: 10.1016/j.asoc.2016.12.014.

[147] J. Hensman et al. "Locating acoustic emission sources in complex structures using Gaussian processes". In: *Mechanical Systems and Signal Processing* 24.1 (Jan. 2010), pp. 211–223. DOI: 10.1016/j.ymssp.2009.05.018.

[148] J.W. Lee et al. "Health-monitoring method for bridges under ordinary traffic loadings". In: *Journal of Sound and Vibration* 257.2 (2002), pp. 247–264. DOI: 10.1006/jsvi.5056.

[149] Hui Li, Yuequan Bao, and Jinping Ou. "Structural damage identification based on integration of information fusion and shannon entropy". In: *Mechanical Systems and Signal Processing* (2008). DOI: 10.1016/j.ymssp.2007.11.025.

[150] Y. Q. Ni, B. S. Wang, and J. M. Ko. "Constructing input vectors to neural networks for structural damage identification". In: *Smart Materials and Structures* (2002). DOI: 10.1088/0964-1726/11/6/301.

[151] Carl Edward Rasmussen and Christopher K I Williams. *Gaussian Processes for Machine Learning*. Nov. 2005. DOI: 10.7551/mitpress/3206.001.0001.

[152] Luís F. Ramos et al. "A Bayesian approach for NDT data fusion: The Saint Torcato church case study". In: *Engineering Structures* 84 (Feb. 2015), pp. 120–129. DOI: 10.1016/j.engstruct.2014.11.015.

[153] M. Oregui, Z. Li, and R. Dollevoet. "An investigation into the vertical dynamics of tracks with monoblock sleepers with a 3D finite-element model". In: *Proceedings of the Institution of Mechanical Engineers, Part F: Journal of Rail and Rapid Transit* 230.3 (2015), pp. 891–908. DOI: 10.1177/0954409715569558.

[154] Pan Zhang et al. "Multimodal dispersive waves in a free rail: Numerical modeling and experimental investigation". In: *Mechanical Systems and Signal Processing* (2021). DOI: 10.1016/j.ymssp.2020.107305.

[155] Andrea Saltelli. "Making best use of model evaluations to compute sensitivity indices". In: *Computer Physics Communications* (2002). DOI: 10.1016/S0010-4655(02)00280-1.

6

[156] J C O Nielsen. "Dynamic Interaction between Wheel and Track - a Parametric Search Towards an Optimal-Design of Rail Structures". In: *Vehicle System Dynamics* 23.2 (1994), pp. 115–132. DOI: Doi10.1080/00423119408969053.

[157] A. Pieringer and W. Kropp. "A Fast Time-Domain Model for Wheel / Rail Interaction Demonstrated for the Case of Impact Forces Caused by Wheel Flats". In: *Journal of the Acoustical Society of America* 123.5 (2008), pp. 2643–2648. DOI: 10.1121/1.2933584.

[158] Y. Q. Sun and M. Dhanasekar. "A dynamic model for the vertical interaction of the rail track and wagon system". In: *International Journal of Solids and Structures* 39.5 (2002), pp. 1337–1359. DOI: 10.1016/S0020-7683(01)00224-4.

[159] Robin Andersson et al. "The influence of rail surface irregularities on contact forces and local stresses". In: *Vehicle System Dynamics* 53.1 (2014), pp. 68–87. DOI: 10.1080/00423114.2014.982890.

[160] Luis Baeza et al. "Prediction of rail corrugation using a rotating flexible wheelset coupled with a flexible track model and a non-Hertzian/non-steady contact model". In: *Journal of Sound and Vibration* 330.18-19 (2011), pp. 4493–4507. DOI: 10.1016/j.jsv.2011.03.032.

[161] Andrew McHutchon and Carl Edward Rasmussen. "Gaussian Process training with input noise". In: *Advances in Neural Information Processing Systems 24: 25th Annual Conference on Neural Information Processing Systems 2011, NIPS 2011* (2011), pp. 1–9.

[162] Quoc V. Le, Alex J. Smola, and Stéphane Canu. "Heteroscedastic Gaussian process regression". In: *ICML 2005 - Proceedings of the 22nd International Conference on Machine Learning* (2005), pp. 489–496. DOI: 10.1145/1102351.1102413.

[163] Yanshuai Cao and David J. Fleet. *Generalized Product of Experts for Automatic and Principled Fusion of Gaussian Process Predictions*. 2014. DOI: 10.48550/ARXIV.1410.7827.

[164] Faisal Shabbir and Piotr Omenzetter. "Particle swarm optimization with sequential niche technique for dynamic finite element model updating". In: *Computer-Aided Civil and Infrastructure Engineering* 30.5 (2015), pp. 359–375. DOI: 10.1111/mice.12100.

[165] Hua-Ping Wan and Wei-Xin Ren. "A residual-based Gaussian process model framework for finite element model updating". In: *Computers & Structures* 156 (Aug. 2015), pp. 149–159. DOI: 10.1016/J.COMPSTRUC.2015.05.003.

[166] J.T. Wang, C.J. Wang, and J.P. Zhao. "Frequency response function-based model updating using Kriging model". In: *Mechanical Systems and Signal Processing* 87 (Mar. 2017), pp. 218–228. DOI: 10.1016/j.ymssp.2016.10.023.

[167] Kye Si Kwon and Rong Ming Lin. "Frequency selection method for FRF-based model updating". In: *Journal of Sound and Vibration* 278.1-2 (2004), pp. 285–306. DOI: 10.1016/j.jsv.2003.10.003.

[168]   Jens C.O. Nielsen et al. "Degradation of railway track geometry – Correlation be-
        tween track stiffness gradient and differential settlement". In: *Proceedings of the
        Institution of Mechanical Engineers, Part F: Journal of Rail and Rapid Transit*
        234.1 (Jan. 2020), pp. 108–119. DOI: 10.1177/0954409718819581.

[169]   I. Grossoni et al. "The role of track stiffness and its spatial variability on long-
        term track quality deterioration". In: *Proceedings of the Institution of Mechani-
        cal Engineers, Part F: Journal of Rail and Rapid Transit* (2019). DOI: 10.1177/
        0954409718777372.

[170]   Jannik S. Theyssen et al. "Calibration and validation of the dynamic response of
        two slab track models using data from a full-scale test rig". In: *Engineering Struc-
        tures* 234 (May 2021), p. 111980. DOI: 10.1016/j.engstruct.2021.111980.

[171]   M X D Li and E. G. Berggren. "A Study of the Effect of Global Track Stiffness and
        Its Variations on Track Performance: Simulation and Measurement". In: *Proceed-
        ings of the Institution of Mechanical Engineers, Part F: Journal of Rail and Rapid
        Transit* 224.5 (Sept. 2010), pp. 375–382. DOI: 10.1243/09544097JRRT361.

[172]   Kai Wei et al. "The influence of amplitude- and frequency-dependent stiffness of
        rail pads on the random vibration of a vehicle-track coupled system". In: *Shock
        and Vibration* (2016). DOI: 10.1155/2016/7674124.

[173]   Ping Wang et al. "Overview and outlook on railway track stiffness measurement".
        In: *Journal of Modern Transportation* 24.2 (June 2016), pp. 89–102. DOI: 10.1007/
        s40534-016-0104-8.

[174]   André Paixão, Eduardo Fortunato, and Rui Calçada. "Transition zones to railway
        bridges: Track measurements and numerical modelling". In: *Engineering Struc-
        tures* (2014). DOI: 10.1016/j.engstruct.2014.09.024.

[175]   Maider Oregui et al. "Monitoring bolt tightness of rail joints using axle box ac-
        celeration measurements". In: *Structural Control and Health Monitoring* (2016).
        DOI: 10.1002/stc.1848.

[176]   Yao Zhang et al. "Detection of Damaged Supports under Railway Track Using Dy-
        namic Response of a Passing Vehicle". In: *International Journal of Structural Sta-
        bility and Dynamics* (2019). DOI: 10.1142/S0219455419501177.

[177]   Meysam Naeimi et al. "Development of a New Downscale Setup for Wheel-Rail
        Contact Experiments under Impact Loading Conditions". In: *Experimental Tech-
        niques* 42.1 (Feb. 2018), pp. 1–17. DOI: 10.1007/s40799-017-0216-z.

[178]   Pan Zhang, Jan Moraal, and Zili Li. "Design, calibration and validation of a wheel-
        rail contact force measurement system in V-Track". In: *Measurement* 175 (Apr.
        2021), p. 109105. DOI: 10.1016/j.measurement.2021.109105.

[179]   Gaurav Thakur et al. "The Synchrosqueezing algorithm for time-varying spectral
        analysis: Robustness properties and new paleoclimate applications". In: *Signal
        Processing* (2013). DOI: 10.1016/j.sigpro.2012.11.029.

[180]   A. Grinsted, J. C. Moore, and S. Jevrejeva. "Application of the cross wavelet trans-
        form and wavelet coherence to geophysical time series". In: *Nonlinear Processes
        in Geophysics* (2004). DOI: 10.5194/npg-11-561-2004.

6

[181]   Z. Friedman and J. B. Kosmatka. "An improved two-node timoshenko beam finite element". In: *Computers and Structures* 47.3 (1993), pp. 473–481. DOI: 10.1016/0045-7949(93)90243-7.

[182]   X. Lei and N. A. Noda. "Analyses of dynamic response of vehicle and track coupling system with random irregularity of track vertical profile". In: *Journal of Sound and Vibration* (2002). DOI: 10.1006/jsvi.2002.5107.

[183]   Amandine Marrel et al. "Calculations of Sobol indices for the Gaussian process metamodel". In: *Reliability Engineering & System Safety* 94.3 (Mar. 2009), pp. 742–751. DOI: 10.1016/J.RESS.2008.07.008.

[184]   Zili Li et al. "Improvements in Axle Box Acceleration Measurements for the Detection of Light Squats in Railway Infrastructure". In: *IEEE Transactions on Industrial Electronics* 62.7 (2015), pp. 4385–4397. DOI: 10.1109/TIE.2015.2389761.

[185]   Zilong Wei et al. "An Integrated Approach for Characterizing the Dynamic Behavior of the Wheel – Rail Interaction at Crossings". In: 67.10 (2018), pp. 2332–2344. DOI: 10.1109/TIM.2018.2816800.

[186]   Zhen Yang et al. "Numerical and experimental study of wheel-rail impact vibration and noise generated at an insulated rail joint". In: *International Journal of Impact Engineering* 113 (Mar. 2018), pp. 29–39. DOI: 10.1016/J.IJIMPENG.2017.11.008.

[187]   Y. Bezin et al. "Multibody simulation benchmark for dynamic vehicle–track interaction in switches and crossings: results and method statements". In: *Vehicle System Dynamics* (2021). DOI: 10.1080/00423114.2021.1959038.

[188]   Jonas Nitzler et al. "A generalized probabilistic learning approach for multi-fidelity uncertainty quantification in complex physical simulations". In: *Computer Methods in Applied Mechanics and Engineering* 400 (Jan. 2022). DOI: 10.1016/j.cma.2022.115600.

6

ACKNOWLEDGEMENTS

I am deeply grateful to have reached this moment, the completion of my PhD thesis. The journey has been a long and challenging one, and without the support of many, I could not have reached the end.

First and foremost, I would like to extend my heartfelt thanks to my promoters, Prof. Zili Li and Prof. Rolf Dollevoet. I owe a great deal of gratitude to Prof. Zili Li, who helped me get into TU Delft and has been my daily supervisor ever since. His extensive knowledge, expertise, and perceptive understanding of railway engineering have been invaluable in shaping my research and professional development. His patience and active encouragement and support were crucial during the times when I struggled with writing this thesis. My sincere gratitude also goes to Prof. Rolf Dollevoet for his valuable guidance and knowledge in practical railway engineering problems associated with my research. His broad and in-depth insights have been essential in deepening the practicality and application of my research. I also learned a lot from both of them about strong work ethics, which helps transform me from a student to a professional. Thank you, Zili and Rolf, for being such good mentors and role models these past years!

I cannot stress enough how much of a team effort this PhD journey has been. I am so grateful to have received help and support from many along the way. My thanks go to Dr. Alfredo Nunez for organizing the successful field test campaigns that provided the measurement data for this thesis. To Jan Moraal, Jurjen Hendriks, and Bojan Bogojevic, thank you for setting up and carrying out the ABA measurements. Thank you also to Dr. Shaoguang Li, Dr. Pan Zhang, and Dr. Ali Jamshidi for assisting with the field measurements. Dr. Pan Zhang also helped with the lab tests. Thank you to Dr. Zilong Wei and Dr. Xiangyun Deng for their guidance in developing the 3D finite element model. I would also like to express my appreciation to Dr. Maria Molodova for sharing her insights and details on the finite element model. Thanks to Dr. Yuanchen Zeng for preprocessing some of the measurement data and providing the nice photo on the cover of this thesis. My thanks also go to Dr. Arjen Zoeteman for his review of part of this thesis.

Some additional work has been done that is not included in this thesis but is definitely a valuable part of my PhD research. I thank Dr. Nico Burgelman for our collaborative research on the effects of wheelset flexibility, which was my first project after I arrived in Delft. Thank you to Anthonie Boogaard for introducing me to your test sites, patiently answering my questions about field tests, and helping me troubleshoot issues related to sensors and DAQ systems. To Ruud, Greg, and Ivan, thank you for accompanying me on site visits, day and night, and for sharing your expertise on everything related to railways.

This work would not have been possible without the financial support from the Chinese Scholarship Council. I would also like to acknowledge the support of the EU Horizon 2020 project NetiRail-Infra (Grant No. 636237) for the field test. Parts of the study have been funded by the EU Horizon 2020 research and innovation programme in the

I also want to acknowledge the colleagues (past and present) of the Railway and Pavement Engineering section for their support along the way. Special thanks to Jacqueline Barnhoorn for her daily assistance with various tasks, from the day I arrived in Delft to the final printing of this thesis. I would like to express my gratitude to Dr. Valeri Markine and Dr. Michael Steenbergen for the nice introduction course on railway structure design. Thank you to Dongya, Jin Gang, Xiangming, Yuewei & Zhou Hongxia, Haoyu, Lizuo, Qian Zhiwei, and Hongrui & Yongqiu for organizing various parties and activities during my first few years at Delft. Thank you, Siwarak, Wassamon, Taniya, and Omid, for the awesome lunch breaks and chats. My thanks also go to Meysam Naeimi, Maider Oregui, Lv Tao, Joris van Dijk, Ellard Groenewegen, Guo Yunlong, Wang Li, He Chunyan, Jia Wenli, Jin Yang, Gokul, Ren Fang, Yu Xinxin, for all the fun group activities and the wide-ranging discussions we've had about railways and beyond.

To my friends, Ke Lu & Yu Ye, Yang Zhen & Xiao Lin, Qin Yanxin & Wang Jing, Wang Ying & Natalie Zheng, along with their lovely little ones, thank you for the enjoyable trips and moments we shared together, and perhaps more importantly, for those without me, so that I could focus on writing this thesis while you kept my daughter happily occupied.

Finally, I would like to express my deepest gratitude to my family. Mom, Dad, Shen Xi, and Gao Yao, while we may be miles apart, your love, support, and constant belief in me have never faded. Being a member of this family is a source of great pride and joy for me, and I am grateful for everything you have done for me.

To my daughter, Yirui, thank you for constantly distracting me from (the stress of) writing this thesis. You may not realize it, but your endless energy and enthusiasm for life have kept me going on the days when I felt like giving up, and I am truly grateful for that.

To my wife, Miao Lei, while I am not sure if you understand any part of this thesis, I am confident that you know the tears and joy behind every word. I am so fortunate and grateful to have all your love and support throughout the journey. You made this thesis, along with many other milestones in our lives, possible. I owe you so much that transcends any words.

Chen Shen
February 2023
Delft, the Netherlands

Curriculum Vitæ

Chen SHEN

14-01-1989   Born in Xiangyang, China.

EDUCATION

2007–2011   B.Sc. in Civil Engineering
Tonji University, China

2011–2014   M.Eng. in Communication and Transportation engineering
Tonji University, China

2014–2019   Ph.D. student
Delft University of Technology, the Netherlands

EXPERIENCE

2011   Intern Engineer
Lingjing Architecture Design Company, Shanghai, China

2019–Present   Researcher
Delft University of Technology, the Netherlands

LIST OF PUBLICATIONS

11. **Shen, C.**, Deng, X., Wei, Z., Dollevoet, R., Zoeteman, A., & Li, Z. (2021). *Comparisons between beam and continuum models for modelling wheel-rail impact at a singular rail surface defect.* International Journal of Mechanical Sciences, 198, 1-16. [106400].

10. **Shen, C.**, Dollevoet, R., & Li, Z. (2021). *Fast and robust identification of railway track stiffness from simple field measurement.* Mechanical Systems and Signal Processing, 152, [107431].

9. **Shen, C.**, Li, Z., & Dollevoet, R. (2020) *A Novel Method for Railway Crossing Monitoring Based on Ambient Vibration Caused by Train-Track Interaction.* In: Klomp M., Bruzelius F., Nielsen J., Hillemyr A. (eds) Advances in Dynamics of Vehicles on Roads and Tracks. IAVSD 2019. Lecture Notes in Mechanical Engineering. Springer, Cham.

8. Zeng, Y., **Shen, C.**, Núñez, A., Dollevoet, R., Zhang, W., & Li, Z., "An interpretable method for operational modal analysis in time-frequency representation and its applications to railway sleepers". Accepted, Structural Control and Health Monitoring.

7. Wei, Z., **Shen, C.**, Li, Z., & Dollevoet, R. (2017). *Wheel-Rail Impact at Crossings: Relating Dynamic Frictional Contact to Degradation.* Journal of Computational and Nonlinear Dynamics, 12(4), [041016].

6. Wei, Z., Sun, X., Yang, F., Ke, Z., Lu, T., Zhang, P., & **Shen, C.** (2022). *Carriage interior noise-based inspection for rail corrugation on high-speed railway track.* Applied Acoustics, 196, [108881].

5. Yang, F., Wei, Z., Sun, X., **Shen, C.**, & Núñez, A. (2021). *Wheel-rail rolling contact behavior induced by both rail surface irregularity and sleeper hanging defects on a high-speed railway line.* Engineering Failure Analysis, 128, [105604].

4. **Shen, C.**, Sabbatini, L., Wei, Z., Dollevoet, R., & Li, Z. (2018). *Comparison of vehicle-track interaction models to simulate vertical wheel/rail impact contact.* In M. Spiryagin, T. Gordon, C. Cole, & T. McSweeney (Eds.), Dynamics of Vehicles on Roads and Tracks: Proceedings of the 25th International Symposium on Dynamics of Vehicles on Roads and Tracks (IAVSD 2017), 14-18 August 2017, Rockhampton, Queensland, Australia (Vol. 2, pp. 1-7). CRC Press.

3. **Shen, C.**, Wei, Z., Burgelman, NDM., Dollevoet, RPBJ., & Li, Z. (2016). *Effects of wheelset flexibility on the simulation of vehicle-track interaction at crossings.* In M. Plochl, M. Rosenberger, K. Six, & J. Edelmann (Eds.), Proceedings of the 24th international symposium on dynamics of vehicles on roads and tracks, IAVSD 2015 (pp. 1565-1574). CRC Press.

2. Zhang, P., **Shen, C.**, & Li, Z. (2021) *Numerical and experimental investigation on vehicle-track high frequency dynamic interaction via V-track test rig.* Abstract from 27th IAVSD Symposium on Dynamics of Vehicles on Roads and Tracks, Saint-Pertsburg, Russia.

1. Wei, Z., **Shen, C.**, Li, Z., & Dollevoet, R. (2015). *Modelling of wheel-rail impact-like interaction at crossing panel.* Abstract from 10th international conference on contact mechanics and wear of rail/wheel systems, Colorado Springs, United States.

This thesis transforms the way we understand and monitor rail infrastructure with a digital twin that merges measurement data and physics-based models to deliver instant insights. This thesis will be of particular interest to professionals in the rail industry seeking to answer the following questions: What are the key features in the measurement data? How can an accurate physics-based vehicle-track interaction model be developed for a specific problem? And, how can mearsurement data and models be combined to deliver actionable insights in real-time?

Measurements   +   Models   =   Instant insights